Changes in volume and extent of NW Svalbard glaciers using airborne lidar and digital photogrammetry.

Barrand, Nicholas Edward

Barrand, Nicholas Edward (2007) *Changes in volume and extent of NW Svalbard glaciers using airborne lidar and digital photogrammetry..* thesis, Swansea University.
http://cronfa.swan.ac.uk/Record/cronfa43028

Changes in Volume and Extent of NW Svalbard Glaciers using Airborne Lidar and Digital Photogrammetry

Nicholas Edward Barrand

School of the Environment & Society
University of Wales Swansea

Submitted to the University of Wales in fulfilment of the requirements for
the Degree of Doctor of Philosophy

October 2007

Declaration

This work has not previously been accepted in substance for any degree and is not being concurrently submitted in candidature for any degree.

Signed . . . .

Date . . . .

Statement 1

This thesis is the result of my own investigations, except where otherwise stated. Other sources are acknowledged by footnotes giving explicit references. A bibliography is appended.

Signed . . . .

Date . . . .

Statement 2

I hereby give consent for my thesis, if accepted, to be available for photocopying and inter-library loan, and for the title and summary to be made available to outside organisations.

Signed . . . .

Date . . . .

Summary

Monitoring fluctuations in the mass of the Earth's ice-sheets, ice-caps and glaciers is of fundamental societal importance due to their direct and measurable effects on global sea-levels. Uncertainty in the sea-level rise contribution from small glaciers and ice-sheets exists in part due to problems of sample size, distribution and scaling of long-term mass balance measurements. Photogrammetric processing of aerial photography archives offers the opportunity to reconstruct historical mass changes for regions where no such data are available. The ability to derive DEM measurements of glacier volume from photogrammetry is dependent on image texture for surface-matching and good quality, well-distributed ground reference data, which are often difficult to acquire. The aim of this research was to examine the quality (vertical elevation accuracy) of airborne laser scanning (lidar) data in order to utilise raw point data as ground control in historical photogrammetric models. This technique was then used to measure volume changes at NW Svalbard glaciers, thus circumventing the need to measure control in the field. Precision and accuracy of lidar data were found to vary both within and between the lidar swaths, and large numbers of raw lidar points were successfully used to control photogrammetric models. DEMs produced using lidar-derived points were optimised to produce volume change measurements comparable to those from lidar-lidar model differencing. Poorly controlled photogrammetry was shown to overestimate changes in glacier volume by as much as 50%. Two glaciers in NW Svalbard were shown to be losing mass at an accelerating rate, since 1966 and 1990 respectively, in response in increases in average summer air temperatures. Average present-day mass loss was greater than previously estimated, suggesting an increased contribution to sea-level rise from Svalbard glaciers. This method provides a powerful tool for exploiting image archives and may be used in the future to generate high-quality measurements of glacier mass balance.

Acknowledgements

First and foremost, I owe by far the most thanks to my supervisor, Tavi Murray. Tavi first conceived this project more than five years ago and has been there to witness the various twists and turns that have transformed it into something almost unrecognisable from the proposal I started work on in 2003. Her academic guidance, enthusiasm and energy have been invaluable to me and I count myself as incredibly lucky to have had Tavi as a supervisor. Having moved from Leeds mid-way through this project I am also thankful to Tavi for providing the opportunity to live in a beautiful part of the country and to be part of establishing Swansea as one of the UK's principal centres for glaciological research.

Tavi hasn't done all the supervisory work alone though, and for that I must thank Tim James and Stu Barr for the time and effort they have both given me. I've pestered Tim much more than anyone else over the course of this work and after wading through his sarcasm, insults and fraternal practical jokes, he has helped me more than anyone and provided both amusement and good company. I would like to thank Stu for his attention to detail, his generosity in giving up his time to discuss my work, and his triathlon training tips. I have also been fortunate enough to have a number of other individuals acting in semi-official supervisory roles. My thanks are therefore owed to Adrian Luckman, Jack Kohler (in particular for all the data) and Jon Mills, for their contributions to my training and help with numerous technical aspects of this work. I would like to thank my examiners Peter North and Andreas Kääb for their commitment and taking the time to read and discuss my thesis.

The first half of my time working on this thesis was spent at the University of Leeds. I would like to thank Stuart Lane and Katherine Arrell for their discussions within my research support group. I would also like to thank the following people for good times both in and outside the department; Patrice Carbonneau, Ransome Corney, Andy Evans, Mark Franklin, Rick Hunt, Chris Keylock, Dave Mould, Simon Reid, Rob Thomas and Dan Vickers. Thanks to the various members past and present of Leeds / Swansea Glaciology Group, particularly Peter Abbott, Tolly Adalgeirsdottir, Benedict Reinardy, Adam Booth, Aaron Lockwood, Addy Pope, Hamish Pritchard and Dave Rippin. I have enjoyed attending glaciological conferences worldwide and would like to thank Ted Scambos, Andrew Shepherd, Chris Shuman, Lonnie Thompson, David Vaughan and Jay Zwally for inspirational conversations. Within the UK community I have particularly enjoyed attending the IGS British Branch meetings and the company of Owain Bayley, Rob Bingham, Dave Chandler, Tris Irvine-Fynn, Dave Rippin, Nick Rutter, Andy Wright and Peter Wynn. I would also like to thank

Matt King, the NERC Geophysical Equipment Facility (particularly Alan Hobbs), past and present crew members of the NERC Airborne Research and Survey Facility and Cambridge University's Unit for Landscape Modelling

Most of the data in this thesis were collected over the course of three successive summer field seasons on Svalbard. Living and working in such a beautiful environment has undoubtably been among the most enjoyable experiences of my research career. I would like to thank Jack Kohler and Elisabeth Isaksson for their hospitality, and Chris Nuth, Ola Brandt and Harald Faste Ås for their help during our visit to Tromsø. I owe thanks to the following people for their company and assistance over the course of three summers in Ny Ålesund: Gry Selte, Frank Skogen, Hilde Western and the staff of Kings Bay AS; Geir Wing Gabrielsen, Kim Holmén, Wojtek Moskal and Trond Svenøe at Norsk Polarinsitutt; Leif Morten Tangen and Helge Digre at Statens Kartverk; Suzanne Bevan and Remko de Lange for their help in the field, and Alexandre Anesio, Jurjen Annen, Neil Arnold, Anita Asadullah, Claire Couldridge, Edward Hanna, Tim Hawes, Andy Hodson, Maarten Loonen, Birgit Mindl, Gareth Rees, Birgit Sattler and Daan Vreugdenhil. Brian Barrett deserves a mention all of his own for his amazing efforts in the field. I think Brian must be the ultimate field-worker as he never stopped lifting and carrying, inspired me out of torpidity on long and trying days, and even managed to cheer me up the day I remembered hot water but forgot the teabags. He's top of my list should I ever need someone to help drag 'boxy' around a glacier. Nick Cox provided logistical support, consummate professionalism, great company and the best stories (even if I did hear some more than once!). And, of course, thanks to Tris 'TDL' Irvine-Fynn and the recipient of Ny Ålesund's ten thousandth cup of coffee, Phil 'The Pocket' Porter, for the chat and the adventures on the green baize.

On a more personal note, I would like to thank my parents and my brother James for their support throughout. Additionally, the generosity of Horace Larner allowed to me to follow my interests and without which I probably would not be where I am today. Finally, I thank Johanne for the love, encouragement and so much more that have given me the happiest 4 years of my life.

This research was funded by a Natural Environment Research Council studentship (NER/S/A /11279), bursaries from the Remote Sensing and Photogrammetry Society and the National Snow and Ice Data Centre, and supported by the NERC Airborne Research and Survey Facility, the NERC Geophysical Equipment Facility, Applied Imagery and BAE Systems.

Contents

List of Figures

List of Tables

List of Abbreviations

Abbreviation / Acronym	
AAR	Accumulation area ratio
AB	Austre Brøggerbreen
ACIA	Arctic Climate Impact Assessment
ALA	Airborne laser altimetry
ALS	Airborne laser scanning
ALTM	Airborne laser terrain mapper
AMSL	Average metres above sea-level
API	Aerial photo interpretation
AR4	IPCC Fourth Assessment Report (also, TAR)
ARSF	Airborne Remote Sensing Facility (NERC)
ASCII	American Standard Code for Information Interchange
ASTER	Advanced Spaceborne Thermal Emission and Reflection Radiometer (NASA)
ATE	Automatic terrain extraction
ATM	Airborne Topographic Mapper (NASA)
ATM	also, Airborne Thematic Mapper
CCD	Charge coupled device
CW	Continuous wave
DEM	Digital elevation model
DGPS	Differential GPS
DTM	Digital terrain model
EA	Environment Agency
ELA	Equilibrium line altitude
GCP	Ground control point
GIS	Geographic information system
GPR	Ground penetrating radar
GPS	Global positioning system
GRACE	Gravity Recovery and Climate Experiment (NASA)
IGS	International GPS Service
IGS	also, International Glaciological Society
InSAR	Interferometric synthetic aperture radar
IPCC	Intergovernmental Panel on Climate Change
Ladar	Laser detection and ranging
LAS	Log ascii standard
Lidar	Light detection and ranging

Abbreviations continued

Abbreviation / Acronym	
LGM	Last glacial maximum
MEE	Maximum expected error
ML	Midtre Lovénbreen
NASA	National Aeronautics and Space Administration
NERC	Natural Environment Research Council
NP/NPI	Norsk Polarinstitutt
PDIM	Present day ice melting
PDOP	Position dilution of precision
PGR	Post glacial rebound
PPA	Principle point of auto-collineation
PPS	Principle point of symmetry
PW	Pulse wave
RMS	Root mean square
RMSE	Root mean square error
RSPSoc	Remote Sensing and Photogrammetry Society
SDE	Standard deviation of error
SE	Standard error
SLE	Sea level equivalent
SNR	Signal to noise ratio
SPOT	Systéme Pour l'Observation de la Terre
SPP	Single point position
SPRI	Scott Polar Research Institute
SRA	Satellite radar altimeter
SRTM	Satellite Radar Topography Mission (NASA)
TAR	IPCC third assessment report
TIFF	Tagged image file format
TIN	Triangular irregular network
ULM	Unit for Landscape Modelling
VLBI	Very long baseline interferometry
VNIR	Visible near infra-red
WE	Water equivalent
WGS84	World geodetic system (1984)

List of Symbols

Symbol Notation	Description
A_L	Laser ground footprint diameter (m)
b_b	Specific mass balance (base)
b_s	Specific mass balance (surface)
δV	Ice volume change (m^3)
δx	Scanning resolution (μm)
dx_{across}	Across-track point spacing (m)
dx_{along}	Along-track point spacing (m)
F	Laser pulse rate (KHz)
f_{sc}	Scan rate (Hz)
h_f	Flying height (m)
H	Ice thickness (m)
K	Camera rotation about the x axis (°)
l_p	DEM grid spacing (m)
${l_p}^2$	Pixel area (m^2)
M_a	Annual surface accumulation (m a^{-1})
M_b	Annual basal mass balance (m a^{-1})
M_c	Annual loss by iceberg calving (m^3 a^{-1})
M_m	Annual loss by surface melting (m a^{-1})
N	Number of scan points per line
p_{sample}	Sample density (points per m^2)
p_t	Vertical precision (m)
SW	Swath width (m)
s	Photo scale
$\bar{u}$	Depth averaged velocity (m a^{-1})
u_s	Horizontal component of velocity (m a^{-1})
v	Average flying speed (m s^{-1})
γ	Laser beam divergence (mrad)
Ω	Camera rotation about the y axis (°)
Φ	Camera rotation about the z axis (°)
θ	Scan angle (°)

Chapter 1

Introduction and Aims

1.1 Introduction

Monitoring of fluctuations in the mass of the Earth's ice-sheets, ice-caps and many glaciers is of fundamental societal importance due to their direct and measurable effects on global sea-levels. In addition, glacier fluctuations in a changing climate may have considerable impacts on the availability of water resources to downstream communities, hydroelectric power generation schemes and the prevalence of glacier hazards. In order to accurately gauge the contribution to sea-level rise of various components of the cryosphere there is a need to continue and extend existing records of glacier mass balance. Our knowledge of contemporary mass imbalance of the large Greenland and Antarctic ice-sheets has been transformed over the past 10 years by a series of satellite-based sensors measuring altimetric volume changes (e.g. Wingham *et al.*, 1998; Johannessen *et al.*, 2005; Zwally *et al.*, 2006), mass-budget using interferometric synthetic aperture radar (InSAR) (e.g. Rignot and Thomas, 2002; Rignot and Kanagaratnam, 2006), and observations of changing gravitational fields (e.g. Luthcke *et al.*, 2006; Velicogna and Wahr, 2006b). However, these techniques are limited in their temporal resolution to at most the last 15 years and are often unsuitable for small glaciers and ice-caps (outside Greenland and Antarctica) due to problems of data coverage and a variety of issues related to spatial resolution.

Small glaciers and ice-caps contributed 0.77 ± 0.22 mm a^{-1} to observed rates of sea-level rise between 1993 and 2003, an increase from 0.50 ± 0.18 mm a^{-1} for the period 1961-2003 (IPCC, 2007). This rate outweighs the estimated contributions from both the Greenland and Antarctic ice-sheets (0.21 ± 0.07 and 0.21 ± 0.35 mm a^{-1} respectively) for the same period. The uncertainties in these predictions derive in part from increased glacier dynamic behaviour in Greenland (e.g. Joughin *et al.*, 2004; Luckman *et al.*, 2006; Howat *et al.*, 2007) and West Antarctica (e.g. Shepherd *et al.*, 2001; Rignot *et al.*, 2002), and from problems of sample size distribution and scaling in global records of small glacier and ice-sheet mass balance. In order to reduce uncertainty in estimates of sea-level contribution from small glaciers and ice-caps there is a need to continue and extend current glacier monitoring programs. Improvements to both spatial and temporal resolution of mass balance records are required given that the data currently available are strongly biased towards North American and Western European glacier populations and that there are fewer than 40 glaciers worldwide with mass balance records exceeding 30 years in length (Braithwaite, 2002).

The collection of remotely-sensed data from sensors mounted on airborne platforms permits detailed coverage of glacier and ice-sheet surface topography at high-precision and resolution. These data offer widespread, synoptic coverage over potentially inaccessible areas and in many cases provide the highest-resolution datasets available. Advances in measurement and sampling rates offer the possibility of viewing and studying glaciers and glacial processes in unprecedented detail. Likewise, the development of new approaches to optimise and combine information from different airborne sensors has allowed users to beneficially exploit the strengths of each respective technique. In this thesis the techniques of digital photogrammetry and laser altimetry are combined to provide time-retrospective glacier surface models to examine changes in mass balance of a sample of glaciers on Brøggerhalvoya, NW Svalbard (Norwegian High Arctic).

1.2 Mass Balance of Arctic Glaciers

Glaciers and ice-caps in the Arctic (excluding the Greenland ice-sheet) cover an area of some 275 000 km^2, include both the heavily glaciarised archipelagos of the Norwegian, Canadian and Russian High Arctic and areas North of around 60° N in North America (Alaska), Scandinavia and Iceland, and contain enough water to raise sea-level by an estimated 0.5 m (Church *et al.*, 2001). As most of these ice masses exist at relatively high average air temperatures compared to other glaciated regions (e.g. Antarctica), they are expected to display a more rapid response to external climate forcings (ACIA, 2005), perhaps contributing as much as 20 cm sea-level equivalent (SLE) in the next 100 years (Church *et al.*, 2001). In addition, Arctic ice masses are thought to be particularly important within the global climate system due to regional-scale positive albedo feedbacks and interactions between ocean, atmosphere and sea ice which may amplify the effects of climate change (Cubasch *et al.*, 2001). Measurements of net surface mass balance from around 40 Arctic glaciers and ice-caps have shown that most glaciers have experienced predominantly negative balance over the last 20 years. This negative mean net balance has been countered slightly by some small positive balances at maritime Icelandic and Scandinavian glaciers, driven by increases in winter precipitation. The contribution of Arctic glaciers and ice-caps to sea-level rise has been estimated as 0.13 mm yr^{-1}, or >30% of the contribution of all small glaciers and ice-caps outside Greenland and Antarctica (Dowdeswell *et al.*, 1997). However, this contribution is probably an underestimate as it does not include any thinning rates observed at Arctic tidewater-terminating glaciers.

1.2.1 The Glaciology of Svalbard

The archipelago of Svalbard consists of a group of islands in the Arctic Ocean between 76°- 81° North and 10°- 35° East (Figure 1.1). The total ice-covered area of Svalbard is approximately 36 600 km^2 which makes it among the largest glaciated areas in the Arctic outside Greenland. Estimated total ice volume is around 7000 km^3, or SLE of ~0.02 m. Of a total of 1029 glaciers larger than 1 km^2 (Hagen *et al.*, 1993), annual mass balance records longer than 30 years exist for just 13, covering slightly more than 0.5% of the total glaciated area (Hagen *et al.*, 2003). Average net mass balance from these glaciers has been calculated as -0.55 m yr^{-1} or 0.056 mm yr^{-1} SLE; the strongest regional negative balance signal of land-terminating Arctic glaciers (Dowdeswell *et al.*, 1997). A study by Hagen *et al.* (2003) utilising data from both land and tide-water terminating glaciers estimated an average sea-level contribution of 0.01 mm yr^{-1} over the past 30 years. Recent studies incorporating thickness changes of both land and tidewater-terminating glaciers suggest that greater contributions to sea-level rise have occurred in the Canadian Arctic (0.064 mm yr^{-1}, (Abdalati *et al.*, 2004)) and Alaska (0.14 ± 0.04 mm yr^{-1} from the mid 1950s to mid 1990s and 0.27 ± 0.10 mm yr^{-1} from the mid 1990s to 2000/2001 (Arendt *et al.*, 2002)). The discrepancies reported between estimates of the mass balance of Svalbard glaciers and the potentially large contribution from tidewater-terminating glaciers suggest a need for improved observations of mass change. Reducing the uncertainties in these measurements should be a major goal of glaciological research on Svalbard.

1.2.2 Brøggerhalvoya, NW Svalbard

Brøggerhalvoya (The Brøgger Peninsula) is situated at 78° 55' N, 11° 56' E in NW Svalbard (see inset-box BH, Figure 1.1). The ~30 km long peninsula intersects Kongsfjorden to the North and Forlandsundet (between Spitsbergen and Prins Karls Forland) to the South and is dominated by a central belt of steep-sided mountainous topography rising to more than 1000 m above sea level (a.s.l.) in places. The majority of glaciers flow in a Northerly direction from the mountains, terminating on land some 50–75 m a.s.l. An outer belt of thick till deposits intersected by seasonal meltwater channels fringe the mountains and glaciated terrain (Hambrey *et al.*, 1999). Extensive moraine deposits are evident within forefield areas and have provided reconstructions of maximum ice extent and retreat history since the Last Glacial Maximum (LGM) (Bennett *et al.*, 1996).

The international scientific settlement of Ny Ålesund, situated on the Northern side of the Peninsula, provides the base for scientific studies in the fjord and its surrounds. Originally a coal mining settlement, the town was established as a scientific base in 1963 by the Norsk Polarinstitutt (NPI), is owned and operated by Kings Bay AS, and hosts permanent research bases funded by the governments of Norway, Germany, Great Britain, Italy, Japan, France, South Korea and China. Ny Ålesund provides the ideal base from which to study the glaciers of Brøggerhalvoya.

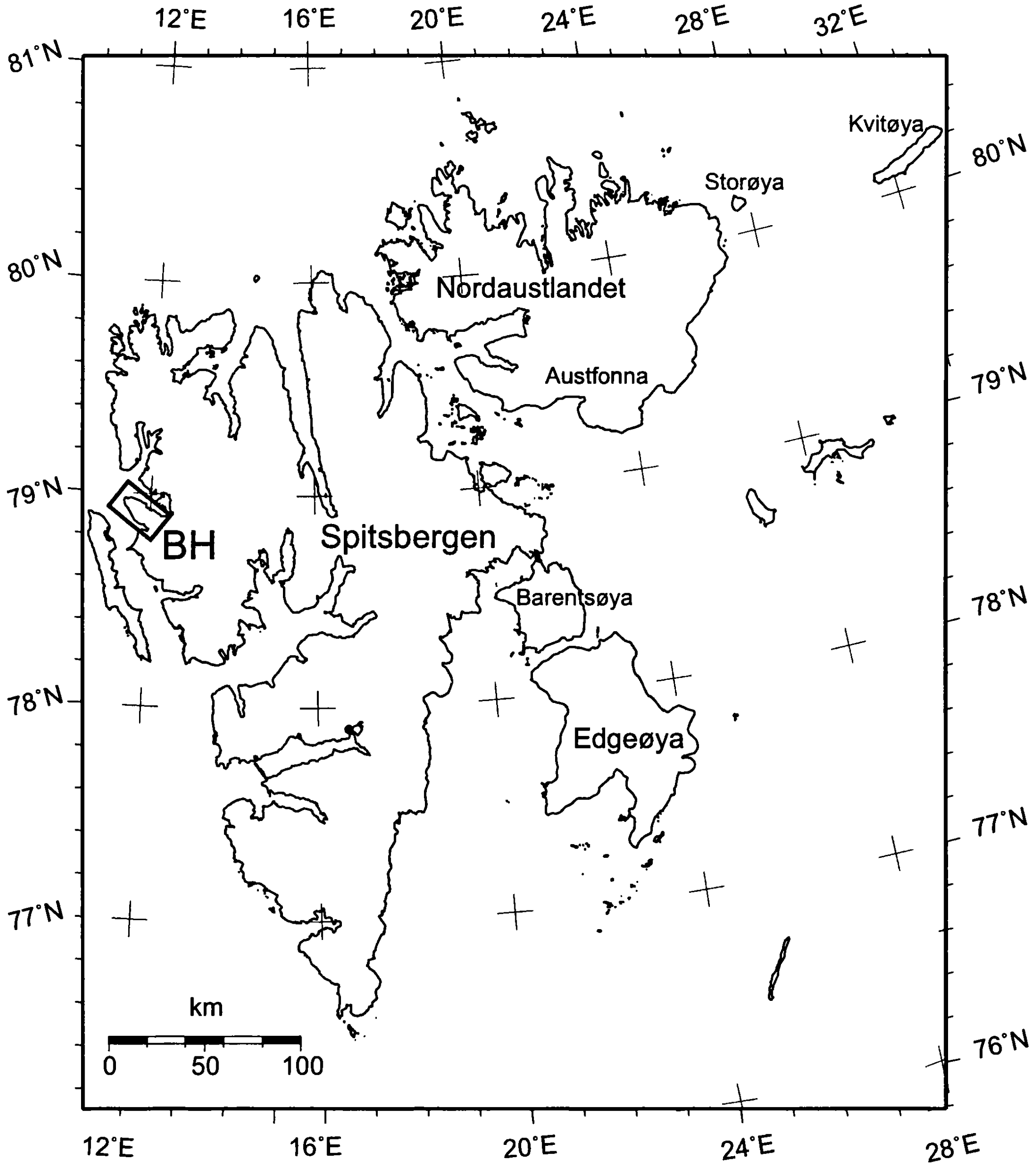

Figure 1.1: Map of the Svalbard archipelago including the largest islands Spitsbergen and Nordaustlandet and smaller islands Edgeøya, Barentsøya, Storøya and Kvitøya. Locations of the Austfonna ice-cap on Nordaustlandet and Brøggerhalvoya (BH) in the northwest are also marked.

This research focuses on polythermal Midtre Lovénbreen (ML) and the predominantly cold-based Austre Brøggerbreen (AB), two neighbouring valley glaciers located within 5 km of the settlement. These glaciers were chosen for study as they have the longest complete Arctic annual mass balance records (AB from 1966 and ML from 1967, to the present) with which remote-sensing estimates of mass change could be compared.

1.3 Airborne Remote-Sensing of the Cryosphere

The collection of topographic data from aircraft-mounted sensor platforms has become well-established within glaciological research, primarily as a result of the inaccessibility of remote field locations and the vast areas of land that comprise the cryosphere. In addition, various reconnaisance and exploration programmes have provided a wealth of remotely-sensed data, much of which has yet to be fully examined. Photogrammetry has a long and distinguished history of providing fundamental advances in our understanding of glaciers and glacial processes. The application of photogrammetric techniques to glacial environments has existed since the mid-19th century. Initial methodologies were restricted to the construction of 2-dimensional glacier profiles and the calculation of glacial retreat and changes in volume distribution over time by graphical methods (e.g. Finsterwalder, 1954). These changes, based on empirical measurements from contour maps, were limited due to their failure to measure profile thinning or thickening. Advances in analytical (e.g. Reinhardt and Rentsch, 1986; Etzelmüller *et al.*, 1993) and subsequently digital (e.g. Fox and Nuttall, 1997; Kääb and Funk, 1999) photogrammetry, in line with increased computer processing power and storage capability, have transformed our ability to generate and quantitatively analyse photogrammetrically-derived digital elevation models (DEMs).

The last 15 years have seen a shift from costly, user-intensive processing methods for deriving elevation information from airborne remote-sensing datasets, towards highly-automated, high-resolution, precise measurement techniques. Of these, airborne laser scanning (ALS, or lidar, light detection and ranging) has perhaps had the greatest impact. Developments in laser ranging technology and precise DGPS sensor positioning have allowed glaciologists to measure and map glacier and ice-sheet surface topography in unprecedented detail (e.g. Garvin and Williams, 1993; Krabill *et al.*, 1995a,b; Kennett and Eiken, 1997; Adalgeirsdóttir *et al.*, 1998; Bamber *et al.*, 2004). Datasets of lidar data have been collected over vast swathes of the cryosphere in order to determine ice volume changes (e.g. Sapiano *et al.*, 1998; Abdalati and Krabill, 1999b; Spikes *et al.*, 2003a; Bamber *et al.*, 2005). A decade of seminal studies (e.g. Krabill *et al.*, 1999, 2004; Arendt *et al.*, 2002) and widespread uptake of the technology have seen lidar become the benchmark method of acquiring accurate and precise airborne topographic data for measurements of glacier volume change and mass balance.

1.4 Thesis Aims

The main aims of this thesis are to make an assessment of the quality (elevation accuracy and precision) of swath-based airborne lidar data acquired over a High Arctic small valley-glacier, to utilise this data to construct photogrammetric DEMs without the need for field-measurements of ground control points (GCPs), and to use this new technique to examine the volume and geometry change of two Svalbard glaciers over the past 40 years. This information will be used to contribute to an estimate of the present day mass balance of Svalbard glaciers and their contribution to sea-level rise.

The specific aims are:

- To examine lidar elevation accuracy and precision using crossover (overlap) analysis and comparison with independent check data.
- To use 3-dimensional visualisation and image-processing tools to identify and extract lidar coordinates for use as photogrammetric GCPs.
- To process a series of historical glacier DEMs in order to measure changes in glacier geometry and extent.
- To assess the accuracy of DEMs constructed and the resultant error of glacier volume change measurements.
- To compare volume changes with field measurements of glacier mass balance and to place results in the context of archipelago-wide balance trends over the last 40 years.

1.5 Thesis Structure

Chapter 2 provides a background to the role of glaciers and ice-sheets in the global climate system. The potential contribution of the cryosphere, and in particular small glaciers and ice-sheets, to global sea-level rise are summarised here. Previous estimates of the SLE contributions from Svalbard and other Arctic components are given, with model predictions of future behaviour under a variety of climate scenarios and the case for continued observations highlighted. This is followed, in chapter 3, by a detailed review of the principles and application in previous glaciological studies of the two remote-sensing techniques used here; airborne lidar and digital photogrammetry. Following from this background material, chapter 4 outlines the airborne lidar and aerial photography datasets used to reconstruct glacier volume changes. The remainder of chapter 4 details a variety of experiments devised to rigourously assess the elevation accuracy and precision of airborne lidar data.

Chapter 5 contains photogrammetric processing results. This chapter outlines in detail the method of point identification and extraction and DEM processing optimisation experiments. Also included is a full DEM validation assessment using independent check data and the results of experiments designed to examine the effect on glacier volume change measurements of changes in photogrammetric model setups. The sixth chapter outlines the DEM differencing procedure and the results of a time-series of glacier volume change and mass balance measurements at Midtre Lovénbreen and Austre Brøggerbreen glaciers. The results presented in chapters 4, 5 and 6 are discussed in chapter 7. The data presented in earlier chapters are compared to other studies using photogrammetry to measure glacier surface elevation, volume and mass changes. Additional, mass balance results are compared to field-measurements, viewed in the context of changing meteorological drivers and compared to previous estimates of mass balance on Svalbard. Results are then placed in the context of global contributions to SLE from small glacier and ice-cap regions. A summary and the conclusions of this research, along with suggestions for future work, are provided in chapter 8.

Chapter 2

Mass Balance of Glaciers and Ice-Sheets

2.1 Introduction

This chapter introduces the cryosphere, and in particular small glaciers and ice-sheets, as sensitive indicators of climate change and substantial contributors to global sea-level rise. Within this context, particular emphasis is placed on Svalbard; its location and climatology, and its global significance as a cryospheric indicator of climate change. The cryosphere influences and is influenced by a variety of oceanic and atmospheric feedbacks and has particular global importance due to the effects on eustatic sea-level of changes in the mass of grounded ice. The first part of the chapter (section 2.2) details our current level of understanding regarding the contribution of glaciers and ice-sheets to global sea-level rise. Section 2.3 then describes the concept and measurement of mass balance, a key indicator for determining changes in the cryosphere which directly affect oceanic mass. The following section gives details of mass balance measurement techniques and results as applied to the large continental ice-sheets of Greenland and Antarctica. Following this, section 2.5 provides information regarding mass balance of smaller glaciers and ice-caps, including methods used to measure mass balance and a critical assessment of their relative strengths and weaknesses. The mass balance of Svalbard glaciers forms the basis of section 2.6, with reference to recent climate trends and published studies of mass balance using a variety of measurement techniques. This information is critically analysed and gaps in our knowledge are identified. Chapter sections 2.7 - 2.8 provide some modelled estimates of future changes in the mass balance of small glaciers and ice-caps, and a description of the case for extension and improvement of our observational record of mass changes on Svalbard.

2.2 Contribution of Glaciers and Ice-sheets to Sea-Level Rise

The cryosphere can be defined as the areas of the Earth's surface where water exists in solid form, including grounded and marine ice, permafrost, snow, sea-ice, lake and river-ice. The contribution to observed rates of sea-level rise between 1993 and 2003 from grounded ice, including the Greenland and Antarctic ice-sheets and other smaller glaciers and ice-caps, was estimated to be 1.19 ± 0.64 mm yr^{-1} (IPCC, 2007) (Table 2.1). The rate of sea-level rise from the same constituent components between 1961 and 1993, was 0.69 ± 0.71 mm yr^{-1}.

Source of sea-level rise	Rate 1961-1993 (mm yr^{-1})	Rate 1993-2003 (mm yr^{-1})
Thermal expansion	0.42 ± 0.12	1.6 ± 0.5
(Small) glaciers & ice-caps	0.50 ± 0.18	0.77 ± 0.22
Greenland ice-sheet	0.05 ± 0.12	0.21 ± 0.07
Antarctic ice-sheet	0.14 ± 0.41	0.21 ± 0.35
Sum of individual climate contributions to sea-level rise	1.1 ± 0.5	2.8 ± 0.7
Observed total sea-level rise[1]	1.8 ± 0.5	3.1 ± 0.7
Difference (observed minus sum of estimated climate contributions)	0.7 ± 0.7	0.3 ± 1.0

[1] Data prior to 1993 are from tide gauges and after 1993 from satellite altimetry

Table 2.1: Observed rates of global sea-level rise and estimated contributions from difference sources. Adapted from IPCC (2007)

The IPCC Fourth Assessment Report (AR4) states that 'mountain glaciers and ice-caps have declined on average in both hemispheres' contributing to sea-level rise. In addition, new data since the Third Assessment Report (TAR) (Church *et al.*, 2001) show that the losses from the Greenland and Antarctic ice-sheets have:

'very likely contributed to sea-level rise over 1993-2003. Flow speeds have increased for some Greenland and Antarctic outlet glaciers, which drain ice from the interior of the ice-sheets. The corresponding ice-sheet mass loss has often followed thinning, reduction or loss of ice-shelves or loss of floating glacier tongues. Such dynamical ice loss is sufficient to explain most of the Antarctic net mass loss and ∼ half of the Greenland net mass loss. The

remainder of the ice loss from Greenland has occurred because losses due to melting have exceeded accumulation due to snowfall' (IPCC, 2007).

The following sections give details of three methods by which mass balance of the large ice-sheets may be measured, the published studies that have used these methods to determine the quantity of mass change, and some of the important limitations of each of these studies. Following this, section 2.4 outlines mass balance measurement techniques for smaller glaciers and ice-caps, and section 2.5 gives details of the current level of understanding of Svalbard mass balance.

2.3 Mass Balance

Mass balance or mass budget studies are primarily concerned with changes in the mass of a glacier, and how the distribution of these changes varies in space and time, more specifically from year to year (Paterson, 2001). As changes in mass are typically accompanied by corresponding and direct changes in oceanic mass, measurements of mass balance are key for determining both the effects of climate change, and a number of important aspects of glacier dynamics. Climate variations cause changes in both the amount of snow falling on an ice body, and the amount of snow and ice lost by melting. Changes in mass as a result of climate fluctuations may also bring about a complex series of processes within the flow regime of the glacier which may result in changes to flow rates, the amounts of meltwater produced or the ice-front position. The measurement of mass balance forms the basis of most glacier monitoring schemes (e.g. Braithwaite, 2002) and may also be used in hazard assessments or predictions of the contribution of glacial meltwater to downstream human settlements or hydroelectric power generation plants. Glaciers mainly gain mass (accumulation) through snowfall and lose mass (ablation) by melting and iceberg calving. In addition to snowfall, the accumulation term of the mass balance budget equation may be added to through gain of avalanche material and freezing of rain. The ablation term may be complemented by ice sublimation and wind removal processes (Paterson, 2001). Mass balance at specific points are usually expressed as volumes of water equivalent (WE) per unit area of mass.

2.4 Ice-Sheet Mass Balance

The reduction in uncertainty of measurements of the sea-level rise contributions from the Greenland and Antarctic ice-sheets (Table 2.1) has arisen in large part thanks to advances in Earth observation technology resulting in more than a decade of satellite measurements. Greenland and Antarctica together contain enough ice to raise global sea-levels by ~70 m (Church *et al.*, 2001). Determining the sea-level contribution of these giant ice sheets has long been a goal of glaciological research. However, the size and scale of the problem and the consequent uncertainties involved in upscaling sparse point measurements, have made this an especially difficult task. The last 10 years have seen a transformation in our understanding of the mass changes of the two great ice-sheets thanks to at least 14 predominantly satellite-based estimates of ice-sheet mass balance. These estimates range from -366 to 53 Gt yr^{-1}, or 1.0 to -0.15 mm yr^{-1} SLE, and may explain much of the eustatic component of 20th century sea-level rise, although the precise contribution is still debated (Shepherd and Wingham, 2007).

2.4.1 Altimetric Ice Volume Change

Altimetric volume changes measured by aircraft and satellite, laser, and radar altimeters have provided a detailed picture of ice-sheet surface elevation changes (e.g. Wingham *et al.*, 1998, 2006; Krabill *et al.*, 1999, 2004; Johannessen *et al.*, 2005; Zwally *et al.*, 2006). The longest records to date span the period 1992 to 2003 and are comprised of radar altimeter data from the European Space Agency (ESA) satellites ERS1, ERS2 and Envisat (Davis *et al.*, 2005; Wingham *et al.*, 2006; Zwally *et al.*, 2006). Although these studies used the same data and calculate the same volume changes, differences in calculations of mass change occur due to different approaches for converting volume to mass (Shepherd and Wingham, 2007). Wingham *et al.* (2006) showed that an altimeter covering 73% of the Antarctic interior could produce mass change results that vary by 90 Gt yr^{-1} (360 Gt of ice is equivalent to 1 mm of eustatic sea-level rise) given the same calculation of volume change. As radar altimeter data degrades over slopes greater than 1°, and observed interior ice-sheet growth (along with marginal thinning) has been observed in Greenland (Johannessen *et al.*, 2005) and in parts of Antarctica (Davis *et al.*, 2005), this technique may underestimate mass loss. Satellite altimeters with smaller ground footprints such as the Geoscience Laser Altimeter System (GLAS) onboard NASAs Ice Cloud and Land Elevation satellite (ICESat), and in the future ESAs high-resolution radar altimeter CryoSat-2, will be able to partially avoid this problem.

Airborne lidar is well-suited for measuring steeply-sloping ice-sheet margins. Repeat surveys over Greenland have revealed widespread thinning at the margins and near balance in the ice-sheet interior (Krabill *et al.*, 2000a, 2004). Ground tracks of airborne lidar data are determined in pre-flight planning and given sufficient time and favourable weather conditions, large areas of coverage may be achieved. Repeat surveys over coastal outlet glaciers (Krabill *et al.*, 2004) and flight lines within the ice-sheet interior (e.g. Krabill *et al.*, 1995a, 2002) have allowed a detailed picture of ice surface elevation change. Along with marginal thinning and interior balance or slight thickening these surveys have revealed a regional picture of elevation changes, with the greatest mass loss occuring in south-east Greenland (Krabill *et al.*, 1999).

A problem common to all types of altimetric volume change measurements is that signal echoes or pulses are returned from the snow surface or near surface. This means that all measurements are highly sensitive to changes in snow accumulation and ablation. Ice core studies and model reanalyses reveal that fluctuations of snow accumulation and ablation about the mean may reach as much as 15 % in any individual year (van Lipzig *et al.*, 2002; Box *et al.*, 2006). As the density of snow differs from that of ice by a factor of three, decadal fluctuations in snowfall mass are exaggerated compared to those due to ice dynamics in observed volume change calculations (Shepherd and Wingham, 2007).

2.4.2 (Interferometric) Mass-Budget

The mass budget method compares gains due to snow accumulation with losses due to runoff, sublimation and iceberg calving. This approach now commonly uses ice surface velocities gained from interferometric synthetic aperture radar (InSAR) remote-sensing (e.g. Rignot and Thomas, 2002; Rignot and Kanagaratnam, 2006), which means that increases in flow speed can be identified. As well as accurate velocity data this approach requires knowledge of ice thickness (usually derived from airborne radio-echo sounding) and snow accumulation data. Similar to altimetric ice volume change estimates, accurate snow accumulation data is essential to this method. These data are generated from either metereological forecast models (e.g. Monaghan *et al.*, 2006b), snowfall accumulation from ice cores (e.g. Morgan *et al.*, 1991; Monaghan *et al.*, 2006a) or satellite observations of microwave temperatures which can be correlated with accumulation (e.g. Arthern *et al.*, 2006). In each case, these measures of accumulation are problematic; forecast models have poor accuracy (Monaghan *et al.*, 2006b), ice core records are only applicable to Antarctica where there is little or no surface melting and accumulation is spatially averaged from a handful of core sites, and microwave measurements depend on factors other than accumulation which may bias results. The InSAR approach requires image pair data acquired by tandem satellite missions which are currently unavailable, although derivation of velocities by speckle-tracking techniques may be possible (e.g. Joughin, 2002; Liu *et al.*, 2007).

2.4.3 Gravimetry

Gravitational surveys of the Greenland and Antarctic ice-sheets have been provided by data from the Gravity Recovery and Climate Experiment (GRACE) satellites. GRACE consists of 2 satellites in identical orbits separated by $\sim$220 km, using microwaves to monitor their separation distance and accelerometers and GPS to map the Earth's gravity field every 30 days. These monthly estimates of gravity fields can be used to estimate changes in Earth's mass distribution. Ice-sheet mass changes have been estimated using GRACE data (e.g. Velicogna and Wahr, 2005, 2006a,b; Chen *et al.*, 2006; Luthcke *et al.*, 2006) and predominantly show more negative changes than estimates provided by altimetry or mass budget approaches (Shepherd and Wingham, 2007). GRACE mass solutions however have no vertical resolution (Velicogna and Wahr, 2006b) and therefore do not reveal whether a gravity variation is caused by changes in post-glacial rebound (PGR, the visco-elastic response of the Earth to glacial unloading over several thousand years), changes in snow and ice at the ice-sheet surface, or changes in atmospheric mass above the ice-sheet surface. In addition to these effects, contamination from oceanic mass changes may also degrade results. GRACE observations are thought to be particularly sensitive to PGR, the effects of which are large and must be modelled independently. The PGR contribution can be much larger than uncorrected GRACE trends (e.g. Velicogna and Wahr, 2006b) and significant ice mass trends may not appear before PGR contributions are removed. For this reason, GRACE results are particularly sensitive to the choice of PGR model used. Although GRACE records are short (presently 5 years) they have been used to show accelerated melting of the Greenland ice-sheet (Chen *et al.*, 2006; Velicogna and Wahr, 2006a), and at improved spatial resolution, to show Greenland mass loss by drainage basin (Luthcke *et al.*, 2006).

2.5 Mass Balance of Small Glaciers and Ice-Caps

Small glaciers and ice-sheets, defined as glaciers and ice-sheets outside the large Greenland and Antarctic ice-sheets, account for ~4% of the Earth's surface and 0.5% of the total volume of ice on land. If this ice were to melt completely it would account for ~0.5 m of global sea-level rise (Meier, 1984; Dyurgerov and Meier, 1997). The contribution to sea-level of small glaciers and ice-caps currently outweighs the contributions from both the Greenland and Antarctic ice-sheets (Table 2.1), and is thought likely to continue at least into the next century (Meier, 1984; Church *et al.*, 2001). Uncertainty in estimates of the causes and future changes in global sea-level arise in part from inaccurate and incomplete records of mass change of small glaciers and ice-sheets. The concept of mass change is used to estimate the contribution of melt from individual ice bodies, via specific measurements of glacier mass balance.

2.5.1 Methods of Determining Mass Balance

2.5.1.1. Glaciological / 'Field' Mass Balance

In a glaciological context the term 'mass balance' is used in two ways, each with distinctly difference meanings. The terms *specific mass balance* and *local mass balance* are defined according to Hagen and Reeh (2003), wherein more detailed explanations may be found. The term *specific mass balance* designates the sum of accumulation and ablation at a specific points on the ice. This signal may be positive or negative as it depends on local conditions, specifically whether accumulation or ablation dominate at the point where the measurement is taken. The specific mass balance does not give any information regarding changes in ice thickness or changes in the mass of ice in a vertical column through the glacier. This means that the specific mass balance signal may be complicated or even overruled by changes due to the effects of the gradient of the horizontal ice flux. The *local mass balance* is therefore defined as the local change in ice thickness or change in mass in a a vertical column at a specific point on the glacier. Local mass balance at a certain locality of an ice-sheet or glacier is expressed by:

$$\delta H/\delta t = b_s + b_b - F\left[H\left(\delta u_s/\delta x + \delta v_s/\delta y\right) + u_s \delta H/\delta x\right], \tag{2.1}$$

where H = ice thickness, t = time, b_s and b_b are respectively specific mass balances at the surface and the base of the ice, u_s and v_s = horizontal components of the surface velocity (u_s is in the direction of ice flow), and $F = \bar{u}/u_s$ ($\bar{u}$ = depth-averaged velocity). Ice flow is assumed to be in the x direction and all quantities are expressed in ice equivalents (Reeh and Gunderstrup, 1985; Reeh, 1999).

'Mass balance' can also be used as a global indicator of the total change in mass over an entire glacier or region of glacier. Integrating local or specific mass balance measurements over the total glacier area is an approach which places emphasis on this particular interpretation of the term. This can be done by integrating the local or specific balance, and subtracting the loss through possible vertical boundary surfaces such as calving fronts (Hagen and Reeh, 2003). The *total* mass balance equation is therefore expressed as:

$$\delta v/\delta a = M_a - M_m - M_c - M_b, \tag{2.2}$$

where the term $\delta v/\delta a$ represents the annual ice volume change per year, M_a = the annual surface accumulation, M_m = the annual loss by surface ablation, M_c = the annual loss by iceberg calving and M_b = the annual basal mass balance (melting of ice). All volumes are expressed in terms of ice equivalents. For land-based glaciers outside geothermally active regions it may be assumed that M_b is zero or negligable. Equation 2.2 suggests that the total mass balance of a glacier or ice-sheet can be determined in two distinct ways: (i) the budget method whereby each term on the right side of the equation is determined seperately; and (ii) direct measurement of change in volume by monitoring surface elevation change at different time intervals. Obtaining local mass balance from equation 2.1 requires measurement of the specific balance at a number of individual points along with horizontal ice velocity and ice thickness.

2.5.1.2. Limitations of the Glaciological Method

The budget method of measuring small glacier and ice-cap mass balance has a number of problems. For economic and logistical reasons (problems of access, very remote areas, crevasses), full surface mass balance programmes can be problematic or impossible to accomplish. Determining mass balance from the total mass budget approach or a series of local mass balance measurements also requires an adequate sampling strategy. A number of authors have suggested that a measuring density of one stake per km^2 is sufficient for small valley glaciers (accumulation and ablation being measured using a stake and snow-pit approach, see Østrem and Brugman (1991), for comprehensive details), with a higher density ten per square kilometer staked area to provide a reliable interpolation function (Funk *et al.*, 1997; Cogley, 1999; Fountain and Vecchia, 1999).

The dominant gradient of mass balance for smaller glaciers is thought to be related to altitude rather than transverse variations, therefore up-glacier stake lines are usually measured, requiring access to most of the glacier and often including ice zones at increasing altitudes. It may be extremely difficult or impossible to gain access to all but a few areas of a glacier resulting in an inadequate sampling density. A number of studies have also described varying components of systematic error in the individual terms of the budget method when compared to direct measurements of surface elevation using models controlled by fixed reference features (Krimmel, 1999; Østrem and Haakensen, 1999). As errors associated with traditional mass balance measurement tend to be systematic, geodetic measurement (see below) is thought to be more accurate over longer time scales (Cox and March, 2004). In some studies (e.g. Elseberg *et al.*, 2000) geodetic balances have been used to adjust glaciological balances.

Mass balance may also be derived by the spectral method when changes in the mass of a glacier are inferred from changes in the surface albedo of the ice surface and energy balance modelling of related meteorological parameters (e.g. Zuo and Oerlemans, 1996; Brock *et al.*, 2000; Greuell and Oerlemans, 2004).

2.5.1.3. Geodetic Mass Balance

The $\delta v/\delta a$ term of equation 2.2 may be solved to provide direct measurement of ice volume change and thus average total net mass balance of a glacier over a given time period. This is done by calculating geometry changes of the entire ice surface, or changes in altitude integrated over the whole area of the glacier (Hagen and Reeh, 2003). By far the easiest and most efficient way of obtaining reliable volume changes is by subtracting two digital elevation models (DEMs) of the glacier surface at the beginning and end of the time period under study. Repeat ice thickness measurements throughout a single year would show considerable variety; the greatest thickness being in late spring/ early summer and the minimum thickness during late summer. The time period in between two successive summer surfaces t_1 and t_2 (surfaces of minimum thickness in two consecutive years) is known as the balance year. If time t_m is an intervening maximum thickness, then t_1 to t_m is known as the summer season and t_2 to t_m the winter season. Timing of data or imagery collection is therefore important. The resulting DEM ideally should show the glacier at or close to the end of the balance year. When this is not the case, resultant changes may partly reflect the fact that timing of melt varied between seasons rather than year-on-year changes in mass. If DEMs are created before the end of the summer it is recommended that ablation data between the time of collecting the DEM and the end of the balance year are provided.

In order to infer changes in mass balance from changes in volume, constant ice density must be assumed. This assumption is probably reasonable in the case of most sub-polar ice masses where the depth of the firn layer (the compacted and wetted snow overlying the glacier ice that has survived one summer without itself being turned to ice) is usually less than a few metres (Paterson, 2001). This assumption however, does not hold for the ice sheets of Antarctica and central Greenland where the firn layer can be more than 100 m deep, and contain snow and ice of a variety of densities. Should this criteria be satisfied then there are a number of ways in which direct measurements of surface elevation change and subsequent mass balance may be generated. These can be divided into geodetic surface point or profile measurements, and measurements by differencing elevation surfaces or profiles derived from active or passive optical imaging sensors mounted on remote platforms.

Surface geodetic measurements are used to derive point or profile comparisons of like areas on the surface of a glacier. Measurements are timed to coincide with either the end of the melt season and its corresponding minimum ice thickness or (for operational or logistical reasons such as ease of transport) at earlier, equivalent times in the balance year and in combination with ablation measurements. Methods used to derive surface measurements commonly include traditional survey techniques using theodolite and distance meter, analysis of topographic maps generated using surveying techniques (e.g. Andreassen, 1999; Krimmel, 1999) or differential GPS profiling (e.g. Eiken *et al.*, 1997; Jacobsen and Theakston, 1997; Hagen *et al.*, 1999).

2.5.1.4. Geodetic Mass Balance: A Remote-Sensing Approach

Measures of mass balance using the budget and surface geodetic approaches rely on expensive, difficult and labour-intensive fieldwork. The total number of glaciers world-wide is not known precisely but is thought to number more than 160 000. Investigation of this number of glaciers, totalling ~4% of the Earth's surface, most often in extremely remote and challenging environments, is particularly suited to the synoptic coverage offered by modern remote-sensing methods. Mass balance can be measured by solving the $\delta v/\delta a$ term of equation 2.2 using differenced DEMs or profile measurements derived from remotely-sensed data. There are a number of ways of generating DEMs from satellite data including stereo processing of imagery from combined nadir and backward-looking satellite sensors such as the VNIR band of the Advanced Spaceborne Thermal Emission and Reflection Radiometer (ASTER) (e.g. Kääb, 2004; Howat *et al.*, 2007) and Systéme Pour l'Observation de la Terre (SPOT) (e.g. Berthier *et al.*, 2004), and from fixed-baseline interferometric radar processing of Shuttle Radar Topography Mission (SRTM) data (Rabus *et al.*, 2003). However, validation studies have shown that these techniques may suffer from systematic elevation errors of greater than 10 m (San and Suzen, 2005; Berthier *et al.*, 2006).

The issues of spatial resolution and achievable elevation accuracy from satellite stereo-based DEM retrieval techniques means that the most accurate remote measures of small glacier volume and geometry change are achieved using data collected from an airborne sensor platform. Airborne remote-sensing permits collection of the highest-resolution data available and given the right conditions, sub-decimeter elevation accuracy may be achieved from photogrammetric and laser altimetric processing. A comprehensive review of the background, principles and glaciological applications of both airborne lidar and digital photogrammetry is provided in chapter 3.

2.5.2 Observations of Small Glacier and Ice-Cap Mass Changes

Small glaciers and ice-caps contributed 0.77 ± 0.22 mm a^{-1} to observed rates of sea-level rise between the period 1993–2003 (IPCC, 2007). This represents an increase from the estimate of 0.50 ± 0.18 mm a^{-1} for the period between 1961 and 2003 (Table 2.1) (IPCC, 2007). An early estimate by Meier (1984) found that small glaciers may account for up to 30% of the observed sea-level change during the last 100 years. This estimate was severely constrained by the paucity of long-term mass balance data as at the time only 25 glaciers worldwide had been monitored for more than 40 years. Based on data from just 21 glaciers, Meier (1984) calculated that small glaciers were contributing 0.46 ± 0.26 mm y^{-1} to global sea-levels. Field-measured winter, summer and net balances are now calculated every year for more than 300 glaciers worldwide as part of the World Glacier Monitoring Service (WGMS) program (Haeberli, 1998). The most recent and comprehensive collection of small glacier and ice-cap direct mass balance measurements is provided by Kaser *et al.* (2006). This paper collects and summarises global estimates of mass balance based on three approaches: arithmetic averaging (Cogley, 2005), area-weighting (Ohmura, 2004; Dyugerov and Meier, 2005), and polynomial spatial interpolation (Cogley, 2005). These measures show broad agreement since 1960, slightly negative mass balance around 1970, and increasingly negative balances since then. Excluding all peripheral glaciers in Greenland and Antarctica, global average specific balance for 1961–1990 was -219 ± 112 kg m^{-2} y^{-1}, giving a SLE contribution of 0.33 ± 0.17 mm a^{-1}. For the time period 2001–2004 the equivalent figures are -510 ± 101 kg m^{-2} y^{-1} or 0.77 ± 0.15 mm a^{-1} SLE (Kaser *et al.*, 2006).

Measurements by geodetic methods were mostly omitted from the work of Kaser *et al.* (2006) as these measures have variable time spans (and are likely to yield less information about temporal variability) and were therefore difficult to assimilate into their assessments based on annual direct measures. A number of studies have measured region-wide glacier volume changes from areas for which little or no field-measured mass balance data exists. Volume changes of the largest 63 glaciers in the northern and southern Patagonian icefields were derived by comparing SRTM elevations with earlier cartographic data (Rignot *et al.*, 2003). During the period 1963/1975–2000 these glaciers lost ice at a rate of 0.042 ± 0.0002 mm yr^{-1} SLE. Between the years 1995–2000 average thinning rates doubled to 0.105 ± 0.011 mm yr^{-1}. The authors note that the observed mass losses cannot be fully explained by changes in surface mass balance but also require increased dynamic ice discharge. This may be triggered by increased tidewater glacier calving, or increases in meltwater production enhancing basal sliding.

A similar dynamic thinning mechanism has been suggested for Alaskan glaciers (Arendt *et al.*, 2002). A combination of cartographic maps and contemporary airborne laser altimetry revealed an average rate of thickness change of -0.52 m yr^{-1} from 67 glaciers. These glaciers in Alaska and neighbouring Canada cover ~90,000 km^2, or 13% of the small glacier and ice-cap population. This study extrapolated measured volume change profiles to over ~20% of the total glaciated area of Alaska and neighbouring western Canada and found a total annual volume change of -52 ± 15 km^3 yr^{-1}, equivalent to sea-level rise of 0.14 ± 0.05 mm

yr^{-1}, from the mid 1950s to the mid 1990s. Repeat measurements of 28 glaciers between 1995–2000/2001 showed an increased thinning of -1.8 m yr^{-1}. Extrapolations lead to a SLE estimate of 0.27 ± 0.10 mm yr^{-1} throughout the 1990s, suggesting that Alaskan glaciers provide the largest glaciological contribution to sea-level rise yet measured. Repeat airborne laser altimetry surveys over the major ice-caps of the Canadian Arctic archipelago in spring 1995 and 2000 revealed substantial low elevation thinning leading to mass balance estimates of -25 km^3 yr^{-1}, or 0.064 mm yr^{-1} SLE (Abdalati *et al.*, 2004). This places the Canadian Arctic as a substantial contributor to global sea-level rise, albeit less so than small glaciers and ice-caps of the Patagonian, Alaskan and western Canadian icefields.

2.6 Svalbard Mass Balance

This section provides information regarding mass balance measurements made on Svalbard. The available data and published work include a variety of measurement approaches including a few long-term field monitoring programmes, one-off and repeat airborne survey sorties, and gravity-derived direct measurements of mass change.

2.6.1 Location and Climatological Regime

The Svalbard archipelago is located within the Arctic ocean, between 74° and 81° North, and 10° and 35° East, on the north-west corner of the Barents Shelf section of the European continental shelf. Svalbard consists of the islands Spitsbergen, Nordaustlandet, Edgeøya, Barentsøya, Kvitøya, Storøya, Hopen, Prins Karls Forland, and a number of smaller land masses (Figure 2.1). The archipelago experiences anomalously warm average temperatures relative to other land masses at similar latitudes thanks to the warming effect of the West Spitsbergen Current, an extension of the warm North Atlantic Current (or Gulf Stream). Air temperatures are predominantly determined by two prevailing air circulation systems; (i) the transport of mild air from lower latitudes via North Atlantic depressions, and (ii) colder Arctic north-easterly winds caused by areas of low pressure near Iceland and high pressure over Greenland and the Arctic Ocean (Hagen *et al.*, 1993). The contrast between these two systems is greatest in winter and causes summer mean air temperatures to range between 4–5°C, and a winter mean of around -15°C, the lowest temperatures being in the north and east of the archipelago (Hagen *et al.*, 1993). This temperature variation results in substantial sea-ice cover to the north and east of Svalbard for 8-9 months of the year and relatively little fjord ice at southern and westerly locations into the winter months.

The precipitation regime of the region brings in approximately 400 mm of snow per year on the Western coast, with around half as much in central inland areas. Low pressure passing across the Barents sea brings easterly winds that deposit the highest precipitation

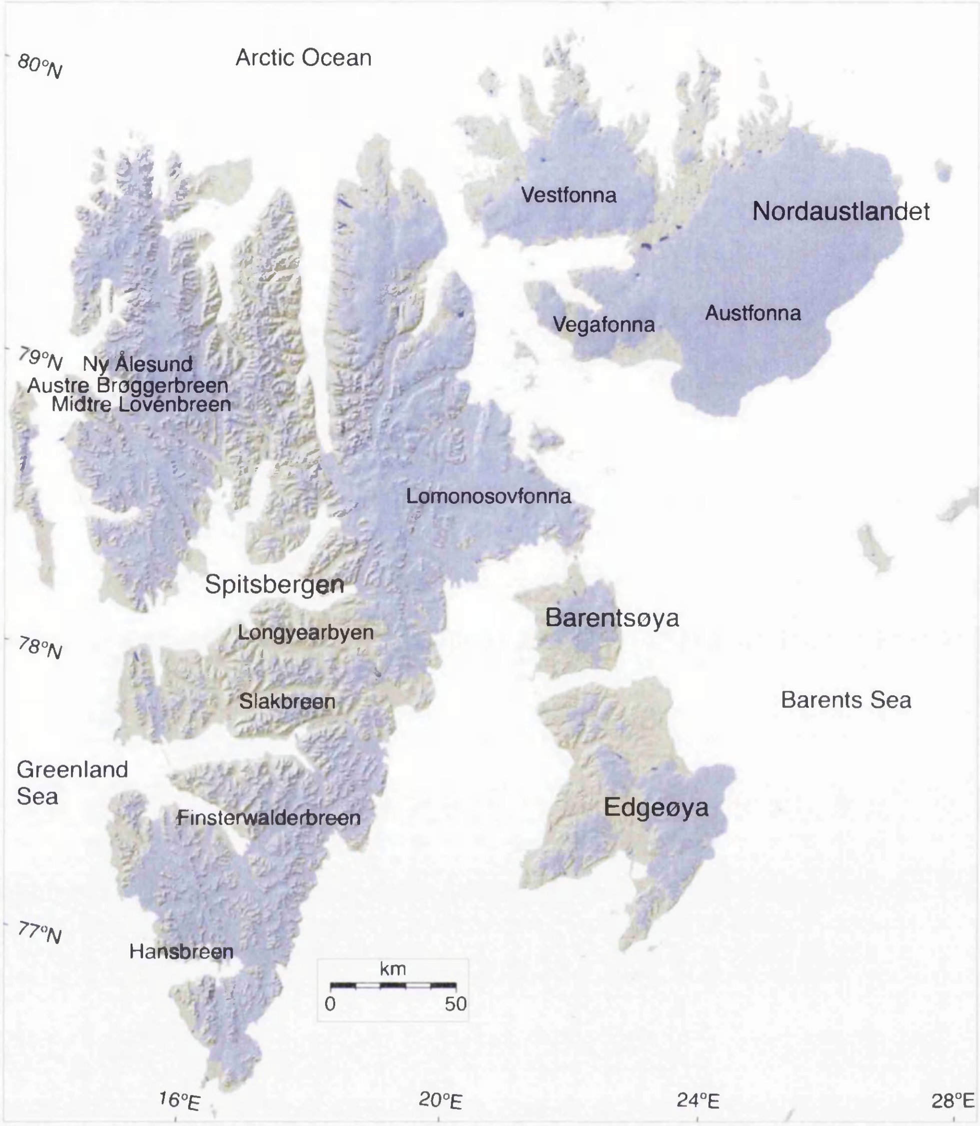

Figure 2.1: Image of Svalbard labelled with island names and locations of the settlements of Longyearbyen and Ny Ålesund, and glaciers referred to in this chapter. Image is based on the Norsk Polarinstitutt digital elevation model

to the eastern and southern parts of the archipelago (Hagen *et al.*, 1993). Temperature and precipitation records collected by the Norwegian Meteorological Institute (met.no) at Longyearbyen show two clear warming periods since records began in 1910 (Figure 2.2). Relatively rapid warming took place between 1915 and 1925, whereby average summer temperatures rose by ~3.5° C. Following a period of relative stability or slight cooling from 1925 to around 1965, temperatures have risen on average 0.5° C per decade up to the present. Oxygen isotope records from the highest ice-cap on Spitsbergen (Lomonosovfonna) indicate that the 20th century warming evident in the instrumental record is unprecedented within

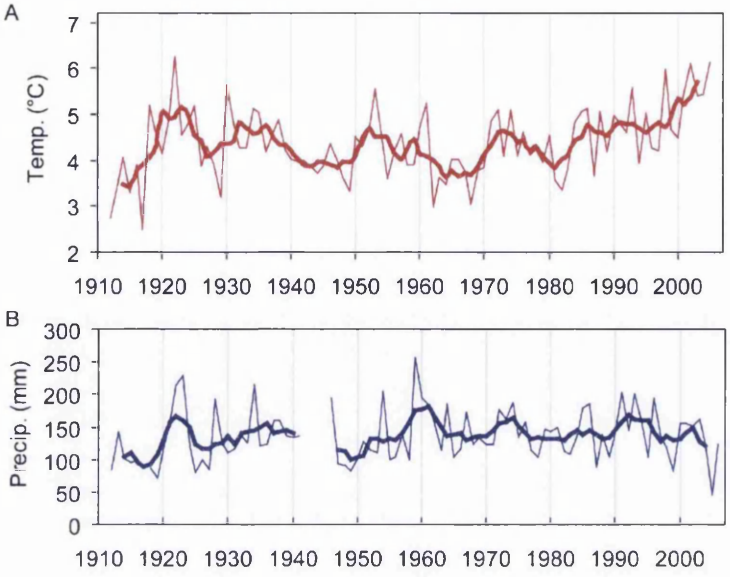

Figure 2.2: Mean summer (June to August) temperature (A) and summed winter precipitation (B) for Longyearbyen, Svalbard, with 5 year moving averages. Adapted from (Kohler *et al.*, 2007).

the last 400 years (Isaksson *et al.*, 2005).

Precipitation data from Longyearbyen show a relatively stable long term trend with a slight decrease in winter precipitation from around 1990 onwards (Figure 2.2). However, a more complicated regional picture of precipitation change is suggested by Hansen-Bauer and Førland (1998) and Førland and Hansen-Bauer (2002) who present an instrumental record of precipitation increases from the west coast of Svalbard, on the order of around 30% from 1912 to 1996 and 1.7% per decade since the late 1960s. This finding appears to be supported by evidence from a Lomonosovfonna ice core, which shows a 25% increase in accumulation rate over the latter half of the 20th century compared to the years 1715–1950 (Pohjola *et al.*, 2002).

2.6.2 Direct Mass Balance Measurements

Austre Brøggerbreen (AB) and Midtre Lovénbreen (ML), west Spitsbergen, have the longest complete Arctic annual mass balance records, extending respectively from 1966 and 1967 to the present. Further south, Finsterwalderbreen has measured balances every other year since 1950. Mean annual specific net balances were -0.43 m and -0.37 m for AB and ML respectively, with only one year of positive net mass balance, thought likely to be caused by anomalously low summer temperatures. The mass balance of AB has been statistically reconstructed to show an ice loss of 35 m averaged over the glacier surface over the last 77 years (Lefauconnier and Hagen, 1990). Finsterwalderbreen showed just two years of net positive balance for the period 1950 to 1968 (Hagen and Liestøl, 1990). An averaged value of Svalbard glacier mass balance derived from measurements at AB, Finsterwalderbreen and Bertilbreen gave -0.55 m yr^{-1}, or 0.056 mm yr^{-1} SLE (Dowdeswell *et al.*, 1997). This estimate placed Svalbard as the largest contributor to sea-level rise of any Arctic region outside Greenland. However, the measurements comprising this sample do not include tidewater-terminating glaciers and are heavily weighted towards smaller, lower-altitude, western Svalbard valley glaciers.

Direct measurements of mass balance were combined by Hagen *et al.* (2003) with point net balances from shallow ice cores, snow-distribution maps from depth-probes and GPR, and ELA distribution maps to produce net balance per altitude curves, representing spatial variability in mass balance for each area. Hagen *et al.* (2003) found total net surface balance, combining all regions of Svalbard, to be slightly negative at -0.5 ±0.1 km^3 yr $^{-1}$ giving a specific net balance of -120 ± 30 mm yr^{-1} WE. The contribution of ice-caps and glaciers on Svalbard to sea-level rise was then estimated to be 0.01 mm yr^{-1}, averaged over the last 30 years, an estimate significantly less than that of Dowdeswell *et al.* (1997). This value is sensitive to measurements of accumulation, which itself varies spatially across the archipelago, and does not include data from more than a few calving glaciers.

2.6.3 Geodetic Measurements of Svalbard Mass Balance

Geodetic measurements of glacier volume change and mass balance at two glaciers for which field-measured mass balance data exist (ML and Finsterwalderbreen) suggest that the glaciological method may underestimate the negative mass balance of Svalbard glaciers. Rippin *et al.* (2003) calculated the mean annual mass balance of ML between 1977 and 1995 to be -0.61 m yr^{-1} WE, which is substantially more negative than the -0.35 m yr^{-1} WE derived from field measurements. They also report a reduction in glacier surface area of 0.9 km^2, equivalent to an annual rate of ~0.05 km^2 and frontal retreat of ~150 m, equivalent to 8.3 m a^{-1}. There is some doubt as to the validity of these results however, given that the error associated with their volume change calculations (± 0.7 m yr^{-1} WE) exceeded the measured changes in glacier volume. However, an energy balance modelling study calculated the mean annual balance of ML between 1980 and 1989 as -0.44 m yr^{-1} WE, compared to a field-measured annual balance of -0.27 m yr^{-1} WE for the same period (Fleming *et al.*, 1997). Similar findings were reported for Finsterwalderbreen in southwest Spitsbergen where the mean annual balance between 1970 and 1990 derived from geodetic comparison of repeat DEM surfaces was -0.65 m yr^{-1}, compared to -0.45 m yr^{-1} from field measurements between 1950 and 1995 (Hagen *et al.*, 2000). Rippin *et al.* (2003) suggest that these discrepancies may result from higher net ablation towards glacier margins than centrelines due to the influence of long-wave radiation or advection of turbulent energy from valley sides, and/ or lower net accumulation towards the glacier margins than the centreline due to the effects of valley sides on winter accumulation. This is plausible given that modelled spatial patterns of surface energy balance and therefore melt have been shown to be highly sensitive to both glacier topography and topographic shading at the solar zenith angles common to high-latitude glaciers such as ML (Arnold *et al.*, 2006b).

Recent analysis of improved geodetic measurements of volume change at ML using data from topographic maps and photogrammetric and lidar-derived DEMs show a clearer agreement with field-measured mass balance data (Figure 2.3). In addition, this study showed that glaciers on Spitsbergen have been losing mass at an increasing rate over the past four decades (Kohler *et al.*, 2007).

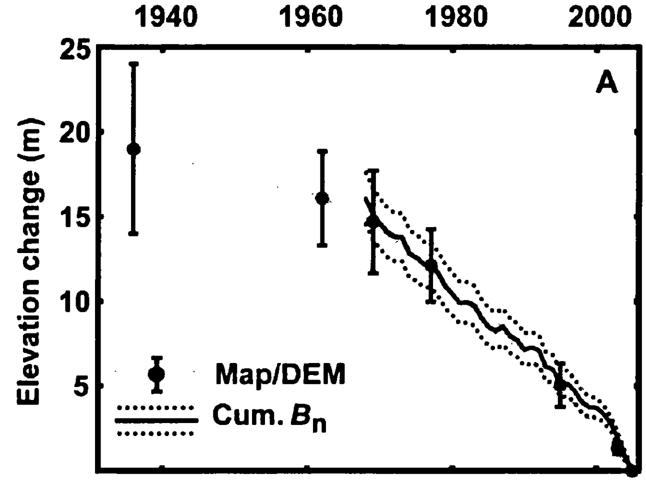

Figure 2.3: Average elevation change on ML (black circles) derived from differencing contour maps and DEMs relative to a 2005 lidar DEM, with error bars obtained from differences of low-slope, non-glaciated terrain. Black line shows cumulative net mass balance from field measurements with accumulated annual error of ± 0.25 m. Adapted from Kohler *et al.* (2007).

Glacier geometry and elevation changes on Spitsbergen have been estimated for the period 1936/ 1938 to 1990 by Nuth *et al.* (2007). This study assessed the accuracy of the oldest topographic map series of Spitsbergen and then compared them to DEM coverage of the island from 1990 aerial photographs. Although the precision of 1936/ 1938 elevation information is low, comparison with known surge events suggests reasonable accuracy of the datasets. A total of 5123 km^2 of the 20000 km^2 glaciated area was analysed and showed a 35% reduction in glaciated area, total volume change of -96.92 ± 2.16 km^3, and mean annual balance of -0.38 m yr^{-1} between the two epochs.

Ice surface elevation profiles measured with the NASA Airborne Topographic Mapper (ATM3) laser altimeter system (e.g. Krabill *et al.*, 2002) over 17 Svalbard glaciers and ice-caps between 1996 and 2002, showed a mean elevation change of -0.19 m a^{-1} WE, estimated to be 1.6 times the net mass balance value determined over the 30 previous years (Bamber *et al.*, 2005). The average elevation change was found to be -0.21 m a^{-1}, which gives a value of -0.19 m a^{-1} WE using a mean ice density of 900 kg m^{-3} (Paterson, 2001). The highest individual and averaged thinning rates were observed in south Spitsbergen, with a mean $\delta h/\delta t$ for four glaciers (excluding surge-type glacier Fridtjovbreen) of -0.47 m a^{-1}, approximately four times the long-term estimate for the archipelago (Hagen *et al.*, 2003). Elevation changes at the highest elevations (the ice-caps of Asgardfonna and Lomonosovfonna) showed respectively, moderate thinning of about -0.05 to 0.1 m a^{-1}, and close to balance conditions. Although there was substantial regional variability in $\delta h/\delta t$ measurements and the surveys were not comprehensive in coverage, all but four ice masses showed higher thinning rates than the published long-term value for Svalbard (Bamber *et al.*, 2005).

Mean $\delta h/\delta t$ values of -0.23 m a^{-1} were recorded for both the ice-caps of Vegafonna and Vestfonna on Nordaustlandet despite these glaciers experiencing local elevation change asymmetry, with higher thinning on the western side of Vegafonna and the opposite on Vestfonna (Bamber *et al.*, 2005). This contrasts with the reported growth for the same period of the larger ice-cap Austfonna (Bamber *et al.*, 2004). Measurements reported an anomalous positive ice-surface elevation change for the central accumulation area, equivalent to 35% of the long-term annual accumulation rate, and concluded to be the result of sea-ice loss in the adjacent Barents Sea producing localised increases in precipitation (Bamber *et al.*, 2004; Raper *et al.*, 2005). An approach utilising balance flux calculations derived from surface velocities using satellite radar interferometry measured the mass balance of the whole ice-cap during the 1990s as $5.6 \pm 2\times10^8$ m^3 a^{-1}, and attributed 75% of the total mass accumulation to the quiescent phase of the surge cycle of three individual drainage basins (Bevan, 2006; Bevan *et al.*, 2007). These results emphasise the importance of considering glacial surge dynamics when attempting to interpret a climate signal from limited observations of glacier change.

2.6.4 Alternative Methods of Mass Balance Measurement

Changes in the mass of Svalbard glaciers may also be inferred on a regional scale from satellite gravity measurements. The GRACE experiment (section 2.3.3.) has been mapping the Earth's changing gravity fields every 30 days since 2002. Although research has concentrated on the large ice-sheets of Greenland and Antarctica, observations from north Greenland and surrounding regions suggest a significant mass loss of around -75 km^3 yr^{-1} over Svalbard (Figure 2.4) (Chen *et al.*, 2006). A recent study based on gravity and surface deformation measurements by GPS and Very Long Baseline Interferometry (VLBI) in Svalbard suggests significant amounts of present day ice melting (PDIM) in the region. Absolute gravity rates indicate a melt rate of $\sim$ -50 km^3 yr^{-1}, while surface deformation measurements suggest a rate of $\sim$ -25 km^3 yr^{-1}, suggesting an equivalent mean mass balance of at least -0.75 m a^{-1} over the entire ice-covered area of Svalbard (Sato *et al.*, 2006). This estimate of mass balance is almost twice that observed at AB and ML by Hagen and Liestøl (1990) but corresponds well with the most recent observed rates of mass change of Kohler *et al.* (2007).

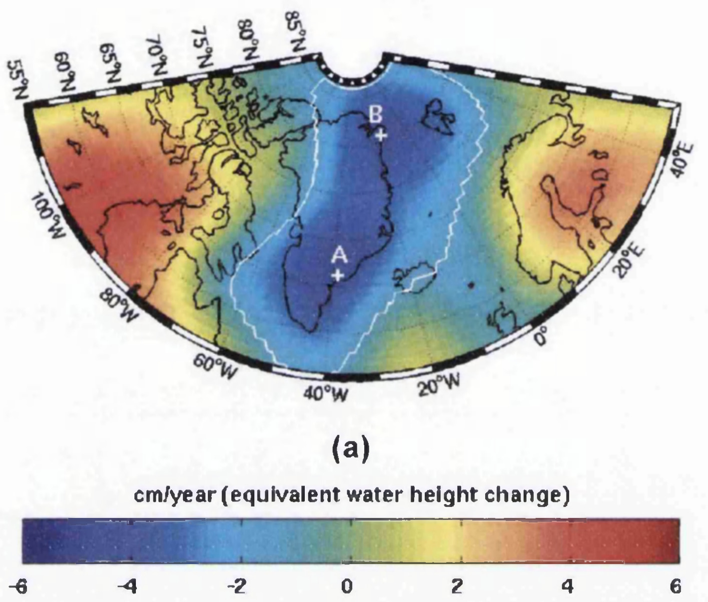

Figure 2.4: Long-term GRACE mass rates over Greenland and surrounding regions (including Svalbard) during the period April 2002 to November 2005 determined from mass change time-series on a 1° grid. Adapted from (Chen *et al.*, 2006).

2.7 Model Predictions of Future Change

Mass balance modelling studies predict a variety of future scenarios for small glaciers and ice-sheets. The IPCC TAR sea-level rise chapter (Church *et al.*, 2001) presents future small glacier and ice-sheet melt assessments based on the work of Gregory and Oerlemans (1998) and Van de Wal and Wild (2001). Gregory and Oerlemans (1998) provided a calculation of glacier melt using temperature patterns generated by a coupled atmosphere-ocean general circulation model (GCM) (Mitchell *et al.*, 1995; Johns *et al.*, 1997) inputted to a seasonally and regionally differentiated glacier model (Zuo and Oerlemans, 1997). Under IPCC emissions scenarios this model predicted small glacier and ice-sheet melt equivalent to 132 mm of sea-level rise between 1990–2100. Inclusion of seasonal and regional temperature variations had the effect of increasing calculated glacier melt by 20% (Gregory and Oerlemans, 1998).

The approach taken by Van de Wal and Wild (2001) also used a seasonally and regionally differentiated mass balance model with a high-resolution GCM, but applied volume-area scaling relations (Bahr *et al.*, 1997) to take into account the reduction in glacier area as a result of warming. Their model predicted a global sea-level rise of 57 mm over a period of 70 years. Previous models assuming a constant glacier area (e.g. Gregory and Oerlemans, 1998) were found to overestimate the small glacier and ice-sheet sea-level rise contribution by 19% (Van de Wal and Wild, 2001).

The IPCC TAR estimated that the largest contributions to sea-level rise would come from thermal expansion of the oceans (0.288 m), followed by melting of small glaciers and ice caps (0.106 m), with small contributions from Greenland (0.024 m) and Antarctica (-0.074 m) (Church *et al.*, 2001). Model studies since the TAR have continued to utilise glacier volume-area scaling methods but have since improved the global estimates of total small glacier and ice-cap volume (e.g. Raper and Braithwaite, 2005; Meier *et al.*, 2005). The most recent assessment of small glacier and ice-cap contributions to sea-level rise suggests a smaller contribution than that estimated by the TAR (Raper and Braithwaite, 2006). This study utilised a melt model (Braithwaite *et al.*, 2002) and a geometric volume model (Raper *et al.*, 2000), applied to the improved estimates of ice volume (Raper and Braithwaite, 2005; Meier *et al.*, 2005) to seperately calculate the melt contributions of mountain glaciers and ice-caps, and improve estimates of ice volume shrinkage. Results showed that ice-caps melt more slowly than mountain glaciers, and mountain glacier volume declines rapidly throughout the 21st century making these ice masses a limiting source of melt. Total sea-level rise from melting mountain glaciers and ice-caps is estimated as 0.046 m and 0.051 m by 2100 respectively (Figure 2.5), approximately half that of TAR projections (Raper and Braithwaite, 2006).

2.8 The Case for Continued Observations

According to the World Glacier Monitoring Service (geo.unizh.ch/wgms/index.html) mass balance measurements on Svalbard exist for only 6 glaciers; AB and ML since 1967 and 1968 respectively, Kongsvegen since 1987, Werenskioldbreen since 1980, Hansbreen since 1989, and Waldermarbreen since 1995. Data from the Norsk Polarinstitutt show that measurements have also been made at Finsterwalderbreen every other year between 1950–1966, and sporadically at Storbreen since 1949 and Vøringbreen in Grønfjorden since 1966 (Hagen *et al.*, 1993), although these records are not included in the WGMS assessment. All these glaciers are situated on Spitsbergen at relatively low altitudes and are within proximity of nearby settlements. With the exception of AB and ML, none of the records comprise complete annual mass balance data for a time period of more than 20 years. In order to

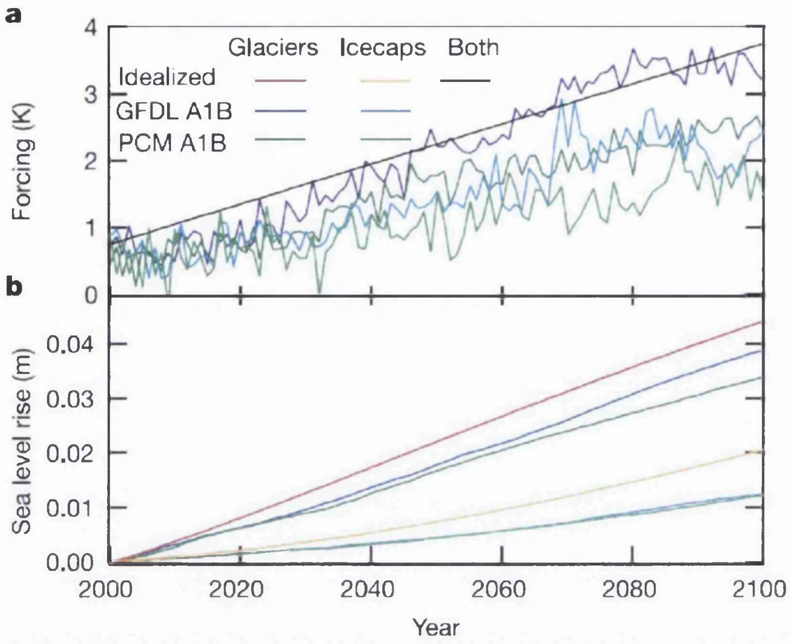

Figure 2.5: Temperature forcing from an idealised scenario and two climate model outputs (a), and SLR contribution for mountain glaciers and ice-caps over the 21st century (b), adapted from Raper and Braithwaite (2006).

determine long-term trends in mass balance it is essential to have long time-series datasets, particularly given the large number of surge-type glaciers on Svalbard (Jiskoot *et al.*, 2000) whose dynamic mass change effects complicate the extraction of a climate signal. The lack of archipelago-wide measurements (particularly in the North and East of Spitsbergen, and the other islands) also mean that it is difficult to convincingly upscale mass balance to provide a Svalbard sea-level rise contribution signal. In order to accurately gauge the contribution to sea-level rise of melting land ice on Svalbard it is essential to continue current measurement programmes, and to extend both current records of mass change retrospectively and derive volume change estimates for previously unstudied ice masses.

The only way to derive direct volume change measurements retrospectively for previously unstudied glaciers and ice-caps is to exploit the information provided by remotely-sensed image archives. Stereo-processing of overlapping satellite imagery will allow reconstruction of large spatial extents, but is somewhat limited in terms of temporal resolution. In the case of ASTER stereo image processing, the imagery archive is both weather dependent and limited to the last 8 years since the launch of the Terra spacecraft in 1999. Aerial photography archives offer a greater temporal resolution; in the case of Svalbard, oblique imagery dating from 1936/1938 and vertical imagery epochs at approximately 10–15 year intervals since 1966. Developments in the methods for retrieving elevation information from historical aerial photography, and photogrammetric processing of large and relatively unexploited image archives will allow improved estimates of glacial mass changes for Svalbard as well as other regions of the cryosphere.

2.9 Chapter Summary

This chapter has related how the cryosphere plays a fundamentally important role in determining the Earth's mean sea-level. Contributions from the melt of small glaciers and ice-sheets and sections of the large Greenland and Antarctic ice-sheets, make up more than half of the observed 20th century sea-level rise (Table 2.1). Uncertainties associated with measurement of mass balance of the large ice-sheets have been reduced by data from dedicated satellite missions but still remain significant. Likewise, uncertainties in the estimation of the small glacier and ice-sheet contribution to sea-level rise are significant, primarily as the result of a lack of global mass balance data. Mass balance datasets extending more than a couple of decades are both rare and usually limited to a small selection of easily accessible glaciers in Western Europe, North America and Russia. Where field measurements exist there are also questions as to whether the glaciological method may underestimate mass balance in comparison to the geodetic method. Field measurement of mass balance is based on the assumption that altitude is the dominant gradient rather than any transverse variations. This may be true for small glaciers but has yet to be exhaustively examined, mainly due to a lack of detailed elevation change information.

Even a relatively well-studied region such as Svalbard has a severe lack of long-term mass balance datasets. Such data do exist (at AB and ML) but are by no means spatially extensive and cannot be said to be representative of the Svalbard archipelago as a whole. Analysis of long-term mass balance data along with recent geodetic volume change measurements from Slakbreen (Kohler *et al.*, 2007), and additionally from independent crustal deformation data (Sato *et al.*, 2006), suggests that the rate of negative mass balance and present day ice-melt is unprecedented since measurements became available, and continues to increase. This work and that of others (Bamber *et al.*, 2004, 2005; Bevan *et al.*, 2007) presents a complicated picture of increasing rates of glacier thinning and negative mass balance especially at lower elevations, along with some regions of thickening, the precise causes of which remain debated. It is clear that more measurements are needed, in terms of both longer records of glacier geometry and volume change, and more spatially representative samples. Improvements in remote-sensing sensor development, data assimilation and integration, and improved processing strategies will help this process.

Chapter 3

Lidar & Photogrammetry; Principles and Applications

3.1 Introduction

The previous chapter outlined the need for high-resolution, time-retrospective, repeat measurements of glacier surface topographic change. This chapter firstly outlines the background and principles of lidar (light detection and ranging, also known as airborne laser scanning) remote-sensing with particular emphasis on mapping glacier topography. Secondly, from section 3.3, the principles and recent glaciological application of digital photogrammetry are summarised. This material forms the background for the processing and results presented in chapters 4 and 5.

3.2 Lidar / Airborne Laser Scanning: A Review

3.2.1 Introduction

The aims of this section are to provide an introduction to the principles of ALS / lidar, to review the current state of knowledge regarding the limitations of the technique and controls on data quality, and to review some specific examples of its use in glaciology. Lidar is a technology that uses the measured properties of scattered light to determine range and / or other properties of a remote target. Range is determined from lidar by measuring the time delay between transmission of a laser pulse and detection of its returned signal. Following the development of GPS technology in the 1980s, downward looking lidar systems combined with GPS measurements of the precise position of aircraft allowed precise surveying of large areas from the air, known as Airborne Laser Scanning (ALS). ALS is often used as a catch-all term which encompasses a number of subtlely different laser scanning systems (Baltsavias *et al.*, 2001). Variously known as Airborne Laser Altimetry (ALA) (e.g. Favey *et al.*, 1999; Hofton *et al.*, 2000), Laser Detection and Ranging (Ladar) (e.g. Wehr and Lohr, 1999), Airborne Laser Terrain Mapper (ALTM) (e.g. Hansen and Jonas, 2000), and most commonly Airborne Light Detection and Ranging (Lidar) (e.g. FEMA, 2000; Latypov, 2002). Airborne lidar instruments collecting both 2 and 3D data are often referred to as airborne laser scanners and when used to specifically collect height measurements may also be known as laser altimeters. The naming convention followed in this thesis will follow that of the Remote Sensing and Photogrammetry Society (RSPSoc), referring to 2D data scanners as laser profilers and instruments collecting 3D data as lidar.

Lidar provides a means of generating high-quality topographic data. It works in principle by precisely measuring the distance between the sensor and the ground surface, from a known position and in a known direction. The advent of lidar systems closely followed the development of the laser in the 1960s with primitive systems being mounted to aircraft during the 1970s and 1980s (Ackermann, 1999; Wehr and Lohr, 1999). The growth of integrated, real-time GPS technology in the early 1990s allowed lidar systems to gain competitive ground toward existing technologies and brought the first commercial production and usage among the mapping and surveying community (Wehr and Lohr, 1999). The first commercially available lidar system was delivered in 1993 (Jonas and Byrne, 2003). Recent developments in its supporting technology have encouraged growth of lidar applications to the field of topographic modelling. Lidar has emerged an increasingly attractive alternative to existing topographic data collection techniques, in particular photogrammetry. The ability to generate large volumes of high-quality data have meant that lidar is now being seen as a cost-effective alternative, with authors quoting savings of as much as 33% of total acquisition and operator costs of equivalent photogrammetric surveys (Petzold *et al.*, 1999).

As a result of the increasing popularity and cost-effectiveness of lidar scanning systems a number of governmental agencies and research council facilities have acquired systems. In the UK this has most prominently included the Environment Agency (EA) who have adopted the technique for data capture over many river catchments (Cobby, 2002; James, 2003) and the Natural Environment Research Council (NERC) Airborne Research and Survey Facility (ARSF) who fly operations in the UK and at a number of overseas locations. This is in addition to a variety of private contracting companies offering topographic data collection services. The increasing popularity of lidar as a source of topographic information has led to its adoption for a number of applications including forest mapping (e.g. Magnussen and Boudewyn, 1998), anthropogenic feature extraction (including hedges, walls, ditches and dams) (e.g. Ackermann, 1999), geoid determination (e.g. Geiger *et al.*, 1994; Cocard *et al.*, 1997; Favey and Schlatter, 1998), crop height measurement (e.g. Davenport *et al.*, 2000), remote sensing of urban areas (e.g. McIntosh *et al.*, 2000), coastal zone mapping (e.g. Adams and Chandler, 2002), geomorphological modelling (e.g. French, 2003), hydrology (e.g. Cobby *et al.*, 2001; Charlton *et al.*, 2003; Cobby *et al.*, 2003; Lane *et al.*, 2003; Mason *et al.*, 2003) and glaciology (e.g. Kennett and Eiken, 1997; Favey *et al.*, 1999; Baltsavias *et al.*, 2001; Favey *et al.*, 2002; Spikes *et al.*, 2003a).

In order to better understand both the nature and the quality of the data collected using lidar it is necessary to examine its theoretical principles and the method of its acquisition. The following sections will do this by providing a review of the principles of a lidar scanning system, followed by a review of the controls on lidar data quality and previous attempts to identify and correct for these errors. A more comprehensive review of the basic relations and formulas of lasers, laser ranging devices and airborne lidar, along with important factors influencing 3D positional accuracy of derived coordinates is provided by Baltsavias (1999a).

3.2.2 Lidar Principles

Lidar systems consist of an aircraft-mounted active pulse-wave (PW) or continuous-wave (CW) laser scanner used to image ground targets in order to produce x,y,z coordinates of terrain or surface features. The generation of such information is the result of the synchronisation in post-processing routines of three independent systems (Figure 3.1). They include:

1. a laser scanner (or ranger), used to measure the distance between the sensor platform and the ground;
2. an inertial navigation system (INS) which measures the attitude (roll, pitch and yaw) of the scanning platform. This is sometimes referred to as an inertial reference system (IRS), inertial measurement system (IMS) or inertial navigation unit (INU); and
3. a GPS antenna, combined in differential processing with ground basestation observations to measure the position of the sensor platform (two additional GPS antennas may also be used to determine the aircraft attitude angles, as an alternative to INS).

A range of different lidar systems available offer flexibility in: (i) the type of scanning beam used (CW or PW) (Ackermann, 1999); (ii) the range of the electromagnetic spectrum in which they operate (scanners designed to image through water may sense in the green and red parts of the spectrum (Fowler, 2000)); and (iii) the ability to record multiple returned signals (Wehr and Lohr, 1999). Since the data used in this thesis were collected with a PW scanner operating in the near infra-red (NIR) part of the spectrum, a configuration which is most commonly used to collect terrestrial topographic data, other types of laser are not considered further in this review.

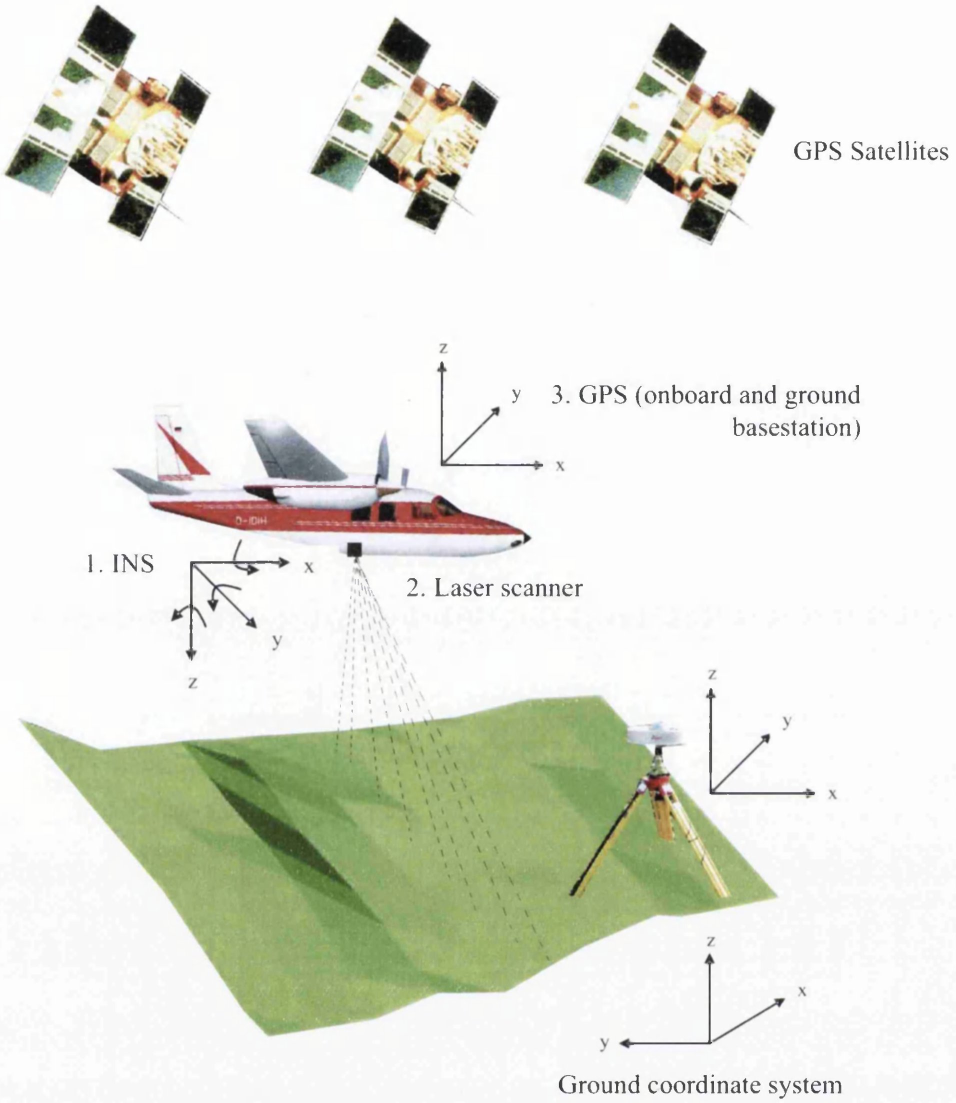

Figure 3.1: The three principal components of a standard airborne laser scanning system; 1) the plane roll, pitch and yaw measuring Inertial Navigation System, 2) the laser scanner itself and 3) GPS technology in the form of satellite signal-receiving antennas onboard the plane and nearby ground reference basestation.

The laser scanner works by emitting a discrete beam of light toward the surface then recording the time taken for the signal to return to the sensor, as well as the intensity of the returned signal. The time taken for the beam to return to the platform is used to calculate distance from the surface, while the intensity signal may be used to generate information regarding the terrain below using surface reflectance characteristics. Intensity information may also be used to infer the quality of returned elevation measurements, particularly in areas of low return which are often discarded when deemed unreliable. The principle of laser height determination has been used previously for cross-sectional and profile measurements in active glacial (e.g. Echelmeyer *et al.*, 1996; Adalgeirsdóttir *et al.*, 1998) and volcanic (e.g. Hofton *et al.*, 2000) environments. PW lidar systems usually emit light beneath the aircraft in swathes, typically emitting and receiving between 5000 and 100 000 pulses per second (Hansen and Jonas, 2000). Most proprietary lidar systems are configured to record either the initial first-return or final last-return reflection received (Huising and Gomes-Pereira, 1998), although newer systems are now capable of recording both returns, multiple returns, or the full laser waveform (Baltsavias, 1999a).

Laser rangers provide extremely accurate and precise results. Depending on the system used and local conditions, lasers are typically able to derive distance measurements from as much as several kilometres with an accuracy of less than 2 cm (Huising and Gomes-Pereira, 1998; Fowler, 2000). The fact that the scanner is mounted on a fast-moving platform means that measurement of the sensor location and orientation is crucial in order to derive high-quality 3D topographic information.

The location of the sensor is provided by a combination of both GPS and INS measurements. These two components of the system (Figure 3.1) when combined with laser ranging data provide 3D georeferenced topographic data. Both the onboard and ground basestation GPS typically measure at 20 Hz or more. The ground basestation is usually located within 50 km of the study area. Aircraft attitude is continually monitored using onboard INS at a measuring rate of ~50 Hz. The combination of GPS positioning, kinematic phase-tracking, and orientation and tilt along a flight path can be integrated using a Kalman filter (Skaloud *et al.*, 1996), resulting in an airborne position processed to a theoretical precision of better than 10 cm (Geiger *et al.*, 1994; Thomas *et al.*, 1995).

Lidar systems support an entirely digital processing stream from which the construction of digital models of the Earth's surface (DSMs), digital models of an elevation surface (DEMs), and digital models of natural terrain (without features such as trees / buildings, DTMs), are possible. Post-processing is usually undertaken 'in-house' by the service provider contracted to collect the data. This often means that the user has little or no control over any aspect of initial post-processing (Baltsavias, 1999d). As raw elevation heights are determined using GPS, they are initially computed in the UTM coordinate system (WGS84 Datum). The accuracy of final x,y,z output may deteriorate if an orthometric height conversion using the local geoid-spheroid seperation distance is required (Fraser *et al.*, 1999).

A summary of the major technical parameters of commercial lidar systems is provided in Table 3.1.

	Minimum value	Maximum value	Typical value range
Scan angle (°)	14	75	20–40
Pulse rate (KHz)	5	100	5–30
Scan rate (Hz)	20	630	25–40
Flying height (h)(m)	20	6100	200–300(H), 500–1000(A)[1]
GPS frequency (Hz)	1	10	1–2
INS frequency (Hz)	40	200	50
Beam divergence (mrad)	0.05	4	0.3–2
Swath width (m)	0.25 h	1.5 h	0.35–0.7 h
Across-track spacing (m)	0.1	ca. 10	0.5–2
Along-track spacing (m)	0.06	ca. 10	0.3–1
Angle precision (roll, pitch)(°)	0.004/0.008	0.05/0.08, 0.5/0.2 [2]	0.02–0.04/ 0.03–0.05
Range accuracy (cm)	2	30	5–15
Height accuracy (cm)	10	60	15–20
Planimetric accuracy (m)	0.1	3	0.3–1

[1] H = Helicopter, A = Aeroplane

[2] Value refers to systems without INS, rather using a combination of 3-4 GPS antennas for attitude determination

Table 3.1: A summary of the major technical parameters of commercial lidar systems, adapted from Baltsavias (1999b). A larger and more comprehensive review is available in appendix 1 of Baltsavias (1999b).

3.2.3 Pre-Survey Planning and Instrument Calibration

To avoid the introduction of further error into final lidar-derived coordinates it is necessary to undertake correct calibration of the the instrumentation prior to surveying. This section describes the standard pre-survey, calibration and data collection procedures used to minimise inaccuracies in lidar data.

In order for the data user to receive sufficient coverage of the area under study at the appropriate sample density for their needs, a collaborative process should take place involving the user and flight crew of the survey organisation. The data user supplies the flight crew with survey details including the bounding coordinates of the study area, and either the crew or automatic software programmes compute the necessary flying height and number of strips required to image the entire area with sufficient overlap to avoid 'slivers' of no data between strips. To obtain complete coverage of the study area it is necessary for the pilot to manouevre the plane accurately within flight tracks determined during pre-flight planning. This is achieved through the use of on onboard real-time GPS that allows pilots to maintain flight paths to an accuracy of less than 50 m (Krabill *et al.*, 2000b). It is recommended that pilots attempt to keep the aircraft roll angle below approximately 15° and keep within visible range of at least 4 satellites so as to maintain the quality of onboard GPS observations. The need to stay within range of at least 4 GPS satellites is required to derive three-dimensional positional data and to compensate for time delays from the GPS atomic clock. High wind speeds are known to have caused large aircraft roll angles resulting in loss of satellite lock and significant systematic errors in resultant lidar datasets.

Cobby (2002) recommended the adoption of two seperate laser instrument calibration routines prior to take-off. Range error may be corrected (if necessary) by firing the laser at a target of fixed distance over a range of return-strength amplitudes. Laser pulse angle may be tested and corrected if appropriate by assessing its angular bias when fired at a known flat surface (e.g. Latypov, 2005). Errors in laser pulse angle can be particularly important as even small discrepancies during testing will translate to increasingly large errors as the aircraft scans from greater flying heights. A number of surveys have been known to check the flight performance of range and scanning angle by flying test surveys over known flat areas such as runways, and correcting for discrepancies before beginning principle survey operations (e.g. Krabill *et al.*, 1995b, 2000b).

3.2.4 Lidar Data

Raw lidar data is delivered in the form of an irregularly-spaced cloud of data points whose spatial distribution is determined by a number of instrumental and flight parameters. Important laser properties include pulse frequency (expressed as the number of pulses emitted per second), scan width and scan frequency (the number of whole scans per second). Scan or swath width (SW) is given by

$$SW = 2\,h \tan\left(\frac{\theta}{2}\right) = ah, \tag{3.1}$$

with $a = 2 \tan\ (\theta\ /\ 2)$, where θ is the scan angle and h is the flying height (Baltsavias, 1999a). Ground sampling density depends on a combination of the pulse frequency, scan angle, flying speed and flying height (Ackermann, 1999). For a Z or saw-tooth shaped scan, the number of scan points per line (N) is given by

$$N = F/f_{sc}, \tag{3.2}$$

where F is the laser pulse rate and f_{sc} is the scan rate (Baltsavias, 1999a). Along-track point spacing (dx_{along}) of one complete bidirectional scan is given by

$$dx_{along} = v/2f_{sc}, \tag{3.3}$$

and across-track point spacing (dx_{across}) by

$$dx_{across} = 2SW/N, \tag{3.4}$$

where v is average flying speed (Baltsavias, 1999a; Wehr and Lohr, 1999). Measuring rates typically lie between 5 Khz and the 100 KHz reported by the most recent Optech ALTM 3100 instruments (Optech, 2005). Accordingly, at a scanning height of 1000 m and an average flying speed, ground sample density will range from approximately 1 point per 20 m^2 up to more than 50 points per m^2. Much like photogrammetry, there is a trade-off between flying height (which increases swath width and reduces overall flying time and operational costs) and point density (which increases overall surface representation, and data redundancy).

While ground sampling patterns are pre-determined by system and flight-plan design (which allows a certain amount of control over coverage and resolution), data resolution will also depend on the nature of the flight path and the topography of the underlying terrain. For example, a constant flying height over steeply-sloping terrain will produce a different point density distribution than the same flying height over flatter terrain. Likewise changes in flying height over terrain of a similar height will produce uneven point spacing. Flexibility in the upper range of operational flying height is limited by the power of the laser while the lower range is limited by flight safety guidelines and the possibility of laser-induced damage to the human eye. Flight speed is affected by the need for smooth movement of the aircraft along with the lidar scan rate and restrictions on data storage capacity (Baltsavias, 1999c).

An important aspect of lidar data is the potential for collection of multiple laser return and beam intensity information. Although the laser usually has a low radial beam divergence (γ) it will produce a small ground footprint, the diameter (A_L) of which over flat terrain is given as

$$A_L = h_{f\gamma} \tag{3.5}$$

As well as flying height (h_f) and beam divergence (γ), the size of the footprint also depends on the slope characteristics of the underlying topography (Ackermann, 1999). The laser beam is reflected from all surfaces within the footprint, rather than just a single point, potentially producing a number of returned signals. This feature presents an opportunity for the more sophisticated lidar systems to model small-scale surface characteristics and has been used extensively in crop and vegetation monitoring whereby multiple return information is used to record the tops of crops / trees, the ground suface beneath and any intervening structures between the two (e.g. Kraus and Pfeifer, 1998; Harding *et al.*, 2001; Clark *et al.*, 2004; Hall *et al.*, 2005). Older lidar systems will usually record either first or last return, whereas newer systems may record both, multiple returns or full laser waveforms along with corresponding laser intensity information.

3.2.5 Lidar Data Quality

The issue of lidar data quality is a crucial one as it has a direct effect on the quality of derived data products, the decisions made on them and the validity of the results generated with them. In order to design effective data collection and processing strategies for the minimisation of error it is essential to have a sound knowledge of the individual error components of the system and the interrelationships between them (Huising and Gomes-Pereira, 1998). The quality of 3D coordinates generated using lidar is determined by the effects of a number of individual factors that may be combined to produce an estimate of overall system performance. This combination is not straightforward and seriously complicates the derivation of theoretical models of accuracy, the predicted accuracy of any one system and the way that error propagates throughout data collection and processing routines (Baltsavias, 1999c). Despite these difficulties, the identification and quantification of disturbances in lidar measurements form the basis of any analysis of system performance, and through the construction of error budgets allow the user to consider the theoretical limits on the performance of the system.

It is possible to describe the error sources of lidar (or indeed any topographic) data in terms of three components generally adopted in surveying and terrain modelling: *accuracy, precision* and *reliability* (Cooper and Cross, 1988; Cooper, 1998). Each of which will be described in turn and with their relevent lidar operational error sources in this review. The term lidar data *quality* refers to the degree to which the data represents the real ground surface in the context of these three error components:

- *Accuracy* may be considered in terms of systematic error, that is error that is persistent and cannot be considered truly random. Systematic errors cannot be detected by repeat measurements and may commonly cause persistent error to one side of a true value. Although systematic errors can be very large they can be modelled and are generally avoidable by the employment of correction methods and can be determined relatively easily by comparison with independent check data.
- *Precision* is described in terms of random error; that is the non-persistent error that is normally distributed and varies around the true value being measured. This cannot be modelled but may be decreased by calculating an average error from repeat measurements.
- *Reliability* of lidar data may be considered as gross error or blunders that are caused by operator error or the catastrophic failure of systems elements. Cooper and Cross

> (1988) define reliability as a measure of how easily blunders can be detected in a dataset. Therefore the reliability of the data is good if outliers are obvious and can be removed easily. Likewise reliability is said to be poor if erroneous values are indistinct and difficult to identify and remove.

The quality of 3D positional lidar measurements depend on a number of influences. They may be divided into the three following factors: accuracy of range, position of the laser scanner platform and the direction of the laser beam (Baltsavias, 1999a). Errors may be compounded by the effects of insufficient calibration of the operating instruments (Huising and Gomes-Pereira, 1998), and (if applicable) problems arising during georeferencing to local coordinate systems (Vaughn *et al.*, 1996; Daniels, 2001).

3.2.4.1. Range Accuracy

Range accuracy is the most complicated of the accuracy factors as it is mainly dependent on the laser's signal-to-noise ratio (SNR). SNR is determined by: a) the reflection characteristics of the ground surface (i.e. multiple reflective targets in the footprint, discontinuous terrain in the footprint, reflectivity of the target); b) the amplitude or intensity of the received signal; c) the size of the ground footprint; d) atmospheric factors (including reflection or scattering of light returning to the sensor or signal transmittance from moisture); and e) the size and sensitivity of the scanning aperture. Sensors with lower pulse rates are more likely to experience systematic inaccuracies due to long-term signal drift and signal variation fluctuations while higher pulse rate scanners may experience greater levels of detector noise and range-timer resolution problems (Baltsavias, 1999a). Factors such as temperature operating levels and ambient light sources might also have a small effect on range accuracy but overall, if careful instrument calibration precautions are undertaken, then the contribution of range errors should be among the smallest of the major error sources.

3.2.4.2. Scanner Platform Positioning

The position of the scanning platform is a crucial component of the error budget of a lidar system and is mainly determined by the quality of DGPS post-processing. Other important factors are the position, measuring rate and synchronicity of the ground reference basestation, the quality of lock and number of satellites available during the survey, the GPS hardware used, and the accuracy of offset and misalignment between GPS, INS and the laser scanner. Depending on the type and quality of DGPS post-processing, theoretical positional accuracies of 5–15 cm are considered to be achievable on a moving aircraft if tropospheric, ionospheric, multipath and precise satellite orbit (ephemerides) corrections are employed during post-processing (Shi and Cannon, 1995; Huising and Gomes-Pereira, 1998;

Baltsavias, 1999a). Attitudinal accuracy is determined by the quality of the INS instrument, INS measuring frequency and the methods of post-processing with GPS. Problems such as INS misalignment and gyro drift may cause systematic error of cm range over flat terrain rising to potentially dm range over steep slopes. The effects of attitudinal errors on the accuracy of 3D points is likely to increase with flying height and scan angle. Unfortunately GPS-INS integration and GPS post-processing is usually carried out by the service provider contracted to collect the data, and as such this stage is typically out of the control of the user. Therefore, these components of system accuracy are considered no further in this review.

3.2.4.3. Laser Beam Direction

Laser beam direction errors comprise a relatively small component of the total lidar error budget. However, it is important to note that the quality of measurements will also be affected by small variations in the quality of pulse detection, pointing jitter and the accuracy of the time interval counter. Table 3.2 gives a summary of the quantification of accuracy and precision (and reliability) controls on lidar measurements based on theoretical system considerations, for a variety of idealised terrain types. This is instructive as the characteristics of the surface being scanned are likely to have a large effect on the precision of the data collected (Westaway, 2001).

Lidar instruments are not capable of being pointed directly at surface points or features. Rather, the coordinates generated refer to the ground-track of each scan line, often in a saw-tooth pattern as the laser scans from side to side up a flightline. It has been described for this reason as a 'blind' system (Ackermann, 1999). This means that it cannot automatically filter unwanted objects and artefacts. When the scanner comes across objects that are unwanted in the data, perhaps buildings or trees, the data has to be filtered using corrective algorithms in the post-processing stage.

Despite best estimates to assess the contribution of various error sources to lidar data quality it is inevitable that optimal theoretical system performance is generally not achievable in the field. There are also no simple procedures for establishing global accuracy of lidar datasets as the error changes over a variety of spatial scales. For example, quality assessment results will differ if an average value computed over an entire swath width is compared to several values from the swath edges which are likely to be of poorer quality. The outcome of the combined effect of these three types of error and their propagation across a dataset means that a rigorous and accurate description of an entire survey area is not achievable without a spatially coincident independent check dataset. Users are encouraged to conduct ground surveys and check this data against lidar coordinates in order to quantify the quality of

Error source	Terrain type			
	Flat paved	Flat barren	Hilly barren	Hilly grass/ scrub
Systematic error magnitude (accuracy)				
Detector bias and gain	cm	cm	cm	cm
Laser pulse delay	cm	cm	cm	cm
INS misalignment	cm - dm	cm - dm	dm - m	dm - m
INS gyro drift	cm	cm	dm	dm
GPS base-line error (for baselines < 20 km away)	cm	cm	cm	cm
GPS delays in troposphere	cm - dm	cm - dm	cm - dm	cm - dm
Terrain slope effects	0	0	cm	cm
Effect of vegetation	0	0	0	dm - m ?
Positional integration	cm - dm	cm - dm	cm - dm	cm - dm
Overall (cm)	5–20	5–20	5–20	20–200
Random error magnitude (reliability)				
Pulse detection	dm	dm	dm	dm
Pointing jitter	0	0	dm - m	dm - m
INS	cm	cm	cm	cm
GPS	cm	cm	cm	cm
Terrain roughness	0	cm	cm	cm - dm
Reflectivity	cm - dm	cm - dm	cm - dm	cm - dm
Overall (cm)	10–20	10–50	20–200	20–200

Table 3.2: A summary of the quantitative contribution of systematic and random errors on the error of lidar measurements over idealised terrain types based on theoretical considerations, adapted from Huising and Gomes-Pereira (1998).

their data. While GPS-based check data is often time consuming and expensive to collect and usually limited to just a small fraction of the total lidar data it does provide a good assessment of accuracy and precision at localised areas within the data. Along with the comparison of lidar elevations with independent check data, the following section introduces a selection of methods that have been employed to estimate the quality of lidar data.

3.2.6 Assessing and Improving Lidar Data Quality

The development of techniques such as lidar to collect large volumes of topographic data have brought about coincident increases in the importance of methods to identify and correct error. As datasets have grown, largely through increased computer processing and storage capability, it has become increasingly difficult to guarantee data quality (Lane *et al.*, 2000; James, 2003). As lidar datasets commonly comprise upwards of 10 million datapoints, data size is an issue not only for correction of error but also for error identification. Commercial data vendors often do not quote error specifications or confidence levels, or the procedures used to quantify error. The following section provides an introduction to some of the routines suggested in the literature to identify error and improve the quality of lidar data. While a number of authors have proposed filtering algorithms for the removal of small-scale erroneous features such as trees and buildings from raw lidar data (e.g. Vosselman and Maas, 2001), as this is not likely to be a problem in these study areas, they are considered no further in this review.

3.2.5.1. Ground-Truthing

Error is present within lidar data at a variety of spatial scales. Error may occur in the determination of individual laser pulses, within a patch or segment of data, or within offsets consisting of entire flight lines. It is also possible that entire blocks of data from multiple flight lines are offset from true ground coordinates by some amount. Independent check-data collected via ground survey using differential GPS (DGPS) offer the best method for externally assessing lidar data quality and may be used to estimate error magnitude of individual laser pulses (e.g. Hopkinson and Demuth, 2006) or with the use of check data profiles, to examine larger segments of data (e.g. Hodgson and Bresnahan, 2004; Barbarella and Gordini, 2006). The magnitude of elevation error derived using this type of comparison is typically less than root mean square (RMS) ± 0.3 m (e.g. Krabill *et al.*, 2000b; Sallenger *et al.*, 2003; Geist *et al.*, 2005), but may be as little as ± 0.1 m over surfaces of uniform slope such as an aircraft runway, playing field or flatland (e.g. Hopkinson and Demuth, 2006; Montane and Torres, 2006).

Due to issues of cost, logistics and safe access it is often not possible to collect check data over a glacier surface. The studies that have compared lidar elevations with check data have tended to use ground-truth data collected via GPS profiles acquired with a snow-scooter (e.g. Spikes *et al.*, 2003b; Geist *et al.*, 2005). As a snow surface is likely to be more uniform than the summer ablation surface of a maritime or temperate glacier it is likely that these values do not fully reflect the operational accuracy of lidar data over this type of glaciated terrain. In order to adequately assess the quality of lidar data in glaciated terrain, there is a need for time-coincident check data, collected over large samples and the different surface types typical to glacial environments at or close to the end of the balance year. The most significant limitation of ground-truth data for validation of lidar elevations regards data volumes. At most several thousand check points are likely to be collected, several orders of magnitude fewer than the number of lidar elevations collected in under an hour of surveying.

3.2.5.2. Overlap / Crossover Analyses

The use of overlap-based quality control tools is a common way of estimating relative lidar data quality (e.g. Kilian, 1994; Krabill *et al.*, 2000b; Latypov, 2002). Adjacent scan lines should be designed in pre-flight planning to overlap so as to avoid slivers; that is areas of no data that are not covered by any scan line which may be caused by changes in terrain height or plane tilt. Thus there will be a number of points which will run onto adjacent flight lines that can be checked against each other for consistency. For example, commercial vendors TerraPoint (Texas, USA, http://www.terrapoint.com) operate standard surveying operations with adjacent flight line overlap of 30%. This means that potentially 60% of the total collected points may be checked against each other. This procedure is useful in particular to identify systematic errors which when unchecked may translate to significant shifts or tilts between overlapping strips (Huising and Gomes-Pereira, 1998). The standard operating procedure of the ARSF is to fly 20% overlap in good conditions, and up to 30% overlap in sub-optimal conditions to compensate for aircraft roll (P. Goy, pers. comm. 31-03-2007).

Lidar data processing for correction of systematic offsets in individual flight lines is a commonly practised procedure and remains an area of active research (e.g. Barbarella and Gordini, 2006). A number of authors have proposed the use of raster-based least-squares adjustments of overlapping data in coincident flight lines (Kilian, 1994; Behan, 2000; Crombaghs *et al.*, 2000). The main aim of these authors was to compensate for discrepancies between two flightlines in their common areas of overlap. The technique works by using a least-squares matching algorithm to identify coincident points in each overlap before performing either a fixed strip adjustment using laser and ground reference data with correction for along and across-track tilts or correction for further strip disturbances using a cross-strip parabolic deformation correction (e.g. Crombaghs *et al.*, 2000).

Elevation differences between strips at individual points can be determined by comparing an average height value of a group of points with GPS measurements over an area of flat terrain. Strip discrepancies are analysed using least-squares matching of the average height difference between two groups of points in the overlap region. The method suffers from the introduction of interpolation error during the gridding process from raw point cloud to raster data (Crombaghs *et al.*, 2000). Reducing lidar height data to 8 bits, as is required by most standard least-squares implementations, is thought to be insufficient for the precision potential of the lidar instrument, while interpolating to a regular grid may introduce severe systematic errors by creating non-existing points in areas of no data.

To avoid these problems, the method adapted by Maas (2000, 2002) operates on triangular irregular networks (TINs) rather than rasters. However, a problem of using least-squares matching in coincident areas of overlap is that it is likely to perform poorly over flat featureless terrain. For this reason others have proposed that the least-squares matching approach be used only where pre-identification of coincident linear and planar features is possible (Vosselman, 2002) or when common points within lidar intensity data can be used to correct for planimetric errors (Burman, 2000, 2002; Maas, 2001). The planar surface matching approach has been developed further by Schenk *et al.* (2001) who used image segmentation, the process of dividing raw data into regions of strong correlation with real-world features, to extract intersecting planar features such as roads or building edges. Planimetric errors were then estimated and corrected for by evaluating the lidar-derived positions of features with those measured by independent survey. This approach is useful for environments containing a multitude of planar features such as urban areas, but may be of less use for modelling of natural terrain.

The methods described above are strip adjustment procedures which require stochastic models (such as least-squares), mathematical models of strip deformation, ground control points and a method for measuring tie-points, that is the discrepancies between data strips in overlap regions. Rather than compensating for discrepancies through the use of strip adjustment procedures which require independent ground control data, a method to derive an overlap-based quality control measure is offered by Latypov (2002). This method avoids the problems of comparing the positions of individual points by instead matching the positions of small areas of terrain defined by several points. This has the advantage of operating directly on the raw lidar points rather than new information brought about by the use of grids and TINs. It is possible to quantitatively compare large areas throughout the data extent including different land use or terrain types or edges as opposed to centres of strip overlaps. This method avoids the problems of matching points or image segmentation as it is purely statistical and based on a generalised definition of accuracy. It may be used in the absence of independent check data as it compares only the lidar spot heights in overlapping strips and thus allows an estimation of relative accuracy information. The method developed by Latypov may be implemented by selecting random sample points from overlap areas of ungridded raw data and defining sample areas of varying sizes around each of the points. This allows an investigation of the effects of local surface roughness when using larger surface sizes.

For each sample area at each site throughout the overlap(s), the mean (μ) and standard deviation of mean (σ) elevations may be calculated for each flightline and then compared between flightlines. This analysis is a relatively quick and straightforward way of quantitatively evaluating the systematic error within strip overlaps. If a surface, S, of pre-defined size with the true mean height h_S, and standard deviation, σ_S, from this mean exists and is imaged by two lidar datasets, i.e. overlapping flightlines, the following values may be computed: (i) the number of points (N) falling into the area, A_S, comprised by the surface; (ii) the average height of these points, $\hat{h_S}$; (iii) the standard deviation from this average, $\hat{\sigma_S}$; and (iv) normalised xz and xy moments (for equations see Latypov (2002)). For a useful comparison of datasets, the two surfaces must be consistent in terms of size and point density, if not then the surfaces must be excluded from the analysis. Equation 3.1 provides a measure of the closeness of two point datasets of surface S by calculating the difference in average heights of points,

$$\delta h = \hat{h}_S^{(2)} - \hat{h}_S^{(1)} \tag{3.6}$$

This process may be repeated for n surfaces and results in a statistical sample of average height differences for each of the compared surfaces (δh_x, $x = 1, 2, 3..., n_S$). An average value for these samples ($\overline{\delta h}$) and standard deviation ($\sigma_{\delta h}$) can be computed to quantify the generalised accuracy. These measures can be used to provide some general information about the data within the overlap. $\overline{\delta h}$ indicates whether average height in the overlap in one dataset appears to be higher or lower than the corresponding height in the other dataset. The standard deviation ($\sigma_{\delta h}$) quantifies the spread of height differences for all surfaces. It is possible to correct for systematic shifts between datasets to reduce $\overline{\delta h}$ by applying a simple height transformation to either one of the datasets. This method provides a simple way of measuring relative height differences from ungridded lidar data and highlights the potential for lidar elevation precision assessment from overlapping swath data. However, large processing times limit the use of this technique to smaller, specific areas. Precision assessments over whole swaths of data are better suited to more computationally efficient methods such as DEM differencing.

3.2.7 Applications of Lidar in Glaciology

There is considerable potential for the use of lidar and other laser scanning systems in the field of glacier and ice-sheet monitoring and modelling. A number of studies have already undertaken work using a variety of scanning systems to provide high-quality terrain and elevation models of glacial and glaciated surfaces. The use of lidar in glaciology is primarily geared towards the production of DEMs or profile measurements to determine volume changes, in particular for the estimation of mass balance (e.g. Rignot *et al.*, 2004; Bamber *et al.*, 2005; VanLooy *et al.*, 2006). Lidar has been used in conjunction with, or as a replacement for, other more established remote-sensing techniques or traditional field-based mass balance measurements. The section will examine some of the important examples of the application of lidar and laser scanning to glaciological research.

The use of airborne lidar systems in glaciology has occured predominantly within the last 10-15 years. Previous studies have shown that laser altimetry profile instruments can be a valuable tool in mapping and monitoring glacier elevation changes in Alaska (Echelmeyer *et al.*, 1996; Adalgeirsdóttir *et al.*, 1998; Sapiano *et al.*, 1998; Arendt *et al.*, 2002). Those studies used a relatively simple scanning system to provide surface elevation profiles, which were then compared with existing maps to determine volume change over time. Early scanning systems such as these quoted vertical error magnitudes in the region of 20–30 cm over flat or gently sloping surfaces. A number of studies in Greenland have made profile measurements using similar laser scanning technology (Garvin and Williams, 1993; Csathó *et al.*, 1996; Christensen *et al.*, 2000), while scientists from the United States National Aeronautics and Space Administration (NASA) Laboratory for Hydrospheric Processes developed their own laser instrument, the Airborne Topographic Mapper (ATM), in order to measure elevation changes of large sections of the Greenland ice sheet (Krabill *et al.*, 1995a,b; Abdalati and Krabill, 1999b; Krabill *et al.*, 1999, 2002; Thomas *et al.*, 1995).

Lidar systems have also been adopted for measurements of elevation change of Antarctic ice streams, primarily through the United States National Science Foundation's (NSF) Support Office for Aerogeophysical Research (SOAR) facility (Blankenship *et al.*, 1999, 2001; Spikes *et al.*, 1999, 2003a,b). The SOAR instrument is a laser profiler (Azimuth LRY 500) configured to produce a 1.5 m diameter pulse footprint once every 1.5 by 8 m at a flying height of 300 m (Spikes *et al.*, 2003b). Repeat surveys of grid lines of the Whillans, Kamb and Bindschadler ice streams, West Antarctica (formerly ice streams B, C and D), over GPS-surveyed areas following an in-flight calibration routine (Filin and Csathó, 2002) showed agreement between the imaged and check data surfaces of ± 10 cm. Both NASA and SOAR campaigns demonstrated the capability of airborne lidar for high-resolution monitoring of large glaciers, ice streams and ice sheets. The authors showed that laser scanning may provide a viable alternative to, or calibration and validation scheme for, existing remote-sensing techniques commonly used to image large glacier systems and ice sheets.

The application of lidar and laser profiling instruments to European glaciers and ice masses has offered the opportunity to examine the technique over smaller ice sheets and valley glaciers. The majority of operations have been undertaken toward the aim of estimating changes in mass balance for a variety of ice masses in Iceland (e.g. Garvin and Williams, 1993), mainland Norway (e.g. Kennett and Eiken, 1997; Geist *et al.*, 2005), the Swiss Alps (e.g. Favey *et al.*, 1999, 2002) and Svalbard (e.g. Bamber *et al.*, 2004, 2005; Kohler *et al.*, 2007). Recent work by Lutz *et al.* (2003) has attempted to determine the extent to which laser signal intensity is modulated by different glacial surfaces, elevations and pulse geometry with a view to using lidar systems for classification of glacial surface types. Various authors have reviewed the potential contribution of lidar technology to applications in glaciology, including volume change monitoring (e.g. Geist *et al.*, 2003; Arnold *et al.*, 2006a), surface energy balance modelling (e.g. Chasmer and Hopkinson, 2001; Arnold *et al.*, 2006b) and specific comparisons between established monitoring techniques such as photogrammetry (e.g. Baltsavias *et al.*, 2001). Direct comparison between lidar and photogrammetry for production of high-resolution DEMs has showed the superior quality of data derived by the active lidar sensor when compared to that derived from matching algorithms employed in the photogrammetric process within textureless and shadowed regions. Photogrammetry (see section 3.3) was shown to to perform better in poorly reflective areas such as cliffs or debris zones as well as having showing fewer blunders in areas of moisture such as wet snow and ice or standing water. Baltsavias *et al.* (2001) emphasise the complimentary nature of the two approaches suggesting an optimal solution be reached using some combination of the two.

3.2.6.1. The NASA Airborne Topographic Mapper

The Airborne Topographic Mapper (ATM) instrument operates by reflecting its laser signal toward the ground surface with a nutating (nodding) rather than oscillating mirror with an adjustable scanning angle of 5, 10 or 20° off nadir. The mirror operates a rotational frequency of 10 Hz, providing a ground-track of overlapping eliptical spirals. In the same way as a conventional lidar system, the ground point density of the ATM instrument depends on a function of sampling rate, swath width and aircraft flying speed. Under nominal conditions at a flying velocity of 150 m/s the spot density translates to around 1 point every 6 m^2 (Abdalati and Krabill, 1999a). A pilot study using the ATM instrument over a beach proxy test site, selected as its sand displayed a spectral reflectivity close to that encountered over Arctic glacier surfaces, allowed detailed overlap analysis using independently surveyed ground check data. Comparing all ATM measurements falling within 1 m radius of each ground survey measurement showed mean differences of a few centimetres and standard deviations of around 10-20 cm (Krabill *et al.*, 2000b). The Greenland project goal of ±10 cm measurement accuracy was reported to be achieved over a variety of overlapping locations on the ice sheet with the authors reporting total elevation error contributions for point differencing measurements as 8.6 cm (Krabill *et al.*, 2002).

3.2.6.2. Optech

The lidar data analysed in this study were collected with an Optech ALTM 3033 instrument. Full survey and operational instrument parameters of these data are provided in section 4.2. Optech's Airborne Airborne Laser Terrain Mapper (ALTM) system is an integrated laser scanner, INS and GPS system with laptop computer displays offering flight track navigation for aircraft pilots and first-order data quality checks for an instrument operator. The laser scanner instrument has a sensor head which fits standard camera mounts or can be attached directly to the aircraft floor and has an adjustable scanning angle of up to 18°. Optech instruments and data have been successfully applied to glaciological research by studies including Geist *et al.* (2003) and Arnold *et al.* (2006a).

Despite the increasing number of glaciological studies that have utilised airborne lidar and laser scanning technologies, specific assessment of the use of the technique over mountainous and steeply sloping terrain have received relatively little research attention. Authors have usually concentrated on the height and positional quality of point measurements over gently sloping ice sheet, ice stream and glacial surfaces. To achieve the aims of this thesis, it is important to assess the quality of lidar data over a wider range of surface types than has previously been reported. This includes glacier forefields, debris-covered areas, cliffs and breaklines and in particular steep valley sides, glacier backwalls and mountain peaks where it is likely that small x,y errors will translate to significant errors in z.

3.2.8 Lidar Summary

The material in sections 3.2.1 to 3.2.6 has provided an introduction to the principles of lidar and laser profiling instruments, and some of the areas in which researchers have used its products to derive high-quality topographic information for a variety of applications. Some of the typical operational parameters and controls on data density were introduced, alongside references to provide further comprehensive information. Against this background of system principles and operation, a review of data quality issues, error types and error sources was provided. It has been shown that, while the laser scanner itself is an extremely precise instrument, the quality of INS and GPS data, along with its combination in post-processing, provide the major control on data quality. Further issues such as georeferencing, coordinate system conversions and interpolation routines provide additional concerns of which data users should be aware. A number of techniques for dealing with error on a range of spatial scales were reviewed including strip adjustment procedures and methods for estimating absolute and relative accuracy of raw point data. Lidar data and derived data products have been shown to have great potential in the field of glaciology with numerous examples quoting very high-resolution, accurate and precise measurements of ice-mass elevation change and mass balance. Although some work has been undertaken regarding comparisons with established monitoring techniques, it is clear that there are gaps in our knowledge regarding the quality of lidar data over high-mountain, glacial and formerly glaciated environments, and that continued research will provide useful information for monitoring and modelling glacial systems.

3.3 Digital Photogrammetry: A Review

3.3.1 Introduction

A major component of this research is the analysis of contemporary and archival stereo aerial photography using photogrammetry. Photogrammetric methods are explained at length by Ghosh (1988), Lane *et al.* (1993), and Wolf and Dewitt (2000). Photogrammetry can be defined as:

'the art, science and technology of obtaining reliable information about physical objects and the environment through processes of recording, measuring and interpreting photographic images and patterns of electro-magnetic radiant energy and other phenomena' (ASPRS, 2003).

The definition of photogrammetry includes two distinct fields: (i) *interpretive* photogrammetry; and (ii) *metric* photogrammetry. Interpretive photogrammery deals principally with the identification and systematic analysis of ground-based objects. Traditionally, aerial photo interpretation (API) has been used in geomorphological studies as a qualitative for information regarding landform processes and change. Studies to monitor processes such as longshore drift (El-Ashrey and Wanless, 1967) and river channel stability (Lewin and Weir, 1977) have used API from sequential time-series imagery to measure changes in sediment shift between the dates of photography (Lane *et al.*, 1993). Interpretive photogrammetry includes other branches of remote-sensing as well as photographic interpretation; widening its scope to include data from a variety of scanning instruments including infra-red scanners, multi and hyper-sectral sensors and airborne radar (Wolf and Dewitt, 2000). Metric photogrammetry involves making precise measurements from imagery in order to gain information on the location, area, extent, size, or shape of features. Aerial and terrestrial photographs are often used to prepare maps from photographs, and to produce digital orthophotos from scanned photography (Wolf and Dewitt, 2000).

Credit for the invention of photogrammetry as a discipline is usually attributed to Aime Laussedat, a colonel in the French Army, and developer of the first phototheodolite in 1849, subsequently used for mapping purposes (Birdseye, 1940). Traditional analogue photogrammetry uses optical and mechanical instruments to reconstruct three-dimensional geometry from two overlapping photographs. The development of analytical photogrammetry used computers to replace some of the optical and mechanical components of the analogue method. This replacement resulted in so-called analogue-digital hybrids. Outputs of the analytical method include digital products (DEMs and digital maps) as well as topographic maps. Digital photogrammetry may be defined as the application of photogrammetric techniques to images stored and processed on a computer (Wolf and Dewitt, 2000; Konecny, 2003). Analysis of digital images (either captured by digital cameras or scanned from aerial photographs) is aided by a number of semi-automated processes. The principle products of these semi-automated analyses are DEMs and digital orthophotos. Outputs from digital photogrammetry include digital products which may be stored, analysed and managed on desktop workstations by the user, and easily integrated with other remote-sensing products and within geographical information systems (GIS).

3.3.2 Photogrammetric Principles

The purpose of photogrammetry is to generate three-dimensional coordinates for an array of points from two-dimensional overlapping images. This can be done by reconstructing the geometric relationship between the film, camera and ground at the time of capture of each photograph, thereby linking the two-dimensional coordinate system of image space with the three-dimensional coordinate system of object space.

This is described mathematically as a simplified case of the perspective projection (Wolf and Dewitt, 2000). For this idealised case, two conditions are assumed. The first is the condition of collinearity, which requires that a point on the ground (A), the perspective centre of the imaging camera (0), and the corresponding point on the image place (a), lie in a straight line in three-dimensional space (Wolf and Dewitt, 2000), as illustrated as line A0a in Figure 3.2. The relationship between the two-dimensional camera calibrated image-space position of A (${x_a}^1$, ${y_a}^1$), and its corresponding three-dimensional position in object space (X_a,Y_a,Z_a) can be described by:

$$\begin{bmatrix} {x_a}^1 \\ {y_a}^1 \\ -f \end{bmatrix} = kM \begin{bmatrix} X - X_0 \\ Y - Y_0 \\ Z - Z_0 \end{bmatrix}, \tag{3.7}$$

where f is the focal length of the camera lens, X_0, Y_0, Z_0 are object space coordinates of the camera perspective centre, k is a scale factor, and M is the rotation matrix:

$$M = \begin{bmatrix} m_{11} & m_{12} & m_{13} \\ m_{21} & m_{22} & m_{23} \\ m_{31} & m_{32} & m_{33} \end{bmatrix} \tag{3.8}$$

whereby m_{11}... m_{33} are elements of the matrix comprising the three independent rotations of the camera around the x, y and z axes, K, Ω, and Φ (Albertz and Kreiling, 1975; Ghosh, 1988; ASPRS, 2003). Equation 3.7 can be expanded to form the collinearity equations:

$${x_a}^1 = x_o - f \left[\frac{[m_{11}(X - X_0) + m_{12}(Y - Y_0) + m_{13}(Z - Z_0)]}{[m_{31}(X - X_0) + m_{32}(Y - Y_0) + m_{33}(Z - Z_0)]} \right], \tag{3.9}$$

and

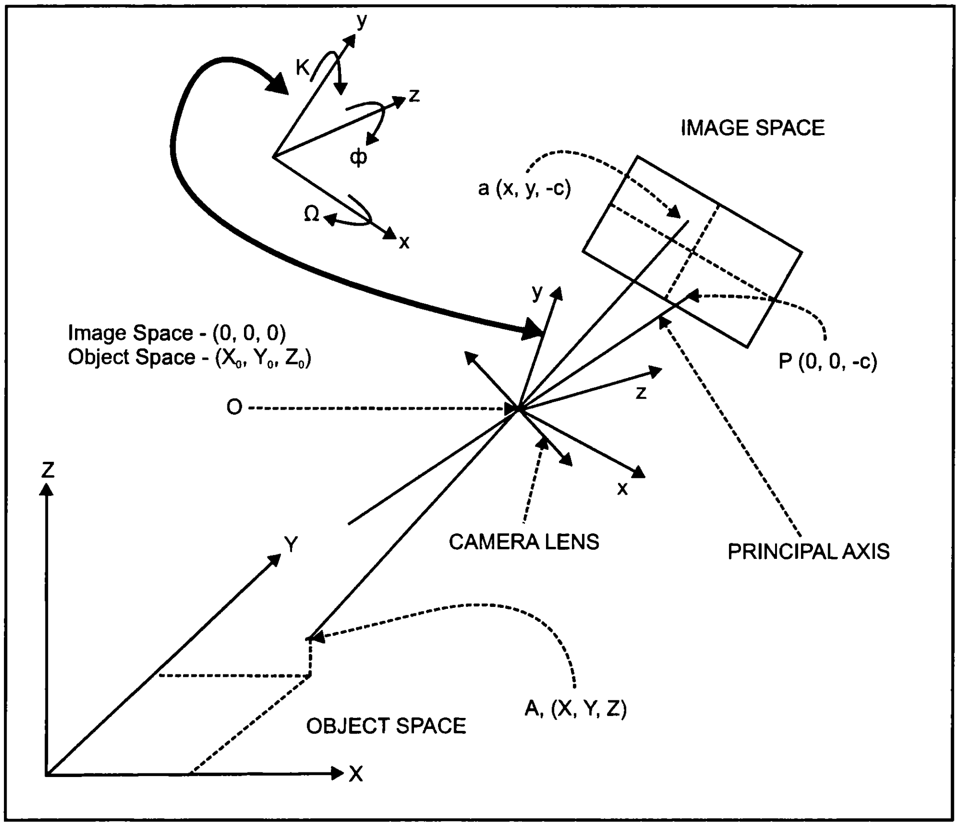

Figure 3.2: The relationship between points in image space and points in object space for a special case of the perspective projection (adapted from Lane *et al.* (1993)).

$$y_a{}^1 = y_o - f\left[\frac{[m_{21}(X - X_0) + m_{22}(Y - Y_0) + m_{23}(Z - Z_0)]}{[m_{31}(X - X_0) + m_{32}(Y - Y_0) + m_{33}(Z - Z_0)]}\right], \qquad (3.10)$$

where x_o and y_o are the principle point coordinates in image space (to correct for offset), and X, Y, Z are object space coordinates of A. The second condition is coplanarity, which extends the collinearity condition to the case of two overlapping images in a stereo pair, and requires that an object point on the ground (X, Y, Z), the perspective centre of the camera in both positions (O_{A1} and O_{A2}), and the corresponding points in the two images (x_{a1}, y_{a1} and x_{a2}, y_{a2}) lie in the same plane (Wolf and Dewitt, 2000).

Solving the collinearity equations (3.9 and 3.10) under the special case of the perspective projection to determine object space coordinates from image space coordinates requires knowledge of: (i) the position of the camera in object space; (ii) the focal length of the camera; (iii) the image coordinates of the camera principle point; and (iv) the rotation of the camera axes. As (ii) and (iii) are held constant, the remaining unknowns are (i) and

(iv) which describe the position and attitude of the camera and are known as the elements of *exterior orientation* (Ghosh, 1988). The process of back-calculation through which the collinearity equations (3.9 and 3.10), and thus the values of these parameters, are solved is known as *space resection.* The space resection process requires at least three points whose positions are known in each coordinate system. Once these parameters are known for each image the collinearity equations can be solved to determine the object space coordinates of any point on the ground within the overlap of two images. The process is known as *space resection* and the points in both coordinate systems are *ground control points* (GCPs). GCPs may be natural or artificial features that can be located on the photographs and for which three-dimensional object space coordinates are known (Lane *et al.*, 1993). GCPs are required to establish an accurate relationship between the images in a project, the sensor, and the ground. Ideally, GCPs should be marked out on the ground prior to aerial survey (Chandler and Moore, 1989), but this may not be possible as ground coverage can be over very large areas with problems of access.

3.3.2.1. Block Adjustment

Solving the collinearity equations for a block of photographs using a least-squares image adjustment is known as *block adjustment* (Granshaw, 1980). This process involves four stages: (i) image digitisation; (ii) interior orientation; (iii) exterior orientation; and (iv) aerotriangulation. Image digitisation is a prerequisite for digital photogrammetry (unlike conventional photogrammetry) and requires that images be input in a digital format. This is possible by either capturing images with a digital camera (e.g. Chandler *et al.*, 2002; Mills *et al.*, 2003) or by scanning analogue imagery using a high-precision photogrammetric scanner. As scanned analogue images are used throughout this thesis, digital cameras are not considered further. In order to achieve the quality comparable to traditional photo prints, photogrammetric scanners must have sufficient resolution as well as geometric accuracy. A scanner should be able to produce digital images with pixel dimensions ranging from at least 5–15 μm to match the resolution of typical aerial photographs.

The process of *interior orientation* aims to reconstruct the internal geometry of the camera at the time the image was captured. For metric frame cameras, this is undertaken using information supplied by camera calibration tests undertaken at regular intervals after manufacture. Camera calibration defines the internal geometry of the camera by measuring the camera parameters that are collectively know as the interior orientation parameters. These include the camera focal length, radial lens distortion and the image space positions (coordinates) of fiducial marks and the principle point. The information entered in interior orientation is used to amend the collinearity equations to account for small distortions in the camera lens which will cause radial distortions in the imagery, film prints or negatives which may experience instabilities from shrinkage or stretching, or atmospheric refraction and Earth curvature effects. For the imagery used in this thesis, lens and film distortions are known from the camera calibration certificate and atmospheric / curvature effects are assumed to be insignificant and accounted for by tie-point and GCP measurement.

Exterior Orientation determines the geometry of the camera relative to the ground surface. This involves measurement of an adequate number of GCPs in order to solve the elements of exterior orientation for each photograph in the block (Wolf and Dewitt, 2000). According to space resection, this is carried out individually for each frame. In analytical photogrammetry entire blocks of images are processed simultaneously using GCPs and the bundle adjustment. Tie-points are also measured to provide redundancy to the solution and to tie the images within the block together, especially for overlapping images where GCPs cannot be measured. The number of control points required for a photogrammetric project depends on the size of the block. In terms of establishing a relationship between the corresponding points in object space and image space for a single image pair, a minimum of 4 points are recommended, consisting of at least two GCPs with X, Y, Z coordinates and one GCP with a Z coordinate associated with it (Wolf and Dewitt, 2000; Kasser and Egels, 2002). Wolf (1983) states that at least two horizontal and three vertical GCPs are required to define the three-dimensional coordinate system in the object space of an entire block, regardless of the number of images, while (ERDAS, 1997) recommend, for a strip of photos, three GCPs should be positioned in the models at the end of the strip and two in every other model.

The process of aerotriangulation applies interior and exterior orientation information in a least-squares adjustment to determine the unknown exterior orientation parameters for each image in the block (Konecny, 2003). A least-squares adjustment finds a best-fit solution by minimising the root mean square (RMS) of the residuals. The elements of interior and exterior orientation are adjusted under the constraint of the uncertainty of their measurement, as determined by standard errors assigned by the user. The least-squares calculation obtains a solution when the residuals associated with the data are minimised following an iterative input process (Chandler and Moore, 1989). This is possible due to the least-squares process allowing data redundancy, or the measurement of a number of observations that exceeds the number required to compute a unique solution. Data redundancy permits the use of large numbers of GCPs, if available, as the effects of their errors may be spread throughout the block and the largest residuals may be removed or re-weighted so as to decrease their influence (Wolf and Dewitt, 2000). It is also possible to triangulate contemporary airphotos without ground control using on-board GPS and INS measurements collected at the time the photographs are taken.

3.3.2.2. Stereo Matching

The concept of stereo-matching in digital photogrammetry concerns the automatic detection of homologous pixel pairs in overlapping stereo images for application to the collinearity equations. The two steps of the stereo-matching concept are; (i) the location of an identifiable point on image 1; and (ii) the identification and location of its match on image 2. Stereo-matching performance is controlled by the camera model, image geometry and quality, and the choice of matching algorithm chosen. Matching algorithms are usually divided into area and feature-based methods.

Area-based algorithms match coincident points in overlapping images by comparing the brightness values of a small window of pixels around each point. A least-squares area-based approach uses an iterative algorithm to compare the grey levels of pixels in one window to the grey level of pixels in the overlapping image. The sum of squares of the differences for each window is then calculated. According to this approach, a homologous pixel pair is the point at the centre of each window pair with the lowest (least) sum of squares. An alternative approach to area-based matching is the correlation function. This is used to determine the statistical significance of the similarity between window brightness values. The correlation coefficient results in values ranging between -1 and +1, with zero no correlation, -1 a perfect negative correlation and +1 a perfect positive correlation. The closer the similarity measure is to +1, the better (more reliable) the matching for that point.

Feature-based matching methods utilise the correspondance between structures extracted from the images using some form of artificial intelligence (Wolf and Dewitt, 2000). This commonly takes place in urban environments and might take the form of edge pixels or line segments (of perhaps roads, buildings or walls) that are picked using an edge enhancement filter (Lane *et al.*, 2000). Feature-based methods are less well-suited to applications outside urban environments where sharp edges are less common. As area-based methods are better suited to natural environments and the SocetSet software uses these algorithms, feature-based methods are considered no further in this review.

3.3.3 The Advantage of Photogrammetry

The use of photogrammetry in glaciological studies has a number of distinct advantages over traditional field sampling methods and other remote sensing techniques. Photogrammetry has the ability to produce DEMs, orthoimages, topographic feature maps and line maps both accurately and efficiently. Geomorphologists traditionally tend to be interested in the morphology and spatial distribution of landforms (Welch *et al.*, 1998). The use of a photograph in this instance is ideal as all points in the image are recorded at a resolution that is in theory only limited by the grain size of the film being used or the pixel size of the digital image. There is therefore almost no limitation on the number of object points that can be measured (Lewin and Manton, 1975). This means that the user has the ability to acquire data at a specified spatial resolution. In comparison to traditional field-based techniques of surface movement, for example, ground survey methods might only provide a few measures of velocity whereas photogrammetry can measure rates of change at a much greater number of locations, limited only by the number of identifiable points on each set of stereo images and the image scale. The nature of sampling strategy may also be improved by the use of photogrammetry. Traditional field-based techniques commit the user to undertaking a pre-defined sampling strategy based upon their interpretation of the feature under study, and a subjective interpretation of the likely course of its development. The retrodictive nature of the photogrammetric approach when designed effectively (Chandler and Moore, 1989) allows the user to obtain data during photographic analysis, and after the full topographic evolution has been observed. In theory, there are no limitations on the amount of surface data that can be observed. This retrodictive approach also means that although re-flying may be cost-prohibitive, photographs are obtained at the level of temporal resolution that is defined, rather than constrained, by the nature of change under investigation (Lane et al.1993).

The use of photographs has a number of clear advantages as a means of providing accurate three-dimensional information. Firstly, the photograph is applicable for a wide range of different modes of scale representation, ranging from micro through meso to macro-scales of measurement. Aerial imagery provides a complete and permanent record of the area under question that can be stored easily, retrieved, and reanalysed at any time. Photographs provide a record of all areas within the image, not just the form in question, which means that extra explanatory information may be recorded. Photographs are area rather than location specific, therefore information is gathered on all areas, not just a few points or sections. Measurements taken from a photo relate directly and precisely to measurements on the ground, so as the image is analysed there is no need to go into the field to measure distances, areas, widths, heights angles or slopes. Compared to field-based measurements, accurate collection from imagery can save considerable amounts of time, energy and money, all the while maintaining accuracy and precision. The retrodictive nature of the technique requires minimal landform contact; this is especially advantageous as large-scale features can be examined without the need for expensive and time-consuming fieldwork in dangerous environments. The problem of access to hazardous landscapes is also avoided if the observing plaform is not in contact with the feature / landscape under question (Small *et al.*, 1984; Brecher, 1986). The problem of sites being disturbed or altered during fieldwork is also avoided.

The move from traditional methods of photogrammetry through analytical and onto digital photogrammetry also has a distinct set of advantages. Chandler (1999) identifies two main advantages of digital photogrammetry over previous photogrammetric methods and other survey techniques: (i) digital photogrammetry allows the production of high-quality DEMs using automated stereo-matching and image-processing algorithms. This allows DEMs of known precision to be generated at rates around 100 times that of earlier photogrammetric methods and approaching 1000 times those of ground surveying techniques (Westaway, 2001); and (ii) photogrammetric software processing packages are now available at commercially competitive prices, particularly for academic usage. Programs such as Leica Photogrammetry Suite (LPS), BAE Systems SocetSet, PCI/EASI-PACE and VirtuoZo have been developed for sale at relatively competitive cost. Photogrammetry is now more cost-effective and available to a greater range of users (Chandler and Padfield, 1989). Both the hardware and software to run photogrammetric analysis are widely available now that desktop photogrammetry software can be run on a variety of operating systems and there is no longer a need for analytical plotters. Advances in digital camera systems coupled to precise GPS positioning will reduce the need for field-measured ground control in the future.

3.3.4 Applications of Photogrammetry in Glaciology

Photogrammetry is a particularly useful technique for monitoring glaciers and remote mountainous regions when compared with traditional field-based methods. Photogrammetric processing transfers the majority of work from the field to the office, which is advantageous when considering the time, expense and uncertainties of fieldwork. As glacier morphologies are dynamic and time-variable, photogrammetry is an ideal medium by which to explore both spatial and temporal changes. Perhaps most importantly, photogrammetry can be used retroactively to reconstruct past glacial conditions, former ice-extent and changes in glacier geometry and volume. This unique advantage means that where historical image archives exist, glacier geometry and elevations can be reconstructed and thus the temporal resolution of mass change estimates can be extended further back in time than that which is available from other remote-sensing approaches.

The application of traditional photogrammetry to glacial environments has existed since the mid 19th century. This work was restricted to the construction of 2-dimensional glacier profiles and the calculation of changes in volume distribution over time by graphical methods (e.g. Finsterwalder, 1954). Modelling glaciers in two dimensions has a number of limitations, principally being the failure to measure profile thinning and thickening. Photogrammetric modelling of glaciers as 3-dimensional entities was limited throughout the 1970s and 1980s due to computation and data handling problems (Fox and Nuttall, 1997). Throughout the 1980s increases in computer processing power and storage capabilities meant that numerical modelling of glaciers and glacial processes developed exponentially. Throughout the 1990s dramatic increases in the availability and usage of high-power computers and dedicated photogrametric workstations, combined with increasingly sophisticated geographical information systems (GIS) meant the ability to generate and handle photogrammetrically-derived DEMs over large areas of terrain became more common. Digital elevation data referring to each point from the image rather than derived contours came to be seen as the primary product. Fox and Nuttall (1997) identify a change in the relationship between photogrammetry and the glaciologist as digital dataset composed of points with plan and elevation coordinates became seen as primary source data.

Numerous examples can be found within the literature of the employment photogrammetric techniques for glacier mapping, in the European Alps and the Antarctic Peninsula (e.g. Wright and Dahl, 1995; Fox and Nuttall, 1997). Likewise, studies have shown glacier geometry changes and terminus retreat at Qori Kalis and Yanamarey glaciers in the Peruvian Andes (Brecher and Thompson, 1993; Hastenrath and Ames, 1995), and retreating glacier fronts on the Antarctic Peninsula (Cook *et al.*, 2005). Photogrammetry has been used to derive surface velocity fields (e.g. Brecher, 1986) and to measure mass balance changes on Erikbreen, North Spitsbergen (Etzelmüller *et al.*, 1993), Haut Glacier d'Arolla, Valais, Switzerland (Willis *et al.*, 1998; Hubbard *et al.*, 2000), Grubengletscher (Kääb and Funk, 1999), Griesgletscher (Kääb, 2000), and Unteraargletscher (Favey *et al.*, 1999; Baltsavias *et al.*, 2001), in the Swiss Alps.

3.3.4.1. Error Handling in Photogrammetric Glacier DEMs

The increases in availability and usage of photogrammetrically-derived glacier DEMs has highlighted a number of significant data quality issues. One of the major weaknesses is the paucity of check data available and subsequently the difficulty of quantifying the accuracy of height data from glacial surfaces. This is principally due to the problems of measuring both ground control and check data points in complex and inhospitable terrain. Types of error inherent to DEMs of glacial terrain are identified by Baltsavias *et al.* (2001), who compared digital photogrammetric processing with manual photogrammetry (generated using an analytical plotter) over a glacier surface, steep-cliff sides and breaklines. They also compared different model fits between a number of proprietary photogrammetric software packages. Results showed that the accuracy of the matching process differed between terrain types, with results for the cliff sections worse than those for the glacier surface, particularly in areas of shadow and sudden height change. RMSE values of these areas ranged between 0.6 - 0.9 m. Results at breaklines were similar or better than the cliffs, yet around 3 - 38 times worse than from flat sections of the glacier surface. Blunders were detected in all areas of the image, although those on the glacier surface were much smaller than those on the cliffs and breaklines. Similar results were reported by Fox and Nuttall (1997) who compared photogrammetrically-derived DEM surfaces of Antarctic terrain with a check data set generated using an analytical plotter. They concluded that there was a clear relationship between DEM quality and terrain type, with successful matches for regions including heavily-crevassed ice-falls, debris-covered lower glacier zones and well-defined boundaries between snow and snow-free areas. Areas with the largest residual errors (> ± 15 m) were associated with homogenous scree-slopes and large open snow-fields with minimal surface texture. Their results showed that area-based image matching worked well for textured areas such as moraine, dirty-ice, heavy-crevassing and rock outcrops. Deep gully systems and widely-spaced crevasses seperated by broad snow areas were more accurately matched using a feature-based algorithm.

A photogrammetric study of volume changes at Midtre Lovénbreen between 1977 and 1995 by Rippin *et al.* (2003) resulted in large errors, estimated to be a combined result of errors inherent in a map of contour elevations (from 1977), 1995 photograph digitisation, and in particular from a small number and poor spatial distribution of GCPs used to process the 1995 DEM. The 1995 images were stereo-matched using just 7 GCPs, each located in the glacier forefield. This lack of ground control (tie-points were used further up the glacier) meant that error estimates (after the application of a correction factor) exceeded the magnitude of the volume changes measured. Calculated volume changes between the two epochs were 11.0 m ± 12.8 m water equivalent (w.e). This study is a good illustration of the need for accurate and well-distributed ground control for photogrammetric glacier DEMs.

3.3.5 Photogrammetry Summary

This section has provided an introduction to the digital photogrammetric method. The first part of the section outlined a brief history of photogrammetry, from analogue through analytical and onto digital stereo-processing of overlapping aerial imagery. The principles of the block adjustment and stereo-matching, whereby elevation information is derived, were then presented. Section 3.3.3 provided an argument for the relevancy of photogrammetry / stereo-processing and showed how the technique can be extremely useful today and holds a number of significant advantages over other field and remote-sensing based methods for deriving high-quality topographic information. Section 3.3.4 gave details of the long and productive relationship between photogrammetry and glaciological research. It is clear from the numerous glaciological examples that the key issues constraining the progress of photogrammetry as a technique for glacier monitoring and modelling are related to image texture and ground control. The problem of image texture is likely to be less of a problem for this research, which is concerned with reconstructing glacier surface models at or close to the end of the balance year at high-Arctic maritime glaciers that are in large proportions snow-free. The issue of ground control however, remains and is crucially important in determining the accuracy of derived DEMs and analyses performed thereon. The following section now outlines a variety of error components related to topographic information derived from both lidar and photogrammetry and illustrates how they may be measured and minimised.

3.4 Topographic Data Quality

The increasingly widespread use of both remotely-sensed image data and automated digital photogrammetric approaches highlights a need for stringent controls on the quality of data if useful information is to be gained from their application. Cooper (1998) argues that the ease with which empirical data can now be generated tends to divert attention away from data quality and towards the processes involved with processing and interpreting results. Increasingly widespread use of automated techniques and procedures may place emphasis on low cost, speed, convenience and ease of use, often to the cost of data quality. In order to place more emphasis on data quality issues it is likely that at least one of the above would be compromised, a trade-off that developers of photogrammetric software packages may not be willing to make. Gooch and Chandler (1999) argue that a technical gap between user and system grows with the advent of automation in more advanced desktop photogrammetric systems. Users must understand the operations and procedures taking place in order to make full use of the instruments at their disposal. Without this understanding the final product is likely to be compromised and not fully utilise the benefits and full capabilities of the system. Clearly undetected error in empirical data can lead to invalid conclusions about the physical processes taking place (Fryer *et al.*, 1994). Digital terrain representations often serve as inputs for detailed study of spatial analyses, particularly for numerical modelling in fields such as glaciology (e.g. Kääb and Funk, 1999). An appreciation of DEM quality is important as small variations in surface values could potentially lead to incorrect modelled results.

Data quality becomes even more significant if two or more surfaces are compared in order to evaluate change over time (e.g. Lane *et al.*, 1994; Brown and Arbogast, 1999). If three-dimensional coordinates describe the location of a point on a topographic surface between two time periods, any difference between the values can be attributed to either, (a) topographic change; (b) error in the surface derived from its interpolation from discrete point measurements; or (c) coordinate datums from the two points not being the same (Cooper, 1998). For those interested in the magnitude of change in topography (or elevation), it is essential to minimise the effects of b and c with respect to a. This can be done by using identical coordinate datums and undertaking careful assessment of error in the dataset. Coordinate differences will be inherent, regardless of whether or not the terrain has actually changed (Cooper, 1998). The following sections describe sources of error in photogrammetrically-derived data and a number of commonly used techniques to assess error and hence, data quality. The components of error referred to for the remainder of this review (accuracy - systematic error; precision - random error; and reliability - gross errors or blunders) refer to definitions outlined in section 3.2.4.

3.4.1 Sources of Error

Desmet (1997) identifies four main sources of error in the production of DEMs. These are: (i) the effects of density and distribution of sample points; (ii) the way in which the data are acquired; (iii) the characteristics of the terrain surface; and (iv) the interpolation method used. While each of these factors has subtly different effects on DEM quality, they are also closely interrelated (Kubik and Botman, 1976).

3.4.1.1. Density and Distribution

As a DEM describes a continuous terrain surface, the density and distribution of discrete points is a crucial factor with regard to data quality. Unless every point on the entire terrain surface is measured, that is if the point spacing between X and Y coordinates in object space and image space tends to zero, then error will occur due to spatial sampling. A number of authors have written about the effects of spatial sampling on terrain surface production with Makarovic (1972), Ackermann (1978) and Li (1988, 1992) identifying it as potentially the most significant control on DEM accuracy. Traditional methods of data collection rely on a vector-based sampling strategy defined by the trade-off between the spatial extent of the study area, the spatial density of measured points and the temporal re-frequency of survey (Westaway, 2001). This means that collection of points has traditionally been controlled by the user. The move towards automated DEM collection through the use of remote-sensing technology such as lidar digital photogrammetry means that points can now be taken at high spatial resolution with high vertical measurement precision. High spatial resolution, when compared to traditional manual methods, comes with only increased file sizes and processing times as significant costs (Smith *et al.*, 1997). Li (1992) concludes that photogrammetrically-derived DEM accuracy is highly correlated with the sampling (grid) interval when gridded data are used, and is also improved by the use of feature specific points (including points measured along breaklines and form lines).

3.4.1.2. Data Acquisition

The ways in which data are collected during a photogrammetric survey are of fundamental importance to the quality of measurements as well as processed end results. Random, systematic and gross error will all occur at different scales during the acquisition phase, therefore it is necessary to separate the causes and effects of each of them before their relative importance can be ascertained. Sources of random error (precision) may include variation in repeat measurements taken in a terrestrial survey, low signal to noise ratios, and GCP positional error and measurement for digital survey techniques. Systematic error (accuracy) might be caused by incorrect calibration of instruments, atmospheric effects, instrument error, and incorrect instrument pointing for a terrestrial survey, and problems of insufficient convergent imagery, incorrect camera calibration, incorrect bundle adjustment techniques and sub-optimal DEM collection parameters for digital photogrammetric surveys. Gross error (reliability) may be adversely affected within the terrestrial survey by such problems as incorrect measurement procedures and the effect of blunders on derived data. Gross error will be affected within digital photogrammetry by a number of factors including poor block triangulation, data input error, effects of viewing problems including shadowing, mismatches in the stereo-matching process and edge effects (Westaway, 2001).

A rigorous digital photogrammetric method will require many of the same controls placed upon conventional photogrammetric surveying along with an appreciation of the adverse effects of the digitisation and automation procedures (Lane *et al.*, 2000). The precision of measurements made in a digital photogrammetric survey is directly related to the image pixel dimensions, both of which relate to the flying height of the camera platform, and the resolution of scanner used to turn photographs into digital images (or, in the case of digital image acquisition, CCD sensor size). Pixel dimensions (in metres), and thus vertical precision, can therefore be calculated before the survey is made using the following formula:

$$\Delta X = s(\delta x/1000000) = p_t \tag{3.11}$$

where 1:s is the photo scale and δx is the scanning resolution (in microns). Vertical precision p_t refers to the standard deviation of error (SDE) associated with all the photogrammetric measurements, such that a stated precision $\pm p_t$, is equivalent to one standard deviation. Around 68% of measurements would be within $\pm p$ of the true value, while around 95% of measurements would be within $\pm 2p$ of the true value.

Some of the adverse effects of the digitisation process and automation procedures in digital photogrammetric surveys are identified by Lane *et al.* (2000). They include digital image creation, stereo-matching performance and feature representation. The creation of digital images requires the use of either a carefully calibrated digital camera or scanned hard-copy images. Problems with camera calibration or image distortion during the scanning process will introduce error. Stereo-matching involves identification of coincident pixel pairs on two adjacent images. In the digital process, this is done using numerical feature-based or area-based algorithms, rather than by a human operator. This relies on sufficient image texture, as well as user-defined parameters such as minimum acceptable correlation indices. Photogrammetry applied to natural terrain surfaces therefore requires careful consideration of optimum parameter sets (Lane *et al.*, 2000). The problem of feature representation is illustrated by traditional photogrammetric approaches which require the user to identify discrete sample points. There may be considerable variability between different users (Chandler and Moore, 1989; Lane *et al.*, 2000). When automated digital photogrammetry is area-based, the density of measured points will represent all features modelled in the landscape. This density must be high enough to include the smallest terrain features being modelled, with consideration for issues of data redundancy and computational efficiency (Lane *et al.*, 2000).

3.4.1.3. Terrain Surface Characteristics

The preceding section has outlined how the effects of terrain have an impact on the quality of data acquisition via the stereo-matching process. A number of authors have previously commented on the effects of terrain roughness on DEM quality and the possible reasons for this (e.g. Li, 1993a,b; Smith *et al.*, 1997; Lane *et al.*, 2000). Baltsavias (1999a) shows that in areas of complex relief, small displacements in X and Y can be translated as significant errors in Z. Planimetric surface error increases on small parts of sloped terrain in images with mostly flat relief. The effect of trees and vegetation is likely to introduce error into photographic measurements of terrain surfaces (Baltsavias, 1999a; Lane *et al.*, 2003). In the case of flooded land and standing water problems will also occur. Photographs may reveal distorted bed surfaces due to refraction effects, or may fail to identify any points at all (e.g. Brown and Arbogast, 1999). The effects of shadowing and relief displacement should be noted as factors that may cause measurement problems through point mismatching (Derose *et al.*, 1998; Lane *et al.*, 2000). These factors are critical when relief is great relative to camera height, or when sun angle is low relative to relief (Westaway, 2001).

3.4.1.4. Interpolation Methods

The effects of interpolation, the method used to create a continuous surface from discrete points measurements, has received less research attention than the three previous error sources. However, it is clear that the method used is potentially critical and has important effects on the quality of the resultant DEM and subsequent model products (Desmet, 1997). Westaway (2001) states that the importance of the interpolation method is increased as stereo-matching performance deteriorates. Commonly used methods of interpolation include bilinear interpolation, inverse distance weighting and kriging (a method of estimation by local wieghted average). Desmet (1997) found that kriging and other related distance-weighting methods produced significant topographic artefacts which had a negative effect of the quality of DEM surfaces. The article goes on to state that an optimal solution for an appropriate interpolation method is a compromise between precision and shape-reliability; the choice of method being determined ultimately by terrain and data type with additional consideration towards computation time and storage space.

3.4.2 Measurement of Error

The importance of data quality in the utility of DEM products places great emphasis on making accurate estimations of error magnitude. There are a number of widely used techniques that can be used to determine photogrammetric DEM error. These can be divided into two categories: static error, referring to errors associated with single DEMs; and dynamic error, referring to errors associated with DEMs of difference (Westaway, 2001).

3.4.2.1. Static DEM Error

There are a variety of error assessment methods that are applicable to a single DEM surface. These range from purely visual assessment, through assessment of model parameters to internal and external assessments. Visual assessment provides a relatively quick and simple qualitative approach to DEM quality through visual comparison of how closely the model resembles known terrain (Brown and Arbogast, 1999; Lane *et al.*, 2000). This assessment usually takes place using visualisation products including shaded-relief maps, ortho-images, paper maps and viewshed images. It provides a particularly useful method of determining the presence of values affected by gross error, which manifest themselves as marked spikes or pits in an otherwise relatively uniform DEM surface. Visual assessment technique may be thought of as a first-order quality control tool.

Assessment of derived model parameters is an approach that developed out of a need to assess DEM quality in the context of the proposed purpose of the DEM. This is seen as being a step towards judging the quality of the DEM on the quality of the output from it, rather than from measured error values. Rather than focusing on point elevation values, empirical approaches such as assessment of visual plots of derivative values and comparison of derived values with independently produced data are considered (Giles and Franklin, 1996; Lane *et al.*, 2000). This method recognises the fact that while inaccuracies may be present in DEM surfaces, they may not be serious problem if they have minimal effect on the derived parameters that are of interest (Lane, 2001).

Internal error assessments can be defined as those which only use information held within the DEM surface. In traditional geostatistical work these methods have been used to estimate unknown values, but in this circumstance can be used to assess uncertainty (Atkinson, 1999). They are particularly useful when there may be little or no available check data. Variously termed 'theoretical-models' and 'simulation-models' these methods work by comparing pixel values with their closest neighbour, leading to identification of the spatial structure of error present in the DEM surface. A comprehensive summary of internal error assessment methods may be found in Westaway (2001). Some of the disadvantages often levelled towards these approaches include the fact that they may provide unreliable estimates of DEM quality; that they are based on mathematical models that are unlikely to apply to real-world situations (Monckton, 1996), and that they require complicated and time-consuming processing procedures in order to compute results (Florinsky, 1998).

External or empirical methods are those which provide a quantitative assessment of the quality of a DEM surface when compared to independent check data of a known higher-order of quality (Li, 1992; Wise, 1998). Traditional error assessments describe the degree of correspondence between DEM height and a true known height as the root mean square error (RMSE), given by:

$$RMSE = \pm\sqrt{\frac{\sum_{i=1}^{n} d_i^2}{n}} \tag{3.12}$$

where d is the height difference between the DEM generated point and the measured or known check point, and n is the number of check points. Measures of RMSE are based on the assumption that errors are random, with a mean of zero and normally distributed around the true value. A number of authors have shown that in the case of DEM error this is not always true (Torlegard *et al.*, 1986; Li, 1988). Li (1988) advocates the use of coupled mean error (ME) and standard deviation of error (SDE) to measure systematic error (accuracy) and random error (precision) respectively, whereby:

$$ME = \sum_{i=1}^{n} \frac{d_i}{n} \tag{3.13}$$

and

$$SDE = \pm\sqrt{\frac{\sum_{i=1}^{n}(d_i - ME)^2)}{n}} \tag{3.14}$$

Equation 3.9 differs from equation 3.7 in that the mean error term is introduced to bypass the assumption of RMSE that no systematic bias exists (Li, 1988). The use of ME and SDE approaches to quantify external DEM quality is gaining increasing usage (e.g. Li, 1988; Desmet, 1997; Butler *et al.*, 1998; Lane *et al.*, 2000).

Empirical assessment of gross errors usually takes place using an evaluation of extreme values. These values, d_{min} and d_{max}, represent the largest negative and positive residuals between DEM and check data elevations (Li, 1988, 1992; Desmet, 1997). In order to seperate all gross errors from the most extreme ones, as this technique may fail to do, a maximum expected error (MEE) measure based on a Gaussian distribution is often proposed (Torlegard *et al.*, 1986). This method works by seperating the majority of values (99.73%) that fall outside 3 standard deviations (SDE) of the mean (ME), and excludes the remaining 0.27% of residuals that can be assumed to be blunders. A common criticism of empirical measures of DEM quality such as this is that they may be unrepresentative as they are often based on small check data samples (usually less than 5% of all photogrammetric DEM points, and potentially even fewer for a lidar survey), and they are aggregated across a whole DEM surface and may therefore reveal little regarding local variations of error (Westaway, 2001).

3.4.2.2. Dynamic DEM Error

The production of DEMs of difference by subtracting one DEM surface from another also produces a number of quality issues that must be considered if we are to use these products as indicators of real morphological / surface change between two time periods. This assessment should allow users to determing whether the results of the differencing are attributable to surface change or are products of error from each surface. Elevation change at each pixel of the DEM surface (represented here by Δh) is calculated by:

$$\Delta h = m_b - m_a \tag{3.15}$$

where m is measured elevation of the same point on two DEM surfaces a and b. Computed elevation change, comprising the true surface elevation change and its associated error is given by:

$$\Delta h = (h_b \pm e_b) - (h_a \pm e_a) \tag{3.16}$$

where h is the true elevation and e is the error occuring at each corresponding point on

DEM surfaces a and b. This expression forms the basis for all calculations of DEM difference, including a global measure of precision e, measured using the RMSE or more correctly SDE, if independent check data are available (Westaway, 2001). The amount of elevation change for each pixel in the difference DEM will be affected by random, systematic and gross errors. The effect of random errors will be uncertainty about the minimum elevation change that can be distinguished from background noise. As both single input DEMs will contain some random error it is necessary to define a detectable level of error (Brasington *et al.*, 2000). A realistic measure of final uncertainty due to random error is provided when precision (or SDE) values are added in quadrature (the root of the sum of squares). Systematic error introduces bias into elevation change values for each pixel which will appear as erroneous elevation increases or decreases in the final DEM. Gross error appears as erroneous elevation changes, often in the form of pits or spikes in the DEM surface, which are relatively easy to identify and remove. Areas of high relative error in difference DEMs may be used to identify areas of error in the input models. This means that difference DEMs can also be used as a tool for single DEM quality assessment.

3.4.2.3. The Failure Warning Model (FWM)

An important method for identifying unreliability (gross errors) in photogrammetric DEM surfaces is provided by the failure warning model (FWM) (Gooch and Chandler, 2001). Errors are often produced in DEMs due to various failures in performance and the choice of image-matching algorithm used. For example, area-based matching may fail in textureless regions with few surface features. If the software used fails to identify matching pixels or matches incorrect pixels, erroneous elevation values will be introduced and the DEM may experience areas of 'image-fallout' or no data. In these cases, traditional methods of error determination (as above) may be used, but there is little help within the software itself to assess the quality of data output (Cooper and Cross, 1988). Gooch and Chandler (2001) identify the importance of strategy parameters in giving the user a degree of control over the automatic DEM collection process. Strategy parameters are the variables that control the acceptance and quality control functions of photogrammetric software. Theoretically, 'correct' strategy parameters should result in an 'accurate' DEM as only succesfully correlated points would be included and unsuccessful points would be identified and excluded from further analysis. An incorrect set of strategy parameters might filter out successful points, include badly correlated points (or false-fixes) or fail altogether to find correlated points (Gooch and Chandler, 2001). The number and nature of strategy parameters is variable between proprietary digital photogrammetric software packages but has been shown to have an appreciable effect on DEM quality (Smith *et al.*, 1997).

Recognising the effect of strategy parameters on DEM accuracy Gooch and Chandler (2001) devised a model allowing the user to focus on specific areas where elevation residuals are greatest. By subtracting two DEMs of the same area generated using different strategy parameter sets, areas where height values are inaccurate are highlighted. Areas on the image where changing parameters have little or no effect, i.e. those with low residual errors, are passed by the FWM and accepted. The algorithm isolates areas of high residuals, areas of significant interpolation, and may be overlaid onto orthophotos to derive height-accuracy maps. The validity of results may be verified by grouping areas and comparing RMSE values between interpolation surfaces and thresholded poor, acceptable and good quality surfaces. The FWM has been successfully applied to DEMs generated from a different terrain types including river environments, rural and residential land cover (Gooch and Chandler, 2001) and Antarctic snow and ice (Fox and Gooch, 2001). An adapted version of the FWM using multiple-input DEMs (MiFWM) has proved successful in assessing DEM quality over glacier surfaces on Svalbard (Pope *et al.*, 2007). The FWM is particularly useful where poor quality or distribution of ground control leads to large numbers of blunder errors in DEM surfaces. The DEM production approach employed in this thesis was to keep extraction strategy parameters constant and to investigate the effects of GCP addition and quality on derived elevation surfaces.

3.5 Chapter Summary

Lidar and photogrammetry provide two methodologically contrasting approaches to measuring glacier surface topography from an airborne platform. Lidar is characterised by high-precision, high-resolution topographic data that has been shown to return centimetre accuracy elevation information over uniform surfaces of low slope, such as an ice-sheet interior. However, models of error from individual lidar components tend to be based on a number of assumptions such as constant flying height, speed and vertical scanning (e.g. Baltsavias, 1999a). While the error inputs of individual lidar elements (laser range, INS, GPS) may be well known, the operational limits on overall elevation quality are highly dynamic and not well characterised within lidar swath footprints and over the complicated terrain typical of high-mountain glacial environments. Existing accuracy assessments of lidar data in glacial environments have taken place using snow-scooter mounted GPS check data, collected in profiles across the snow surface covering a winter or spring ice surface. While useful, this approach does not apply to data acquired over non-uniform summer ablation surfaces. As lidar surveying of many maritime and temperate ice masses takes place during the summer, a comprehensive accuracy assessment of these data is worthwhile. Additionally, the use of lidar data as ground control for photogrammetric models requires that the highest quality points are selected. A thorough lidar elevation quality assessment is therefore essential in order to identify the best GCPs from the raw lidar point cloud data, and assign appropriate standard errors to their three-dimensional coordinates in photogrammetric models.

The literature reviewed in this chapter has highlighted the need for accurate, well-distributed GCPs when controlling blocks of historical aerial photographs. This can be difficult to achieve given the logistical difficulties of fieldwork in glacial environments and the fact that the most appropriate places to position GCPs are often the least accessible locations in the field. The problem of ground control remains the key issue in determining our ability to make precise measurements of glaciers from aerial photographs. Lidar and photogrammetry are competing, yet complimentary techniques. The following chapters will outline how the techniques can be combined and how the advantages of both can be exploited for deriving long time-series measurements of glacier geometry and volume changes.

Chapter 4

Airborne Lidar: Quality Assessment & GCP Selection

4.1 Introduction

This chapter introduces and evaluates the lidar data utilised throughout this thesis and provides the basis for lidar point extraction as photogrammetric ground control. The first sections give details of lidar data collection procedures and pre-processing prior to data delivery. Subsequent sections present a variety of experiments designed to examine the elevation quality of the data. These procedures may be divided into both relative and absolute assessments of lidar data elevation quality. Relative measures were designed to examine the precision of lidar data which principally involved comparison of repeat elevations in areas of data overlap. A variety of metrics were used to assess precision over the different surface types and slopes common to glacial and high mountain environments. Data accuracy was assessed absolutely by comparison with independently surveyed check data of a known higher accuracy. Details of the collection and filtering procedures of DGPS check data are provided, followed by an assessment of the absolute accuracy of returned lidar elevations. The information in this chapter was then used to select those areas within the study area and lidar swath footprint that will provide the best (highest quality) GCPs. Based on these results a list is provided of potential terrain sources of lidar GCPs in glacial environments, together with their likely elevation accuracies and their potential suitability as sources of photogrammetric ground control.

4.2 Lidar Data Collection and Processing

This section provides information regarding lidar data collection by the Natural Environment Research Council (NERC) Airborne Research and Survey Facility (ARSF). Details of the ARSF aircraft and instrumentation are provided before a summary of the principal instrument and survey specifications. Following this is an outline of the data processing steps undertaken prior to data delivery by the Unit for Landscape Modelling (ULM) at the University of Cambridge. This material serves to introduce the important operational aspects of the data on which further analyses were performed.

4.2.1 Pre-Survey Preparation

Airborne data acquisition planning was undertaken in collaboration with the NERC ARSF prior to the 2003 Svalbard campaign. Bounding box coordinates of the Midtre Lovénbreen study site were supplied to the ARSF, including all areas of the the glacier surface, the forefield up to Kongsfjorden waters edge and surrounding mountain peaks and ridges. Data were originally requested at two flying heights; (i) lidar data at 1300 m a.s.l. (for very high-resolution (>1 point per m^2) point density; and (ii) aerial photography at 3000 m a.s.l. to minimise the number of frame images in the block.

Pre-survey instrument calibration routines were undertaken by the ARSF prior to airborne surveying (see section 3.2.3). Lidar flight lines were planned to include 20–30% side overlap to avoid data gaps and compensate for large changes in relief resulting from mountainous topography. Aerial photography surveying at the higher flying height were planned to include 20% side overlap and 60% forward overlap for adequate stereo coverage of the glacier and surrounds.

4.2.2 2003 Data Collection: Midtre Lovénbreen

Data collection during the 2003 field season focused on Midtre Lovénbreen (ML). Airborne data were collected between 10:20 and 11:30 am on August 9th, 2003, by the NERC ARSF using an Optech ALTM3033 lidar instrument. The lidar campaign was supplemented by the acquisition of simultaneous frame vertical aerial photography using an RC10 analogue camera, and multispectral data from an Airborne Thematic Mapper (ATM) optical imaging instrument. Due to poor weather and time constraints both lidar data and aerial photography were acquired at the same time, at an average flying height of 1600 m a.s.l. The instruments were mounted onboard an ARSF Dornier light aircraft. The lidar instrument was configured to record the first and last laser return and intensity information. The significant flight and operating parameters of the airborne survey and ALTM3033 dataset are summarised in Table 4.1. The instrument and survey flight details in Table 4.1 may be used to generate further information specific to this survey using relations provided by Baltsavias (1999a) and Cobby (2002) (Table 4.2).

Average flying speed[1] (v)	~77 ms^{-1}
Average flying height (h_f) (AMSL)	~1600 m
Scan rate (f_{sc})	28 Hz
Laser pulse rate (F)	33 KHz
Scan angle (θ)	±18°
Beam divergence (γ)	0.2 mrad

Table 4.1: Midtre Lovénbreen 2003 lidar survey and instrument specifications.

Swath width (SW)	$2h_f \tan(\theta)$	1040 m
Sample density (p_{sample})	SWv/F	1 per 2.43 m^2
Along-track point spacing (dx_{along})	$v/2f_{sc}$	1.38 m
Across-track point spacing (dx_{across})	$2SWf_{sc}/F$	1.77 m
Ground footprint diameter (A_L)	$h_f\gamma$	0.320 m

Table 4.2: Midtre Lovénbreen 2003 theoretical lidar data survey details.

The ARSF Dornier aircraft was flown at a ground speed of 77 ms^{-1} at an average height of 1600 m a.s.l. The scanning rate of the instrument was 13 Hz which provided 13 complete bi-directional scans per second at a maximum scanning angle of 18° off nadir. This corresponded to an average swath width of 1040 m with a ground footprint of adjacent saw-tooth scans. The laser pulse rate (F) of 33 KHz (33000 individual laser pulses per second) produced an average along and across-track point spacing of 1.38 and 1.77 m respectively (Table 4.2). Point sample density under these survey specifications was approximately 1 point per 2.43 m^2. Laser beam divergence of $\gamma = 0.2$ mrad at 1600 m resulted in a ground footprint diameter of 0.32 m per laser pulse.

The theoretical survey details in Table 4.2 provided an indication of how the lidar data generated in the dataset might appear given these survey and instrument specifications. It must be noted that these values are idealised and relate only to data acquired at a constant flying height, roll, pitch and yaw of the aircraft, and over flat topography at sea level. Given that an average flying height a.s.l. is provided, many of the values would change significantly as the instrument scans terrain closer to the sensor as the aircraft flies over higher altitude terrain. Surface slope and distance from the scanner to the ground surface varied over the course of the survey, and as such caused estimated values of point density, point spacing, scan width and ground footprint size to vary accordingly. A more realistic approximation of operational survey details may be calculated for flat terrain at the mean equilibrium line altitude (ELA) of the glacier, located at approximately 395 m a.s.l. (225 minimum to 650 maximum) (Björnsson *et al.*, 1996) (Table 4.3).

Swath width (SW)	783 m
Sample density (p_{sample})	1 per 1.83 m^2
Along-track point spacing (dx_{along})	1.38 m
Across-track point spacing (dx_{across})	1.33 m
Ground footprint diameter (A_L)	0.241 m

Table 4.3: Theoretical 2003 lidar data survey details at Midtre Lovénbreen mean ELA (395 m).

The full dataset comprised nine adjacent swaths of raw point cloud data totalling approximately 21 million individual datapoints and covering an area of approximately 74 sq km (Figure 4.1). While data density varied according to flying height, topography and the presence of swath overlaps, the spatial resolution of the data was 1.15 point per m^2. Resolution over the glacier surface was approximately 1.05 / m^2. Data within overlapping areas of adjacent swaths had approximately twice the spatial resolution of non-overlapping points.

4.2.2.1. Ground-Based Survey

Ground-based surveying during the course of airborne operations involved the collection of DGPS check data points on the glacier surface and surrounds (for further information see section 4.5.1) and static GPS observations from a fixed basestation. Static GPS data were collected at 10 Hz in order to perform differential processing of GPS positional data from the sensor platform located on the survey aircraft, and to derive the three-dimensional coordinates of raw lidar data (see section 3.2.2). The static basestation was positioned above the known point of a fixed geodetic monument (Latitude 78° 55' 37", Longitude 11° 55' 58", 13.40 m a.s.l.) close to Ny Ålesund, built by the Norwegian State Mapping Agency (Statens Kartverk) (Figure 4.2). The basestation was run continuously throughout each day that the ARSF aircraft was flown. Additionally, observations were collected over a full 24 hour measurement period from 13–14 August in order to obtain a precise single point position (SPP) dataset using all possible satellite positional configurations. The details of all 2003 static GPS basestation surveys are provided in Table 4.4.

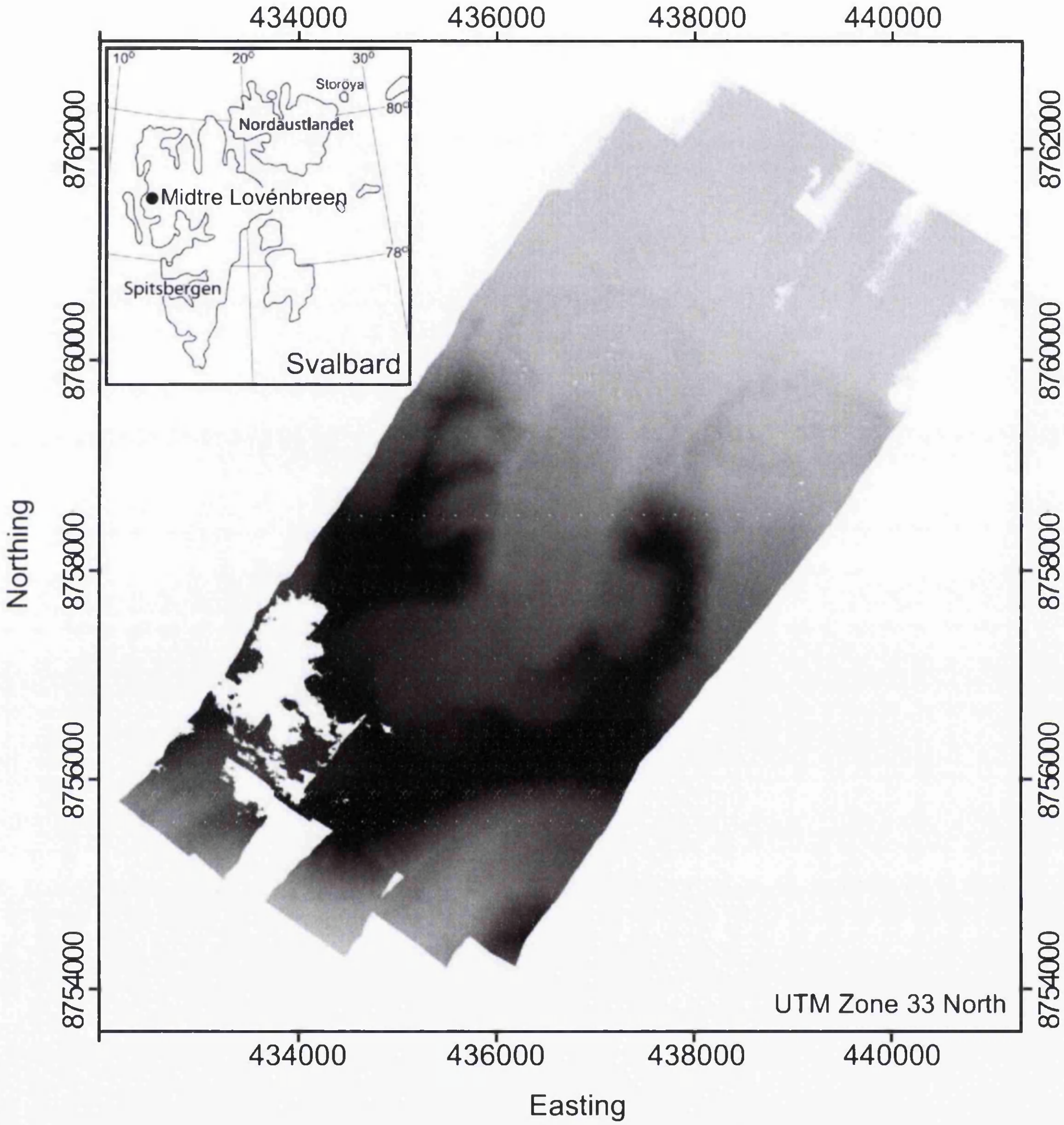

Figure 4.1: Extent of ML 2003 lidar survey data. Image comprises individual lidar data points with greyscale height shading. Darker points represent higher elevations. Inset shows location of ML in NW Svalbard. The cloud affected region in the SW corner of the glacier is clearly visible.

Figure 4.2: Static basestation GPS position during summer 2003. Observations were collected at a fixed height above the Statens Kartverk geodetic known point, Ny Ålesund, Svalbard.

Date	Julian Day	File name	Start (GMT+1)	End (GMT+1)	File Size (Mb)
07-08-03	219	nya1	10:15	18:15	6
08-08-03	220	nya2	09:20	20:25	7.2
09-08-03	221	nya3	08:50	20:20	7
10-08-03	222	nya4	09:00	20:20	7
13-08-03	225	nya5	09:05	-	15
14-08-03	226	nya5	-	09:10	
14-08-03	226	nya6	09:30	17:15	6
15-08-03	227	nya7	09:30	14:00	4

Table 4.4: Static GPS basestation survey details, August 2003. Airborne surveying took place on 10-08-2003.

4.2.3 2005 Data Collection

Following an unsuccesful field campaign in 2004 when instrument failure meant that no new airborne lidar data could be collected, summer 2005 brought the successful acquisition of a repeat lidar survey of Midtre Lovénbreen and surrounds, and a brand new lidar dataset of neighbouring Austre Brøggerbreen. Ground operations focused on collection of GPS check data on the ice surface of Austre Brøggerbreen and operation of the static GPS basestation for differential post-processing of lidar positional data.

4.2.3.1. Midtre Lovénbreen

Repeat survey data were collected between 09:26 and 10:42 on July 5th, 2005 over Midtre Lovénbreen and surrounds by the NERC ARSF. The same Optech ALTM3033 instrument and survey parameters as the 2003 data acquisition were used (see section 4.2.2, Tables 4.1–4.3). Data were collected in 11 overlapping swaths at an average flying height of ~1600 m a.s.l, resulting in coverage of a slightly larger area than the 2003 survey (Figure 4.3). In contrast to the earlier year's survey, the study area was completely cloud free during surveying and thus no signal dropout was recorded.

4.2.3.2. Austre Brøggerbreen

Lidar data were acquired over Austre Brøggerbreen between 14:48 and 16:08 on July 6th, 2005. Due to the larger size of the study site, data were flown at a slightly greater flying height using a larger scan angle than the ML data acquisition (± 20° compared to ± 18°). Full survey and instrument parameters are listed in Table 4.5, and theoretical survey details over flat terrain at sea level and at the ELA (at approximately 413 m a.s.l. (Björnsson *et al.*, 1996)) are provided (Tables 4.6 and 4.7). The full dataset comprised 11 swaths of raw data covering an area of approximately 83 km^2 (Figure 4.4).

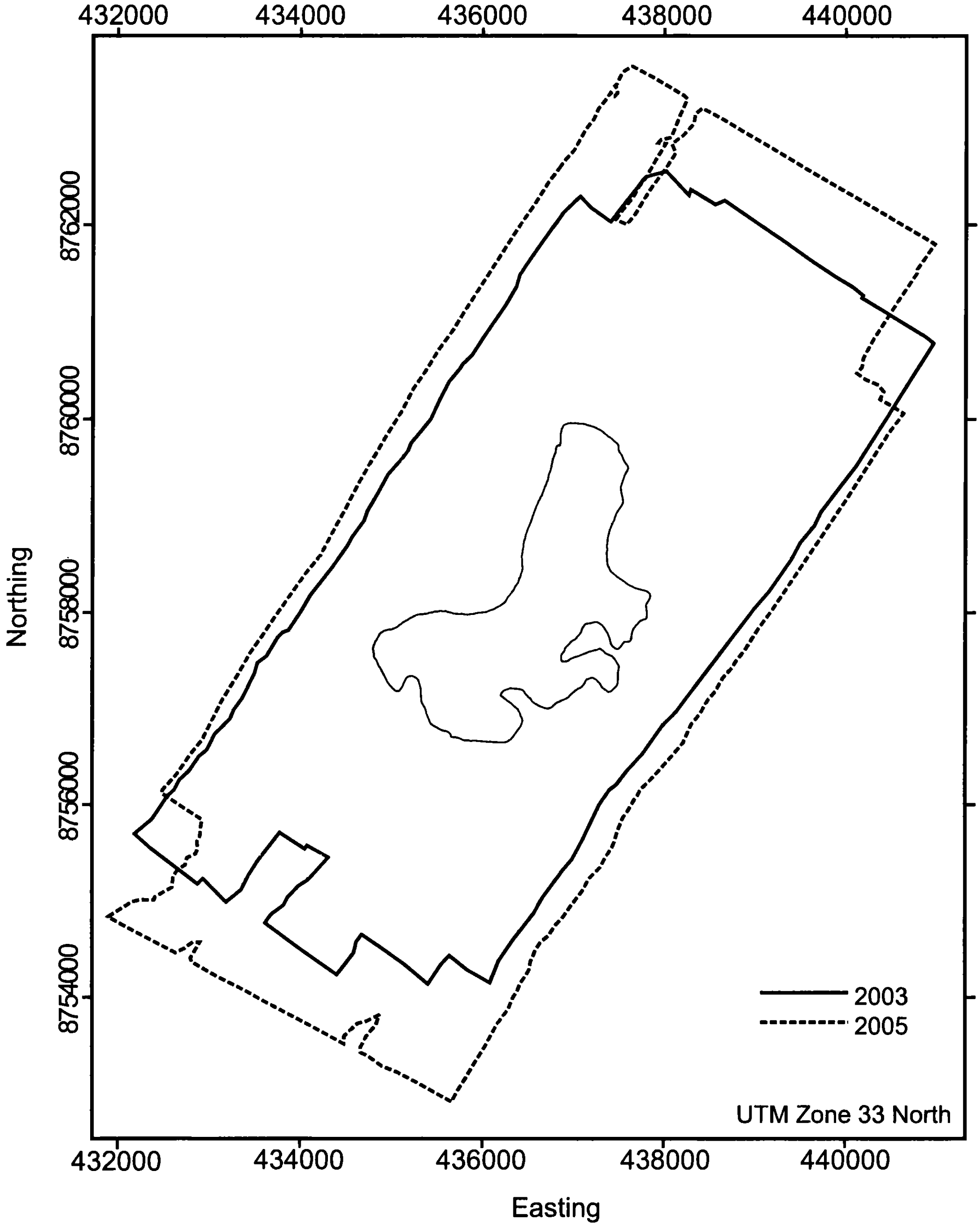

Figure 4.3: Lidar data extent of Midtre Lovénbreen study site (glacier outline within data extents) from 2003 and 2005 repeat survey data.

Average flying speed[2](v)	~69 ms^{-1}
Average flying height (h_f) (AMSL)	~2133 m
Scan rate (f_{sc})	26 Hz
Laser pulse rate (F)	33 KHz
Scan angle (θ)	±20°
Beam divergence (γ)	0.2 mrad

Table 4.5: Austre Brøggerbreen 2005 lidar survey and instrument specifications.

Swath width (SW)	$2h_f \tan(\theta)$	1553 m
Sample density (p_{sample})	SWv/F	1 per 3.25 m^2
Along-track point spacing (dx_{along})	$v/2f_{sc}$	1.48 m
Across-track point spacing (dx_{across})	$2SWf_{sc}/F$	2.45 m
Ground footprint diameter (A_L)	$h_f\gamma$	0.427 m

Table 4.6: Austre Brøggerbreen 2005 theoretical lidar data survey details.

Swath width (SW)	1252 m
Sample density (p_{sample})	1 per 2.92 m^2
Along-track point spacing (dx_{along})	1.38 m
Across-track point spacing (dx_{across})	1.97 m
Ground footprint diameter (A_L)	0.344 m

Table 4.7: Theoretical 2005 lidar data survey details at Austre Brøggerbreen mean ELA (413 m).

4.2.3.3. Ground-Based Survey

As in 2003 (section 4.2.2.1), ground-based operations during the summer 2005 field season were comprised of collection of DGPS check data on the glacier surface (this time at Austre Brøggerbreen) and collection of static GPS observations from a fixed reference basestation. Following negotiations with the Norwegian state mapping agency (Statens Kartverk) permission was granted to collect static GPS observations from an antenna splitter connected to the International GPS Service (IGS) point 'NYA1', located at the Ny Ålesund Geodetic Observatory (Figure 4.5). Improved data storage capacity and access to mains power in the observatory meant that continuous observations could be collected for the entire time the ARSF were on Svalbard. Observations were collected continously from the day prior to the ARSF's arrival until the day after they left, with memory card changeovers, data downloading and backup taking place each morning at 08:00. Differential processing of glacier surface check data points was also possible using these data (see section 4.5.1.2).

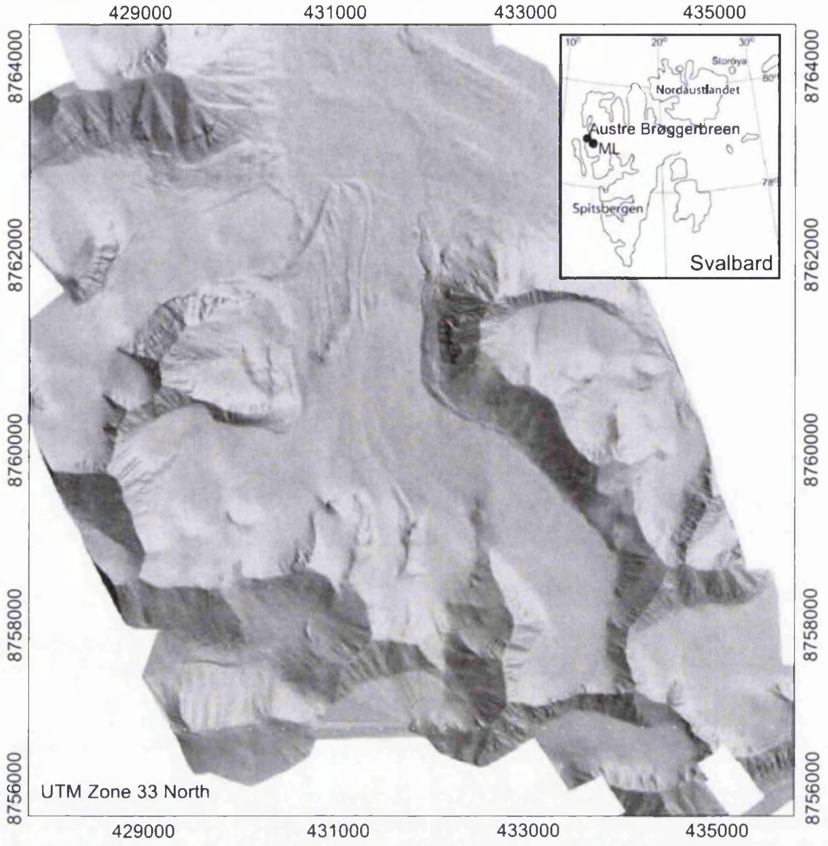

Figure 4.4: Extent of Austre Brøggerbreen 2005 lidar survey. Image shows shaded relief DEM view of the glacier and surrounds. Inset shows location of AB in NW Svalbard.

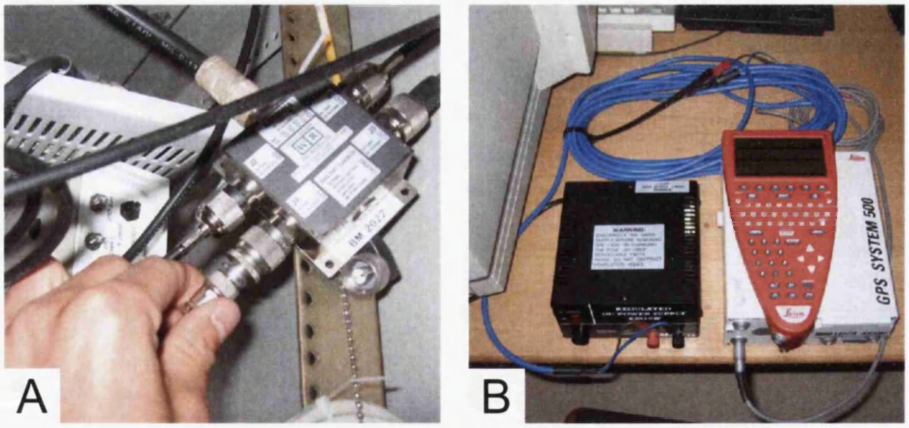

Figure 4.5: Static GPS basestation setup for 2005 data collection. GPS connected to an antenna splitter in the Ny Ålesund Geodetic Observatory (A). The receiver was run from mains power with battery backup (B).

4.2.4 Pre-Delivery Data Processing

Data processing stages prior to delivery to the user are usually undertaken in-house by data providers, and as such can be one of the least transparent stages of the data generation process. Post-processing partners usually use the software supplied to them by lidar hardware manufacturers and, if they do not have the skills or are not prepared to create their own software, may have little alternative or flexibility in post-processing routines. The data used within this thesis (i.e. laser, INS, onboard and ground-based GPS measurements) were input for processing into the Optech ALTM REALM software package (Optech, 2005) by contractors at the Unit for Landscape Modelling (ULM, University of Cambridge, UK). The REALM program checked the quality of GPS data from both receivers using a unitless value of merit known as the Position Dilution of Precision (PDOP). The PDOP expresses errors in user and satellite position as a function of the configuration of satellites visible in the sky at the time of measurement. PDOP values should remain stable and less than $\sim$3; if this is not the case then software will discard the data and they are used no further in the processing (Optech, 2005). Static basestation and aircraft GPS data were combined in differential processing to achieve a solution for the precise position of the scanning platform aboard the aircraft. These data were then merged with laser ranging data to obtain an estimate of the x,y,z position of the aircraft for each laser pulse. The software then proceeded with corrections for atmospheric effects, laser pulse timing errors and instrument biases if applicable, which were determined during the calibration stage. Finally, INS data were reconstructed to accurately determine the attitude of the sensor at the time of each laser pulse.

The REALM software produced single files of ASCII x,y,z coordinates as well as data in the comprehensive binary format Log ASCII Standard (LAS). LAS is an interchange format designed specifically for the transfer of lidar data between vendors, customers and data users. Files are usually output in the WGS84 Universal Transverse Mercator (UTM) coordinate system, although coordinate system transformations may be requested from the data supplier or undertaken in post-processing by the user. Data points were checked first by the data supplier to ensure full coverage of the study site. Systematic errors between swaths were identified by the extraction of data extent-wide cross-sectional profiles, and may be compensated for by re-processing the entire dataset using slightly altered INS calibration coefficients (Cobby, 2002). Following the removal of any systematic errors (which was not applicable in this case), data were output into area tiles or swaths to limit individual file sizes.

4.3 Relative Lidar Quality Assessment: Data Precision

This section and section 4.4 give the methods and results of techniques employed to process lidar data post-delivery from contractors to ULM with the purpose of examining elevation precision and accuracy. The aim of this work was to assess the precision and accuracy of lidar elevation data in a glacial and high-mountain environment in order to select the highest quality control points for photogrammetric models. Operational lidar data precision and accuracy were assessed for the 2003 Midtre Lovénbreen dataset using relative and absolute methods. Relative errors (precision) were assessed by comparing data from coincident areas within overlapping swaths. Absolute errors (accuracy) were assessed by comparing lidar data with independently surveyed DGPS check data.

Assessing the elevation precision of lidar data required no additional survey data as flights were planned to include overlap between adjacent swaths of data (e.g. Latypov, 2002). As the extent of overlaps between data swaths included significant proportions of the total study area, it was possible to compare, on a relative basis, error over large portions of the total data extent. Standard lidar survey procedures operate with an adjacent swath overlap of ~30%, which means that potentially 60% of the total collected points may be checked against each other. The ARSF operate using an overlap of 20% in good flying conditions, rising to 30% in poor conditions to compensate for aircraft roll (P. Goy, 2006, pers. comm.). An overview of the extent of individual swath boundaries gives an indication of the amount of overlapping data present within the 2003 dataset (Figure 4.6).

Large areas of overlapping data existed between the adjacent strips 305–306, 306–307, 307–308, 308–309, 309–310, 310–311, 311–312 and 312–313. Furthermore, strip 313 was re-flown at the end of the survey to compensate for aircraft roll during the collection of strip 310. This meant that strips 313 and 310 were almost completely coincident (Figure 4.7).

The most comprehensive and computationally efficient way of examining the difference between data from two seperate scans of the same terrain was to interpolate the raw cloud points of each dataset and subtract one from the other. This approach had the advantage of comparing data over the entire extent of overlaps, which included overlapping data along the full length of each swath. In the case of large datasets such as these (individual swaths contained upwards of a million raw lidar datapoints), this method provided an efficient approach for comparing very large numbers of points over a variety of terrain and surface types.

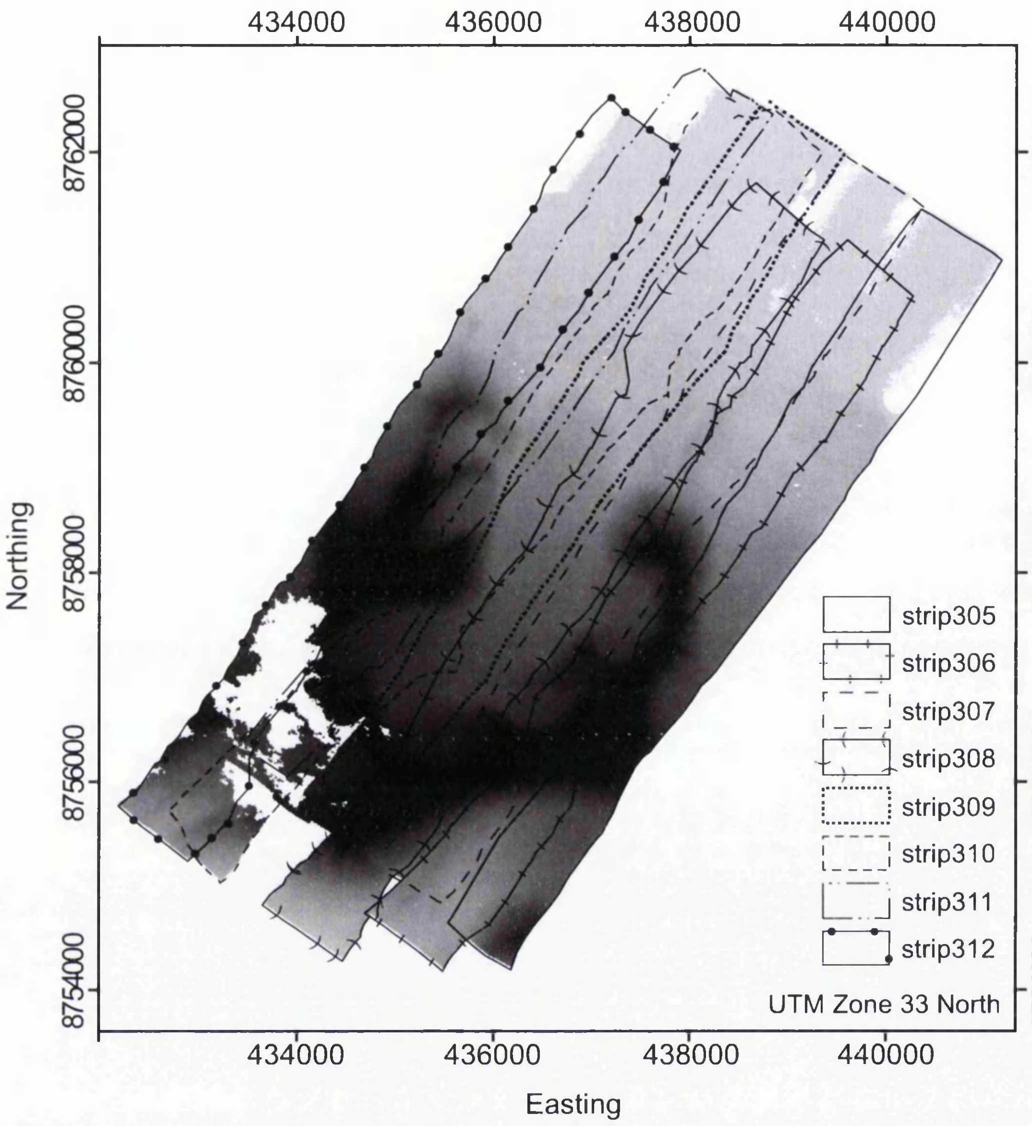

Figure 4.6: Individual swath boundary outlines showing data overlap areas, overlaid onto lidar data points. Strip313, flown to repeat strip310, is not included.

4.3.1 Filtering Cloud Returns

A number of non-surface elevation points were returned from cloud cover present within the southwest corner of the study area during airborne surveying (see Figure 4.6). To filter these data from further analysis raw lidar point files were processed with scripts 'cloudthresh.gawk' and 'remblun.gawk' (Appendix 2). The cloudthresh program filtered all lidar points by elevation, deleting points with a z value of less than 0 m a.s.l. and greater than 850 m a.s.l. (above the highest peak of the study area). This minimised the number of erroneous height points around the glacier backwall in the SW corner. The remblun.gawk script was used

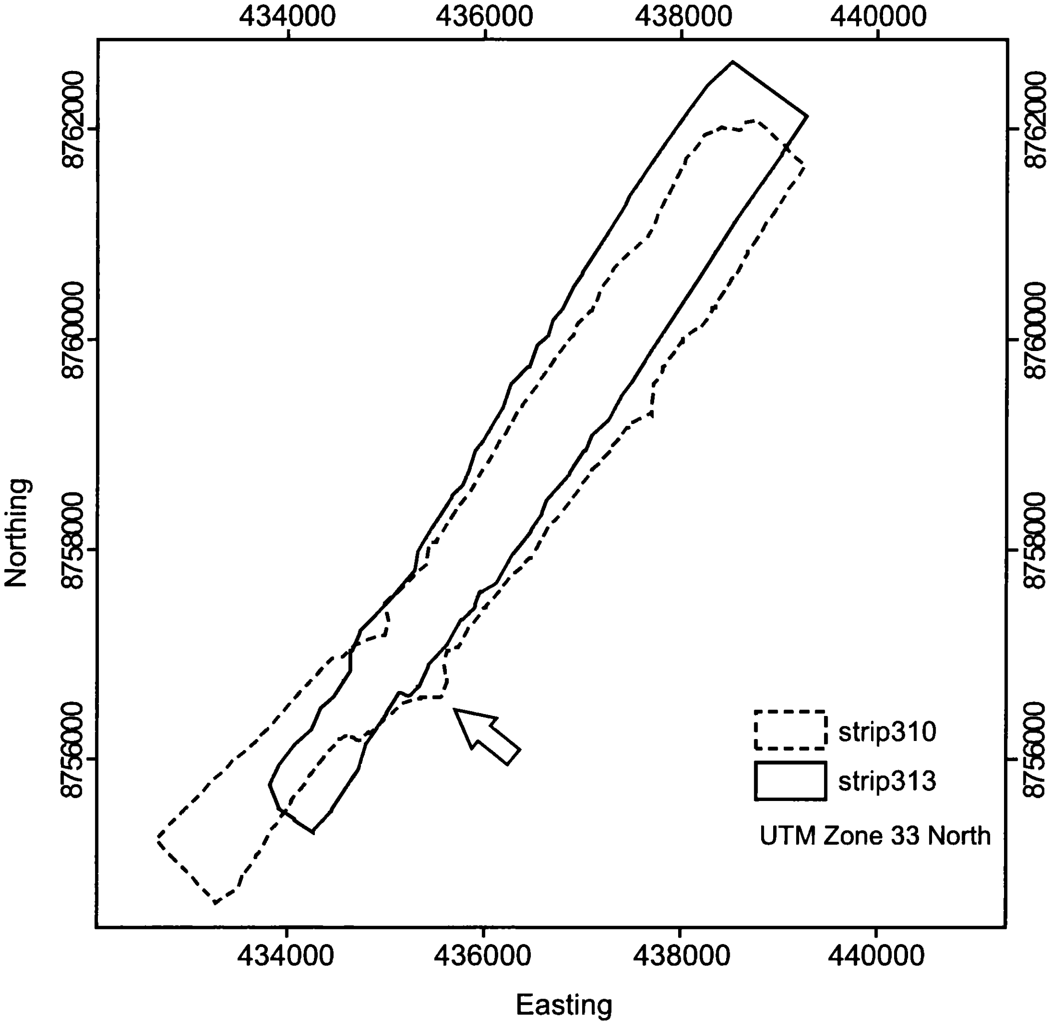

Figure 4.7: Lidar data swath outlines of strip 310 and its repeated flightline, strip 313. Strip 310 was re-flown due to aircraft roll during surveying. The effect of roll on swath pattern and shape is clear at around 435000 East, 8757000 North (see arrow).

to remove points with a returned laser intensity value of 0 (on a scale of 0-256). Although these points were included in the raw data delivery, points of such a weak signal strength are considered to provide unreliable elevation information and recommended to be excluded from any analyses (Optech, 2005). The remaining points above the upper glacier surface and below the highest mountain peak were manually identified and removed using 3-dimensional data visualisation software (Applied Imagery, Quick Terrain Modeler). Around 150 points were identified where elevations were more than 3 meters greater than surrounding points on the ice surface within a 5 m radius (the glacier had very low surface slope in this region). These points were flagged and removed from each point dataset text file before gridding.

4.3.2 Creating Swath DEMs

Creation of continuous DEM surfaces from raw lidar data is likely to introduce error into the resultant surface where the gridding algorithm chosen interpolates between irregularly spaced points. This error will have a direct effect on values generated by differencing overlapping models. To minimise these effects, areas of no data in the lidar point cloud were masked before gridding, and therefore not included in individual swath DEMs. The command 'grdmask' in the software program Generic Mapping Tools (GMT) (Wessel and Smith, 1998) was used to create files of x,y coordinates representing each datapoint location. A binary mask was then set up to exclude all cells more than 1 m from the nearest datapoint. All mask and DEM files were constructed with the same bounding box coordinates to ensure correct coincidence of DEM cell value locations prior to the differencing calculation.

To avoid data redundancy each swath dataset was processed with the GMT command 'blockmean' which averaged the elevation of 1 m pixels containing more than 1 datapoint. Raw lidar points were then interpolated into a DEM at 1 m grid spacing using the same bounding box coordinates as the binary mask. Interpolation was carried out using the GMT command 'surface', which utilises a tensioned spline interpolator. This continuous curvature algorithm offered an adjustable spline tension operator which may be set between 0 (giving a minimum curvature surface - a natural bicubic spline) and 1. DEMs were processed with a spline tension of 0.65, which is a value generally recommended for topographic applications (Smith and Wessel, 1990). The two grid files, one a regularly spaced grid of data including interpolation between areas of no data, the other a binary mask of data extent, were then multiplied together. Areas of no data (NaN, not a number) in the mask output, multiplied by the grid output, resulted in DEM cell values of NaN. This meant that each cell in the output DEM that did not originally contain a raw data point within its 1 × 1 m pixel area was designated NaN. Repeating this process for each of the nine swaths of raw lidar data resulted in 9 individual DEMs for flightlines 305 to 313, with irregular edges and gaps for those cells which did not originally contain a data point.

4.3.3 Differencing Swath DEMs

DEMs of each flightline of data were differenced using the 'grdmath' command. Difference models were created for the following subtractions of adjacent lines: 306-305, 307-306, 308-307, 309-308, 310-309, 311-310, 312-311, 313-312. A further difference model was created for near-coincident strips 313-310 (Figure 4.6). Descriptive statistics were calculated for each of the nine difference models individually, and for the sum of all pixel comparisons from all models (Table 4.8).

The mean residual elevation difference of comparable pixels from all models was 0.02 m,

Diff. model	Strips	Number of pixels	Mean $\overline{\delta h}$ (m)	St. dev. $\overline{\sigma h}$ (m)	Min. (m)	Max. (m)
A	306-305	1512726	-0.05	0.85	-14.98	9.95
B	307-306	1746360	0.12	0.65	-7.72	9.80
C	308-307	1421940	-0.14	0.63	-9.79	7.88
D	309-308	1944291	-0.05	0.40	-8.96	9.38
E	310-309	2125867	0.14	0.38	-8.19	9.97
F	311-310	1066460	-0.06	0.64	-11.87	10.09
G	312-311	906640	0.48	0.66	-9.96	9.94
H	313-312	114173	-0.29	0.36	-3.31	3.94
I	313-310	2360150	-0.02	0.38	-9.29	10.06
All		10524819	0.02	0.71	-14.98	10.09

Table 4.8: Descriptive statistic of lidar elevation difference models (1 m pixel size).

while individual model means ranged from 0.02 m (I) to 0.48 m (G). Standard deviations were all less than 1 m. The total mean elevation residual comprised more than 10 million coincident lidar elevation comparisons, and at close to zero, indicated that there were no significant systematic shifts between overlapping data. Large standard deviations reflected the fact that each of the models covered a different variety of terrain, including the relatively flat braidplain, ice surface and areas of steep-sloping mountain sides.

The spatial distribution of elevation residuals per overlap model were displayed as plots (Figures 4.8–4.12). The plots showed that elevation residuals varied both within and between overlap models. Model E (strips 310-309) appeared to show a greater proportion of large elevation residuals in comparison to the remaining models. This may be a result of poor quality data from strip 310 which had to be re-flown (as strip 313) following excessive aircraft roll during surveying. Examination of the spatial distribution of lidar elevation residuals revealed two distinct trends:

1. Elevation residuals were larger over mountainous terrain.
2. Residuals increased toward the outer edges of overlap models.

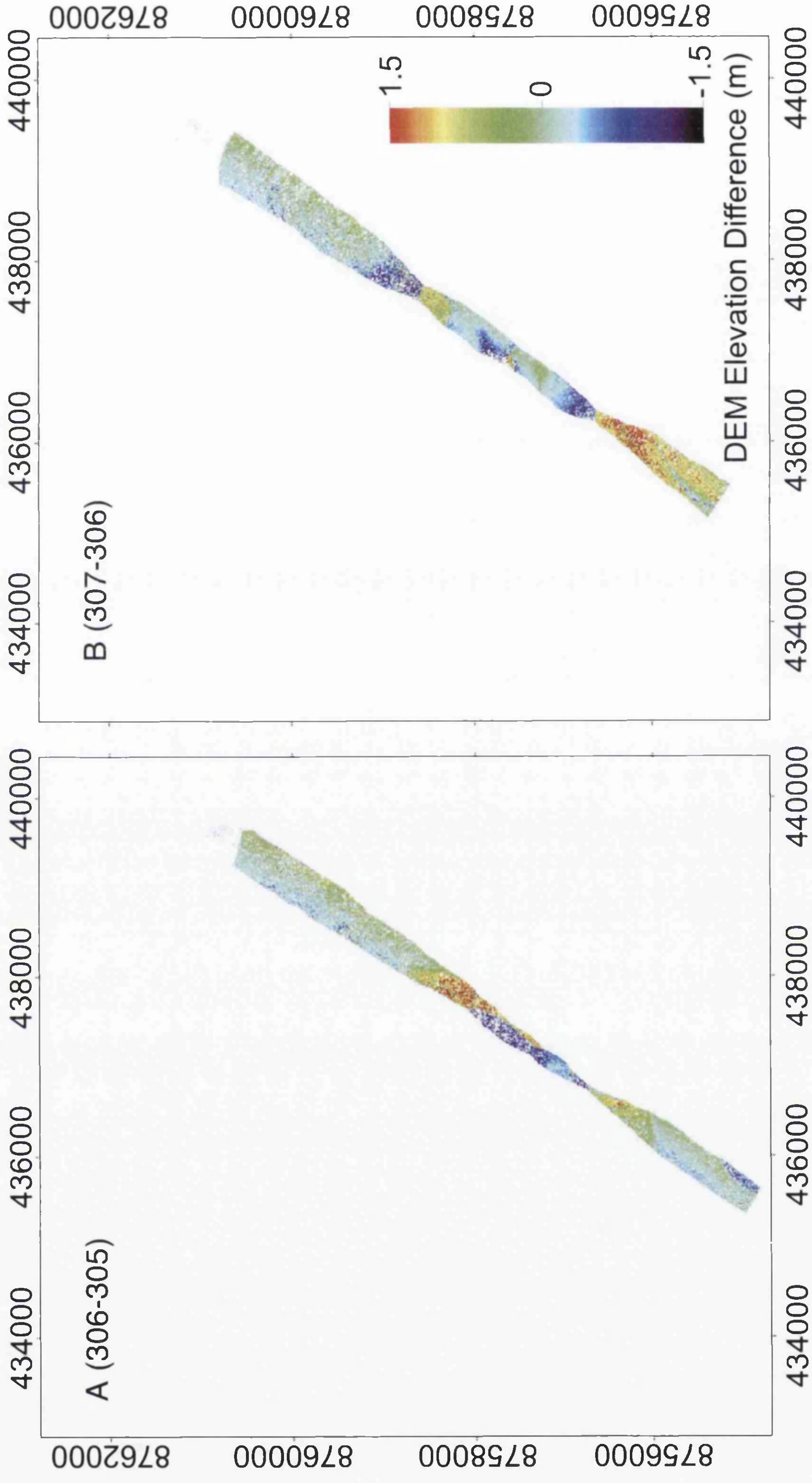

Figure 4.8: Spatial distribution of lidar elevation residuals for overlap difference DEM models A and B.

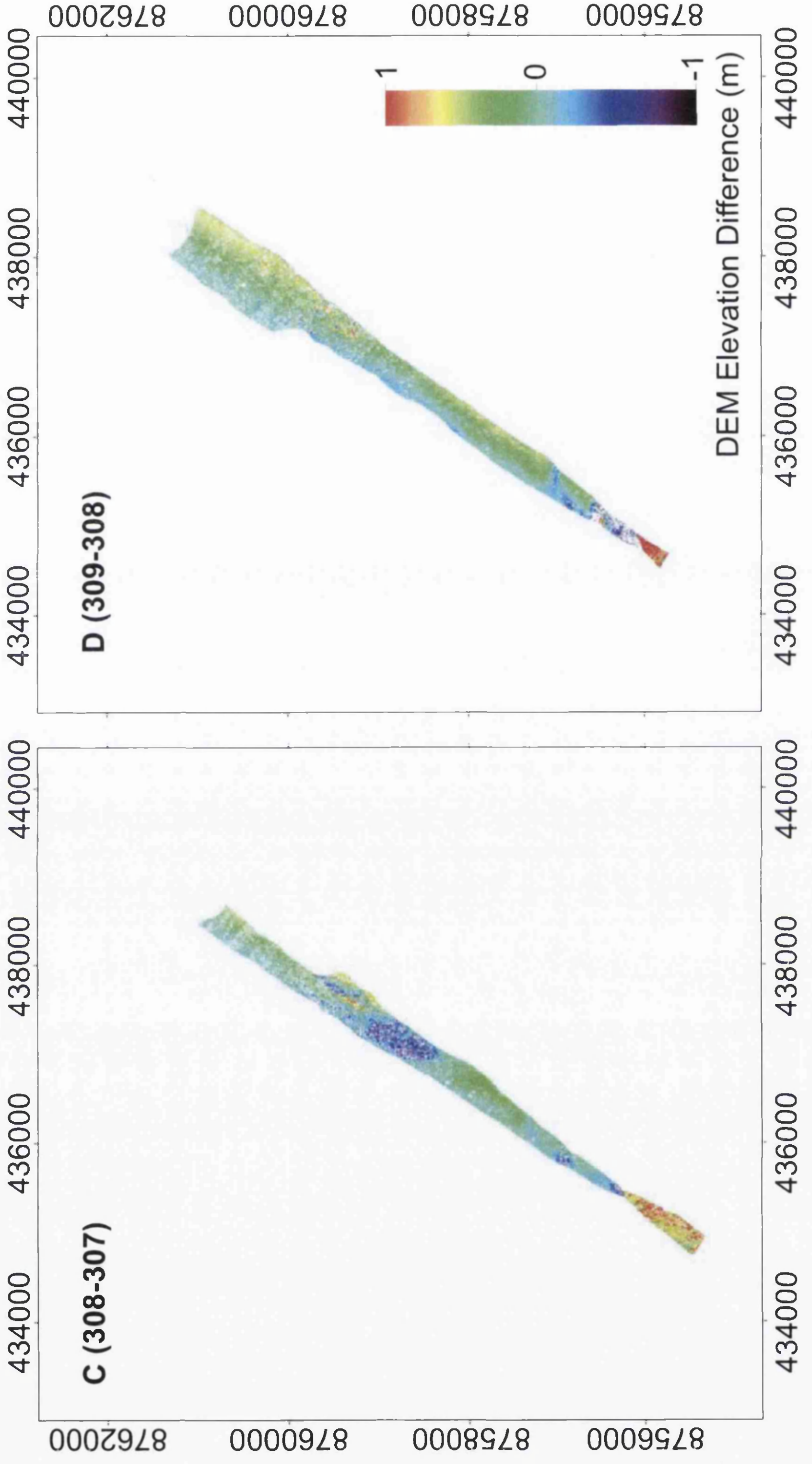

Figure 4.9: Spatial distribution of lidar elevation residuals for overlap difference DEM models C and D.

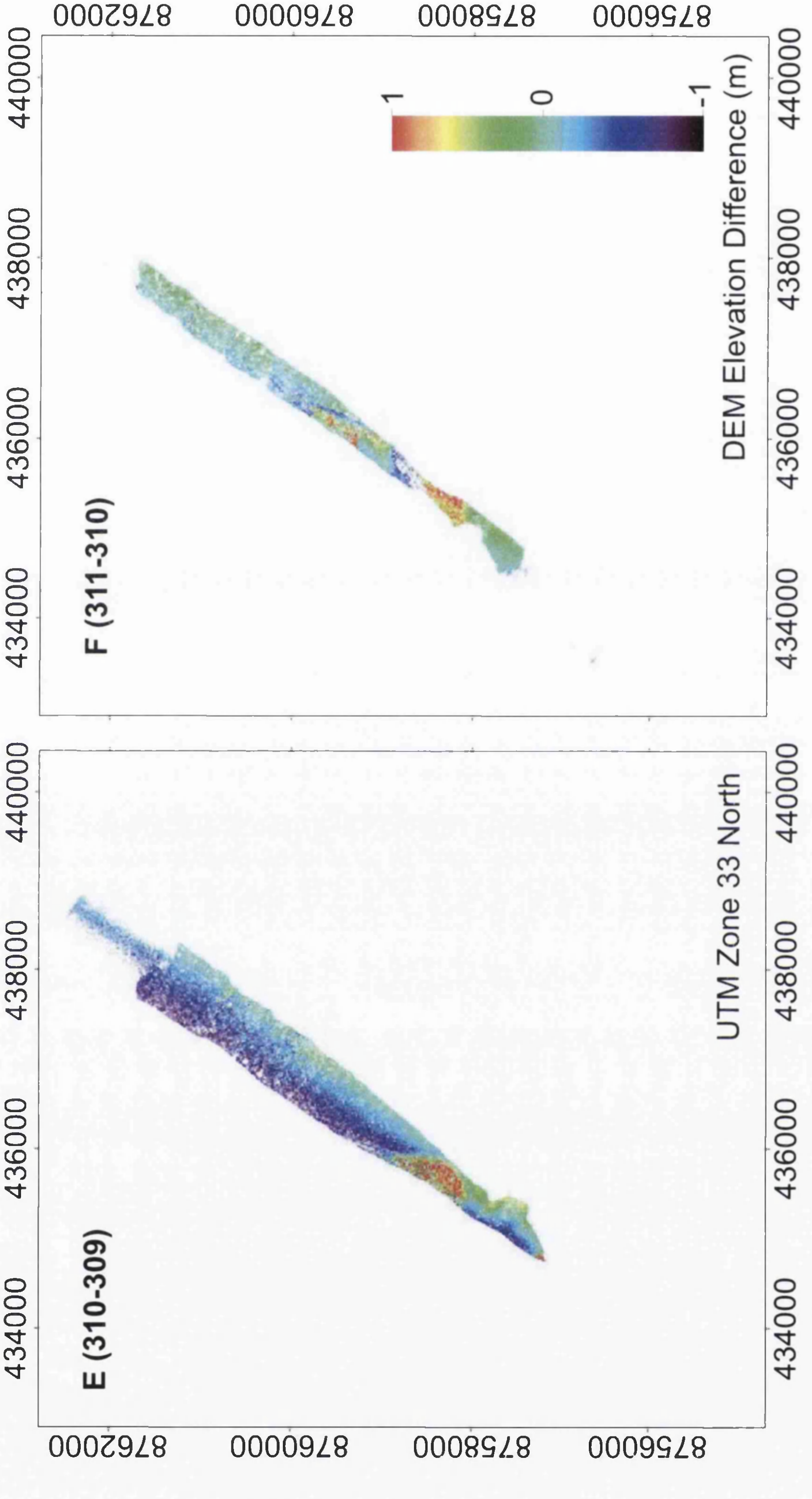

Figure 4.10: Spatial distribution of lidar elevation residuals for overlap difference DEM models E and F.

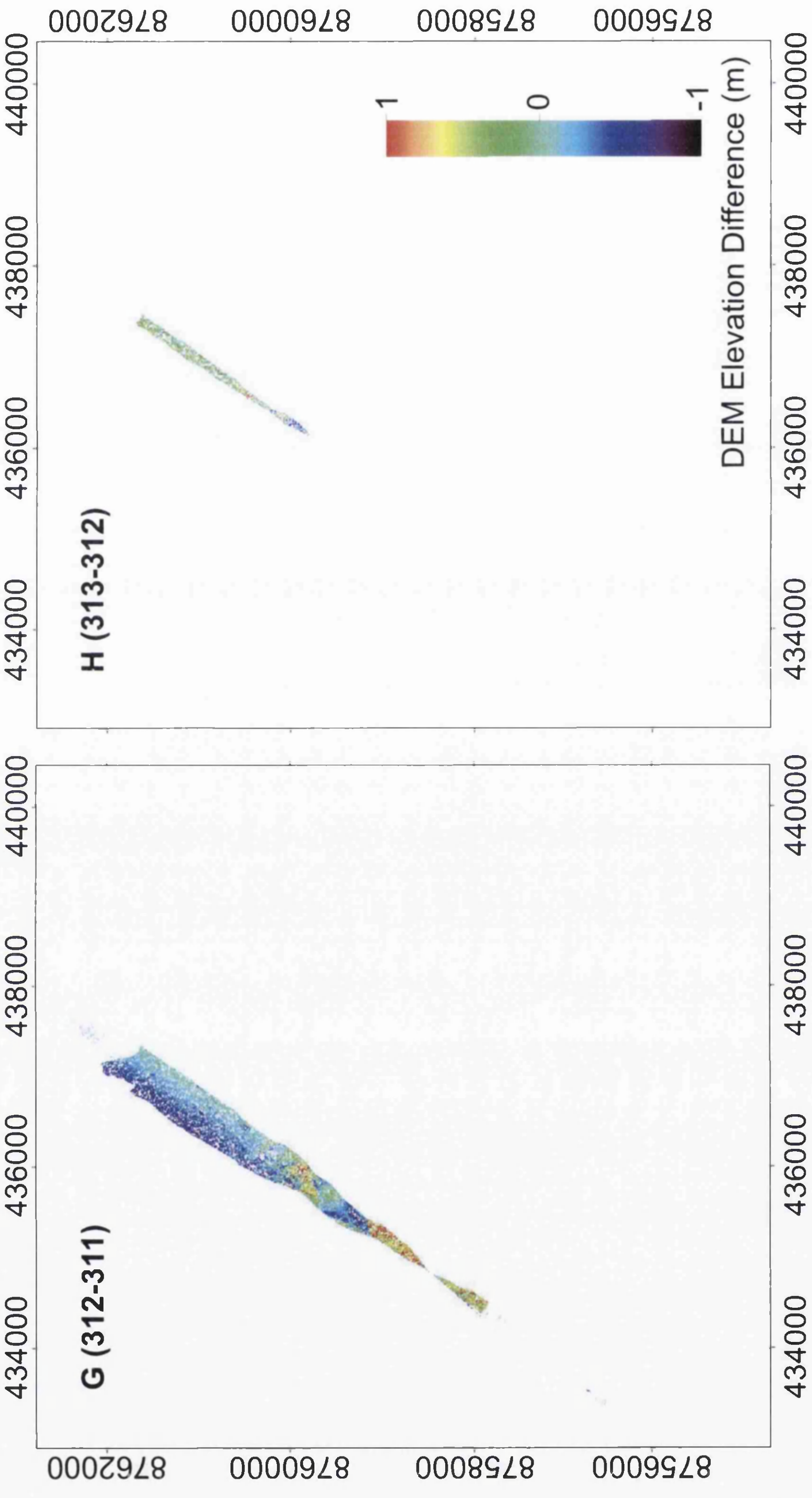

Figure 4.11: Spatial distribution of lidar elevation residuals for overlap difference DEM models G and H.

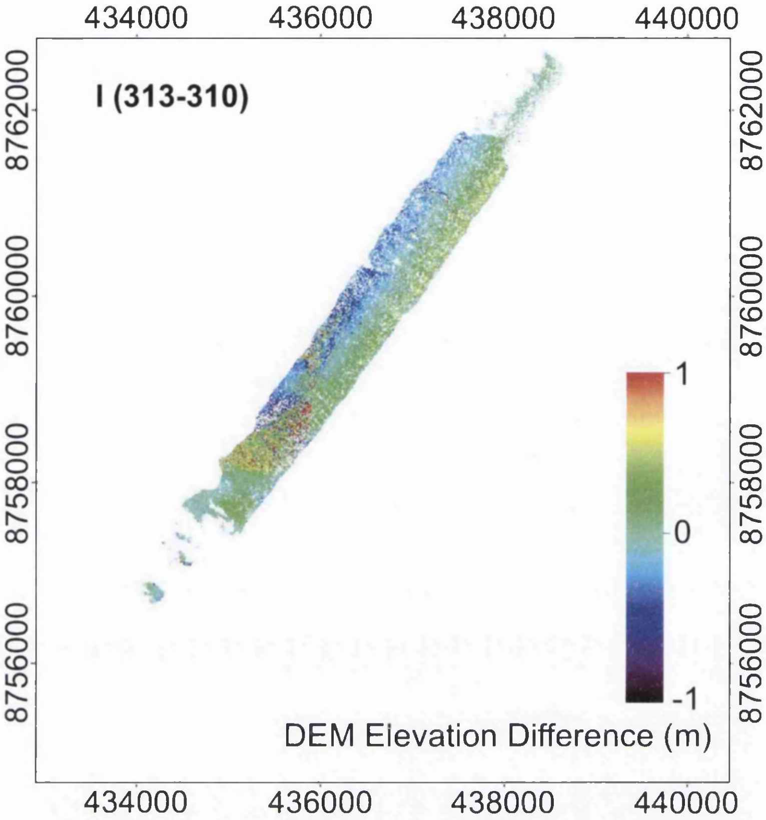

Figure 4.12: Spatial distribution of lidar elevation residuals for overlap difference DEM model I.

Larger elevation residuals over mountainous and steeper sloping terrain were clearly indicated in models A, B, C, E and I, and to a lesser extent in models F and G (Figures 4.10 and 4.11). In particular, models A (around 437000 E, 8758000 N), B (for example at 437500 E, 8759000 N), C (at 437000 E, 8759000 N), E (at 436000 E, 8758000 N), and I (at 435500 E, 8759000 N) showed residuals that commonly exceeded ±0.5 m and coincided with steep-sloping mountain terrain. These values were noticeably larger than those of the surrounding flatter terrain which typically fell within ±0.25 m. The demarcation was clear between mountain-side zones of larger elevation residuals and the less steep areas where residuals were typically smaller. This meant that in several examples, overlap difference models illustrated the morphology of mountain terrain through the spatial pattern of elevation residuals. Particularly good examples of this were model C (at 437000 E, 8759000 N) where the western flank of Slåttofjellet peak is present, and models E and I (at 435500 E, 8758500 N) where the eastern side of Berteltoppenfjellet can be seen.

Overlap difference model plots indicated that elevation residuals were larger at the outer extents of the models (in the direction perpendicular to line of flight, Figures 4.8–4.12).

Residuals were lowest at the centre and increased toward the outer model edges. The trend was apparent in all of the difference models with the exception of model H which had insufficient coverage. Over relatively flat terrain (areas of the lower glacier surface and forefield) the magnitude of differences between swath centre and swath edge residuals was on the order of approximately 0.25 m. Pixels predominantly from the overlap model centre had differences of ~±0.25 m, while values from the edges had differences of as much as ±0.5 m.

To investigate in detail the magnitude and distribution of relative elevation errors (precision) in this lidar dataset, difference DEMs were assessed using three analyses: 1) subsets, 2) profiles, and 3) surface slope analysis. Subsets of data were defined and analysed from within the difference models to assess elevation precision over the surface types common to high mountain glacial environments. Profiles were extracted perpendicular to direction of flight to examine the magnitude of relative errors in the across-track direction and examine further the finding that residuals were larger toward the outer edges of difference models. Finally, DEM cell values were grouped according to surface slope and difference statistics calculated to investigate the influence of slope angle on elevation precision.

4.4.3.1. Surface-Type Subsets

Subsets of elevation residuals were defined in each of the difference models for the following surface types: A) the glacier forefield and braidplain; B) mountain-side slopes bounding the ice surface; C) the glacier surface at lower elevations (50–300 m a.s.l.); and D) the glacier surface at higher elevations (400–550 m a.s.l.). The surface types for each of these classes were delineated from a high-resolution (1 m) lidar DEM. Mountain-side slopes bounding the glacier surface were defined as ice-free areas proximal to the glacier boundary with surface slopes in excess of 20°. Residual values were then extracted from each of the difference models intersecting the four surface types. These values were combined and used to generate descriptive statistics and frequency distributions for each surface type subset (Figure 4.13).

The distribution of relative elevation residuals over the lower and upper ice surfaces of the glacier were very similar with the majority of values falling within ±0.25 m (Figure 4.13 C, D). The upper ice surface sample had larger minimum and maximum residuals which may be due to a greater concentration of crevassed areas in upper basins of the glacier. Large differences in elevation were likely to be a result of differing scan angle geometry of lidar pulses returned from crevasse edges, walls, ledges and perhaps crevasse bases. Means of these two samples were similar (within 0.03 m), but the larger standard deviation of the

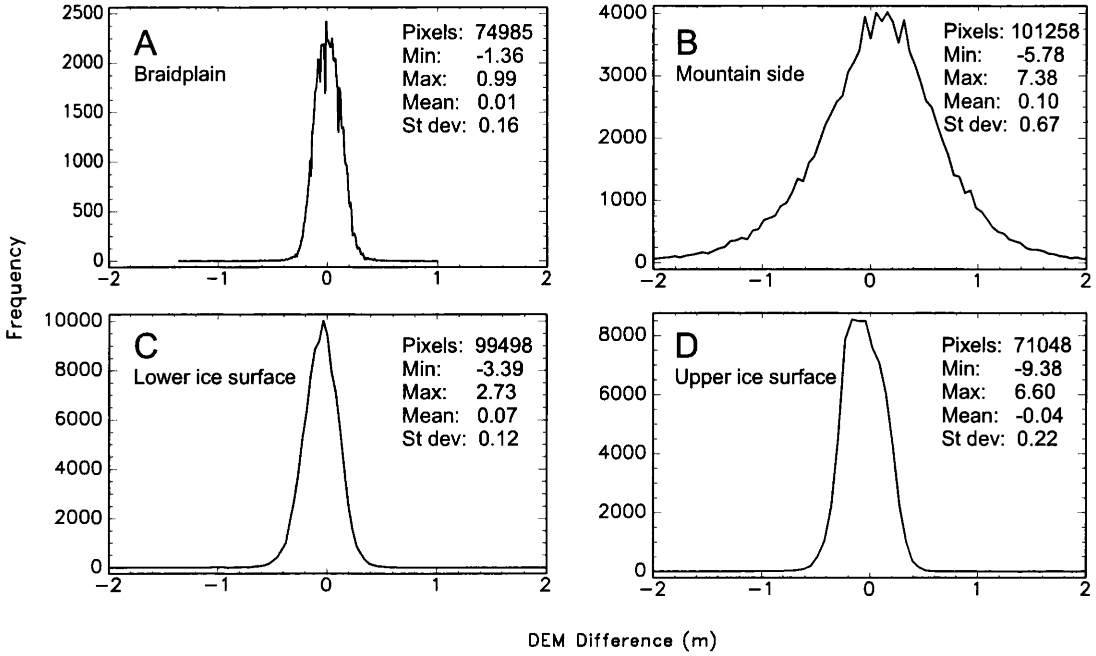

Figure 4.13: Frequency distribution and descriptive statistics of surface type subsets extracted from lidar DEM difference models over A) the glacier forefield and braidplain, B) mountain terrain proximal to the ice surface with > 20° surface slopes, C) the lower ice surface (50–300 m a.s.l.), and D) the upper ice surface (400–550 m a.s.l.).

upper ice surface (0.22 compared to 0.12) suggested that there were more large residuals in the sample. This was probably due to crevasse effects and the prevalence of ice with steeper slope angles in the tributary cirques and upper basins of the glacier. The large minimum and maximum residuals from the lower ice surface sample were unlikely to be a result of crevasses, rather these differences were probably due to heavily incised supra-glacial meltwater channels that occur in the lower reaches of the glacier. These channels were progressively incised further down glacier and can reach depths upwards of 2 m (e.g. Arnold *et al.*, 2006a). These sorts of substantial channel morphologies were likely to produce elevation residuals of the magnitude observed in these results as a consequence of returns from channel edges, sides and within the channel itself.

Residuals extracted from the braidplain and glacier forefield had a similar distribution to those from the glacier surface (Figure 4.13 C). Minimum and maximum residuals were substantially lower than both ice surface subsets, presumably as the braidplain was less steep and did not have over-deepened channelised features such as crevasses or supra-glacial meltwater streams. The mountain-side subset had the largest range of elevation residuals with values commonly more than ±1 m (Figure 4.13 D). Correspondingly, this subset also has the largest sample standard deviation. The distribution of large elevation residuals and high standard deviations indicated that steeper slope angles typical of ice-proximal mountain side terrain provided lower quality elevation returns. This is likely due to an increase in laser pulse ground footprint size over steeper slopes. The relatively high minimum and maximum residuals (> 5 m) may be indicative of very steep or vertical cliff-like terrain whereby small errors in plan (x,y) can translate to substantial errors in elevation (z).

4.4.3.2. Difference Model Cross Profiles

Cross-profiles were extracted perpendicular to direction of flight from the overlap models at 500 m intervals to investigate in detail the magnitude and distribution of relative elevation error in the across-track direction (see Figures 4.8–4.12).

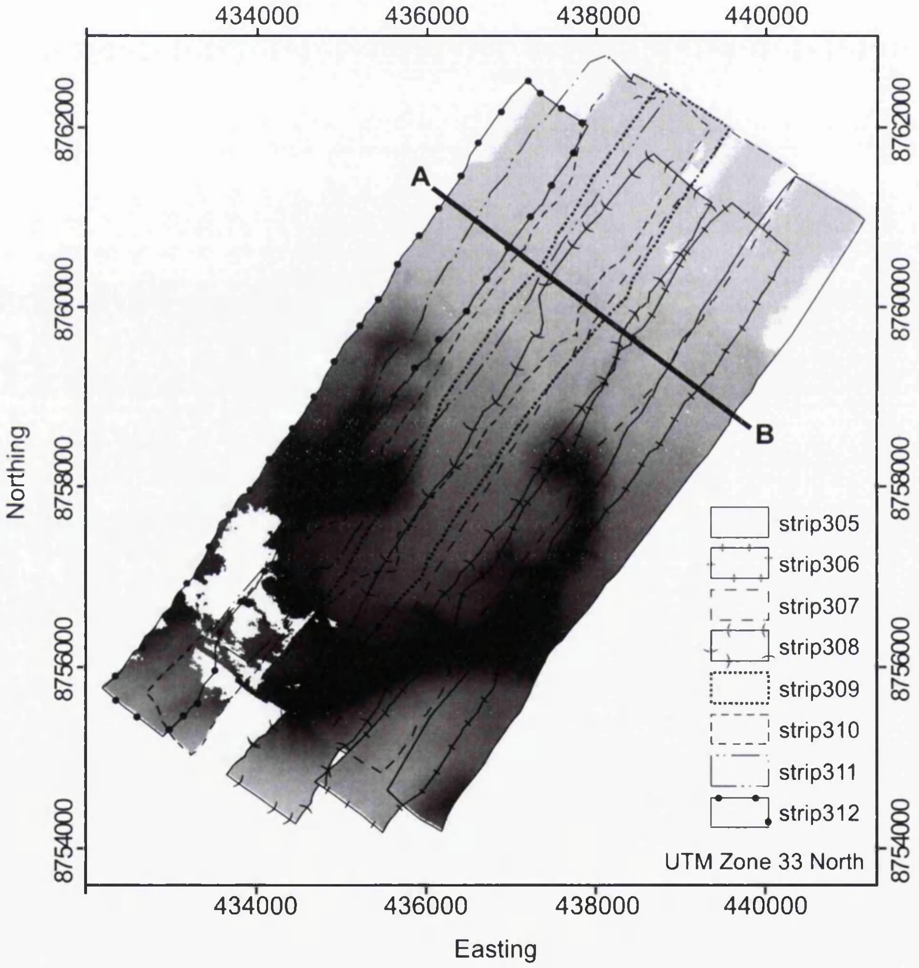

Figure 4.14: Transect A–B, showing the location of cross-profiles extracted from lidar overlap difference models.

To minimise the effects of changes in topography and surface slope the profiles displayed here were extracted along a transect from the relatively gently-sloping braidplain (A–B, Figure 4.14). Profiles from each of the overlap models, with the exception of model H (as there was very little coverage), are displayed (Figures 4.15 and 4.16).

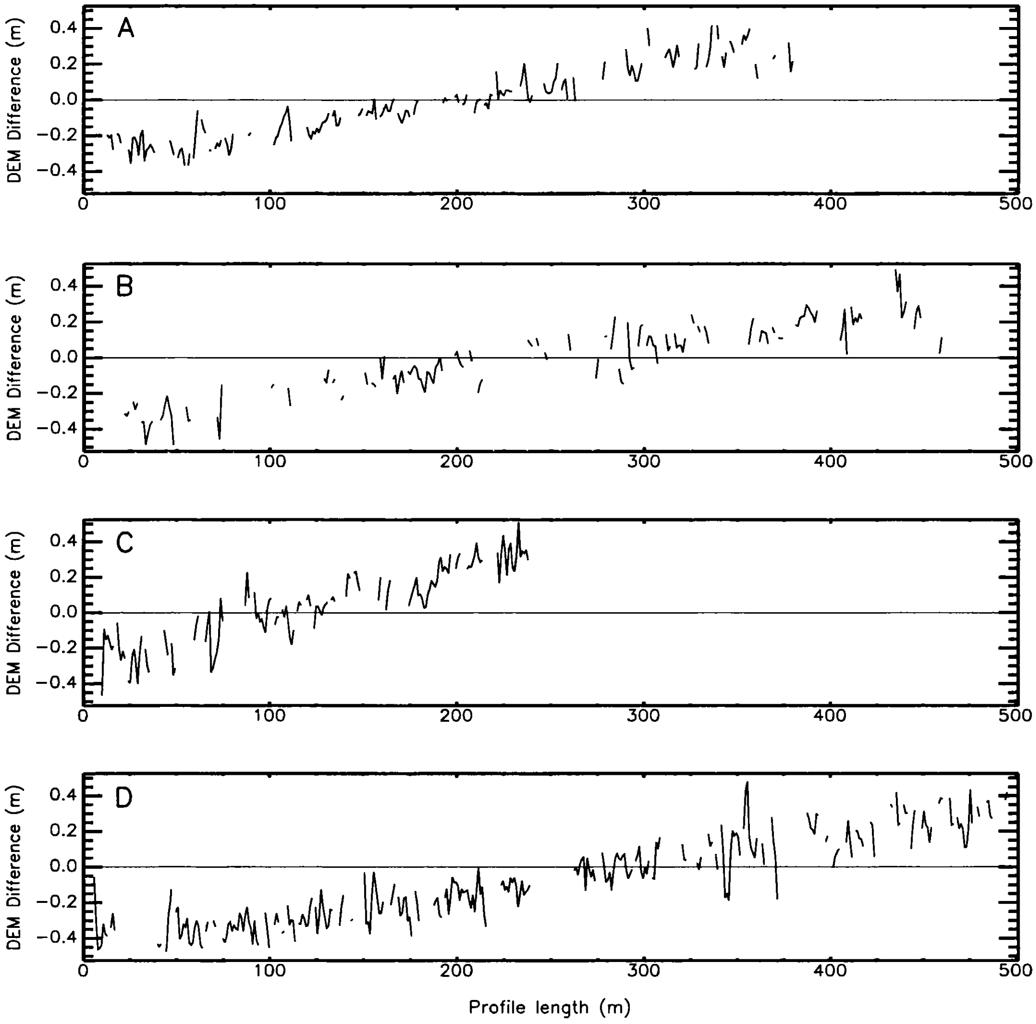

Figure 4.15: Difference model elevation profiles extracted along transect A–B (Figure 4.8) over the ML braidplain from overlap models A–D (strips 306-305, 307-306, 308-307 and 309-308). Gaps in the profile occur where no lidar point fell within the 1 m pixel boundary of one or both of the differenced DEMs.

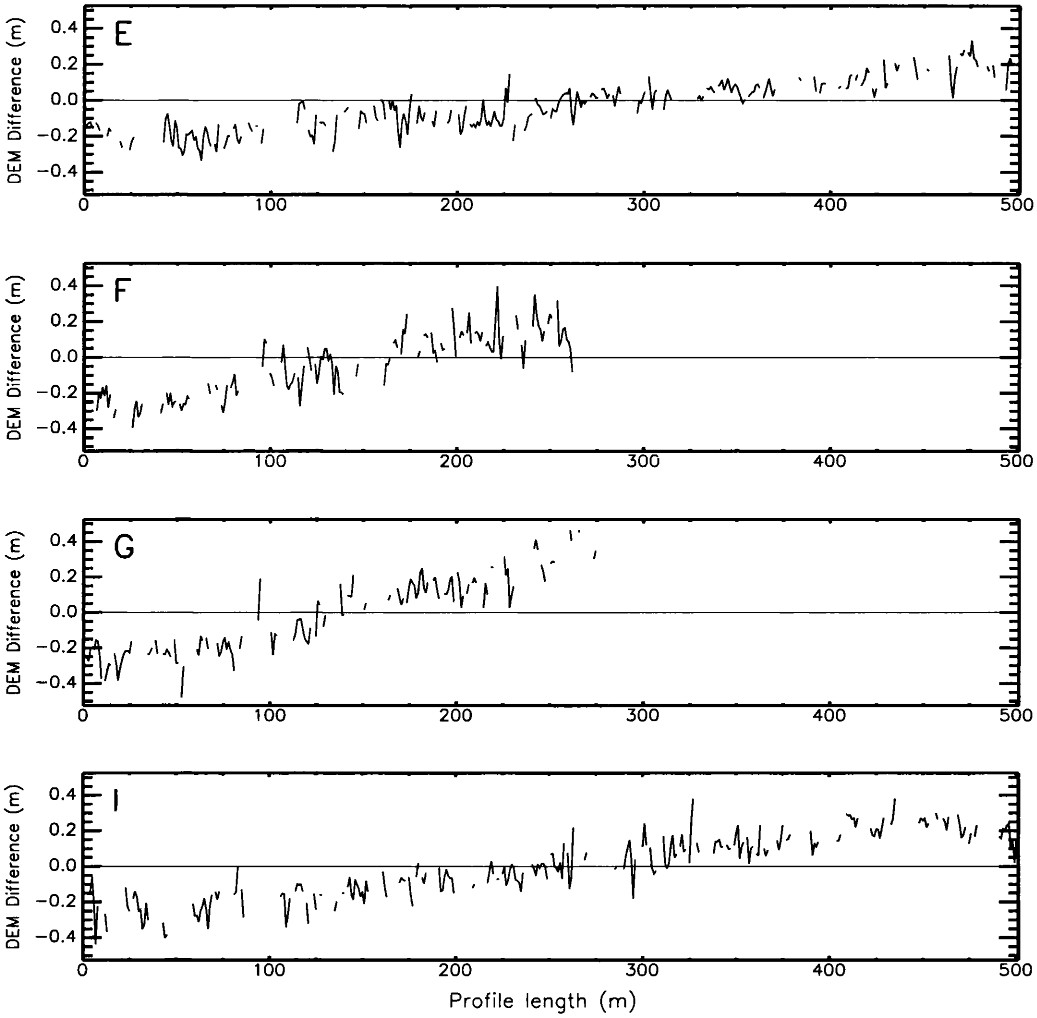

Figure 4.16: Difference model elevation profiles extracted along transect A–B (Figure 4.7) over the ML braidplain from overlap models E–F and I (strips 310-309, 311-310, 312-311 and 313-310). Gaps in the profile occur where no lidar point fell within the 1 m pixel boundary of one or both of the differenced DEMs.

The distribution of elevation residuals extracted from profiles perpendicular to direction of flight (Figures 4.15 and 4.16) confirmed that the largest residuals occurred towards the outer extents of overlap models (e.g. Figures 4.8–4.12). The profiles varied in length due to the amount of overlap between adjacent strips. Profiles from models C, F and G were between 240 and 275 m in length, while models D, E and I (from overlapping strips 313 and 310, Figure 4.12) were closer to 500 m along transect A–B (4.14). Models A–I all showed variability in the magnitude of elevation residuals, typically on the order of ±0.25 m along the length of each extracted profile. Despite this, a clear trend was evident. Residuals were on the order of ±0.3–0.4 m towards the outer extent of overlap models and within ±0.1 m towards the centre of the profiles. This indicated that lidar elevation precision was optimised towards the centre of overlap models, or rather, further from the edges of data swaths.

4.4.3.2. Surface Slope Analysis

The influence of surface slope on lidar elevation precision was investigated by grouping residuals into 10° bins according to their slope angle. Slope maps were derived from a high-resolution (1 m) lidar DEM for 10° bins from 0–10° up to 60–70° (Figure 4.17). Mask files were then derived for each slope class and multiplied by each of the overlap difference models. DEM pixel values from each difference model were combined into each of the slope bins. All areas of overlapping data (and therefore direct lidar elevation comparisons) were therefore grouped into bins based on the slope angle of the terrain from which they were returned.

Slope maps of ML and its surrounding terrain revealed that the majority of the glacier surface fell within the 0–10° slope class (Figure 4.16). The more steeply sloping glacier margins around the snout, tributary basins, and backwall fell mostly within the 10–20° class. Most of the glacier forefield and braidplain was in the lowest slope class, with the exception of some areas of steeper moraine topography which had slopes of 10–20°, and in a few cases, 20–30°. The mountain-sides, peaks and ridges bounding the glacier were clearly demarcated by their steeper slopes, typically 30–40° on the majority of the larger slopes, and 40–50° around the highest peaks.

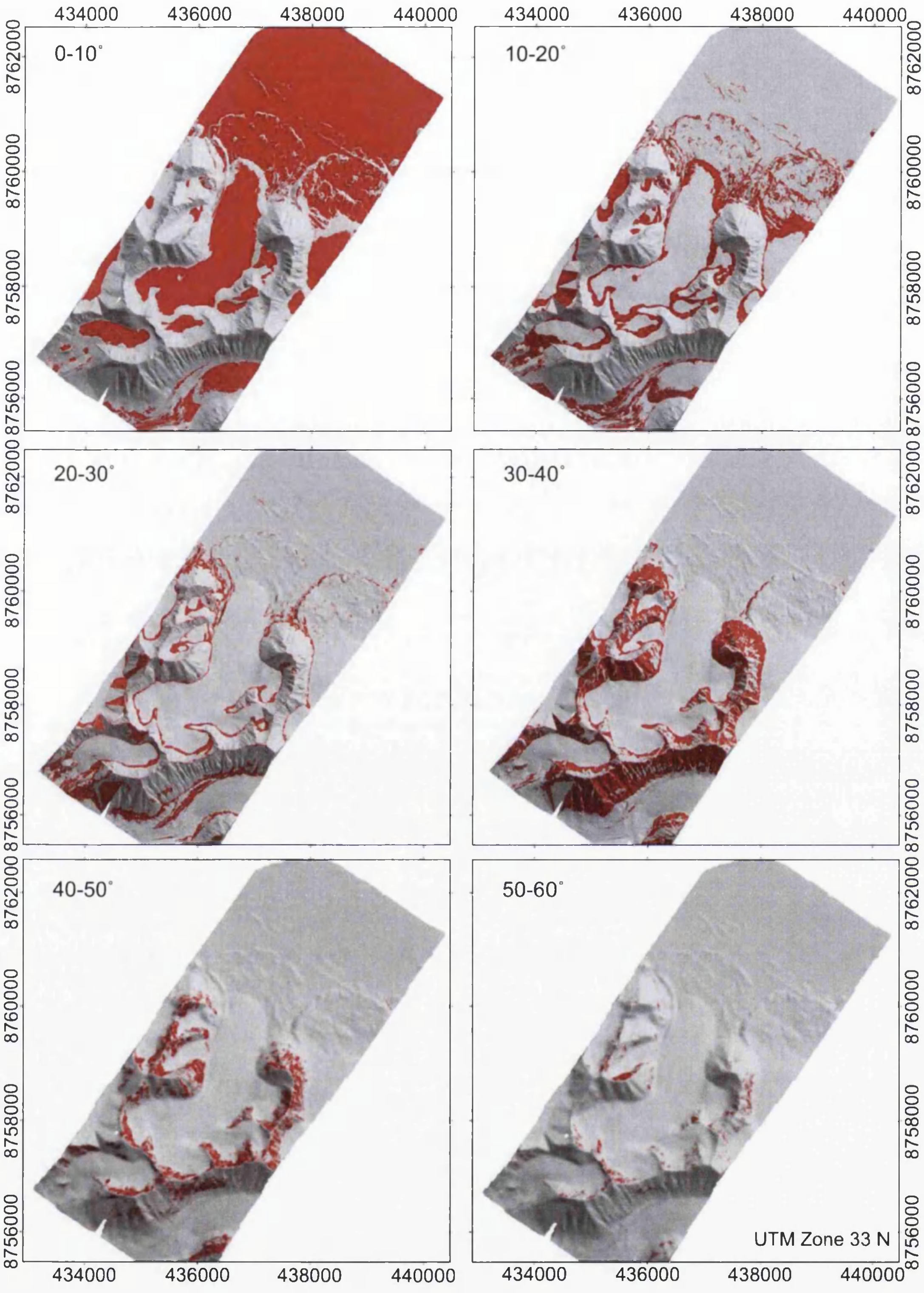

Figure 4.17: Slope maps of Midtre Lovénbreen and surrounds for 10° surface slope angle bins (red shading) derived from, and overlaid onto, a 1 m resolution lidar DEM (60–70° class not shown).

Descriptive statistics of elevation residuals grouped by 10° surface slope class revealed that increasing surface slope resulted in greater variability in elevation (Table 4.9). Slopes of 0–10°, which represented the majority of the glacier surface and forefield and therefore had the largest sample size, had a standard deviation of elevation residuals of 0.25 m. This rose consecutively for each slope class up to 2.51 m for the steepest group (60–70°).

Slope class	Number of pixels	Mean $\overline{\delta h}$ (m)	St. dev. $\overline{\sigma h}$ (m)	Min (m)	Max (m)
0-10°	6463317	-0.02	0.25	-6.96	8.87
10-20°	2203868	-0.06	0.38	-8.93	9.97
20-30°	917014	0.04	0.67	-9.99	7.01
30-40°	1562661	0.17	0.86	-6.97	10.0
40-50°	554223	0.11	1.15	-9.88	11.13
50-60°	178418	-0.04	1.71	-9.51	13.86
60-70°	60143	-0.41	2.51	-12.89	11.96

Table 4.9: Descriptive statistics of lidar elevation residuals grouped into 10° surface slope classes.

Steeper surface slopes caused greater variability in returned elevations due to differences in laser footprint diameter when the same terrain is scanned from two different locations. Over progressively steeper slopes this will result in more beam scattering, reduced signal-to-noise ratio (SNR), and potential degradation of the strength of the laser return and thus the quality of returned elevation information. In addition, even relatively small errors in planimetry (x,y) over steeper slopes will translate to large errors in elevation (z).

4.3.4 Relative Quality Assessment Summary

Analysis of repeat lidar elevations in areas of overlapping data allowed a comprehensive assessment of lidar data precision. Direct comparison of all overlapping pixels within a dataset comprised of nine adjacent swaths of raw data meant that precision could be assessed for a total of more than 10 million elevation measurements. δh values for each individual swath overlap model had means close to zero, thus indicating that there were no significant shifts present between adjacent flightlines of data. Relatively high standard deviations (> 0.4 m) and minimum and maximum residuals ($> \pm 8$ m) for each overlap model indicated that large elevation differences were present in the data. Examination of the spatial distribution of residuals suggested that the largest values were present over mountainous and steep sloping terrain and that residuals were larger at the outer edges of overlap models. Detailed investigation using surface-type subsets and residuals delineated by slope angle showed that residuals were largest over steeply-sloping mountain sides, typically $> \pm 0.5$ m compared to $\sim \pm 0.25$ m over the glacier surface. Although smaller ground footprints on higher terrain (closer to the sensor) are likely to reduce errors due to terrain roughness, large minimum and maximum residuals were present at both lower and higher elevations on the ice surface, probably due to heavily incised meltwater channels in the ablation zone and crevassing at higher elevations. Cross profiles extracted from overlap difference models (Figures 4.15 and 4.16) confirmed that residuals were larger at the outer extents of overlaps (perpendicular to direction of flight) with residuals typically on the order of ±0.4 m at the edges and between ±0.1 m toward the centre of overlap models. Delineating residuals by surface slope rather than surface type confirmed the finding that steeper slopes caused greater variability in returned elevations. The steepest slope classes (50–60° and 60–70°) had the largest sample standard deviations, and largest minimum and maximum residuals of all data from all overlap models.

4.4 Absolute Quality Assessment - Lidar Data Accuracy

Assessing the accuracy or absolute quality of lidar data required access to independently-derived check data of a known higher accuracy. While observed differences between repeat data from seperate flightlines were small it was possible that both these data were themselves erroneous and that all data were in error compared to the true ground surface. A widespread and systematic error such as this might be caused by a variety of GPS positional errors including erroneous baseline data, unmodelled tropospheric delay effects or problems with satellite lock. Lidar elevation accuracy was assessed by comparing elevations with check data points measured using differential GPS (DGPS) data collected both before and after airborne surveying.

4.4.1 Differential GPS

Differential carrier-phase processing of GPS observations from two instruments receiving data from four or more satellites can achieve cm accuracy topographic information (Remondi, 1985). Static and kinematic differential phase measurements determine the vector (the three-dimensional coordinate difference between receivers) based on a number of wavelengths or cycles travelled by a signal from the satellite to each receiver. When the number of cycles (or ambiguity) is determined and the static basestation has collected many observations over time, kinematic or moving vectors can be determined to a high level of accuracy using a real-time radio link (real-time kinematic, or RTK) or via post-processing routines (Hofmann-Wellenhof *et al.*, 2001). Static observations were collected at a basestation fixed in position for the duration of field operations. Kinematic points were collected around the glacier surface and forefield over the course of the field campaign. Data were processed differentially and used to assess the elevation accuracy of returned lidar elevations.

Figure 4.18: Field GPS data collection from static basestation (left) and kinematic rover (right).

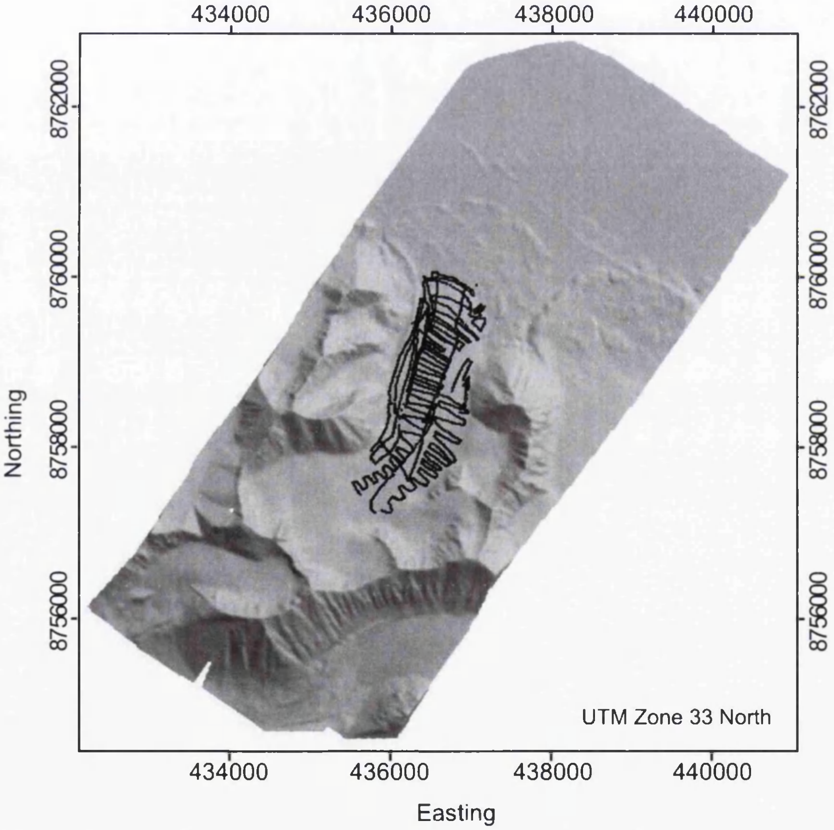

Figure 4.19: Location of field-measured GPS check data points on the ice surface and forefield of Midtre Lovénbreen.

4.5.1.1. Data Collection

GPS data at Midtre Lovénbreen were collected with Leica GPS500 receiver units at a reference basestation placed on a lateral moraine overlooking the glacier (static observations) and at a variety of survey points around the ice surface and forefield (kinematic observations) using a backpack-mounted rover unit (Figure 4.18). Field survey operations took place between 03/08/2003 and 14/08/2003, while airborne surveying took place on the morning of 10 /08/2003. Static basestation observations were collected daily simultaneously with kinematic rover points and additionally in the form of a single-point-position (SPP) at 10 Hz over the course of one 24 hr survey towards the end of the campaign. A total of 3578 kinematic points were surveyed on 6 surveys days during the 12 day campaign. Due to problems of safe access, survey data was limited above approximately 400 m a.s.l. (Figure 4.19).

4.5.1.2. Data Processing and Filtering

Static basestation SPP data were post-processed using Ski-Pro software (Leice Geo Office) which integrated daily International GPS Service (IGS) observations from known point 'NYA1' with observations from the basestation spanning the 24 hour measurement period. A processing routine using GAMIT software supplied by Dr Matt King (Newcastle University, UK) allowed further correction of the basestation location by accounting for previously unmodelled atmospheric effects such as tropospheric signal delay. The locations of kinematic survey points were determined using the rover receiver in real-time kinematic (RTK) mode via a radio link with the basestation. This meant that kinematic points were differentially processed 'on-the-fly'. Rover points were then re-adjusted to the improved basestation location during post-processing. The position and height quality of kinematic points varied due to a number of factors, most importantly being the availability and quality of lock of orbiting satellites at the time of measurement. For this reason, points with position and height quality worse than 5 cm were filtered from further analysis.

4.4.2 Lidar Accuracy Assessment

A full-resolution (1 m) DEM of the entire study area was constructed using the GMT commands 'blockmean' and 'surface' in the same way as DEMs created for individual swaths (section 4.2.2). The remaining 3242 check points (post-quality filtering) were used to calculate elevation residuals between each GPS point and its spatially coincident lidar DEM cell value. Descriptive statistics (including RMSE) were calculated, and residuals were plotted against elevation and displayed according to the survey day in which they were collected

(Figure 4.20).

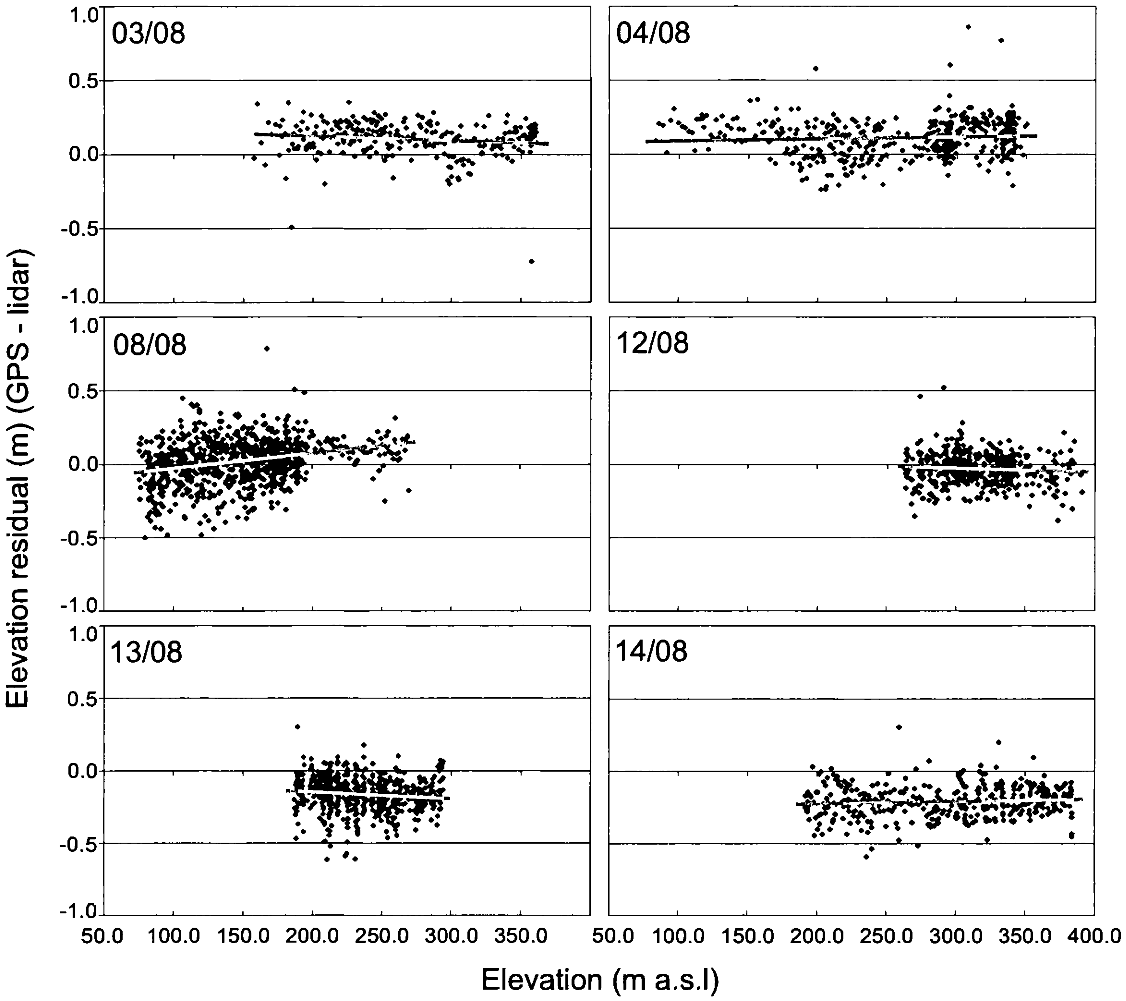

Figure 4.20: Elevation residuals between GPS check points and spatially coincident lidar DEM cell values. Grey lines represent linear fit trendlines fitted to the data. Lidar data were collected on 10/08.

Absolute accuracy residual plots showed that although there were a small number of outliers where residuals exceeded ±0.5 m, the majority of points fell within ±0.25 m (Figure 4.20). The RMS residual of all points from all survey days was ±0.17 m. Linear fit trendlines appeared to indicate a shift from predominantly negative residuals towards the start of the survey period (03/08, 04/08) to average values tending towards zero for the days closest to airborne data acquisition (10/08), and then to positive residuals for the days after surveying (13/08, 14/08). This indicated that GPS elevations were predominantly higher than the lidar surface in the ground surveys 6–7 days before airborne surveying, and predominantly lower than the lidar surface 3–4 days after the flights. This trend was attributed to melt on the glacier surface over the course of field operations. Due to these effects we used only points from the two closest survey days to airborne data acquisition (08/08 and 12/08) in further DEM validation calculations (chapter 5). The RMS residual of the remaining 1429 check points was ±0.14 m.

4.5.2.1. Swath Overlap Accuracy

Following the findings of section 4.4.3 that relative elevation residuals were larger towards the outer edges of overlapping data difference models (e.g. Figures 4.8–4.12), the spatial distribution of absolute elevation residuals with respect to the same overlap model boundaries was also examined. This was done by plotting GPS residuals, which were limited to the glacier surface and forefield, within lidar data strip overlaps (Figures 4.21 and 4.22).

The plots showed that a similar pattern was not evident and that absolute elevation residuals did not appear to be larger towards the edges of data overlaps. The largest residuals were randomly distributed throughout overlap boundaries (Figure 4.21). Some of the larger residuals were clustered together spatially (for example in the overlap of strips G and F, at 436400 E, 8759800 N), which would suggest an explanation other than lidar scan angle geometry. As GPS check data measurements were relatively sparse (approximately 1 point per 20 m compared with >1 lidar point per m^2), it is possible that the trend identified by the relative accuracy assessment did exist yet could not be confirmed by this absolute accuracy assessment.

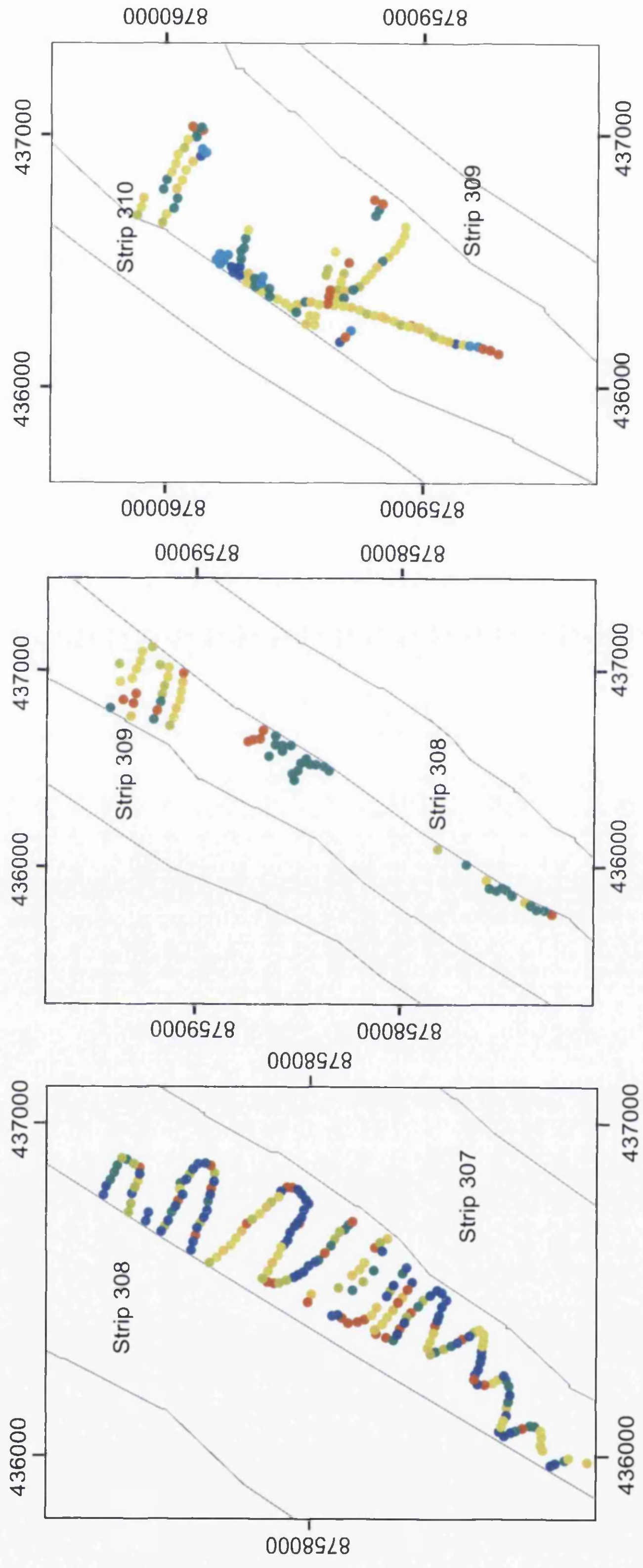

Figure 4.21: Absolute elevation residuals derived by differencing lidar and GPS elevations, plotted within lidar strip 307–310 overlaps. Legend on following page.

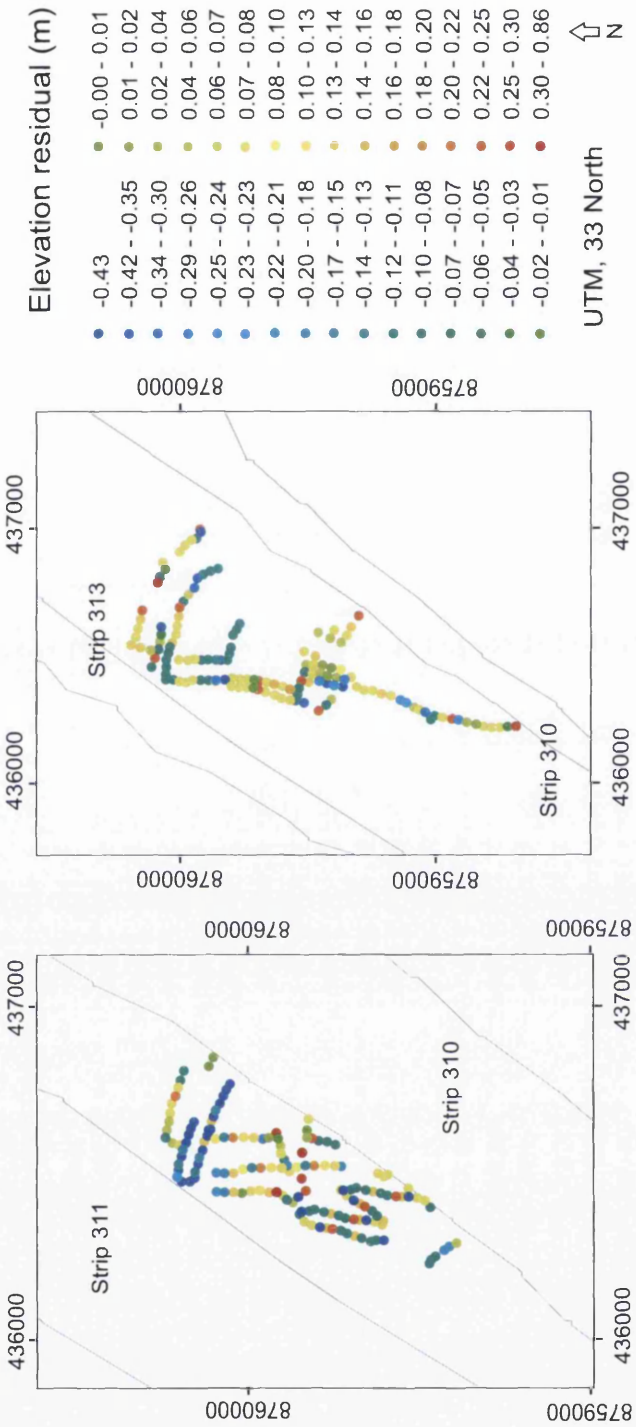

Figure 4.22: Absolute elevation residuals derived by differencing lidar and GPS elevations, plotted within lidar strip 310–311 and 313 overlaps.

4.4.3 Absolute Quality Assessment Summary

Assessment of the absolute quality (or accuracy) of lidar data took place using independent field-measured GPS survey check data. The spatial coverage of check data was limited by the short time period available for field operations and by problems of access to remote areas within the study area. This meant that the number of elevation comparisons was more limited than that which was available through overlap analysis for relative accuracy assessment. For this reason, it was not possible to compare elevation accuracy over different surface types and for a large range of surface slopes. However, despite the relatively small number of survey points, it was possible to draw important conclusions from the analysis. Firstly, comparison of all survey points from all days over a large proportion of the glacier surface (Figure 4.19) resulted in a RMS error of ±0.17 m. This meant that with respect to the external coordinate system, lidar elevations did not have any significant systematic error. Plotting residuals by survey day showed that some of this variability was due to surface melt on the glacier (Figure 4.20). When points more than two days either side of airborne surveying were excluded from the analysis, RMS error fell to ±0.14 m. This value was slightly higher than those reported by Krabill *et al.* (1995b) and Geist *et al.* (2003), and probably reflects the fact that their measurements took place over the relatively smooth topography of a summer snow surface, whereas these elevations were returned from an uneven summer melt surface. Plotting residuals within the overlap boundaries of lidar data swaths showed that the effects of scan angle geometry (larger relative elevation residuals towards the edges of data swaths) were not evident in this analysis. It is possible that elevation accuracy was reduced at the outer edges of individual lidar scan swaths, but these data were probably of insufficient density to confirm this finding.

4.5 Implications for GCP Selection

The results of lidar elevation precision and accuracy assessments have implications for the selection of GCPs from lidar data. In order to select the highest quality GCPs it was necessary to examine both the magnitude and spatial distribution of lidar data elevation quality. Based on photogrammetric theory (chapter 3) and the results presented in this chapter, a list of explicit requirements of lidar-derived GCPs was constructed. GCPs should therefore be:

- Evenly distributed throughout image space,
- Measured over a wide range of elevations,
- Located towards the centre of lidar data swaths,
- Avoided from very steep sloping terrain ($> 60°$),

- On stable (non-moving) and easily identifiable ground terrain, and
- consist of a combination of horizontal (x,y), vertical (z), and 3-dimensional (x,y,z) points.

A common problem for studies using field-measured GCPs in glacial environments is that higher elevations are more difficult to access and thus models may be poorly controlled in upper glacier reaches. This typically leads to DEMs of inferior quality at high elevations (e.g. Rippin *et al.*, 2003) (section 3.3.4.1). The needs listed above were combined with the terrain features typical of glacial and high-mountain environments to provide a list of potential terrain sources of lidar GCPs, their likely achievable elevation accuracies, and their suitability as sources of photogrammetric ground control (Table 4.10). An analysis that assesses the effect of choosing optimal versus sub-optimal GCPs for photogrammetry is presented in the next chapter.

Potential terrain source of lidar GCP	Likely elevation error (± m)	Suitability as GCP
Glacier surface (boulders, melt channels, crevasse edges)	0–0.15 (0–0.30 at swath edges)	Unsuitable for repeat survey, only as single epoch GCP
Forefield proglacial zone (river channels, moraine ridges boulders, icing limits)	0–0.25 (0–0.50 at swath edges)	Unsuitable if dynamic (ice-proximal) If well established then suitable, may require independent evidence
Ice-marginal, low-slope terrain (0-20° slopes)	0–0.25 (0–0.50 at swath edges)	Suitable, providing reasonable distance from former glacial limits Unsuitable if ice-cored
Ice-free plateaus (usually low-slope, < 5°)	0–0.15 (0–0.30 at swath edges)	Ideal as z control, x,y,z control if point can be precisely located
Nunataks (slope variable)	0–0.50+ (dependent on on slope and within-swath position)	Good, as close vicinity to ice surface. May be only bedrock control available
Mountain-side slopes (30–40°, common to alpine-style terrain)	0–0.80 (depending on within-swath position	Suitable, but larger slope angles may cause greater elevation errors
Peaks and ridges	0–1.0 (2.0+ at swath edges)	Very suitable, essential to locate GCPs at swath centres as small shifts in x,y cause large errors in z. Ideal as x,y control

Table 4.10: Potential terrain sources of lidar GCPs in glaciated / alpine-style environments, their likely achievable elevation accuracies in lidar DEMs, and suitability as sources of photogrammetric ground control.

4.6 Chapter Summary

This chapter has provided a comprehensive assessment of the precision and accuracy of a lidar dataset collected over the summer ice surface and surrounding areas of a High Arctic valley glacier. Following the operational details of lidar data collection and pre-processing, elevation precision was assessed by comparing large areas of overlapping (or repeat) data. Using a computationally efficient differencing method it was possible to directly compare more than 10 million lidar elevation returns. Viewing the full extent of DEM difference models revealed that lidar elevation precision was poorer towards the outer edges of data swaths, perpendicular to direction of flight. This discrepancy resulted in elevation precision of approximately ±0.4 m at swath edges compared to ±0.1 m towards the centre of overlaps (and thus closer to the scan nadir point). Examining elevation residuals by surface type revealed that precision was lower over mountain-sides, a result presumably attributable to larger slope angles. This finding was confirmed by the results of experiments which showed that larger surface slope angles resulted in greater variability in lidar elevations. Comparison of lidar elevations with external, independent check data showed that elevations were accurate (±0.17 m RMS) with respect to the external coordinate system. Data were also of sufficient accuracy and temporal resolution to show a melt rate (surface lowering) equivalent to several cm per day on the glacier. Elevation accuracy derived by comparing check data points collected closest to airborne surveying was ±0.14 m RMS, a value which is slightly higher than those reported by comparable studies in glacial environments, and probably attributable to variable slopes and the topography of a summer melt surface. The systematic component of elevation residuals between two DEM surfaces consists of the combined effects of both vertical and horizontal offsets. It may be possible to separate and correct these offsets using a variety of de-noising and filtering techniques (e.g. Kääb, 2005). Finally, results were used to derive a list of desirable qualities for identifying and extracting the highest quality GCPs from lidar data.

Chapter 5

Digital Photogrammetry: Optimising Surface Models

5.1 Introduction

The previous chapter described the high spatial resolution and variable precision and accuracy of lidar data collected over Midtre Lovénbreen, NW Svalbard. In this chapter this information is used to identify and extract large numbers of GCPs from raw point cloud lidar data and to control photogrammetric models, thus negating the need for field-measured ground control (e.g. James *et al.*, 2006). Details of the photogrammetric survey parameters and block setup are provided, before a comprehensive description of the GCP selection and extraction method based on the recommendations provided in chapter 4. Details are provided of all extracted GCPs, their appropriate standard errors and their extraction from both lidar swath edge and swath centre locations. Extracted GCPs are used to control the photogrammetric block and the results of experiments using optimal and sub-optimal GCPs and iterative addition of control points are given. All block adjustment configurations were then used to process DEMs which were validated using independent GPS check data. The last section of the chapter provides calculations of glacier volume change, firstly using a benchmark lidar-lidar DEM differencing comparison using repeat lidar survey data of the glacier in 2005, and then subsequently with each of the derived photogrammetric models. The effects of optimised GCP configurations on DEM accuracy and the geodetic measurement of glacier volume change are given. Finally, these results were used to provide recommendations for processing historical aerial imagery for glacier mass balance assessment, of which several examples in NW Svalbard are provided in chapter 6.

5.2 Photogrammetric Processing

The following sections detail the setup, processing steps, and experiments designed to optimise collection of photogrammetric DEMs of glacial and high-mountain terrain using lidar-derived GCPs. Details of photo and stereo model coverage are presented first, before GCP selection, extraction, measurement and the results of photo model block triangulation experiments.

5.2.1 Photo Configuration and Block Setup

Vertical frame aerial photographs over Midtre Lovénbreen and surrounds were collected coincidently with lidar data on the morning of 10/08/2003. The imaging camera was a Wild RC-10 loaded with AGFA colour film. The camera exposure / frame numbers are provided in Table 5.1. To provide suitable stereo coverage photos were acquired with approximately 60% overlap in the direction of flight and 20% between adjacent photo strips (Figure 5.1).

Flightline number	Equivalent lidar strip number	RC-10 exposure numbers	Time (GMT) start – stop	Notes
1	305	3021–3037	10:21 – 10:23	
2	306	-	10:28 – 10:30	
3	307	3038–3050	10:34 – 10:37	
4	308	-	10:40 – 10:44	
5	309	3051–3063	10:46 – 10:49	
6	310	-	10:56 – 10:59	Some cloud
7	311	3064	11:02 – 11:05	Cloud at start
8	312	3065–3077	11:09 – 11:12	
9	313	3078–3090	11:22 – 11:25	Cloud at end

Table 5.1: Aerial photo survey details.

Of the 69 photos comprising the entire survey, a total of 19 were selected to provide adequate stereo coverage of the glacier, forefield and surrounding mountain peaks and ridges. These 19 images were digitally scanned using a calibrated high-precision drum scanner by DSM Geodata Ltd (Bo'ness, Edinburgh, UK) at a resolution of 16 μm which resulted in TIFF digital images with a pixel size of around 0.7 m and individual file sizes of 624 mega-bytes per photo. The projected image resolution and digital image file sizes were deemed to be suitable for the expected accuracy of ground control data and permitted DEM collection with post spacings up to 2 m. The 19 photos comprising the 2003 Midtre Lovénbreen block were selected from 4 of the survey flightlines. Complete coverage of the glacier and surrounding mountain peaks were provided by photos 3058–3060 from flightline 5, 3071 and

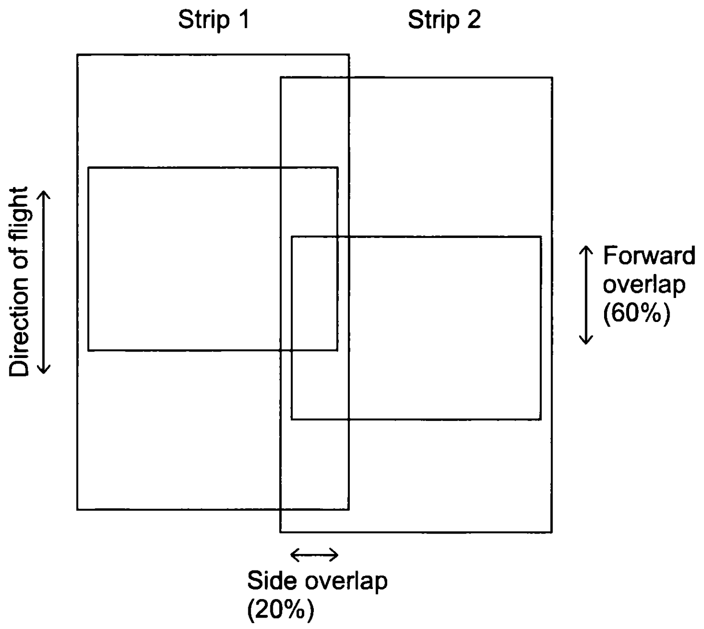

Figure 5.1: Photo overlap extents for stereo coverage in an aerial survey

3073–3076 from line 8, 3041–3049 from line 3 and 3030–3031 from line 1 (Table 5.1). The relative locations and orientations of individual photo frames within the block are displayed in Figure 5.2.

5.2.1.1. Interior Orientation

Correction for lens distortion and generation of an image space coordinate system were performed during interior orientation using information contained within the camera calibration certificate. Providing that correct and up to date calibration has taken place, lens and scanning distortions and camera orientation problems can be modelled during interior orientation. A camera calibration certificate for the Wild RC-10 was used to enter information regarding radial lens distortions and the focal length of the camera into photogrammetric processing software (BAE Systems SocetSet, version 5.3.0). Information relating to the location of the principal point of symmetry (PPS) and principle point of auto-collineation (PPA) were also entered, along with photo fiducial mark coordinates. The fiducial marks of each photo scan were measured using the automatic (and manual, in those cases where the automatic process failed) interior orientation tools within SocetSet.

Figure 5.2: Relative photo outline locations, orientations and tie point positions (triangles) for the Midtre Lovénbreen 2003 photo model block setup. Frame exposure numbers are located in the upper left corner of each photo outline. Rotated frames 3071–3076 may have been due to gusting wind during surveying

5.2.1.2. Tie-Point Measurement

Tie points were measured in SocetSet using an automatic collection strategy utilising a 5 × 5 pixel search window. This process resulted in the measurement of around 80 tie-points of which 68% were measured succesfully. The unsuccessful points were identified and remeasured manually (along with several more) to give a total of 98 points, distributed throughout all of the overlapping areas of imagery (Figure 5.2).

5.2.2 GCP Selection and Extraction

GCPs were manually selected from lidar data in the following manner. Firstly, potential control point locations were identified throughout the study area. Photogrammetric theory recommends that ground control for a strip of photos should consist of a minimum of about two horizontal and three vertical GCPs in approximately every fifth stereomodel along a strip (Wolf and Dewitt, 2000). In addition, GCPs should be well distributed throughout the stereo models and should represent a range of elevations within the study area (Wolf and Dewitt, 2000; Kasser and Egels, 2002). Control locations were therefore preferred from points well distributed around the glacier and over a range of elevations, from the lowest areas of the study reach on the forefield and braidplain to the highest points at the glacier backwall. Potential control point locations were then identified where possible in the lidar data. This was aided by interpolating raw points to a high-resolution (1 m) DEM, overlaying laser intensity information onto the DEM surface, and utilising 3-D lidar visualisation software (Quick Terrain Modeler, Applied Imagery, Silver Spring, MD, USA). Point markers were located on the DEM surface at the identified aerial image location (Figure 5.3 A,B,C). The marker locations were then saved and imported into a model of the raw point cloud data (Figure 5.3 D). The coordinates of the nearest raw lidar point to the marker location were extracted as the coordinates of the GCP. Each GCP was assigned as either horizontal (x,y), vertical (z), or three-dimensional (x,y,z) control depending on the terrain surface characteristics from which it was extracted. GCPs were assigned as horizontal control when the point could be clearly identified in planimetry in the image, yet where very steep slopes may have caused error in GCP elevation. Vertical control points were located on flat or very gently sloping terrain where elevations were likely to be similar proximal to the point, yet precise identification in x,y could not be relied upon. The points that were confidently locatable in x,y, and z were designated as three-dimensional control (e.g. James *et al.*, 2006).

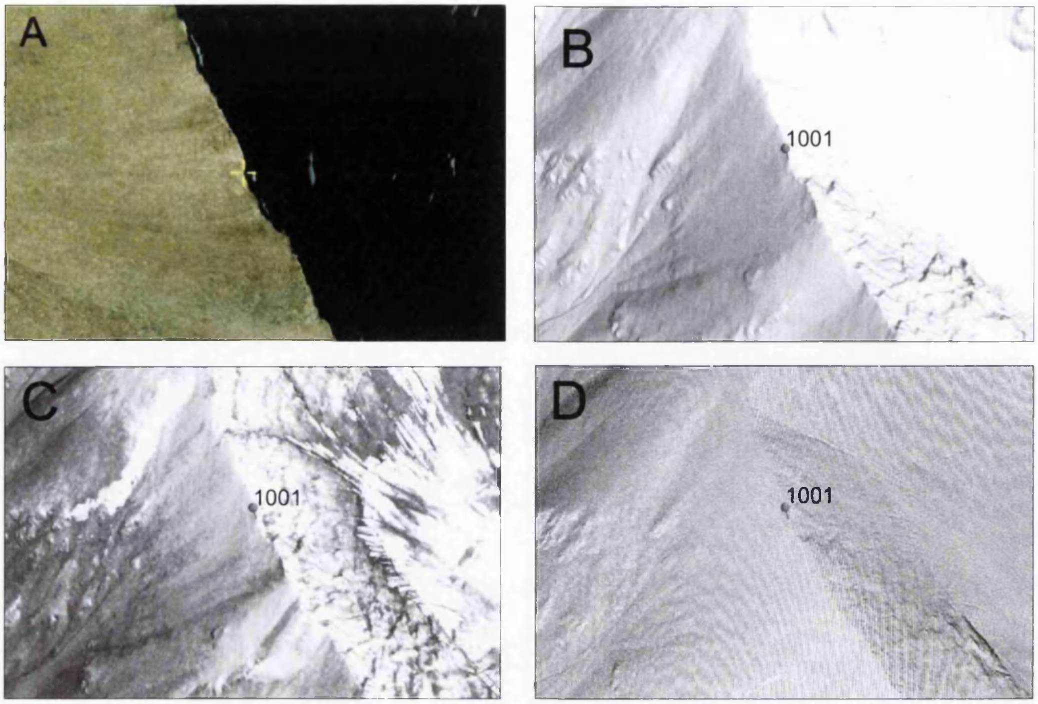

Figure 5.3: GCP selection: Points identifiable on vertical aerial imagery (A) and a lidar-derived DEM (shaded relief perspective view, B) were selected. Point 1001 (within cross-hairs in A) is identified in C with the help of laser return intensity information. D shows the raw point cloud data.

5.2.2.1. Swath Centre GCPs

Based on the finding that lidar elevation precision was reduced at the edges of swaths, away from the nadir scan point perpendicular to direction of flight (Figures 4.4, 4.5, 4.8, 4.9), GCPs were extracted from both swath centre and swath edge locations. The purpose of this was to investigate the effects on photogrammetric model performance and DEM quality (elevation accuracy) of lidar-derived GCPs from optimal (centre) and sub-optimal (edge) locations. Swath-centre GCP extraction was therefore limited to a zone 200 m either side of the nadir point of the scan (perpendicular to direction of flight). This zone represented approximately 25% of the total swath width, given an average scan width of 783 m (Table 4.3).

5.2.2.2. Swath Edge GCPs

As lidar elevation precision decreased to $\sim \pm 0.3$ m at the outer extent of swaths, lower precision GCPs were identified at the outer edges of lidar swaths. The GCPs chosen as edge points were those that could be identified in the central area of a swath (as above), and also lay close to the edge of an adjacent and overlapping swath. The criteria for swath edge GCPs was that points should lie within the outer 5% of swath widths, or within approximately 40 m of the swath edge. As these points would be measured in the photographs as swath centre GCPs, it was possible to simply change the coordinates of the GCP in the photo model from those of the swath centre strip to those of the swath edge strip. This avoided any introduction of error due to differences in image coordinates. A total of 52 GCPs were identifiable in both the lidar data and the aerial photographs according to these criteria, of which 20 were additionally identified along swath edges.

5.2.2.3. GCP Standard Errors

The photogrammetric block triangulation process requires standard errors to be assigned to the three-dimensional coordinates of GCPs. This allows the least-squares adjustment an appropriate amount of redundancy to solve the adjustment equations (Wolf and Dewitt, 2000). Based on lidar instrument manufacturer recommendations (Optech, 2005), standard errors were assigned to GCPs of 0.5 m in x and y. Standard errors in elevation (z) were assigned based on the results of the lidar elevation error assessments (chapter 4). All swath centre GCPs were given standard errors of 0.25 m in z. Swath edge GCPs were firstly assigned the same errors as swath centre GCPs. Standard errors were then increased to 0.5 m in z to take account of the lower precision observed at swath edges. Photogrammetric model solutions were processed using both these standard error configurations for swath edge control points.

5.2.3 Block Triangulation

The block triangulation stage of the photogrammetric process consisted of exterior orientation (GCP measurement) and the bundle adjustment, whereby the collinearity equations (3.4 and 3.5) were solved for each model setup. The following sections describe the addition of GCPs to the photogrammetric block setup, and the results of bundle adjustments for each GCP configuration.

5.2.3.1. Exterior Orientation: GCP Addition

The effects of different GCP configurations on photogrammetric block adjustment results were examined by setting up and adjusting a block containing all 19 photographs from 4 flightline strips, 98 tie-points (Figure 5.2) and 8 varying GCP configurations (Figure 5.4–5.6. Of a total of 50 GCPs, 5 were used to control an initial model and an additional 5 randomly selected points were added to each subsequent model. The block setup and tie-points remained the same throughout the experiment while the remaining GCPs were added to each model, re-running the triangulation adjustment at each step. The effects of addition of GCPs to the initial model (5 GCPs), up to a final model controlled using 50 GCPs, were investigated by examining the RMS error of adjusted GCP positions and the total image unit weight RMS error of the block adjustment. These values showed how well the photography could be fitted to the external coordinate system of the control network (UTM, WGS-84). The RMS error of adjusted GCP positions gave the values (in metres) of adjustments to each control point in x,y,z in the triangulation solution. The total image unit weight statistic gave the RMS error of all adjusted image coordinate residuals (in pixels), and is seen as a good indicator of the quality of the entire solution.

5.2.3.2. Bundle Adjustment

Photogrammetric bundle adjustment results for each model are provided in Table 5.2. Increasing the number of GCPs in each model resulted in an improvement (lowering) of the RMS residual of adjusted GCP positions for each model solution. Although this trend was not entirely uniform it was clear overall that addition of ground control improved the quality of the solution and reduced the amount of adjustment of GCP positions. The total image unit weight RMS error also improved, reducing consistently for each model from 0.54 pixels (Model 1) to 0.37 pixels (Model 10) after the measurement of an additional 45 GCPs. These results indicated that the quality of the block adjustment could be improved with the addition of extra control information.

Model	Number of GCPs	RMS of GCP positions x, y, z (m)	Total image unit weight RMS (pixels)
1	5	0.98, 0.96, 1.18	0.54
2	10	0.95, 0.93, 1.13	0.53
3	15	0.97, 0.88, 1.07	0.48
4	20	0.96, 0.83, 1.30	0.48
5	25	0.96, 0.91, 0.98	0.46
6	30	0.94, 0.95, 0.95	0.44
7	35	0.94, 0.93, 0.91	0.42
8	40	0.93, 0.92, 0.89	0.39
9	45	0.79, 0.98, 0.90	0.38
10	50	0.79, 0.98, 0.89	0.37
edge	20	1.16, 1.20, 0.95	0.83
edge[1]	20	1.16, 1.20, 0.96	0.83

[1] Edge model with 0.5 m standard errors assigned to z coordinates.

Table 5.2: Bundle adjustments results for photogrammetric models 1–10 and edge.

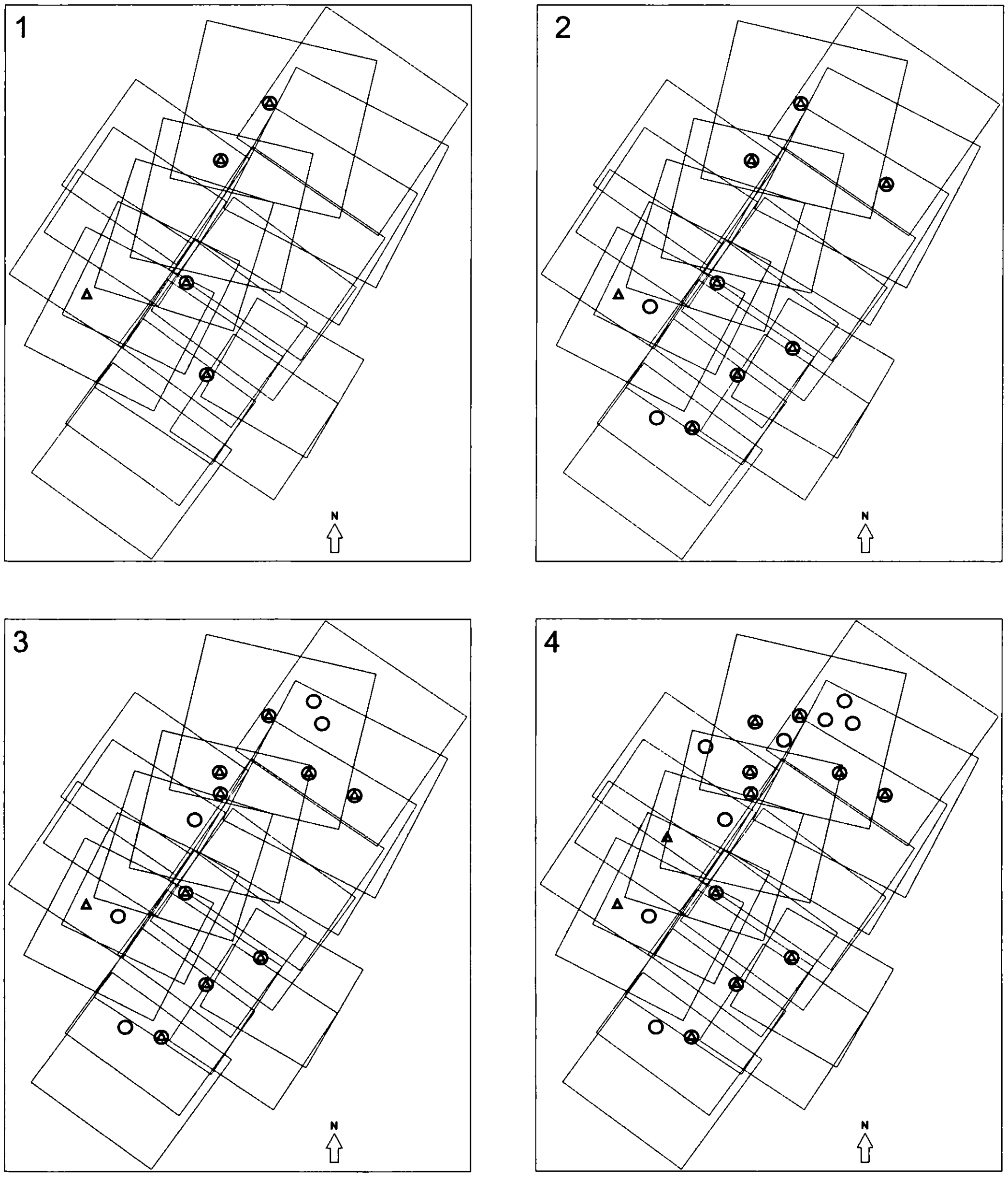

Figure 5.4: GCP configurations for photogrammetric models 1–4 with respectively 5, 10, 15 and 20 GCPs. Triangles = horizontal control, circles = vertical, circles containing triangle = 3D control

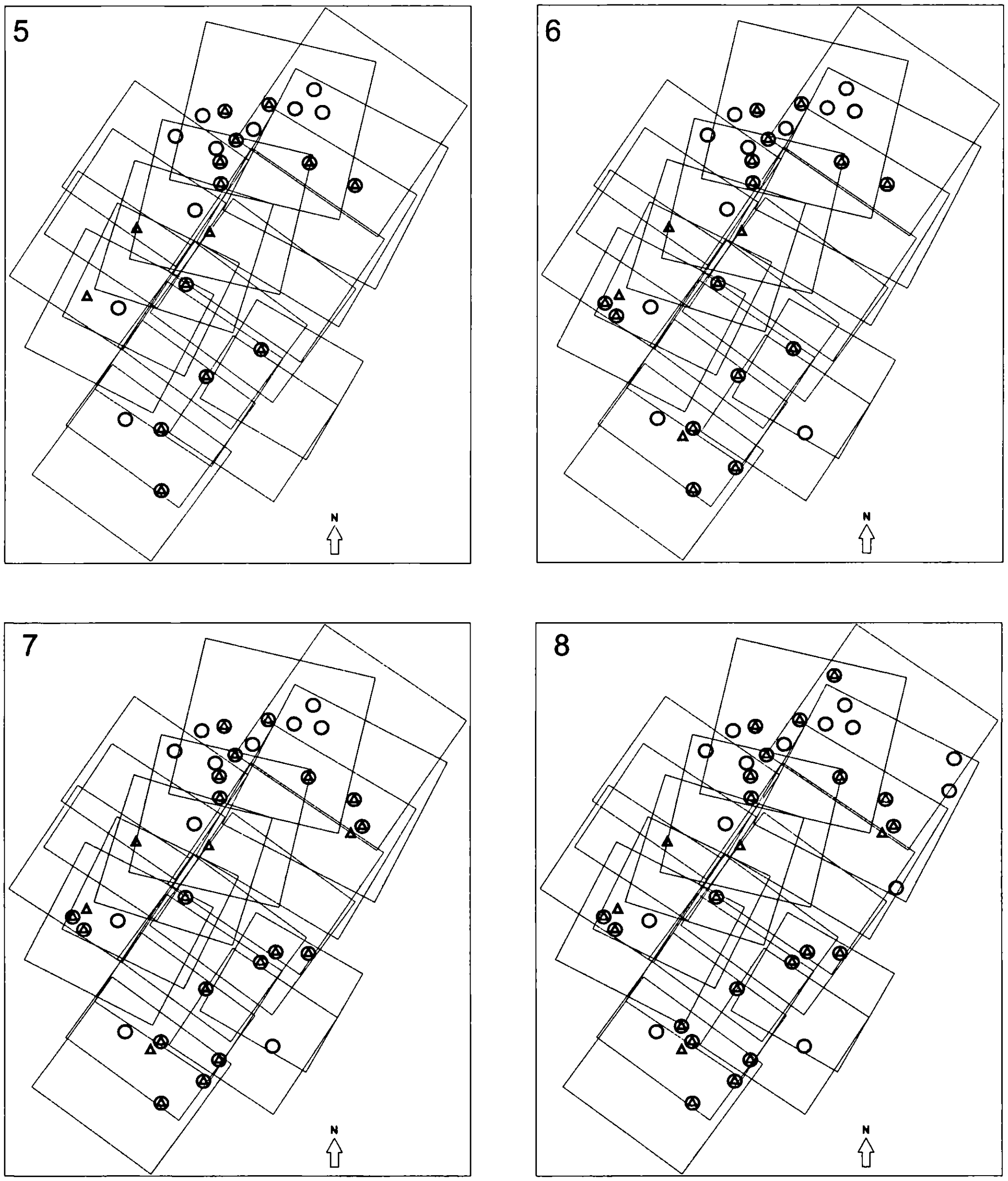

Figure 5.5: GCP configurations for photogrammetric models 5–8 with respectively 25, 30, 35, and 40 GCPs. Triangles = horizontal control, circles = vertical, circles containing triangle = 3D control

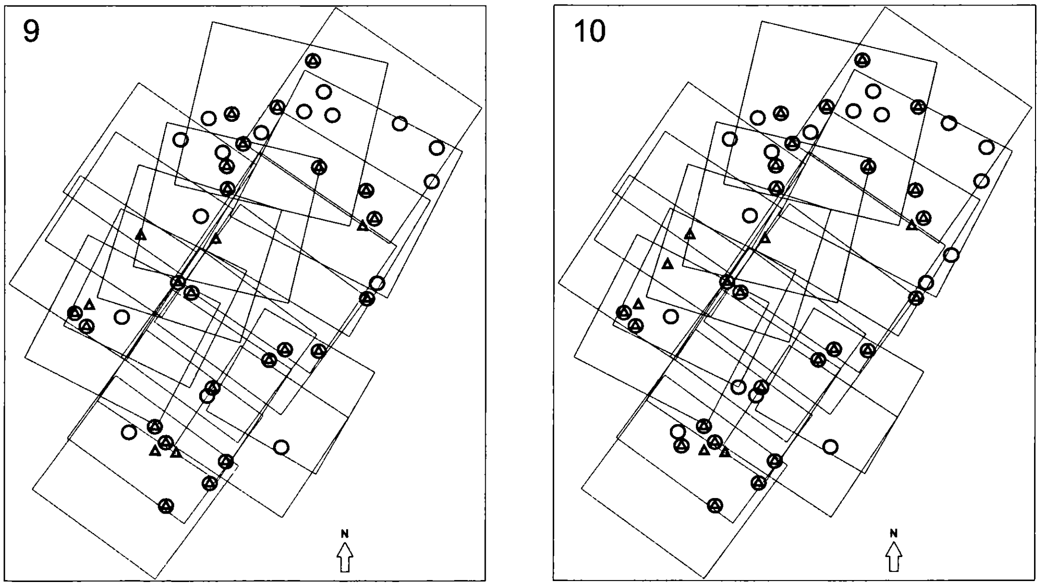

Figure 5.6: GCP configurations for photogrammetric models 9 and 10 with respectively 45, and 50 GCPs. Triangles = horizontal control, circles = vertical, circles containing triangle = 3D control

The edge model, controlled with 20 GCP coordinates extracted from lower precision swath edge locations, had larger RMS of GCP positions in x and y than all the other models. The RMS of adjusted positions in z however, compared favourably with Model 4, which has the same number of GCPs, from swath centres. However, total image unit weight RMS at 0.83 pixels is poorer (higher) than all of the swath-centre GCP models. Altering the z standard error of lower-precision swath edge GCPs in the photogrammetric solution had no effect on the total image unit weight, or the RMS of adjusted GCP positions in x and y, and slightly increased the RMS of adjusted GCP elevations (z), from 0.95 to 0.96 m.

5.2.4 DEM Processing and Validation

DEMs of the glacier surface and surrounds were collected using each of the 11 GCP model configurations to investigate the effects of GCP addition and quality on resultant DEM elevation accuracy. DEMs were processed using SocetSet's automatic image matching algorithm and validated against independent check data (see section 4.5). The workflow for DEM collection is given in Figure 5.7.

Each bundle adjusted model solution had the same polygon area defined around the glacier

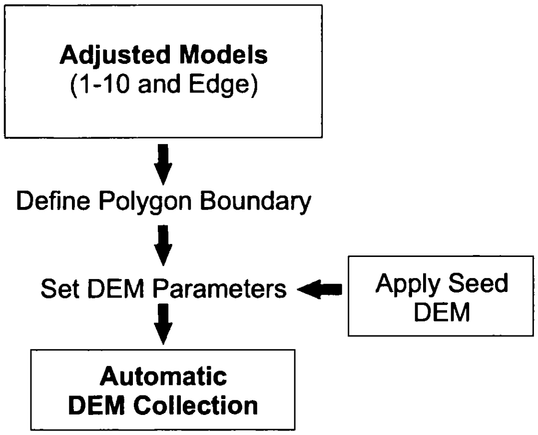

Figure 5.7: Photogrammetric DEM collection workflow

surface, forefield and surrounding mountains within the range of stereo coverage of all 19 images. DEM extraction parameters in SocetSet were selected and kept constant for each DEM collection (Table 5.3).

DEM format	TIN triangles
X post spacing	10 m
Y post spacing	10 m
DEM boundary	Defined by polygon
Automatic Terrain Extraction (ATE)	Adaptive
Maximum image pairs per post	1
Back-matching	On
Adaptive ATE filters	None (default)
Smoothing	None (default)
Precision	High (default)
TIN breaklines	None (default)
TIN Masspoints	No thinning (default)
Seed points	Preserve permanent

Table 5.3: SocetSet DEM extraction parameters for all photogrammetric models.

An adaptive automatic terrain extraction (ATE) strategy was deemed most appropriate for DEM collection in this terrain. The adaptive strategy used an inference engine to generate image correlation strategies adaptively, based on the terrain. When the terrain changed (for example from the relatively gently sloping glacier surface to the steeper slopes of the mountains) the adaptive approach used different ATE strategies accordingly. DEMs were collected in a triangular irregular network (TIN) format which stored critical points and breaklines rather than forcing DEM points onto a regularly spaced grid, leaving holes where good image matches could not be acquired. This meant that terrain was comprehensively modelled, yet the likelihood of false image matches was reduced and data redundancy was kept to a minimum (Burrough and McDonnell, 2000). A 'seed' DEM of several hundred elevation points along the glacier boundary and breaklines was manually constructed for each DEM run using 3D interactive terrain edit tools. This model consisted of points on the glacier surface and various substantial breaklines such as the glacier boundary and mountain ridges. The model was used as a starting point for each of the automatic DEM collection runs and helped the ATE process to produce more accurate DEMs.

5.2.4.1. DEM Accuracy Assessment

DEMs were constructed by exporting SocetSet's processed output as ASCII raw point files and converting TIN points to 10 m spaced regular grids using the linear interpolator in ENVI's topographic modeling tools. The accuracy of DEM surfaces was examined by comparing elevations derived from photogrammetry with elevations from independent GPS check data. Check points from the two closest days to airborne data acquisition (08/08 and 12/08) (see section 4.5.2) were used to validate DEMs by calculating residuals between each GPS point and its spatially coincident photogrammetric DEM cell value. Residuals for each model were plotted by elevation and fitted with linear trendlines (Figure 5.8).

Residual RMS values indicated that the addition of extra control information improved the elevation accuracy of resultant DEMs (Figure 5.8). Although the RMS reduction was not as uniform as the improvement of RMS errors in GCP positions and total image unit weight in each of the bundle adjustments (5.2.3.1), elevation residual RMS values were predominantly higher for the earlier (fewer GCP) models (e.g. model 1) and lower for the later (larger numbers of GCPs) models (e.g. models 9 and 10). Validating the edge model against check data gave an RMS residual of 0.32 m which compared favourably with the model using a similar number of swath-centre GCPs. Examination of the distribution of residuals for each model revealed that there were a number of very large residuals, in several cases $> \pm 4$ m. This contrasted with the majority of lidar elevation errors which were almost all less than ± 1 m and predominantly within ± 0.25 m (Figure 4.13). This finding highlighted the importance of false image matches on resultant DEM accuracy. Distributions also revealed a number of locations where residuals appeared to be anomalously large (Figure 5.8). These included regions of positive residuals at around 80 m a.s.l (of magnitude 2–4 m) and between 225–250 m a.s.l (of magnitude 1–5 m), both indicating that photogrammetric elevations were lower than GPS elevations. These errors were presumably caused by persistent false image matches, most likely due to poor surface texture. However, in later models (8–10, with improved residual RMS values) these errors appeared to be reduced, with fewer large residuals in the first region and lower magnitude residuals (0–1 m) in the second region.

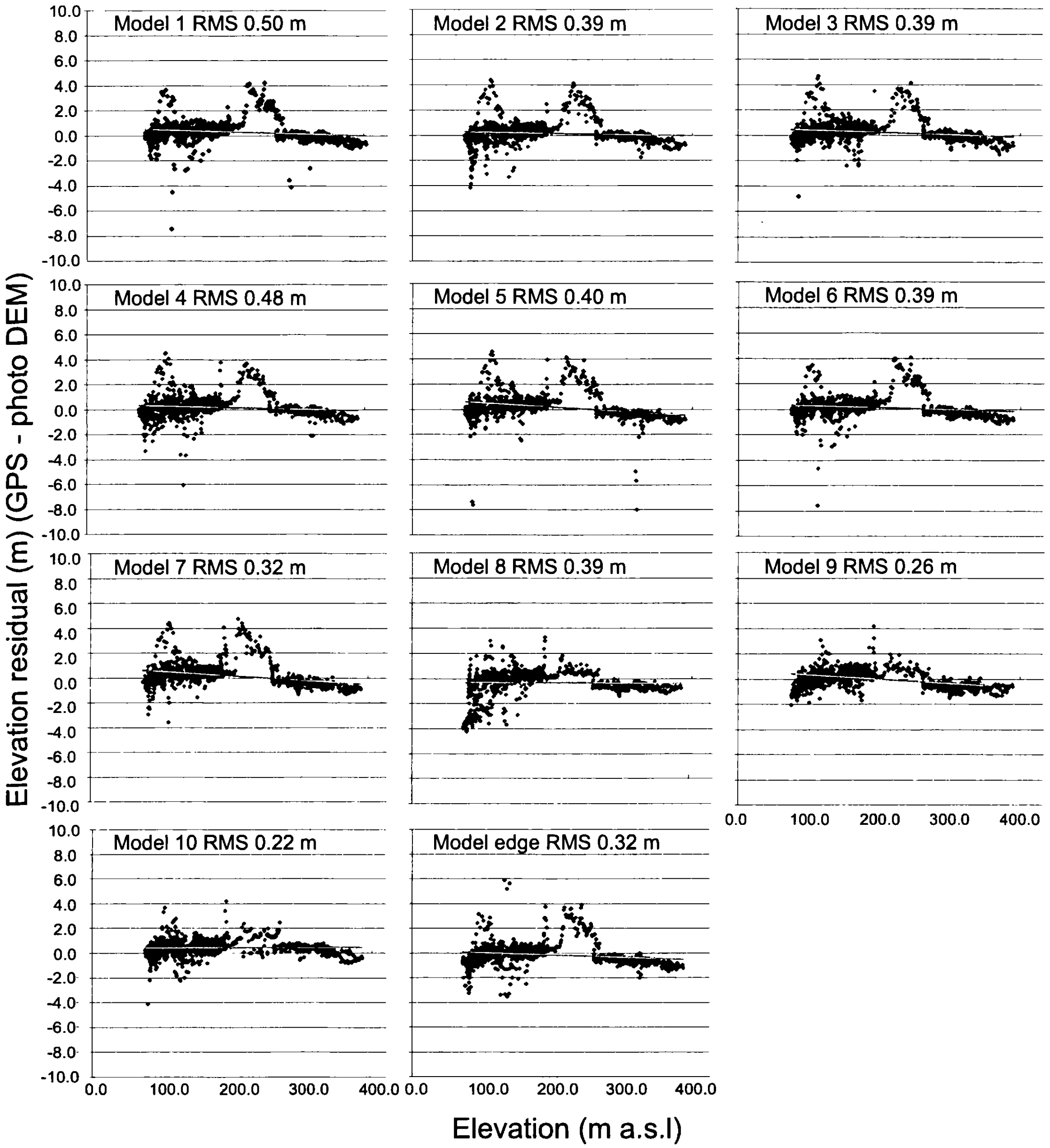

Figure 5.8: Photogrammetric DEM accuracy assessment. Plot points represent the difference between photogrammetric elevations and GPS check data elevations for each photo model. The RMS of each distribution of residuals is given above each plot.

5.2.5 Photogrammetry Optimisation Summary

The automatic collection of photogrammetric DEMs of Midtre Lovénbreen was optimised using different lidar-derived GCP configurations. The use of high-resolution lidar data as control information firstly negated the need for field-measured ground control. Secondly, large numbers of points could be extracted. In this case, for a small valley glacier, 50 GCPs were identified, extracted and measured in the aerial photos. Based on lidar elevation quality results, GCPs were extracted from swath-centre locations and also lower precision swath edges. The addition of GCPs and subsequent bundle adjustments showed that the quality of photogrammetric models could be improved by increasing the number of control points and by using swath-centre points rather than those from the poorer quality swath edges. Models saw steady improvements in both the RMS of adjusted GCP positions and the total image unit weight RMS. Altering the elevation standard error of edge GCPs had little effect on bundle adjusted model parameters. These results described the statistical performance of individual model solutions. In order to examine the effect of these changes on elevation accuracy, models were processed into DEMs and validated with independent GPS check data. Residual RMS errors were calculated and showed that in general increasing the amount of ground control resulted in improved DEM elevation accuracy. However, this trend was not uniform and individual DEMs were affected by errors introduced by false image matches. Two distinct areas of erroneous DEM elevations were identified by this assessment, which were shown to improve for later (more GCPs) models. The improvements displayed by later models (8, 9, 10) were not reflected in the edge GCPs model which displayed a similar distribution of residuals as the earlier (fewer GCP) DEMs.

5.3 Implications for Glacier Volume Change

This section investigates the implications of lidar-controlled photogrammetric model optimisation on measurements of glacier volume change. In particular, the question of how different GCP configurations affect estimates of volume change, is addressed. This was done by firstly comparing glacier-wide photogrammetric DEMs with a lidar-derived DEM of the glacier from the same year. Secondly, a repeat lidar survey of the glacier surface two years after the original survey, allowed measurement of glacier-wide volume changes between the two years (2003–2005). The volume changes generated by differencing photogrammetric models (2003) from the 2005 lidar model were compared to this ‘benchmark’ lidar2003 to lidar2005 volume change estimate. This allowed detailed comparison of automatic photogrammetric DEM collection performance for the measurement of glacier volume change.

5.3.1 2003 Photogrammetry - 2003 Lidar

Each photogrammetric DEM of ML in summer 2003 (controlled using lidar-derived GCPs) was differenced from a lidar DEM of the glacier captured concurrently, to investigate the effects of different GCP configurations on measurements of glacier volume change. As lidar is assumed to be of better quality than photogrammetric elevations this provided a straightforward quality control test whereby differences closest to zero represented the best quality photogrammetric DEM surfaces. In addition, this test allowed comparison of photogrammetric elevations over the entire glacier surface, rather than the limited spatial coverage offered by check data comparison. Both DEMs (created in the UTM projection and WGS-84 datum) were layer stacked and differenced (photo DEM x - lidar DEM) using ENVI's band math commands. The resultant difference models were cropped to the outline of the glacier which was delineated manually in SocetSet using terrain editing tools.

5.3.1.1. Elevation Changes

Difference DEMs between each photogrammetric model and the lidar DEM are displayed (Figures 5.9 and 5.10). Two areas of no data coverage within the glacier boundary were present in the DEMs. These were a portion of the south-west tributary and the upper part of the second east tributary. The south west tributary was affected by small amounts of cloud cover during surveying (e.g. Figure 4.1), and therefore had insufficient surface texture available for image matching. The upper reaches of the second eastern tributary were not within stereo coverage of the aerial photo survey.

Figures 5.9 and 5.10 showed generally good agreement between photogrammetric and lidar elevations, with values predominantly less than ±0.5 m. However, variability was present both within and between individual model difference DEMs. Almost all the models showed large positive differences (photogrammetric elevations higher than lidar elevations) in regions adjacent to the glacier backwall and in some of the highest elevation tributary basins. These values (of 2 m or more) were particularly prevalent around the main glacier backwall (UTM Northing 8756500) and in the second eastern tributary (UTM Easting 436500, Northing 8757000). Examination of original aerial photographs revealed that these errors occured over regions of poor image texture resulting from seasonal snow cover. While these errors remained throughout all models they appeared to reduce in size throughout the later models. Difference DEMs from models 7–10 for example, had fewer large positive differences at the main glacier backwall than models 1 and 2, and model 10 (50 GCPs) appeared to have fewer than all the other models.

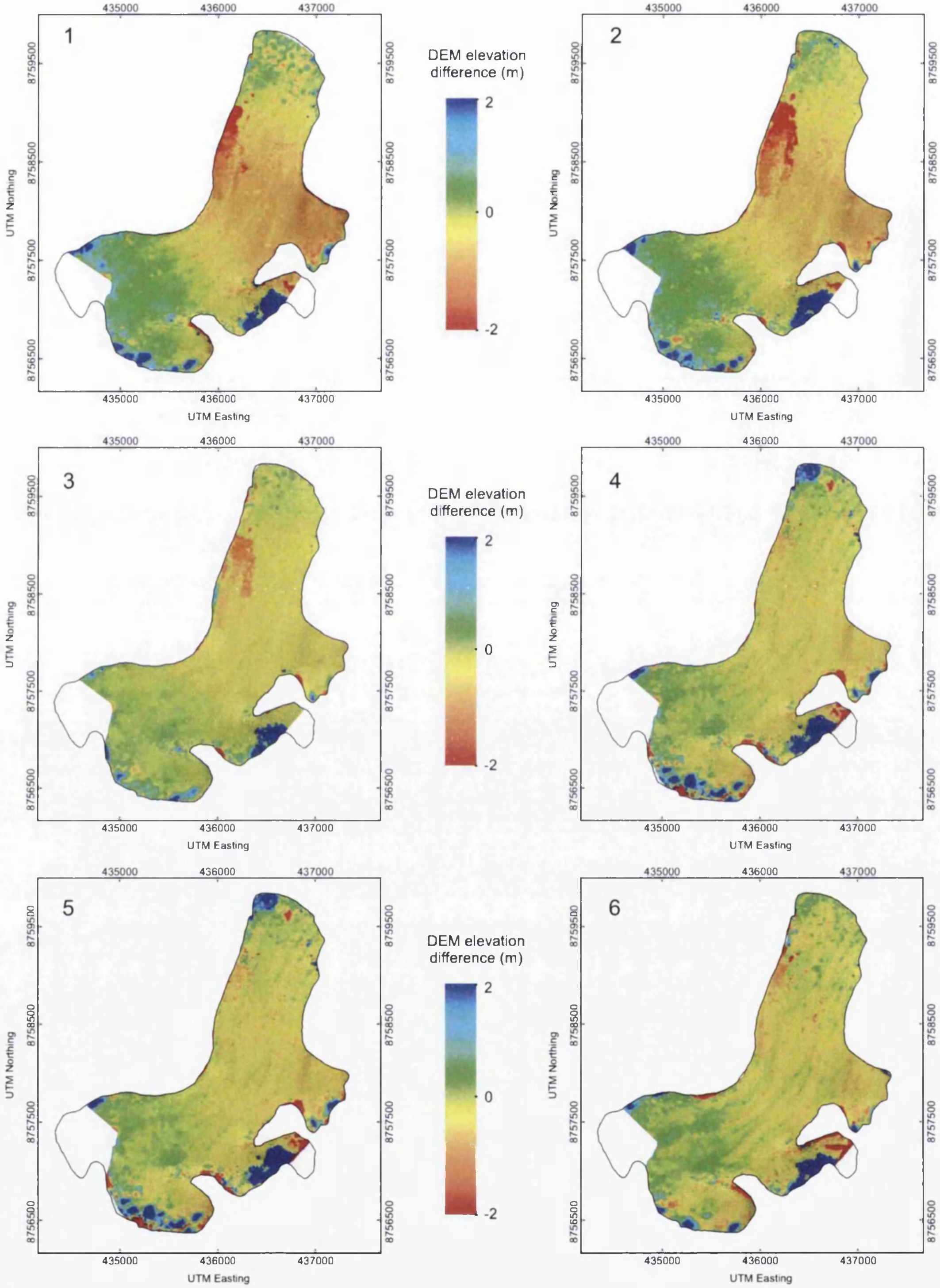

Figure 5.9: Difference images between lidar-controlled photogrammetric DEMs (models 1–6, detailed in text) and a lidar-derived DEM of Midtre Lovénbreen, Svalbard.

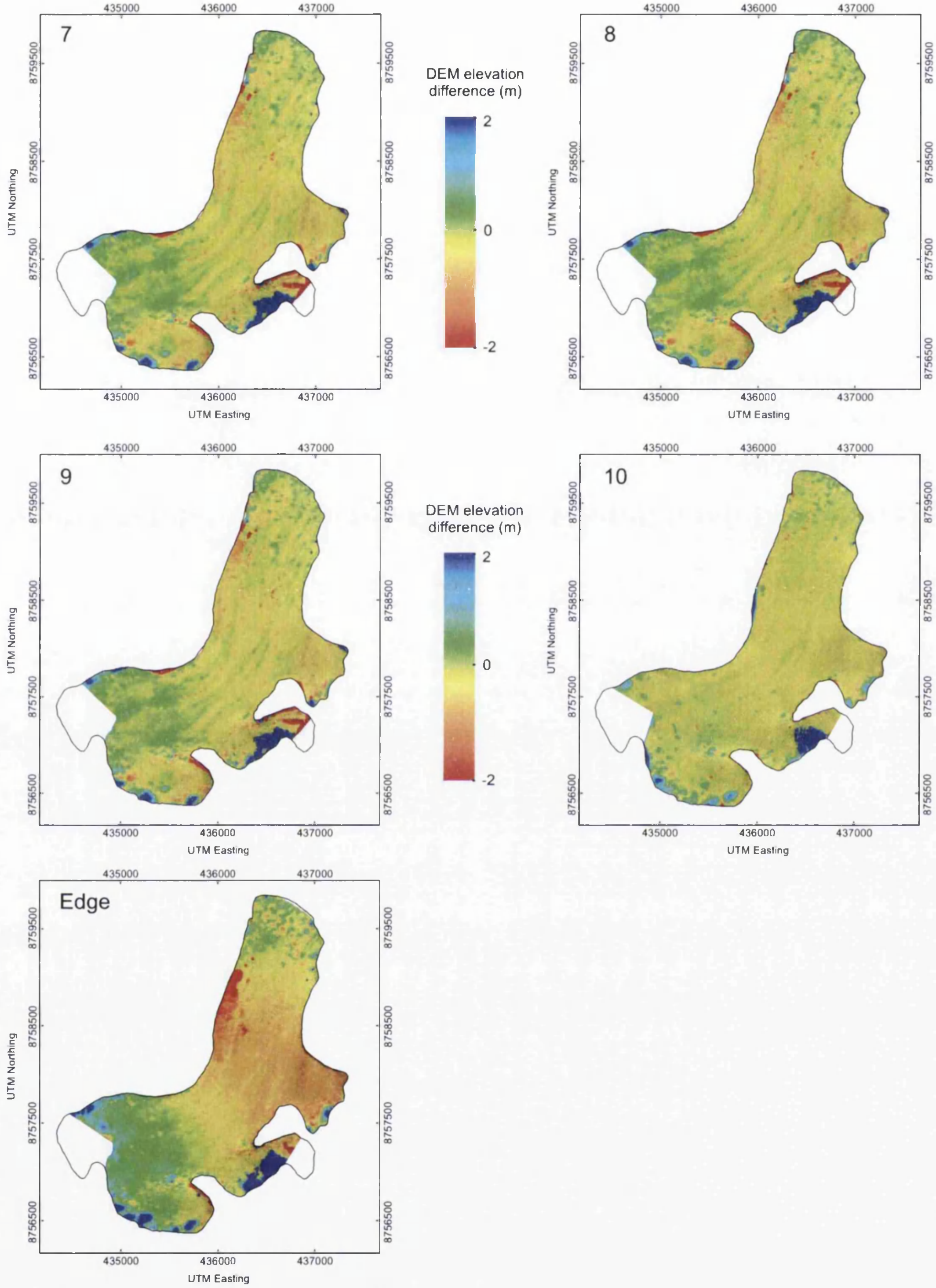

Figure 5.10: Difference images between lidar-controlled photogrammetric DEMs (models 7–10 and 'edge') and a lidar-derived DEM of Midtre Lovénbreen, Svalbard.

The DEMs with the fewest GCPs (1–3) displayed a region of large negative elevation differences (photogrammetric elevations lower than lidar elevations) on the western side of the glacier between approximately Easting 436000–436500 and Northing 8758000–8759000. This apparently systematic trend of differences up to -2 m may have been caused by a lack of ground control in one of the images from the second strip of photos (Figure 5.2). The trend was no longer evident from model 4 (20 GCPs) onwards, although it does appear again in the model controlled using edge GCPs (Figure 5.10).

Models 1 and 2 (controlled with 5 and 10 GCPs) appeared to show a large region of negative DEM difference values, represented by red shading (up to ~ 1 m), within the central part of the glacier (Easting 436000–437000, Northing 8757000–8758000). These predominantly negative values indicated that photogrammetric elevations were consistently underestimating elevation (as compared to lidar measurements) and was the result of poor distribution of GCPs in earlier models. The addition of ground control to subsequent models appeared to eliminate this problematic area. However, it was also evident in the model derived by differencing the 'edge' controlled photogrammetric DEM (Figure 5.10). Other large elevation differences occurred at individual points or small groups of points in discrete locations throughout each of the models. Examples of up to ± 2 m were evident around the steep sloping (and relatively poorly textured) glacier snout (Easting 436500, Northing 8759700), particularly in models 2, 4 and 5, and at the confluence of the large central tributary and main glacier flow (Easting 435500, Northing 8757000) where very steep-sloping, crevassed terrain existed. It is likely that these differences were due to false image matches caused by poor image texture or large surface slopes.

5.3.1.2. Ice Volume Changes

Ice volume changes were calculated using pixel summation of difference DEMs (e.g. Kohler *et al.*, 2007). Total volume change, δV, was obtained by summing the i pixel values ($h_{iphoto2003} - h_{ilidar2003}$) between each difference DEM of surface area, A, and multiplying by the area, ${l_p}^2$, represented by each pixel (where l_p is the grid spacing), expressed as:

$$\delta V = {l_p}^2 \sum_A (h_{iphoto2003} - h_{ilidar2003}). \tag{5.1}$$

Mean volume change $\overline{\delta h}$, averaged over the glacier surface, was calculated by dividing δV by area A. $\overline{\delta h}$ was divided by the time between epochs (t, 23 months) and multiplied by 12 to calculate mean annual volume changes ($\overline{\delta h / \delta t}$).

Volume errors (the difference in volume between each photogrammetric model from 2003 and the lidar model of the same year) are provided in Table 5.4. The model with the fewest control points (model 1, 5 GCPs) showed the largest difference in volume (-3.37 $\times 10^5$ m^3). Total volume differences reduced as more GCPs were added until models 6 and 7 which both showed the same total volume difference (-0.23 $\times 10^5$ m^3). Models 8–10 had slightly higher volume differences (perhaps due to blunder errors) but were still significantly lower than models 1–3. The DEM controlled using edge GCPs performed poorly, with total volume difference of 3.23 $\times 10^5$ m^3, only slightly better than model 1, despite having some 15 more GCPs.

Photo Model	Volume Error: model2003--lidar2003 ($\times 10^6$ m^3)
1	-3.37
2	-2.67
3	-2.19
4	0.94
5	0.98
6	-0.23
7	-0.23
8	-1.26
9	-0.48
10	-0.28
edge	-3.23

Table 5.4: Total volume errors between 2003 photo models and 2003 lidar model.

5.3.2 2003 Lidar - 2005 Lidar

In order to investigate the performance of lidar-derived photogrammetric DEMs for estimating glacier volume change, differences were computed between photogrammetric DEMs of ML in summer 2003 and a lidar-derived repeat survey DEM of the glacier in 2005. In addition to providing a two year record of glacier volume change it was also possible to compare the measurement of volume change from photogrammetric model–lidar model differencing with that of lidar model–lidar model differencing. Differencing two lidar models of the same surface two years apart was expected to provide the most accurate 'benchmark' measurement of glacier volume change. Photogrammetric models from 2003 were then differenced from the lidar 2005 model and the volume change estimates of each subtraction compared to the 'benchmark' estimate. Volume changes were calculated using the same approach as section 5.3.1.2 (pixel summation), however glacier boundaries were delineated for both years (2003 and 2005) and 2005 elevations were subtracted from each of the 2003 models. δV was calculated by summing the i pixel values from the larger glacier surface, A (2003), and multiplying by the area of each pixel (see equation 5.1).

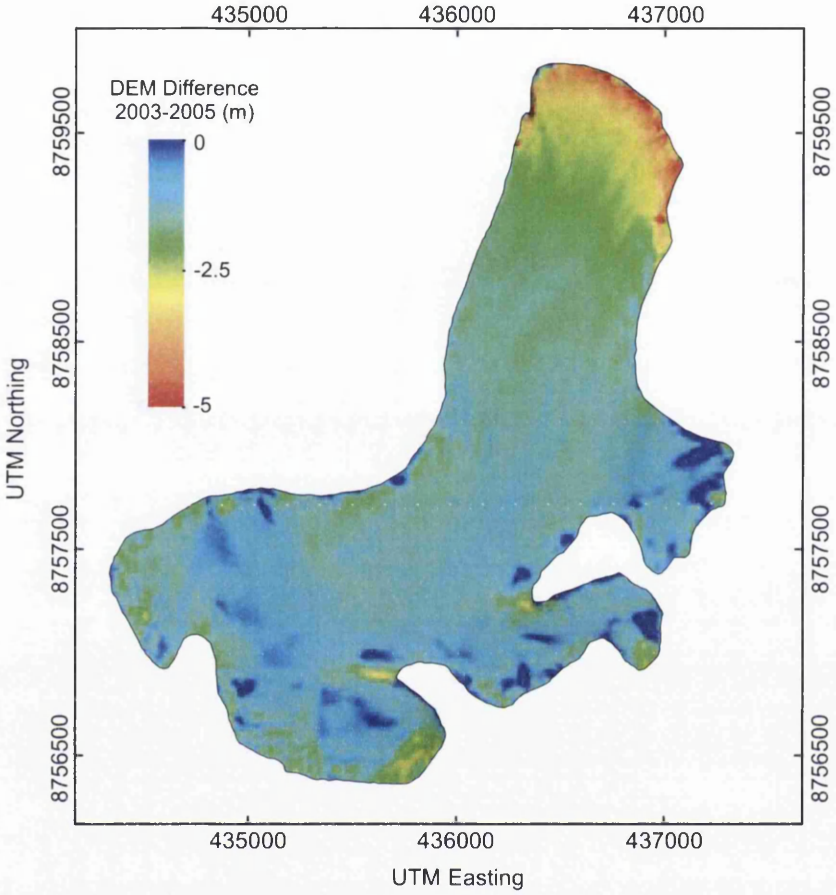

Figure 5.11: Midtre Lovénbreen 'benchmark' lidar-lidar volume change difference DEM, 2003–2005.

5.3.3 2003 Photogrammetry - 2005 Lidar

Difference images showed surface elevation change at Midtre Lovénbreen between each photogrammetric model and the lidar-derived repeat survey from 2005 (Figures 5.12 and 5.13). Traces of the problematic area towards the eastern side of the glacier in the earlier photogrammetric model differencing (Figure 5.8, 1–3) were also evident in the two year difference images.

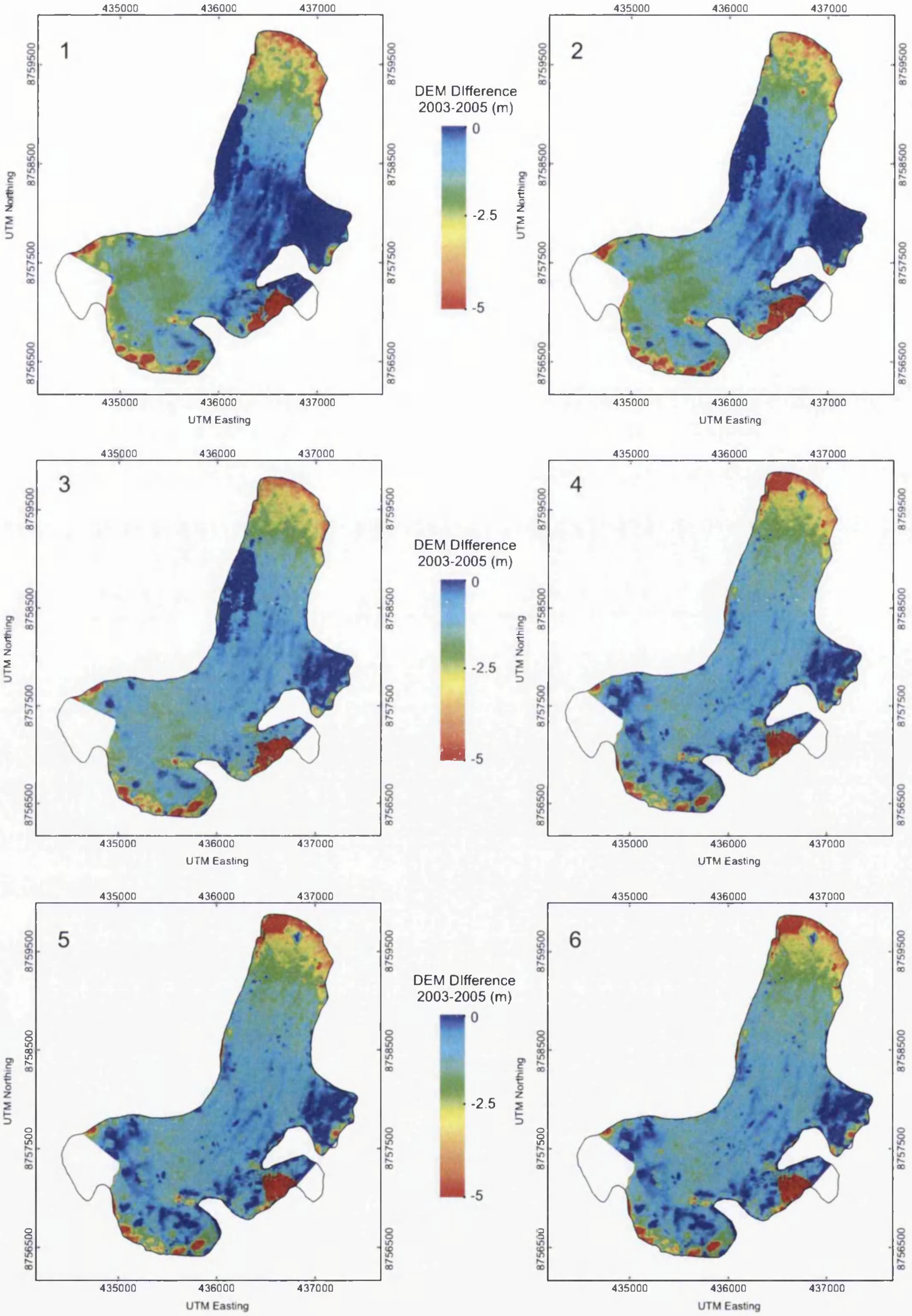

Figure 5.12: Midtre Lovénbreen surface elevation change, 2003–2005, measured by lidar-derived photogrammetric models 1–6 and repeat survey lidar data.

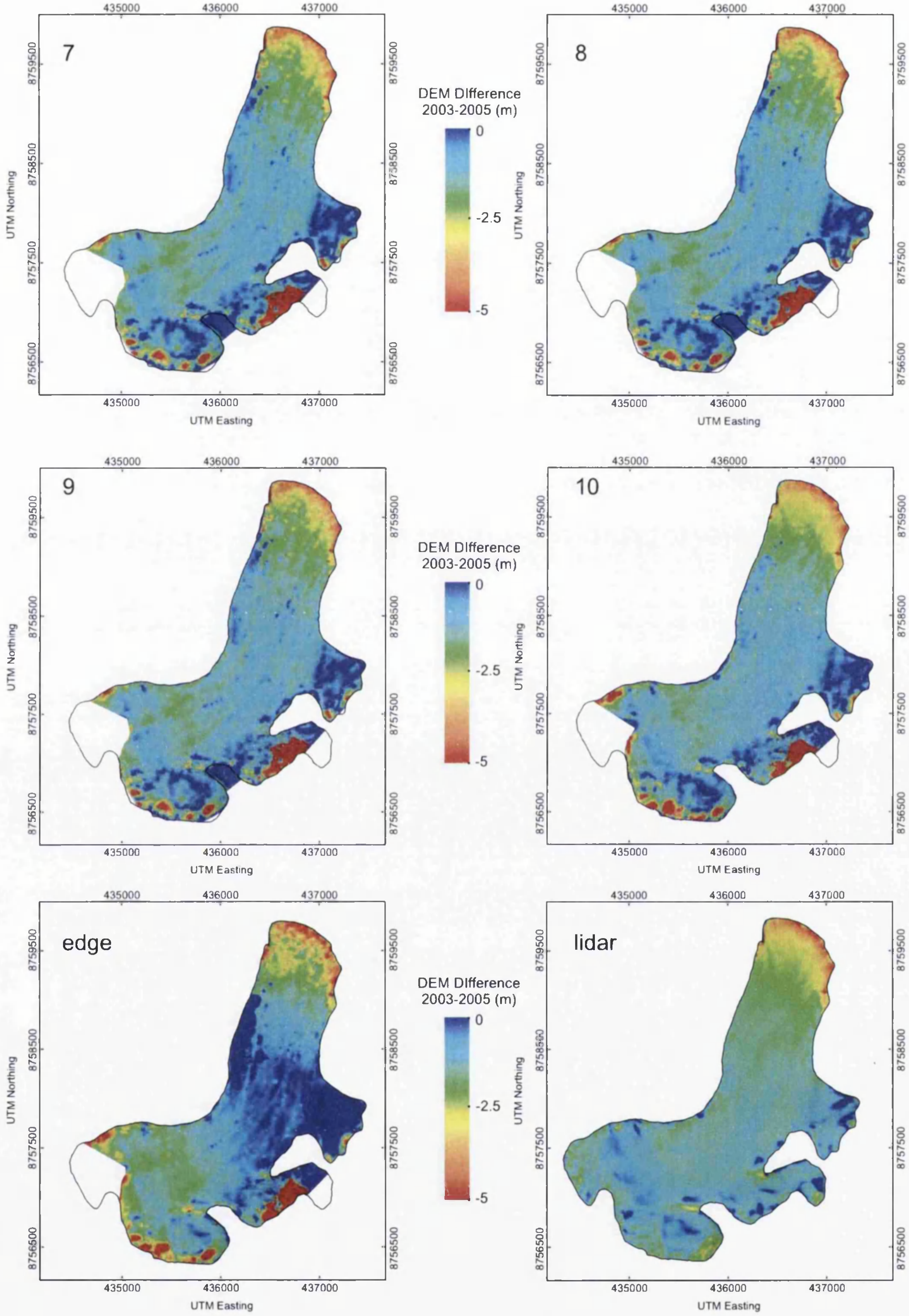

Figure 5.13: Midtre Lovénbreen surface elevation change, 2003–2005, measured by lidar-derived photogrammetric models 7–10 and edge, and repeat survey lidar data. 'Benchmark' lidar-lidar differencing is included for comparison.

Errors in the earlier difference images on the west side of the glacier (models 1–3 and edge, Figures 5.9 and 5.10) were manifested as relatively small elevation differences (as 2003 photogrammetric elevations were lower than 2003 lidar elevations). The images showed that the general pattern of elevation changes were consistent with those derived from the benchmark measurement (Figure 5.11). Elevation changes were predominantly largest at the snout (up to 5 m of thinning) and progressively smaller up-glacier. In comparison to the benchmark, earlier photogrammetric models (1–3) appeared to underestimate elevation change at the mid-section of the glacier (Northing 8758000–8759000), yet slightly overestimate elevation change at higher elevations (Northing 8756500–8757500). This trend was less pronounced in later models (4 onwards), although it was evident in the edge-controlled model. Models 7–10 reproduced the benchmark pattern of thinning the best, with model 10 most resembling the overall elevation change of the lidar-lidar model. Each of the photogrammetric models showed larger differences at the highest parts of the glacier, in particular around the backwall and in the second eastern tributary. Here, photogrammetric models suggested up to 5 m of thinning, whereas in the same location in the benchmark model elevation changes were mostly less than -2.5 m. It was clear that even when controlled with large numbers of GCPs, the image-matching algorithm struggled to accurately reproduce the true ground surface in areas of poor surface texture.

The effects of photogrammetric GCP addition on glacier volume change measurements are summarised by Table 5.5. Comparison of photogrammetric model differencing revealed a wide variety of volume change estimates. When compared to the lidar2003–lidar2005 volume change (4.72×10^5 m^3), earlier models (1–4) overestimated volume loss by between 14% (model 3) and 53% (model 1). With the exception of model 7 (which underestimated volume loss by 27%) models 5–10 provided estimates that were within 10% of the lidar-lidar measurement. The edge GCPs model overestimated volume change by 31%, a similar magnitude to model 2 (using 10 swath centre GCPs).

Surface lowering between models from each of the two epochs translated to markedly different estimates of the mean annual volume change ($\overline{\delta h/\delta t}$). Differencing of photogrammetric model 1 revealed a mean $\delta h/\delta t$ of 0.79 m a^{-1}. With the addition of 5 GCPs (model 2) this was reduced to 0.73 m a^{-1} and yet further to 0.65 m a^{-1} for model 4 (20 GCPs). The best estimates of mean $\delta h/\delta t$ were provided by models 5, 6, 9 and 10 which were all within 0.02 m a^{-1} (4%) of the benchmark value. This result indicated that for a large block of images (19 photos), above a threshold level of ground control (in this case, between 20-25 GCPs), when compared to a benchmark lidar-lidar measurement, there was no significant improvement in photogrammetric model performance for the estimation of glacier volume change. There was some degradation beyond this amount of ground control (model 7) but in general the findings indicated that lidar-controlled photogrammetry can provide glacier volume change

Photo Model	model2003-lidar2005 δV ($\times 10^6$ m^3)	$\overline{\delta h}$ (m)	$\overline{\delta h/\delta t}$ (m a^{-1})	% difference from *
1	7.21	1.51	0.79	+53
2	6.63	1.39	0.73	+40
3	5.37	1.13	0.58	+14
4	5.96	1.25	0.65	+26
5	4.56	0.95	0.50	-3
6	4.46	0.93	0.49	-6
7	3.43	0.72	0.38	+27
8	4.17	0.87	0.45	-12
9	4.86	1.02	0.53	+3
10	4.50	0.94	0.49	-5
edge	6.20	1.30	0.69	+31
lidar2003	**4.72**	**0.98**	**0.51**	-

Table 5.5: Total (δV), area-averaged ($\overline{\delta h}$), and annual area-averaged ($\overline{\delta h/\delta t}$) volume changes at Midtre Lovénbreen, Svalbard, 2003–2005, as measured by lidar–lidar DEM differencing (bold font) and photogrammetry–lidar DEM differencing using 11 different GCP configurations. Values in the 6th column represent the percentage difference in volume change between each photo model and the 'benchmark' lidar-lidar volume change measurement.

measurements similar to those derived from repeat lidar elevation data (within $\sim$ 4%) providing GCPs are well chosen and at least 20–25 points can be measured. The exception to this was provided by the edge model, which despite having 20 GCPs, overestimated mean annual volume change by 0.18 m a^{-1} (31%).

5.3.4 Glacier Volume Change Summary

A series of experiments were designed to investigate the use of lidar-controlled photogrammetric DEM processing to improve measurements of glacier volume change. Previous sections (5.2–5.3) had shown that the quality of a block adjustment and subsequent DEM accuracy could be improved with the addition of extra GCPs. The implications of this for measurements of glacier volume change were shown to be significant. Firstly, photogrammetric DEMs were differenced from a lidar-derived DEM imaged coincidently. The results of this process showed that models produced with fewer control points and with points from the poorer-quality swath edges had systematic errors of up to 2 m in their DEM surfaces. The addition of ground control reduced these errors. Repeat survey lidar data in 2005 allowed a direct comparison between lidar-lidar 'benchmark' and lidar-controlled photogrammetry-lidar volume changes, between the two years. Compared to the benchmark, earlier (fewer GCP) photogrammetric models overstimated volume loss by 14-53%. Models 5–10 (with one exception) provided estimates within ~10% of the benchmark measurement. Elevation surfaces should be manually checked for blunder errors to guard against the exceptions that may occur even for well controlled models (e.g. model 7, table 5.5). A DEM controlled using sub-optimal edge GCPs overestimated glacier volume changes by a third. The findings indicated that beyond a threshold level of ground control (in this case, ~ 20–25 well-located GCPs) lidar-controlled photogrammetry can provide glacier volume change measurements similar to those derived from repeat lidar elevation data (within ~ 4%).

5.4 Recommendations for Glacier Photogrammetry

The previous chapter suggested a number of potential terrain locations for the selection and extraction of lidar GCPs (section 4.6). Based on the results of GCP measurement, DEM collection and DEM differencing, the following recommendations were made for photogrammetric DEM processing for measurement of glacier volume change:

- For a multi-model block (in this case, 19 photos) a minimum of 20–25, and ideally more than 40 GCPs should be measured. Bundle adjustment solution parameters and RMS residual elevation accuracy were improved using models with larger numbers of GCPs. DEM validation showed that when > 40 GCPs were measured, systematic elevation errors were minimised and RMS errors reduced to approach those achievable from a lidar-derived DEM. Using models controlled with 20–25 GCPs or more, annual area-averaged volume changes were within 4% of those achievable from repeat lidar measurement.
- GCPs should be measured from raw lidar data swath centres. Points remeasured in images using swath-edge coordinates were shown to have poorer overall model solutions, systematic errors when compared to a lidar-derived DEM and independent check data, and overestimate volume change by 31% over a two year measurement period.

5.5 Chapter Summary

The research presented in this chapter described the production and optimisation of glacier surface models (DEMs) using ground control information derived from airborne lidar data. This approach allowed the production of high-quality, high-resolution DEMs of a remote high-Arctic glacier without the need for field-measured ground control. Given that locations for ground control were manually identified on stable, non-moving (usually bedrock) points, the technique is equally applicable to historical frame imagery and therefore offers the opportunity to accurately reconstruct past changes in glacier volume and extent (see chapter 6). A series of experiments were designed to examine the effects on photogrammetric solutions and automatically-derived DEMs of changes in both GCP frequency and point elevation quality. Models were set up using increasing numbers of GCPs, and with lower quality point coordinates from the edges of lidar data swaths (chapter 4). Photogrammetric bundle adjustment results were improved (i.e. RMS of adjusted GCP positions and total image unit weight RMS errors were reduced) with the addition of extra control information. Likewise, addition of control resulted in lower RMS elevation residuals when DEM surfaces were compared to independent GPS check data. These improvements in model solution parameters and DEM accuracy resulted in improved measurements of glacier volume change. Photogrammetric models, when differenced from a repeat lidar survey DEM, were shown to provide a variety of total volume change estimates. Earlier models (with fewer GCPs) tended to display systematic errors and overestimated volume loss by between 14 and 53%. Models with 20-25 or more GCPs provided estimates within 10% of a benchmark lidar-lidar measurement, while a DEM controlled with edge GCPs overestimated volume loss by a third. These results imply that photogrammetry controlled with low quantities or poor quality of ground control may result in seriously erroneous estimates of glacier volume change. Recommendations were made for further processing of frame imagery based on these results. Chapter 6 gives the results of around 40 years of glacier volume changes in NW Svalbard derived using this technique and according to the recommendations for DEM optimisation provided in this chapter.

Chapter 6

Recent Change of NW Svalbard Glaciers

6.1 Introduction

This chapter provides the application of the previously outlined remote-sensing technique for measuring changes in glacier volume and geometry. The methodology and optimisation procedures provided in chapter 5 were applied to archival aerial photography to derive a time-series of historical measurements at Midtre Lovénbreen and Austre Brøggerbreen, NW Svalbard. Section 6.2 provides details of the photographic archive, and in particular the spatial and temporal resolution of imagery covering the two glaciers. This is followed in section 6.3 by a description of the application of contemporary (lidar-derived) ground control to historical imagery. This section also contains descriptions of the photogrammetric block setup for each glacier at each epoch and the statistical measures of photogrammetric block adjustment quality. Following block setup and DEM processing, measurements of changes in glacier geometry and frontal position are described in section 6.4. Glacier surface elevation and volume changes between epochs are presented for both glaciers in sections 6.5 and 6.6 respectively. This chapter provides numerous examples of the utility of the lidar-as-ground-control methodology and derives a new record of high-quality, high-resolution changes in glacier volume and geometry for two NW Svalbard glaciers over the past 40 years.

6.2 Archive Aerial Photography Coverage

The archive of aerial photography coverage of the Svalbard archipelago is held at the Norwegian Polar Institute (NPI) in Tromsø, Norway. A variety of survey and reconnaisance campaigns have resulted in photographic coverage of the islands at regular intervals since the mid 1930s. The first airborne surveys for mapping purposes took place in 1936 and 1938. These images were collected at oblique angles from the survey aircraft and are of variable quality. Due to the difficulties associated with photogrammetric processing of oblique imagery and the relatively poor expected accuracy of resultant elevations these photos were not used in this research. A study of Svalbard ice volume changes between 1936 and 1990 estimated errors of ±12.22 m in elevations based on contour maps derived from oblique aerial imagery (Nuth *et al.*, 2007). Photo sorties throughout the 1940s (1948/9) and 1950s (1956) were primarily undertaken to map previously inaccessible interior regions of Nordaustlandet, Bjørnøya and Nordenskiøldland (Hagen *et al.*, 1993). Large-scale photographic sorties of the entire archipelago began in the 1960s with archipelago-wide 1:50 000 scale stereo imagery acquired towards the end of summer 1966. While additional sorties took place in 1960/1961, 1969, and at various years throughout the 1970s, primarily as a means to fill in gaps in previously unphotographed regions (including Prins Karls Forland and Dordmannsoden), emphasis had shifted towards repeat coverage of the entire archipelago for change detection studies. Subsequent large-scale, archipelago-wide surveys took place in 1977, 1990, and 1995. The areal coverage, image scale, and quality of the 1995 images is particularly good and has led to their use by NPI in generating (photogrammetrically) a standard DEM product of most of Svalbard. This DEM has been utilised in a number of glacier change detection studies (e.g. Nuth *et al.*, 2007; Kohler *et al.*, 2007).

6.2.1 Image Selection: Midtre Lovénbreen

Image selection was based on visual inspection of archival image prints. A number of conditions were considered when choosing imagery. Firstly, temporal resolution was maximised by selecting images from as many photo epochs as possible, particularly from the earliest sorties. As automatic image matching algorithms are considerably more successful over terrain with good surface texture and contrast (e.g. section 3.3.4.1, Baltsavias *et al.* (2001)), images with low proportions of snow cover and mountain shadowing were chosen where available. Finally, single images or image sorties with very poor contrast were also avoided due to difficulties of measuring ground control and tie-points, and likely poor image-matching performance. From an examination of the complete coverage of Midtre Lovénbreen within the NPI photo archive (Table 6.1), the following images were selected for scanning:

Sortie	Date (day/ month/year)	Flying Height	Image Scale	Film	Camera	Contractor	Photo IDs	Comments
S36	-	3500 m	Oblique	Agfa Aero.	Zeiss 18/18 f = 21cm	Marinens Flyvevåben	1552,1553	Oblique SW
S66	28/7/66	8500 m	1:50 000	-	Wild RC8 717	-	**4454, 4455**	Snowline in high bowls
S69-1	28/7/69	8500 m	1:50 000	-	Wild RC8 15 2/23 cm	Widerøe Flyveselskap	1394,1395	Snow, shadow. Missing from archive.
	28/7/69	3000 m	1:20 000	-	Wild RC8 15 2/23 cm	Widerøe Flyveselskap	1400,1404 1405,1406	
S70	22-25/8/70	2800 m	1:17 000	-	RC8 15/23 cm	Widerøe Flyveselskap	4263,4264 4378–4381 4389–4391	ML backwall. ML centreline. Eastern flank.
S77	5-21/8/77	8230 m	1:50 000	Panchrom.	RC10-15/23 cm	Fjellanger Widerøe	**0729–0731**	Good cover.
S90	20/8/90	-	1:50 000	Kodak IR	Wild RC20	Fotonor A/S	**6525–6527**	Snowline half way up ice. Right flank, poor texture.
	25/9/90	-	1:50 000	Kodak IR	Wild RC20	Fotonor A/S	6765	
	14–16/8/90		1:15 000	-	Wild RC20	Fotonor A/S	5779–5781 5149,5150	
S95	18/9/95		1:15 000	Kodak IR	RMK TOP 15/23 fl= 153.604 mm f/ 5.5. Yellow filter	NLF Fjellanger Widerøe	1068–1071 1082–1084	Significant shadowing throughout.
2003	10/08/03	1600m	1:11 000	AGFA colour	Wild RC10	NERC ARSF	**3030–3031** **3041–3049**	**3058–3060** **3071–3076**

Table 6.1: Midtre Lovénbreen historical aerial photography. Image negatives / diapositives and prints are held in archive at the Norsk Polarinsitutt, Tromsø, Norway. Scanned images in bold font.

Sortie	Date (day/ month/year)	Flying Height	Image Scale	Film	Camera	Contractor	Photo IDs	Comments
S36	-	3500 m	Oblique	Agfa Aero.	Zeiss 18/18 f = 21cm	Marinens Flyvevåben	2885,2886 1550–1552	Incomplete. Snout only.
S66	28/7/66	8500 m	1:50 000	-	Wild RC8 717	-	**4478–4480**	Good coverage.
S69	28/7/69	8500 m	1:50 000	-	Wild RC8 15 2/23 cm	Widerøe Flyveselskap	1393,1394	
S70	22-23/8/70	2800 m	1:17 000	-	RC8 15/23 cm	Widerøe Flyveselskap	4380,4381 4258–4263 4219–4221	Some shadowing.
S77	5-21/8/77	8230 m	1:50 000	Panchrom.	RC10-15/23 cm	Fjellanger Widerøe	**0730–0732**	Good contrast.
S90	20/8/90	-	1:50 000	Kodak IR	Wild RC20	Fotonor A/S	6764–6766	Good contrast, high, snowline, no cloud.
	25/9/90	-	1:50 000	Kodak IR	Wild RC20	Fotonor A/S	6482–6485	
	14–16/8/90		1:15 000	-	Wild RC20	Fotonor A/S	**6525–6527**	
S95	18/9/95		1:15 000	Kodak IR	RMK TOP 15/23 fl= 153.604 mm f/ 5.5. Yellow filter	NLF Fjellanger Widerøe	1063–1069 10852–1087	Heavy shadow throughout.

Table 6.2: Austre Brøggerbreen historical aerial photography. Image negatives / diapositives and prints are held in archive at the Norsk Polarinsitutt, Tromsø, Norway. Scanned images in bold font.

- **1966** - Sortie S66, Images 4454, 4455
- **1977** - Sortie S77, Images 0729, 0730, 0731
- **1990** - Sortie S90-1 Images 6525, 6526, 6527

Aerial photos from the 1995 sortie were not used due to heavy shadowing throughout the images. The photographic epochs above, combined with airborne lidar data from 2003 and 2005, comprised a 5 epoch, 39 year record of volume and geometry change at Midtre Lovénbreen. Due to poor image texture and significant shadowing in the ML 1990 photos, elevations were derived from S90-1 images 6765 and 6766 (Table 6.2). Although these photos did not have complete glacier coverage (approximately 70%) there were fewer shadows and image contrast on the ice surface was superior to the 1995 images.

6.2.2 Image Selection: Austre Brøggerbreen

As AB is the neighbouring glacier to the west of Midtre Lovénbreen similar photographic sorties (Table 6.2) were chosen as suitable for scanning. The following images were selected to provide complete stereo coverage of AB:

- **1966** - Sortie S66, Images 4478, 4479
- **1977** - Sortie S77, Images 0730, 0731, 0732
- **1990** - Sortie S90-1, Images 6765, 6766

Including the 2005 lidar dataset, the Austre Brøggerbreen record comprised 4 epochs spanning the same 39 year measurement period as ML (above). Photo diapositives were scanned at 14 μm by DSM Geodata (see section 5.2.1).

6.3 Photogrammetric Setup and Processing

Following the results of chapter 5, photogrammetric models at each epoch were controlled using 50 GCPs. The same 50 points used to control the best performing 2003 Midtre Lovénbreen model (model 10, Figure 5.5) were re-measured in each of the historical image epochs. The distribution of GCPs in relation to 1:50 000 scale images from the earliest epoch (1966) and the ML glacier outline are displayed in Figure 6.1. A total of 50 swath-centre GCPs were selected in the same way (see section 5.2.2) from the 2005 Austre Brøggerbreen lidar dataset and measured in each of the AB photo epochs (e.g. Figure 6.2).

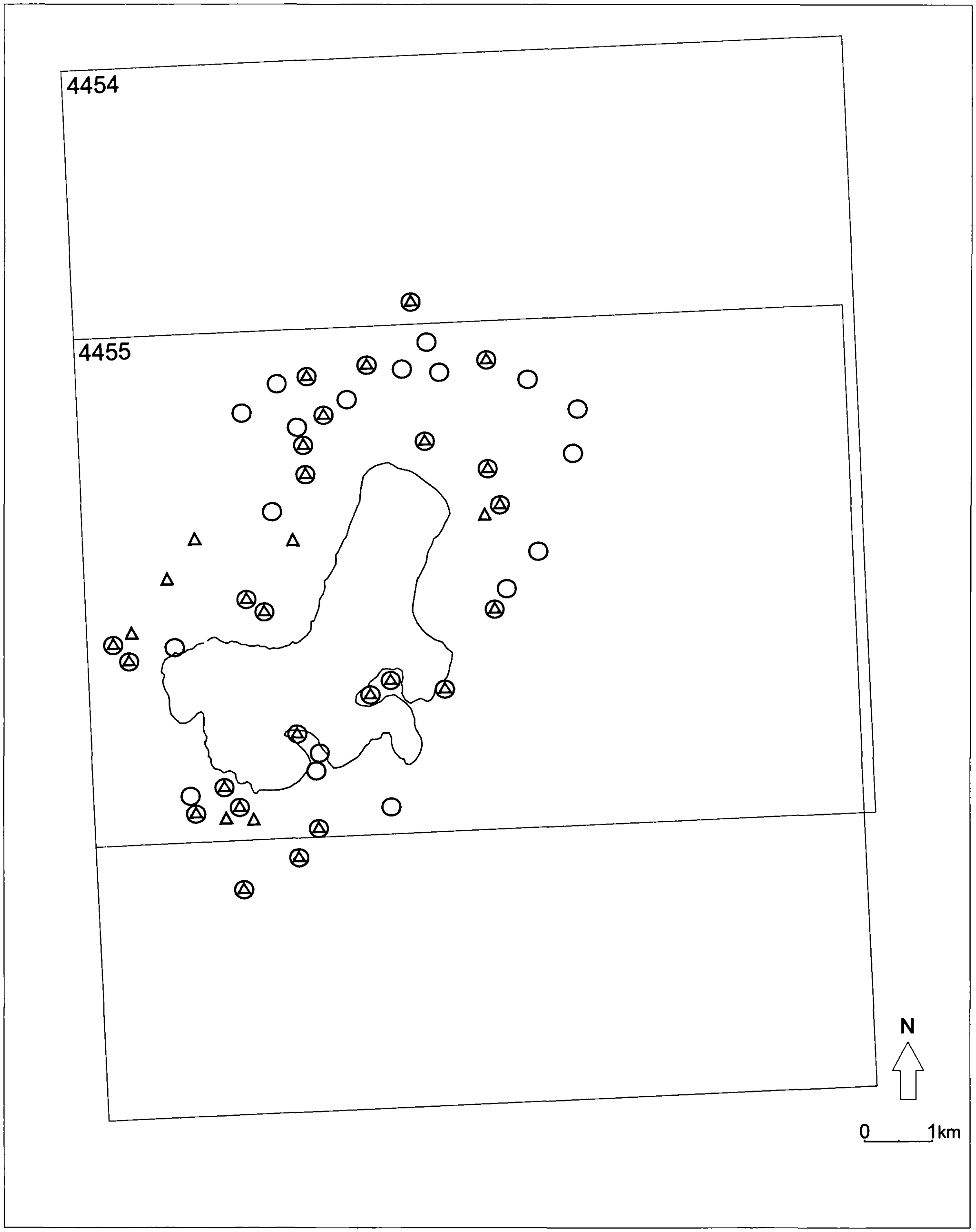

Figure 6.1: Distribution of GCPs for historical photogrammetry at Midtre Lovénbreen, NW Svalbard. Glacier and photo frame outlines were derived from the 1966 epoch. Triangles = horizontal control, circles = vertical, circles containing triangle = 3D control. Frame exposure numbers are located in the upper left hand corner of the photo outline.

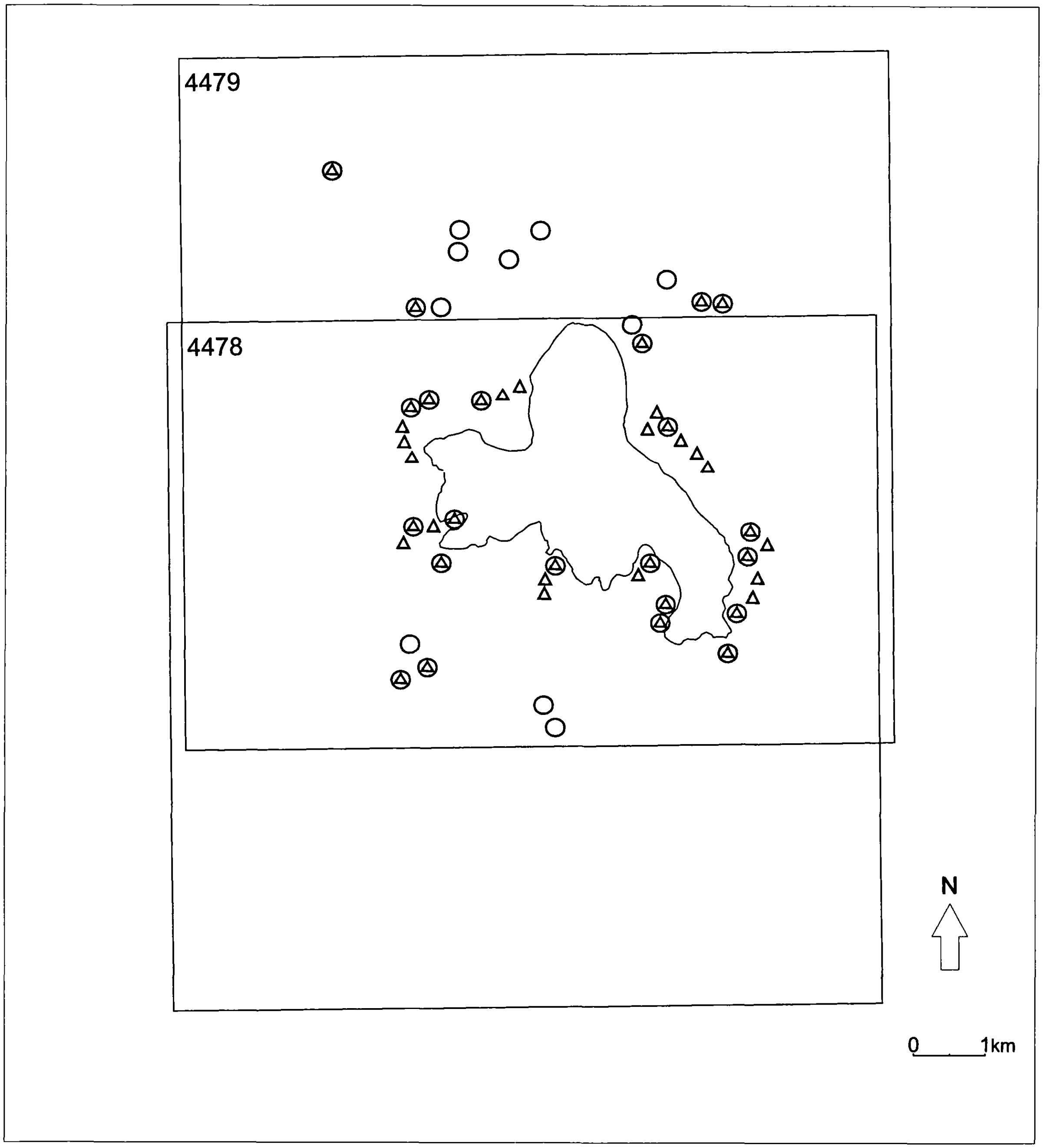

Figure 6.2: Distribution of GCPs for historical photogrammetry at Austre Brøggerbreen, NW Svalbard. Glacier and photo frame outlines were derived from the 1966 epoch. Triangles = horizontal control, circles = vertical, circles containing triangle = 3D control. Frame exposure numbers are located in the upper left hand corner of the photo outline.

6.3.1 Historical Imagery Bundle Adjustment

GCPs (with standard errors assigned as 0.5 m in *x* and *y*, and 0.25 m in *z*, see section 5.2.2.3) extracted from swath-centre locations (see section 5.2.2) were measured in each photo epoch for Midtre Lovénbreen and Austre Brøggerbreen. Solutions were generated for each model adjustment with final block adjustment results detailed below (Table 6.3).

Epoch	**RMS of GCP positions x, y, z (m)**	**Total image unit weight RMS (pixels)**
Midtre Lovénbreen		
1966	0.881, 0.964, 0.345	0.524
1977	0.926, 1.152, 0.351	0.710
1990	0.744, 0.489, 0.213	0.920
Austre Brøggerbreen		
1966	0.983, 0.973, 0.128	0.584
1977	0.954, 0.545, 0.599	0.645
1990	0.692, 0.517, 0.187	0.924

Table 6.3: Bundle block adjustment results for historical photo epochs at Midtre Lovénbreen and Austre Brøggerbreen, Svalbard.

The combination of large numbers of well-distributed GCPs at a range of elevations resulted in good statistical measures of bundle block adjustment quality for all historical models (Table 6.3). RMS of GCP positions in *x, y* and *z* were predominantly less than 1 m. Total image unit weight RMS values were all less than 1 pixel, varying between 0.524 (ML 1966) and 0.924 (AB 1990).

6.4 Frontal Retreat

The extent to which each glacier snout had retreated between epochs was calculated in the following way. Orthorectified aerial images were produced using each set of historical photographs and the elevation data derived from them. A vector was defined along the centre of each glacier (following the centre stake-line used to measure mass balance in the field), extending to beyond the greatest historical ice extent (in these data, 1966). Front positions were then determined in x and y at the intersection of the glacier snout in each orthorectified image and the centreline vector. Front positions from lidar elevation data were determined from the intersection of the centreline vector and the break in slope marking the glacier snout. Glacier frontal retreat was calculated as the distance between intersection locations at each successive epoch.

6.4.1 Midtre Lovénbreen

Retreat of the glacier snout is clearly shown in successive orthorectified images of the ML glacier boundary (Figures 6.3 and 6.4). The ice extent was largest in the earliest epoch (1966, Figure 6.3, A), and had successively retreated to a minimum in the lidar-derived model of 2005 (Figure 6.4, B). The retreat of the frontal position of ML between 1966–2005 is summarised in Table 6.4.

Epoch	**Total Retreat (m)**	**Annual Retreat ($\mathrm{m\ yr^{-1}}$)**
1966–1977	141.24	12.84
1977–1990	276.34	21.26
1990–2003	210.94	16.22
2003–2005	65.91	34.39

Table 6.4: Glacier frontal retreat, 1966–2005, at Midtre Lovénbreen, NW Svalbard.

The glacier retreated a total of 694.43 m between 1966 and 2005, at an average retreat rate of 17.81 m $\mathrm{yr^{-1}}$. There was considerable variability however in the rate of frontal retreat between successive epochs. The smallest rate of retreat occurred between the two earliest epochs when the glacier snout retreated on average 12.84 $\mathrm{yr^{-1}}$. In the following 13 years the rate rose to 21.26 m $\mathrm{yr^{-1}}$, before falling slightly to 16.22 m $\mathrm{yr^{-1}}$ in the 13 years between 1990 and 2003. The highest rates of retreat at ML occured in the two years between lidar surveys (2003–2005) with an average of 34.39 m $\mathrm{yr^{-1}}$ of frontal retreat, almost three times the rate of the earliest epoch (Table 6.4).

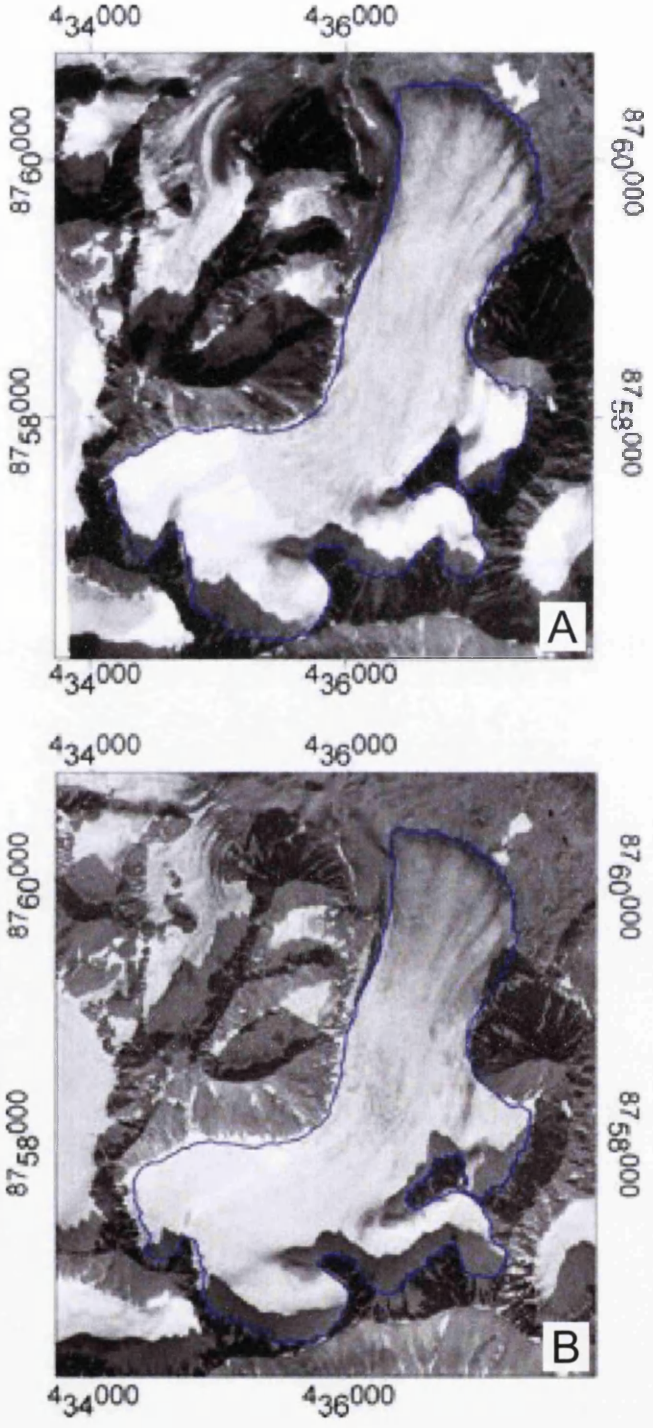

Figure 6.3: Orthorectified aerial photographs showing the extent of Midtre Lovénbreen in A) 1966; and B) 1977.

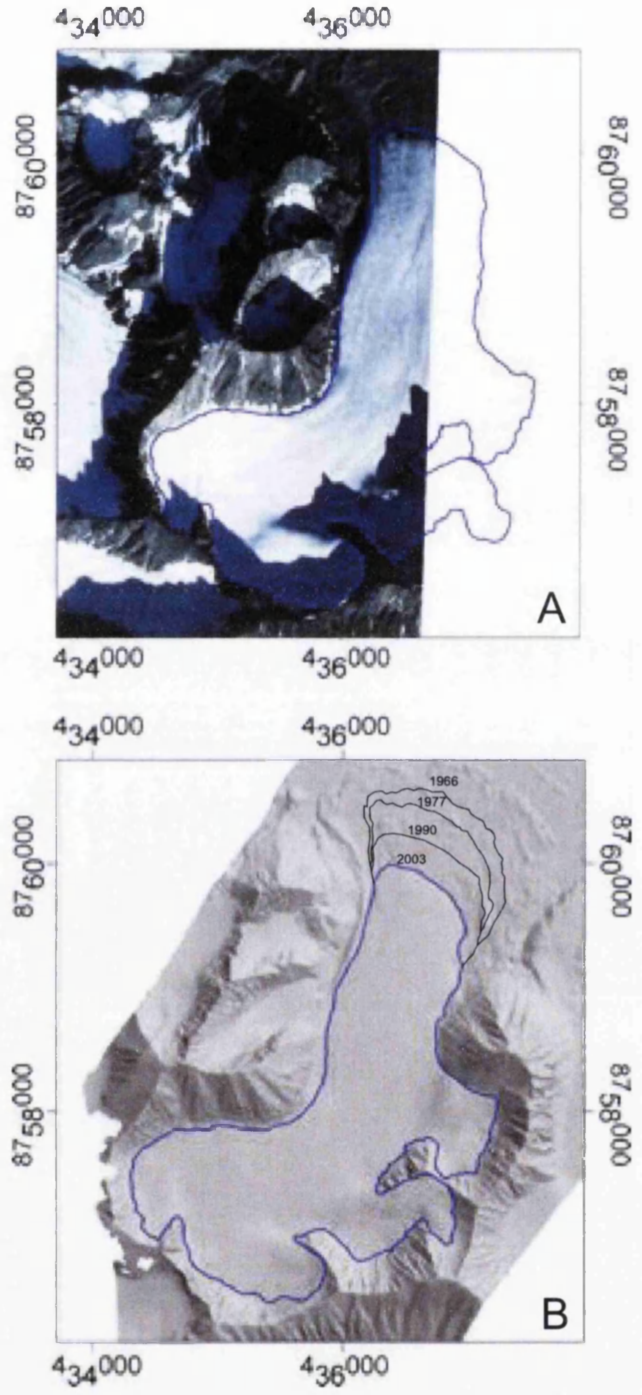

Figure 6.4: Orthorectified aerial photograph and shaded relief lidar DEM showing the extent of Midtre Lovénbreen in A) 1990; and B) 2003. The 1990 image used the boundary of the previous epoch (1977) and adjusted the snout position where possible. The 2003 image shows the approximate locations of the glacier snout from all years.

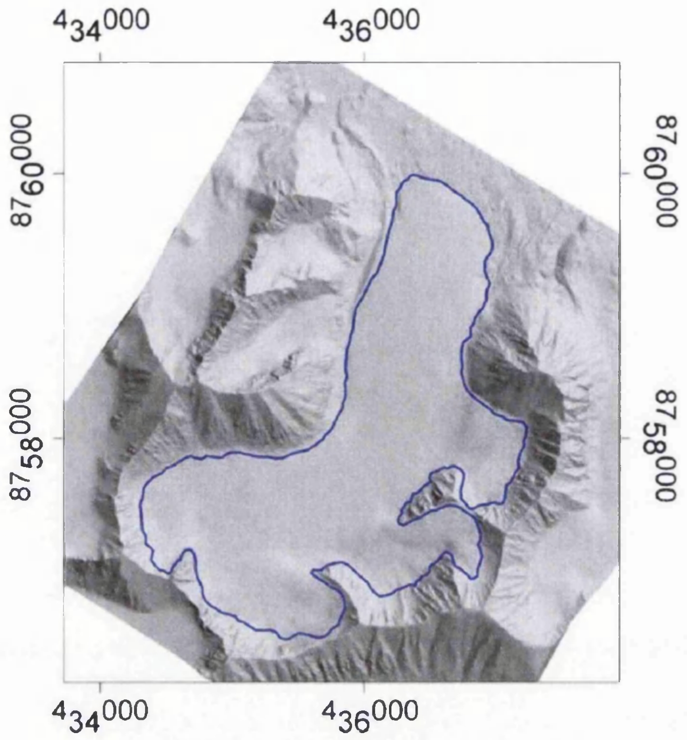

Figure 6.5: Shaded relief lidar DEM showing the extent of Midtre Lovénbreen in 2005.

6.4.2 Austre Brøggerbreen

AB frontal retreat is illustrated by the successively smaller glacier boundaries delineated from orthorectified aerial photographs (Figures 6.6 and 6.7). The glacier snout was confluent with the terminus position of Vestre Brøggerbreen (at 431000 E, 8761000 N) in the earliest photographic epoch (1996, Figure 6.6, A) but by 2005 had progressively retreated to a position 899.90 m from the 1966 ice front. Total frontal retreat distances and annual rates of retreat are provided in Table 6.5.

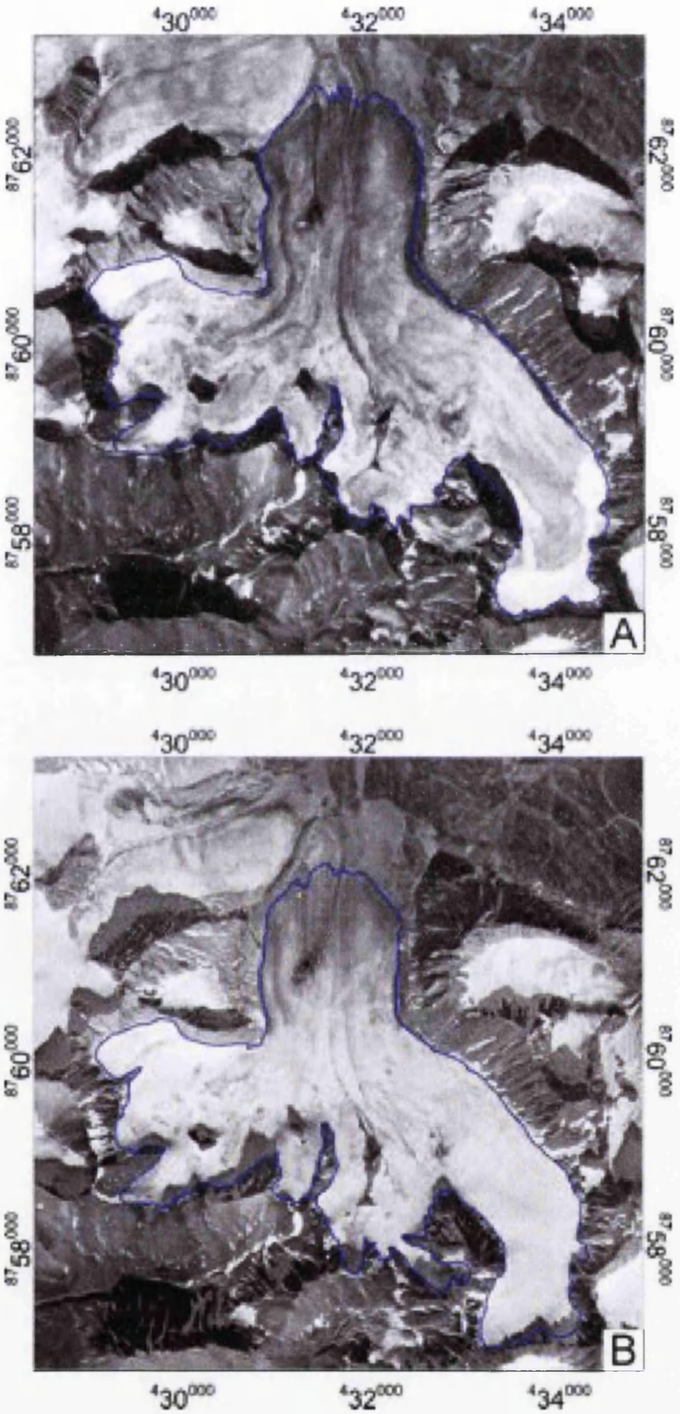

Figure 6.6: Orthorectified aerial photographs showing the extent of Austre Brøggerbreen in A) 1966; and B) 1977.

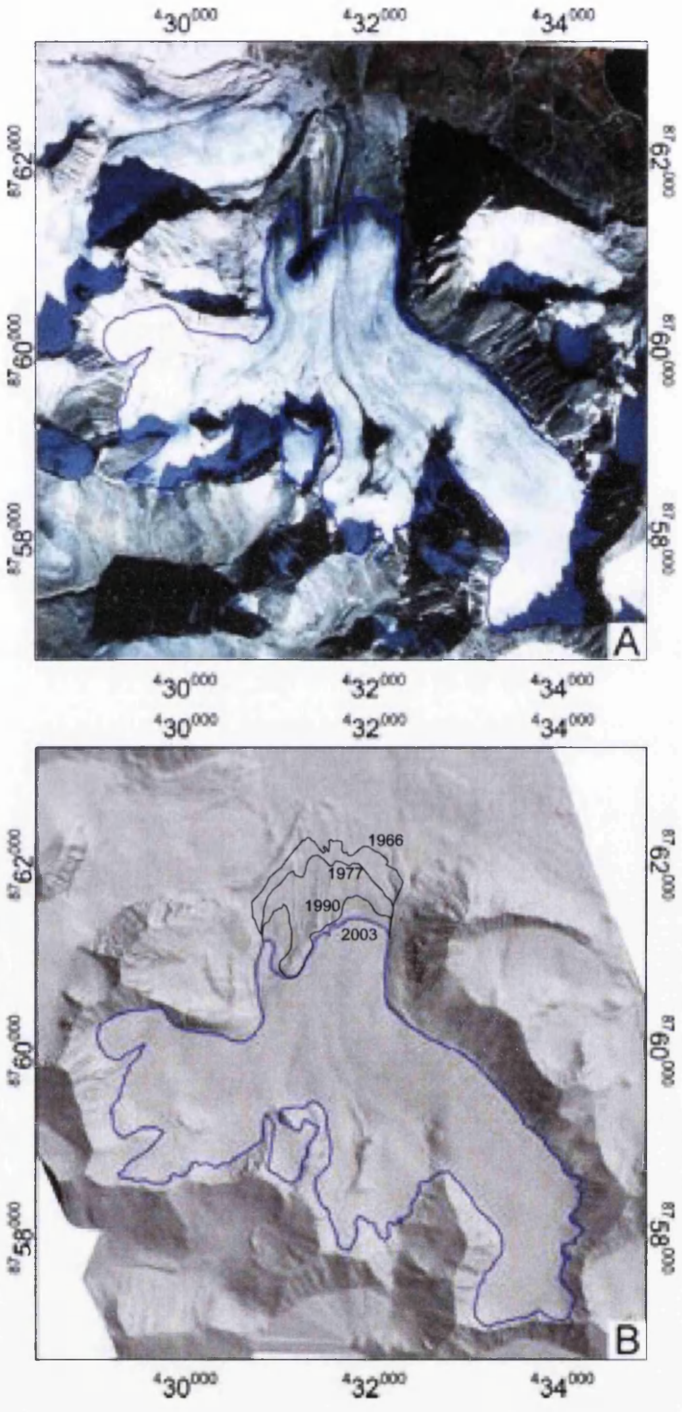

Figure 6.7: Orthorectified aerial photograph and shaded relief lidar DEM showing the extent of Austre Brøggerbreen in A) 1990; and B) 2005. The 2005 image shows the approximate locations of the glacier snout from all years.

Epoch	**Total Retreat (m)**	**Annual Retreat ($\mathbf{m\ yr^{-1}}$)**
1966–1977	198.67	18.06
1977–1990	305.56	23.50
1990–2005	395.67	26.38

Table 6.5: Glacier frontal retreat, 1966–2005, at Austre Brøggerbreen, NW Svalbard.

Annual frontal retreat rates at AB were higher than all but the 2003–2005 ML rate. Both glaciers had the lowest retreat rates during the first period of measurement (1966–1977) with AB retreating at 18.06 m yr^{-1}, some 5.22 m yr^{-1} slower than ML. Both glaciers retreated at a faster rate during the next epoch, ML retreating at 21.26 m yr^{-1} and AB at 23.50 m yr^{-1}. Rates of retreat continued to rise at AB, up to 26.38 m yr^{-1}, between 1990–2005, whereas the rate fell (16.22 m yr^{-1}) and then rose again (34.39 m yr^{-1}) at ML between 1990 and 2003 and 2003–2005 (Table 6.5).

Simple visual inspection of orthorectified aerial photographs can yield useful qualitative information on long-term glacier geometry changes and frontal retreat. However, the use of well-controlled photogrammetric models to generate ortho-rectified images allowed rates of retreat to be quantified. Both glaciers showed similar patterns of change in their retreat rates with the largest retreats occuring inbetween the most recent epochs (2003–2005 at ML and 1990–2005 at AB). Data from an additional epoch (between 2003 and 2005) at ML suggested that present day retreat rates are greater than at any time since 1966. The magnitude of retreat varied between the glaciers with Austre Brøggerbreen experiencing greater total frontal retreat (899.90 m compared to ML 694.43 m, between 1966 and 2005), and thus larger average annual retreat rates over all epochs.

6.5 Glacier Elevation Change

Changes in glacier surface elevation were calculated by differencing lidar-controlled photogrammetric DEMs generated using automatic image-matching algorithms. DEM collection utilised each optimised photogrammetric block setup (Table 6.3) and followed the processing workflow previously outlined in section 5.2.4. Glacier-wide elevation changes at both glaciers were calculated by subtracting each historical DEM surface from a 2005 lidar-derived reference surface.

6.5.1 Midtre Lovénbreen

Difference DEM images of glacier surface elevation change at Midtre Lovénbreen are displayed and described in this section. Difference models are presented in descending order with the most recent epoch first (2003–2005, Figure 6.8). This model compared elevations between two repeat lidar surveys of the glacier (see also, Figure 5.10). Subsequent models display elevation changes between the lidar 2005 model and DEMs generated from historical photographs taken in 1990 (Figure 6.9), 1977 (Figure 6.10), and 1966 (Figure 6.11).

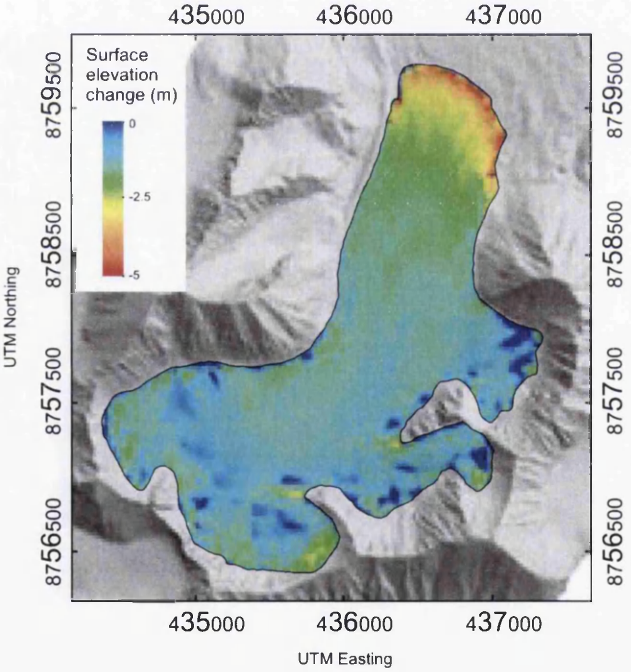

Figure 6.8: Midtre Lovénbreen glacier surface elevation change, 2003–2005. Note different scale to Figures 6.9–6.14. Background is shaded-relief 2005 lidar DEM.

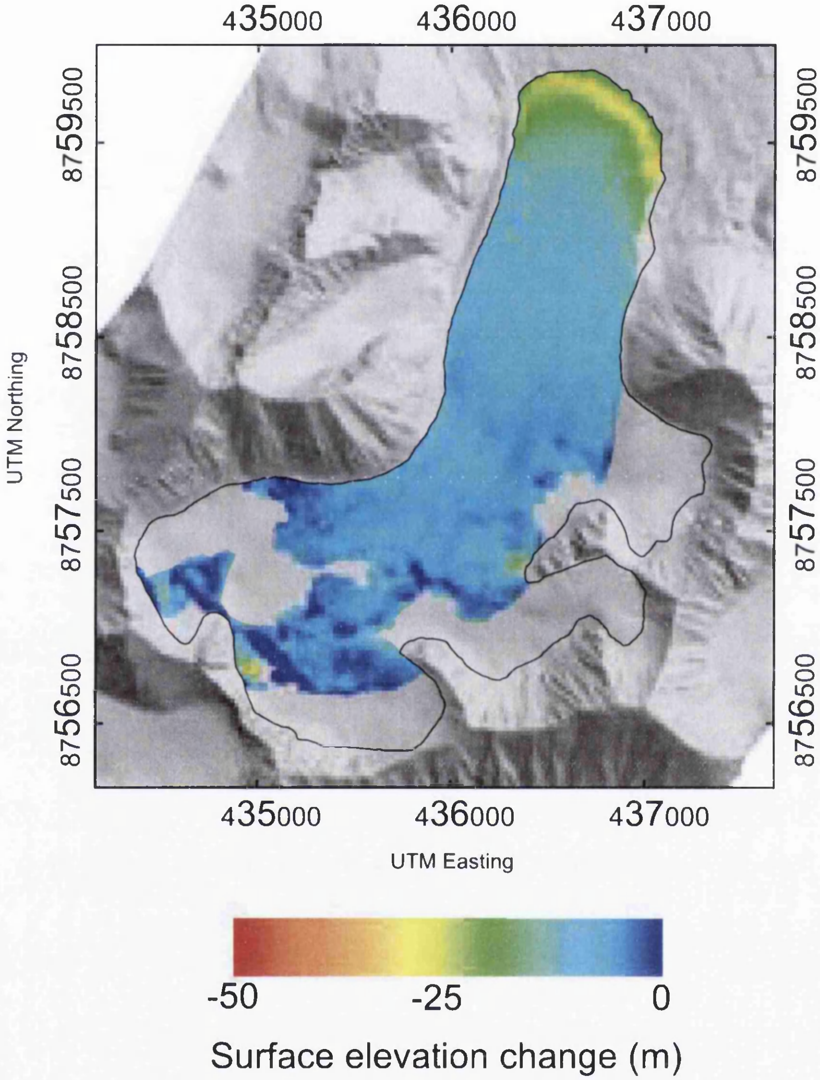

Figure 6.9: Midtre Lovénbreen glacier surface elevation change, 1990–2005. Background is shaded-relief 2005 lidar DEM. Outline marks the 1990 glacier boundary.

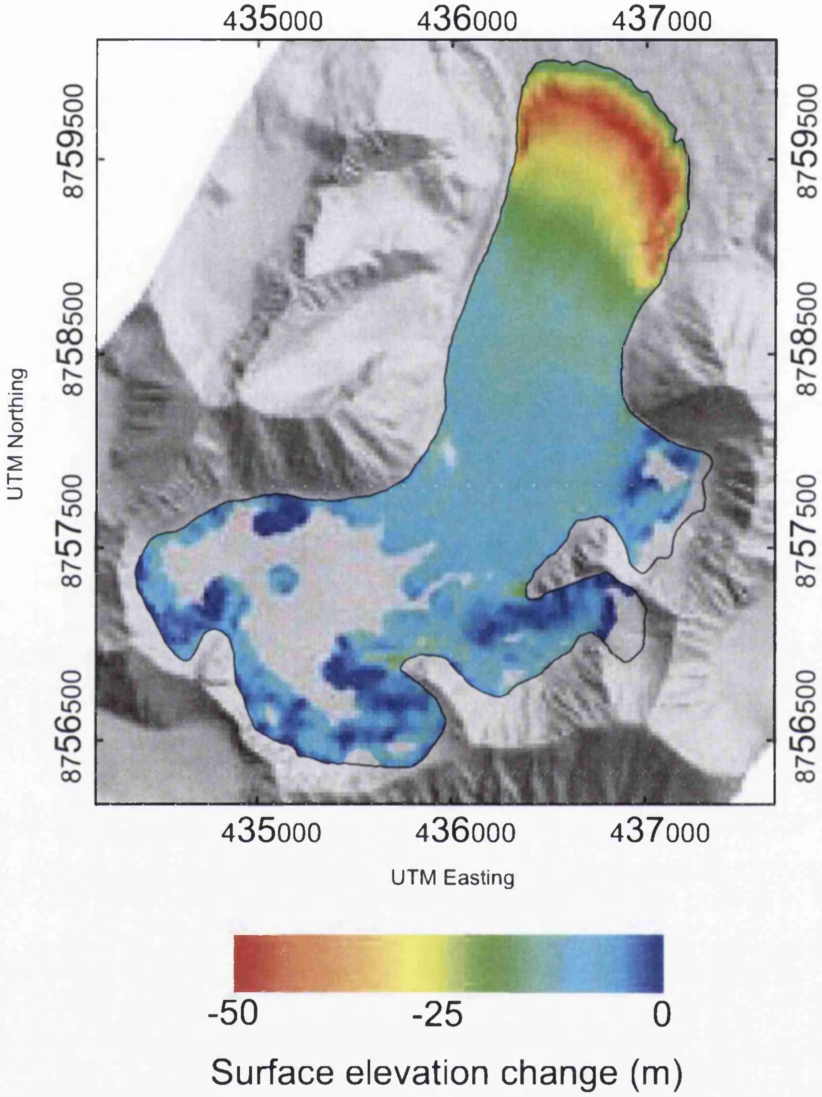

Figure 6.10: Midtre Lovénbreen glacier surface elevation change, 1977–2005. Background is shaded-relief 2005 lidar DEM. Outline marks the 1977 glacier boundary.

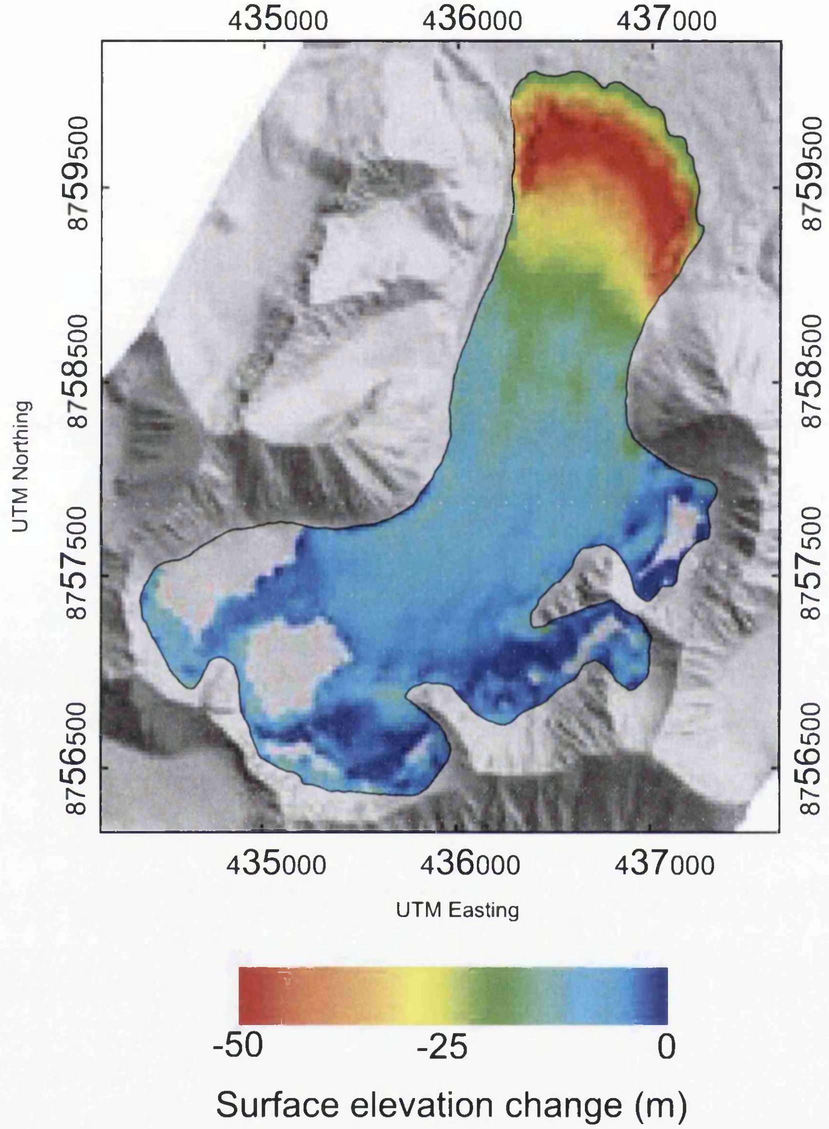

Figure 6.11: Midtre Lovénbreen glacier surface elevation change, 1966–2005. Background is shaded-relief 2005 lidar DEM. Outline marks the 1966 glacier boundary.

6.5.1.1. ML 2003-2005

Lidar surveys of the ice surface of Midtre Lovénbreen in 2003 and 2005 had complete spatial coverage and revealed a pattern of widespread thinning at all elevations (Figure 6.8). The largest elevation changes were at low elevations around the glacier snout (e.g. 436500 E, 8759600 N), with up to 5 m of thinning between surveys. Smaller, isolated regions of enhanced thinning were also evident at some of the highest elevations (e.g. 435800 E, 8756500 N). Elevation changes of up -3 m in these small regions may have been a result of variations in the distribution of seasonal snow cover. Thinning of around -1 to -2.5 m was evident at all elevations, extending from the lower 500 m of the glacier to the highest parts of the tributary basins. Regions of very little or no thinning were sparsely distributed and predominantly occurred at higher elevations, including some tributary basins (e.g. 437400 E, 8757900 N). No evidence of positive elevation changes (thickening) were found between the two years.

6.5.1.2. ML 1990-2005

Elevation changes at Midtre Lovénbreen between 1990 and 2005 showed thinning of around 30 m at the glacier snout (Figure 6.9). Thinning decreased further up-glacier with the upper quarter of the ice surface showing less than 5 m of elevation change. The limited spatial coverage of the 1990 photographs (Figure 6.4, A) resulted in slightly reduced coverage of the glacier. Stereo coverage and therefore elevation data were not available for the two eastern tributaries. Similarly, snow cover and thus poor image texture limited the number of successful image matches in some parts of the two western tributaries. Coverage was however sufficient at a range of elevations (including some of the highest parts of the glacier) to show enhanced thinning at the glacier snout followed by decreasing elevation change further up glacier.

6.5.1.3. ML 1977-2005

Elevation changes between 1977 and 2005 showed a similar pattern to those observed at earlier epochs. The magnitude of thinning however was greater, with as much as -50 m of elevation change at the glacier snout during the 28 years between surveys. Spatial coverage of the glacier surface was greater than the 1990 photographs as full glacier stereo coverage was available. However, substantial regions of snow cover in the upper glacier zones (Figure 6.3, B) meant that elevation measurements could not be generated from all parts of the ice surface. Where available, change measurements from the highest parts of the glacier showed either very little (less than -5 m) or no change, and there was no evidence of positive elevation changes.

6.5.1.4. ML 1966-2005

The spatial coverage of elevation data returned from the 1966 aerial photographs was greater than that from both 1977 and 1990 epochs. This was due to a relatively high snowline in the 1966 photographs (Figure 6.3, A). The 1966–2005 elevation change image therefore had good spatial coverage, with small gaps in data extent only in the higher tributary zones (Figure 6.11). Ice-front retreat (section 6.4.1) and substantial thinning of the snout resulted in surface elevation changes up to -50 m in the lower 1 km of the glacier. Thinning between 1966 and 2005 extended to almost all elevations with small elevation change (less than -5 m) evident in even the highest tributaries.

6.5.2 Austre Brøggerbreen

Elevation change models of the surface of Austre Brøggerbreen derived by DEM differencing are presented and described in this section. Unlike Midtre Lovénbreen, repeat lidar survey data were not collected over AB, so change measurements were restricted to three periods between epochs; 1990–2005 (Figure 6.12); 1977–2005 (Figure 6.13); and 1966–2005 (Figure 6.14). All DEM difference models were displayed on top of a shaded-relief visualisation of the 2005 lidar DEM data and given the same colour scale as Midtre Lovénbreen elevation change images (section 6.5.1).

6.5.2.1. AB 1990-2005

Aerial photographs from 1990 provided complete spatial coverage of Austre Brøggerbreen and with relatively little snow cover allowed photogrammetric derivation of elevations over more-or-less the entire glacier surface (Figure 6.12). Data coverage was incomplete only at the highest elevations towards the back of the main tributary, and at two eastern tributaries. Glacier surface elevation change was evident throughout all elevations including parts of the highest tributaries where data were available (around 10 m of thinning for example at 432500 E, 8758400 N). Areas of very little change were also evident, particularly at points where the glacier flowed around nunataks (e.g. 432000 E, 8759000 N). The largest elevation changes occured at the lowest elevations, with up to 30 m of thinning at the glacier snout. The relatively flat central area of AB (1–1.5 km up glacier from the snout), at the confluence of the three main tributary flows, displayed uniform thinning of 15–20 m between the two years.

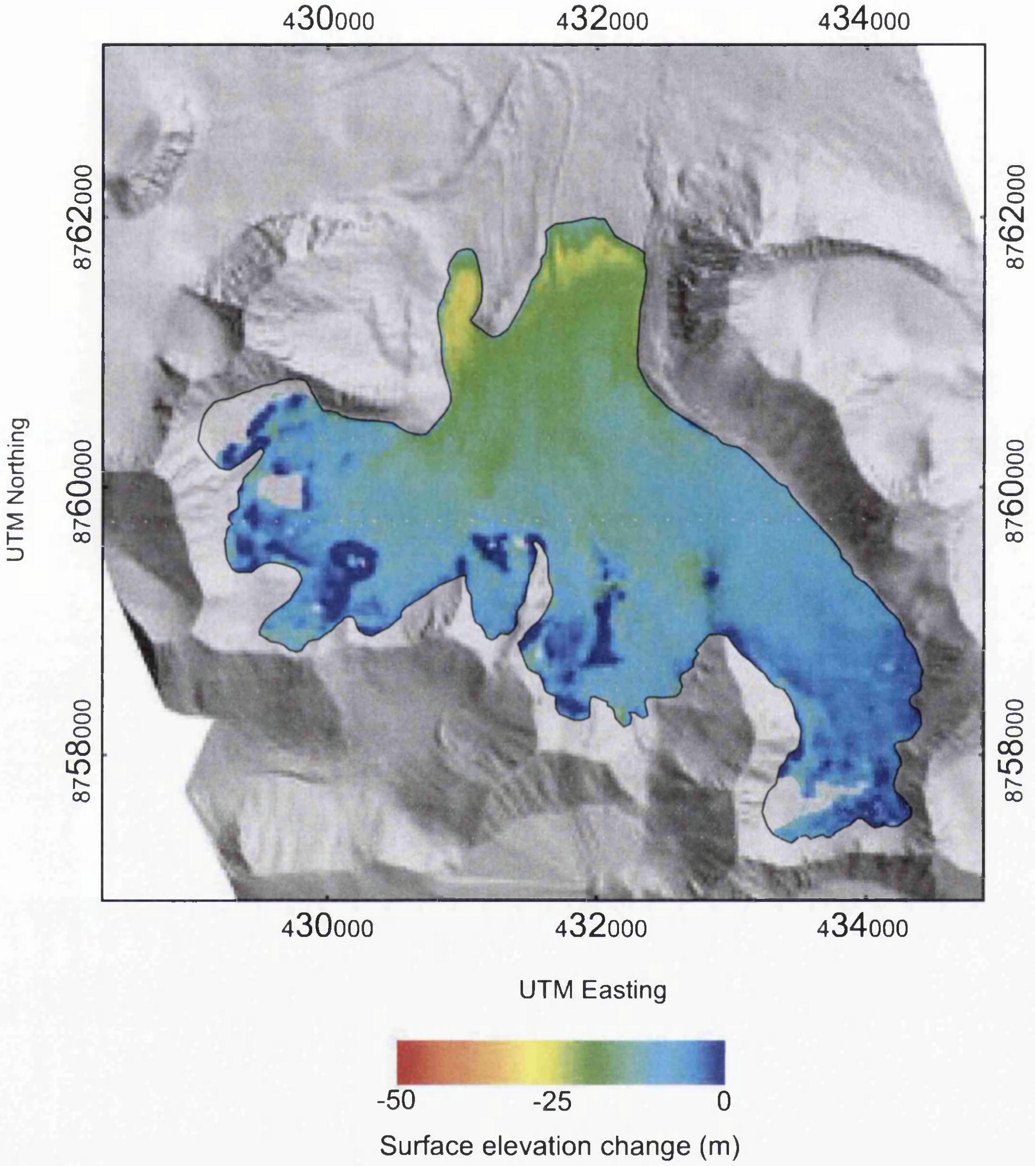

Figure 6.12: Austre Brøggerbreen glacier surface elevation change, 1990–2005. Background is shaded-relief 2005 lidar DEM. Outline marks the 1990 glacier boundary.

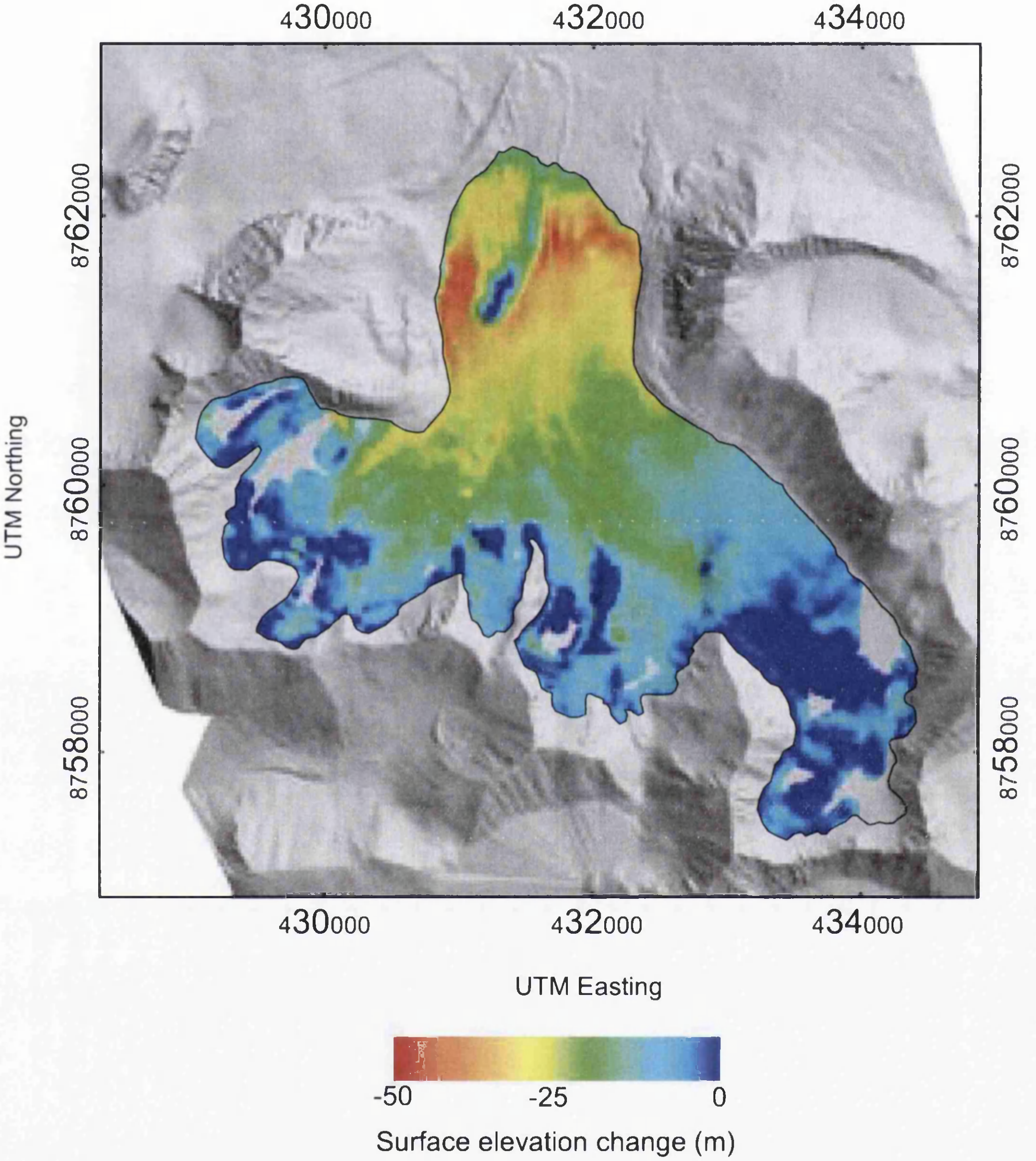

Figure 6.13: Austre Brøggerbreen glacier surface elevation change, 1977–2005. Background is shaded-relief 2005 lidar DEM. Outline marks the 1977 glacier boundary.

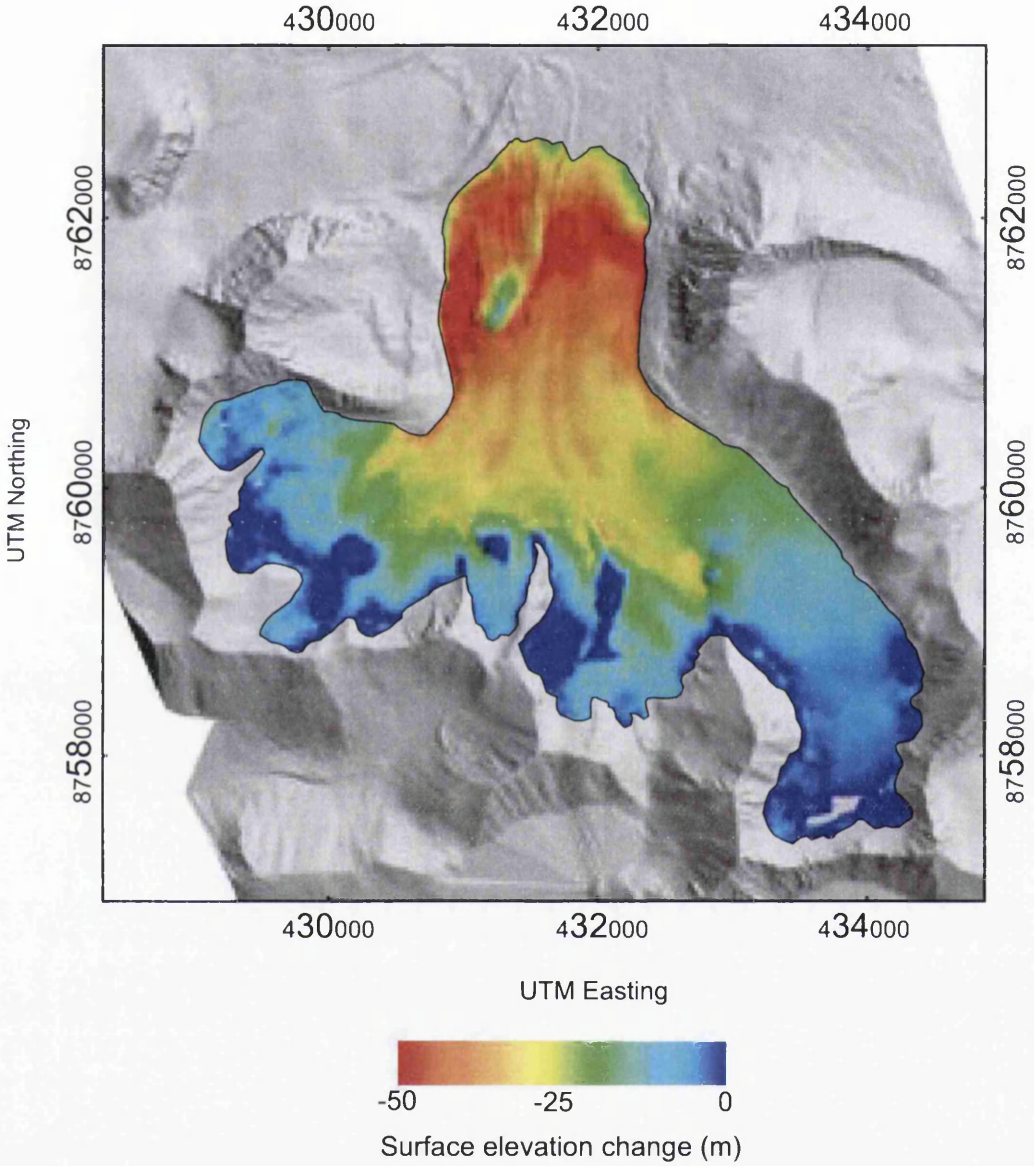

Figure 6.14: Austre Brøggerbreen glacier surface elevation change, 1966–2005. Background is shaded-relief 2005 lidar DEM. Outline marks the 1966 glacier boundary.

6.5.2.2. AB 1977-2005

The pattern of elevation change between 1977 and 2005 showed substantial thinning in the lower reaches of the glacier. A combination of frontal retreat and thinning resulted in elevation loss at the snout of up to 50 m in places (Figure 6.13). The entire lower portion of the glacier (downflow of the confluence of three main tributaries) thinned by around 20–30 m. Negative elevation changes extended up-glacier into the tributary basins, particularly the eastern and central basins which saw thinning of 10–20 m in places. The main tributary of the glacier showed some small areas where elevation changes ranged from 0 to -10 m, but predominantly had little or no elevation change between the two years. No positive elevation changes were observed between the two years.

6.5.2.3. AB 1966-2005

The difference model generated from the lidar DEM and the oldest set of aerial photographs showed the largest total changes in glacier surface elevation (Figure 6.14). Almost the entire lower section of the glacier (below the tributary confluence, as above) thinned between 30 and 50 m. Thinning of up to 30 m extended to the three tributary basins, more than 3 km from the glacier snout. The good contrast and high snowline in the 1966 aerial photographs (Figure 6.6, A) allowed elevation coverage of almost the entire glacier. Data were available for almost all regions of the glacier with the exception of several small patches in the highest parts of the main tributary. Elevation changes decreased from large amounts of thinning (-50 m) at the snout through to very little or no change at the highest elevations.

6.5.3 Elevation Changes

Lidar-derived GCPs were used to control archive aerial photography from which high-quality elevation data were generated. Elevation change errors were estimated by differencing elevations from each model over low-slope ($< 20°$), non-ice terrain (the glacier forefield) with elevations from each respective 2005 lidar survey. Mean elevation differences from models at ML and AB were all close to zero and errors (standard deviation of elevation differences) ranged from 0.09 (ML lidar 2003 model) to 1.91 (ML 1966 model). Errors in elevation change measurements were calculated as the sum of standard deviation of elevation differences from each constituent DEM. In the case of the ML 2005 model, errors were assumed to be the same as the 2003 (also lidar) DEM. All errors were graphically represented by the error bars in Figure 6.15. As the glacier forefield has probably experienced a degree of sediment reworking and redistribution during the time between epochs, these error bounds are considered to be conservative.

The spatial coverage of data were limited only by the quality of photographs, in particular image contrast in snow-covered areas. Although snow cover varied between epochs it was possible to produce measurements over the majority of the glacier surfaces for each set of photographs. Difference images of Midtre Lovénbreen and Austre Brøggerbreen revealed that substantial thinning has occurred throughout the last 39 years, with 50 m or more of thinning at lower elevations (Figures 6.9 to 6.14). Thinning at both glaciers extended well into upper ice zones and little or no thickening was reported between epochs. Elevation changes averaged over both glacier surfaces (between each of the differenced epochs, relative to the 2005 reference) indicated an increasing rate of thinning over time (Figure 6.15).

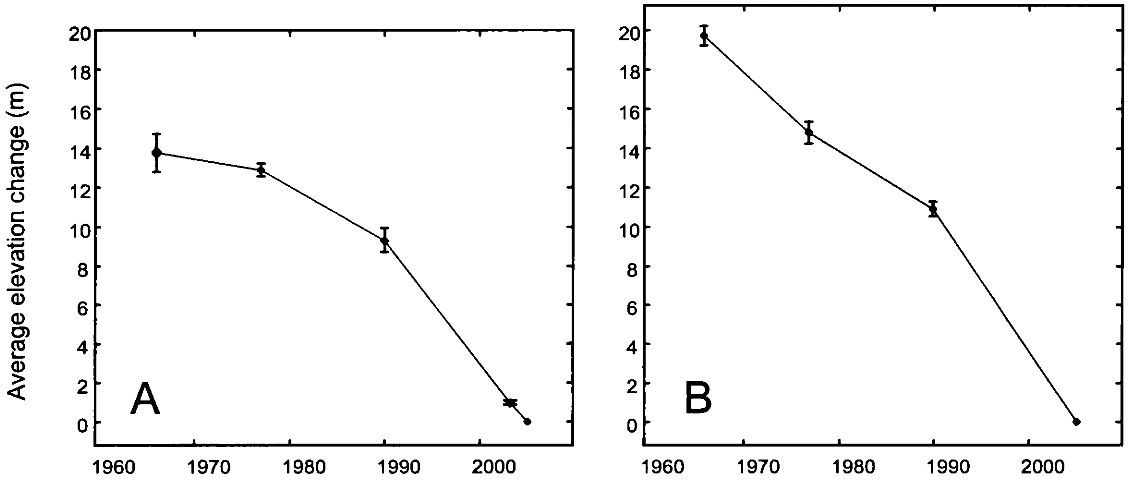

Figure 6.15: Average surface elevation change at each of the epochs at Midtre Lovénbreen (A) and Austre Brøggerbreen (B), relative to the 2005 reference DEM.

At Midtre Lovénbreen (Figure 6.15, A) the average elevation change per pixel between 1966 and 2005 was 13.76 (± 2.00) m. This corresponded to an an average rate of surface thinning of 0.35 (± 0.05) m yr^{-1} (Table 6.6). Over the course of the next epoch of measurement (1977–2005) the average elevation change was 12.86 (± 0.41) m, or 0.46 (± 0.01) m yr^{-1} of thinning. The thinning rate at ML rose yet again between 1990 and 2005, to 0.62 (± 0.07) m yr^{-1}, before falling slightly to 0.56 (± 0.05) m yr^{-1} between 2003 and 2005 (Table 6.6). The present day (2003–2005) rate of thinning at Midtre Lovénbreen was therefore 60% greater than the long-term trend between 1966 and 2005.

Comparison of elevation changes at Austre Brøggerbreen showed a slight decrease in thinning rate between the first two epochs of measurement. The glacier thinned by an average of 19.79 m between 1966–2005 and by 14.45 m from 1977–2005, corresponding to 0.51 (± 0.03) m yr^{-1} and 0.52 (± 0.04) m yr^{-1} respectively. However, the glacier thinned by an average of 10.85 m between 1990 and 2005, representing an average annual elevation change of 0.72 (± 0.05) m yr^{-1} (Table 6.6). The most recent thinning rate (1990 to 2005) was therefore 41% greater than the long term (1966–2005) average.

	Epoch	Average elevation change (m)	Rate of elevation change (m yr^{-1})
ML	1966–2005	13.76 (± 2.00)	0.35 (± 0.05)
	1977–2005	12.86 (± 0.41)	0.46 (± 0.01)
	1990–2005	9.28 (± 1.10)	0.62 (± 0.07)
	2003–2005	1.12 (± 0.18)	0.58 (± 0.05)
AB	1966–2005	19.79 (± 1.05)	0.51 (± 0.03)
	1977–2005	14.45 (± 1.11)	0.52 (± 0.04)
	1990–2005	10.85 (± 0.81)	0.72 (± 0.05)

Table 6.6: Average elevation change and annual rates at Midtre Lovénbreen and Austre Brøggerbreen, NW Svalbard. 2003–2005 rates were derived by divided the average elevation change by 23 (the number of months between surveys) and multiplying by 12.

The results suggested that Austre Brøggerbreen has thinned at a greater rate than Midtre Lovénbreen for all epochs of measurement (Table 6.6). Between 1966 and 2005 AB thinned on average 46% a year more than ML. Between 1977 and 2005 the difference was 13%, while over the most recent comparable epoch (1990–2005), AB thinned 16% more per year than ML.

Elevation changes calculated between each epoch and the 2005 reference surface were useful for examining long-term change rates and for comparing the most recent epoch at AB with changes for the same time period at ML. However, averaging over these longer time periods may have masked trends between consecutive epochs. For this reason, elevation changes were also calculated between consecutive glacier models (i.e. 1966–1977, 1977–1990, and so on) (Table 6.7).

ML	Epoch	Average elevation change (m)	Rate of elevation change (m yr^{-1})
	1966–1977	1.89 (± 2.23)	0.17 (± 0.20)
	1977–1990	5.27 (± 1.33)	0.41 (± 0.10)
	1990–2003	8.25 (± 1.10)	0.63 (± 0.08)
	2003–2005	1.12 (± 0.18)	0.58 (± 0.09)
AB	1966–1977	6.56 (± 1.98)	0.60 (± 0.18)
	1977–1990	6.64 (± 1.74)	0.51 (± 0.13)
	1990–2005	10.85 (± 0.81)	0.72 (± 0.05)

Table 6.7: Average total elevation change and annual rates between consecutive surface models at Midtre Lovénbreen and Austre Brøggerbreen, NW Svalbard.

Midtre Lovénbreen thinned by an average of 1.89 (± 2.23) m between 1966 and 1977, corresponding to an annual rate of 0.17 (± 0.20) m yr^{-1}. From 1977 to 1990 the rate rose sharply to 0.41 (± 0.10) m yr^{-1}. Between 1990 and 2003 the glacier then thinned by an average of 8.25 m, corresponding to a further increased thinning rate of 0.63 (± 0.08) m yr^{-1}. At 0.58 (± 0.09) m yr^{-1} the elevation change rate between 2003 and 2005 was no different to the preceding epoch within the specified confidence limits (Table 6.7).

Austre Brøggerbreen thinned by an average of 6.56 (± 1.98) and 6.64 (± 1.74) m from 1966–1977 and 1977–1990, resulting in no significant change in thinning rates (within specified error margins) (Table 6.7). However, both average elevation change and annual thinning rate rose sharply at the next epoch (1990–2005). Average annual elevation change increased by 41% to 0.72 (± 0.05) m yr^{-1} for the period 1990–2005.

Comparison of elevation changes between the two glaciers revealed that AB thinned at a greater rate than ML for all directly comparable epochs. Notably, over the course of the first epoch (1966–1977) AB thinned at a rate of 0.60 (± 0.18) m yr^{-1}, more than three times the rate of neighbouring ML (0.17 (± 0.20) m yr^{-1}). Rates were more similar between 1977 and 1990 when AB thinned by around 25% more than ML per year. Calculations of ice volume change, derived geodetically from elevation change measurements, are presented in the following section.

6.6 Glacier Volume Change

Changes in total ice volume between consecutive epochs were derived geodetically using pixel summation of difference DEMs (see section 5.3.1.2). Ice volume changes (δV) were calculated by summing the i pixel values of each difference DEM ($h_{i1} - h_{i2}$) for each pair of epochs (1 and 2), comprising the larger glacier surface area A (epoch 1 in all cases), and multiplying by the area ${l_p}^2$ represented by each pixel (where l_p is the pixel spacing):

$$\delta V = {l_p}^2 \sum_A (h_{i1} - h_{i2}). \tag{6.1}$$

Annual area-averaged volume changes ($\overline{\delta h/\delta t}$) were calculated by dividing total volume change δV by area A (the total area of pixels with data from the larger epoch 1 in all cases), and dividing by time t between epochs.

6.6.1 Midtre Lovénbreen

ML lost a total of 7.12 (± 1.00) × 10^7 m^3 of ice volume between the first and last epochs of measurement in 1966 and 2005 (Table 6.8). The annual rate of volume loss rose between the first four epochs yet fell slightly between the fourth and last (most recent) epoch. The rate of volume loss between 1966 and 1977 (0.95 (± 0.11) × 10^6 m^3 yr^{-1}) rose by 69% (to 1.68 (± 0.04) × 10^6 m^3 yr^{-1}) between 1977 and 1990, and then by a further 57% (to 2.63 (± 0.03) × 10^6 m^3 yr^{-1}) between 1990 and 2003. The rate of volume loss between 2003 and 2005 remained high but fell by 0.16 × 10^6 m^3 yr^{-1} compared to the previous epoch (Table 6.8).

Epoch	Total volume change, δV (m^3)	Volume change per year (m^3 yr^{-1})
1966–1977	1.05 (± 1.24) × 10^7	0.95 (± 1.13) × 10^6
1977–1990	2.18 (± 0.55) × 10^7	1.68 (± 0.42) × 10^6
1990–2003	3.42 (± 0.44) × 10^7	2.63 (± 0.34) × 10^6
2003–2005	4.72 (± 0.76) × 10^6	2.46 (± 0.39) × 10^6

Table 6.8: Total and annual volume changes at Midtre Lovénbreen, NW Svalbard, derived from DEM differencing of consecutive historical models.

6.6.2 Austre Brøggerbreen

AB lost a total of 23.56 (± 1.25) × 10^7 m^3 of ice volume between the first and last epochs of measurement in 1966 and 2005 (Table 6.8). Total volume loss at AB was greater in the first epoch (1966–1977) compared to the second (1977–1990) despite it being both earlier and shorter in duration (Table 6.9). However, during the most recent epoch (1990–2005) total volume loss was approximately twice that of the preceding period and greater than the first period. These changes corresponded to annual volume changes of 66.20 × 10^5 m^3 yr^{-1} from 1966–1977, falling to 44.79 × 10^5 m^3 yr^{-1} from 1977 to 1990, and then rising to 70.01 × 10^5 m^3 yr^{-1} for 1990–2005 (Table 6.9). The total volume loss between 1966 and 2005 was 23.56 × 10^7 m^3.

Epoch	Total volume change, δV (m^3)	Volume change per year (m^3 yr^{-1})
1966–1977	7.28 (± 2.47) × 10^7	6.62 (± 2.45) × 10^6
1977–1990	5.78 (± 1.50) × 10^7	4.48 (± 1.15) × 10^6
1990–2005	10.50 (± 0.79) × 10^7	7.00 (± 0.53) × 10^6

Table 6.9: Total and annual volume changes at Austre Brøggerbreen, NW Svalbard, derived from DEM differencing of consecutive historical models.

6.6.3 Geodetic Mass Change

Geodetic mass change was calculated by deriving annual area-averaged volume changes ($\overline{\delta h/\delta t}$) and converting volume to mass (in metres of water equivalent) by multiplying volume change by the density of ice across the whole glacier. This approach assumes Sorge's Law; that the density-depth profile at the initial (epoch 1) and final (epoch 2) time was the same over the entire glacier. Given that the photographs were taken at the end of summer and were predominantly snow-free it was reasonable to assume that changes in surface elevation corresponded to addition/ subtraction of ice rather than snow or firn (e.g. Hubbard *et al.*, 2000). Changes in ice volume between the two epochs were converted to water equivalent (w.e.) my multiplying by 0.9 (e.g. Krimmel, 1987, 1999; Paterson, 2001). Mass change in metres of water equivalent for all epochs at both glaciers are provided in Table 6.10.

Annual area-averaged volume changes ($\overline{\delta h/\delta t}$), showed an increasingly negative trend through time (Figure 6.16). When annual volume changes were averaged over the Midtre Lovénbreen glacier surface (including area changes between epochs) $\overline{\delta h/\delta t}$ became increasingly negative at successive epochs (Figure 6.16, A). Measurements of $\overline{\delta h/\delta t}$ at ML fell from -0.15 (± 0.19) m yr^{-1} from 1966–1977, to -0.30 (± 0.08) m yr^{-1} from 1977 to 1990, and further to -0.49 (± 0.06) m yr^{-1} between 1990 and 2003. The most recent epoch (2003–2005) was more negative than the previous epoch (-0.52 (± 0.08) m yr^{-1}) although this was not significant within the calculated error bounds. Nonetheless, area-averaged volume change and mass change (in metres w.e., see Table 6.10) between 2003–2005 were more than three times the rate of the earliest measurement period.

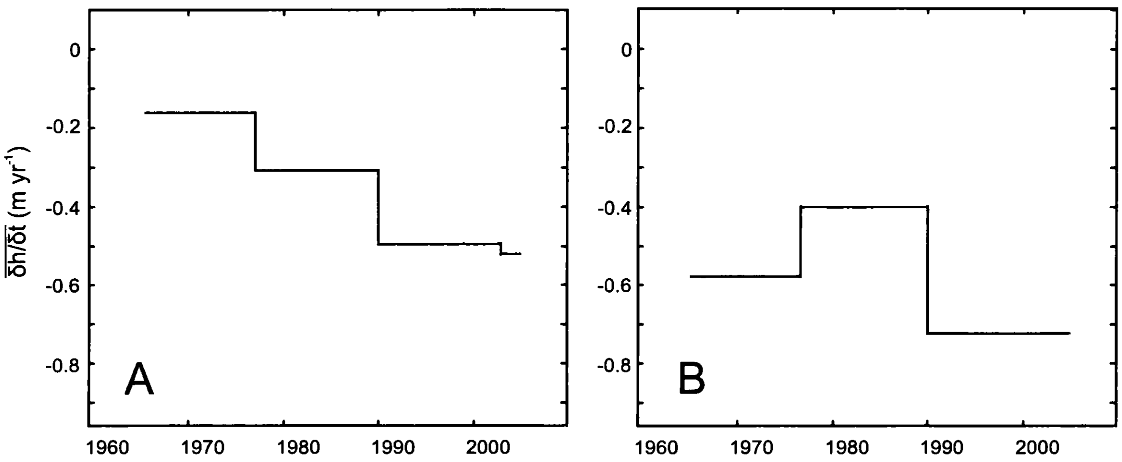

Figure 6.16: Annual area-averaged volume changes at Midtre Lovénbreen (A) and Austre Brøggerbreen (B), NW Svalbard, ($\overline{\delta h/\delta t}$) between consecutive epochs.

The signal at AB was not as clear as that from ML, but nonetheless indicated an increasingly negative $\overline{\delta h/\delta t}$ and mass change trend over time (Figure 6.16, B and Table 6.10). While all epochs showed negative mass change, the 1977–1990 epoch was less negative than the years preceding it (1966–1977), within given error limits. The most recent epoch however (1990–2005) had the largest negative change of the entire record (-0.65 (± 0.05) m yr^{-1} w.e.).

A comparison of mass change trends between ML and AB revealed that mass change was more negative at AB throughout the entire record (Figure 6.16 and Table 6.10). Between 1966 and 1977 annual area-averaged volume changes at AB were more than three times more negative than those at ML. The difference between the two glaciers during 1977–1990 was smaller (-0.36 (± 0.09) m yr^{-1} w.e. at AB compared to -0.27 (± 0.07) m yr^{-1} w.e. for ML). From 1990 to 2005 mass change at ML was -0.44 (± 0.06) m yr^{-1} w.e. (1990–2003) and -0.47 (± 0.08) m yr^{-1} w.e. (2003–2005), compared to -0.65 (± 0.05) m yr^{-1} w.e. at AB.

ML	Annual area-averaged volume change, $\overline{\delta h / \delta t}$, (m yr^{-1})	Annual geodetic mass change, (m yr^{-1} w.e.)
1966–1977	-0.15 (± 0.19)	-0.14 (± 0.16)
1977–1990	-0.30 (± 0.08)	-0.27 (± 0.07)
1990–2003	-0.47 (± 0.06)	-0.42 (± 0.06)
2003–2005	-0.52 (± 0.08)	-0.47 (± 0.08)
AB		
1966–1977	-0.58 (± 0.20)	-0.52 (± 0.18)
1977–1990	-0.40 (± 0.10)	-0.36 (± 0.09)
1990–2005	-0.72 (± 0.05)	-0.65 (± 0.05)

Table 6.10: Annual area-averaged volume changes and mass change in metres of water equivalent at Midtre Lovénbreen and Austre Brøggerbreen between 1966 and 2005.

6.7 Chapter Summary

This chapter has derived high-quality, high-resolution records of changes in glacier geometry and volume at Midtre Lovénbreen and Austre Brøggerbreen, NW Svalbard. The first part of the chapter (sections 6.2 and 6.3) showed how lidar data may be used to precisely control sets of historical aerial photographs. The ability to determine points of stable, non-ice terrain in lidar elevation data meant that the same points could be remeasured in several sets of aerial photographs. The use of the same group of GCPs meant that the introduction of systematic errors from different GCP sources was avoided. Likewise, selection of large numbers of well-distributed points at a range of elevations meant that good model solutions were achieved. Orthorectified aerial images and DEMs were produced from each of the model solutions. Orthorectified aerial images were used to delineate glacier boundaries at each of the historical epochs, from which changes in glacier frontal positions were calculated. The results showed that ML and AB had retreated by around 524 m and 926 m respectively in 39 years, with considerable variability in rates of retreat between the years comprising each photographic epoch. Differencing DEMs derived from digital photogrammetry revealed widespread thinning at all elevations for both glaciers. Elevation changes between epochs indicated increasing rates of thinning over time. At both ML and AB, rates of elevation change for the most recent measurement epoch were greater than the long-term thinning rate. Geodetic measurement of glacier volume change, derived from elevation change results, showed that ML had lost 7.12 (± 1.00) × 10^7 m^3 of ice between 1966 and 2005 with the annual rate of volume loss rising steadily since the first epoch. At AB, total volume loss was even greater, with 23.56 (± 1.25) × 10^7 m^3 of ice lost since 1966, and the most recent epoch contributing a greater rate of volume loss than any other period within the record.

Glacier mass change trends at ML and AB, calculated geodetically as the water equivalent annual area-averaged volume change, showed increasingly negative change throughout the record. Each consecutive epoch at ML produced a more negative mass change, while at AB, mass change for the most recent epoch was more negative than at any other time within the record.

The following chapter discusses the results presented in chapters 4–6. In particular, results from ML and AB are compared to results from alternative methods of measurement and to other published studies of glacier volume and geometry change. The likely causes of the trends shown are discussed along with an assessment of the overall utility of the technique for improved measurement of glacier mass balance.

Chapter 7

Discussion

7.1 Introduction

Measurements of surface elevations at Midtre Lovénbreen (ML) and Austre Brøggerbreen (AB) derived using a combined airborne remote sensing approach and presented in chapters 5 and 6 are unprecedented in their spatial and temporal resolution. This chapter discusses the advantages and limitations of using such an approach to measure small glacier mass change, in the context of current literature. Section 7.2 compares the elevation quality (errors) of DEM surfaces of ML and AB with other studies utilising digital photogrammetry to derive glacier DEMs, where appropriate. Geodetic estimates of volume change derived from these DEM surfaces are then compared with the results of other geodetic studies on Svalbard. The measurements generated in chapters 5 and 6 are compared and contrasted with errors (where appropriate), and spatial and temporal resolution of data from other published sources.

Section 7.4 discusses the geodetic mass change record of ML and AB. Mass changes derived at the two glaciers are compared with other published estimates of geodetic mass balance in 7.4.1 and with results from annual field measurements in 7.4.2. The next section (7.4.3) investigates variations in mass change by elevation and compares area-averaged geodetic mass change within elevation bands to measurements made from discrete points along the glacier centreline. The aim of this analysis was to investigate the extent to which a single point measurement of volume change was indicative of the changes in mass occuring throughout an entire elevation band. Finally, the possible drivers of changes in mass are discussed in section 7.4.4, before an attempt to place these results in the context of both regional and Arctic glacier mass balance, in section 7.4.5.

7.2 DEM Quality

Analytical and digital aerial photogrammetry have been used many times in the past to measure changes in glacier surface elevation (e.g. Etzelmüller *et al.*, 1993; Kääb and Funk, 1999; Kääb, 2000; Hubbard *et al.*, 2000; Baltsavias *et al.*, 2001). In this study, airborne lidar data were used to derive ground control points for photogrammetric glacier surface models. Considering the quality of DEM surfaces obtained with this approach in comparison to those from previously published photogrammetric studies in glacial environments highlighted the advantages and limitations of the method.

Photogrammetric DEMs of the ablation zones of Griesgletscher and Grubengletscher in the Swiss Alps were generated by Kääb and Funk (1999) and Kääb (2000) using standard field-surveyed GCPs. In the first study DEMs were processed from high-resolution aerial photography (flying height $\sim$ 2000 m, image scale 1:15 000) in order to measure changes in both surface elevation and surface displacement. The authors did not detail the number of GCPs measured and no independent check data appears to have been used to verify elevations. The accuracy of one height measurement was given as ±0.4 m, resulting in elevation change errors of ±0.6 m a^{-1} RMS. Kääb (2000) generated a time-series of DEMs of the Grubengletscher tongue from 21 sets of aerial photographs (image scales 1:11 000 to 1:20 000) with stated accuracies of ±0.2 m RMS (elevation change accuracy ±0.3 m a^{-1}). Although the derivation of this value was not explained in the text, photogrammetric error theory would suggest that it was calculated as a function of the quality of GCPs, photo quality, scanning resolution and image scale. Errors were compared to those from the ML 2003 epoch which had a similar image-scale (1:11 000) and returned a value of ±0.22 RMS when compared to independent check data. The similarity between this error and those of Kääb and Funk (1999) and Kääb (2000) suggested that lidar-derived GCPs can produce DEMs of similar elevation accuracy to those derived from standard field-measured control points. This comparison should be made with caution however as it assumes that the images in both studies were scanned at the same resolution.

Errors from earlier photographic epochs (1966, 1977 and 1990) were calculated as being between 0.32 and 1.02 m RMS (Table 7.1). It is likely that in part these larger errors were due to the greater image scale of the sorties (1:50 000) and variability in the photo quality of historical images (all Svalbard aerial photos were scanned at the same resolution, 10 μm). It is possible however that the larger values were partly a result of the procedure used to measure error. In the absence of time-coincident independent check data, estimating historical glacier DEM errors was only possible using stable, non-glacier terrain as an analogue for ice surface elevations. This had a number of disadvantages, potentially the most important being the dynamic nature of the proglacial zone. Paraglacial processes including thermoerosion and proglacial fluvial incision, aggradation and redistribution of sediment were likely to result in changes in the elevation of the forefield terrain surface, particularly over annual to decadal timescales (Ballantyne, 2002). Additionally, image contrast over parts of the forefield was often poorer than that of the ice surface. The differences between errors from the ML 2003 epoch (0.22 m RMS, measured from check data on the glacier surface) and errors from older images (0.32–1.02 m RMS) will be partly due to differences in image scale (see above) but may also be due in part to the problems of comparing elevations over the dynamic forefield zone. For this reason, it is possible that historical imagery errors are conservative.

ML	Epoch	Mean with sign (m)	RMS (m)
	1966	0.41	0.91
	1977	0.21	0.32
	1990	-0.12	0.80
	2003*	0.02	0.22
AB	1966	0.39	0.96
	1977	0.23	1.02
	1990	0.14	0.72

Table 7.1: Summary of historical photogrammetric DEM accuracy assessment statistics. Model statistics for 1966 to 1990 were derived from low-slope, non-glacier differences between each photo model and the lidar 2005 DEM (see section 6.5.3). ML 2003* represents comparison of photogrammetric model 10 with independent check data (section 5.2.4.1).

Analytical photogrammetric reconstruction of surface elevations of Haut Glacier d'Arolla, Valais, Switzerland by Hubbard *et al.* (2000) using 8 off-glacier markers (field-measured GCPs) resulted in DEMs of the bare-ice covered areas with vertical errors 'typically less than a few centimetres' over the glacier tongue and up to ±10 cm over upper parts of the glacier. Again, no details of photogrammetric model adjustment results or methods used to derive errors were provided. Areas of snow cover in the upper parts of the glacier were not included in output DEMs yet their results suggested that snow-free elevations further up glacier experienced larger errors. The elevation accuracy assessment described in chapter 5 for which time-coincident GPS check data were available (section 5.2.4.1) indicated that 2003 photogrammetric models showed no evidence of larger errors at higher elevations (Figure 5.7). The results of Hubbard *et al.* (2000) may have reflected poor distribution of GCPs at higher elevations (which would manifest as systematic DEM errors), although it was not possible to confirm this without further information.

A rigorous comparison of photogrammetric elevations of Unteraargletscher, Switzerland, by Baltsavias *et al.* (2001), was performed by comparing automatically-derived DEMs (using different digital photogrammetric software packages) with a check data set derived manually using an analytical plotter. A block of six 1:13 000 scale images scanned at 14μm forming a single strip was controlled using 26 theodolite-measured GCPs with vertical accuracy better than ±10 cm. Error statistics calculated by differencing photogrammetric elevations from check data over the glacier surface gave RMS errors of ±0.73 m, ±0.72 m, ±0.83 m, ±0.93 m, and ±3.55 m for automatically-generated DEMs using VirtuoZo, Match-T version 2, Match-T version 1, DPW version 2 and DPW version 1 software, respectively. It should be noted that these software packages are no longer particularly new. Kääb (2005) differenced a DEM of Muragl rockglacier, Swiss Alps, derived from 1:6000 scale photographs generated using digital photogrammetry, from a DEM derived manually with an analytical plotter. This procedure resulted in an RMS elevation difference of ±1.4 m, with maximum errors ranging from -16 to +9 m (Kääb and Vollmer, 2000). Elevation error at ML in 2003 (which used images of a similar scale to Baltsavias *et al.* (2001)) was 0.22 m RMS for the best photogrammetric model (model 10, 50 GCPs). Errors of historical DEMs (which ranged between 0.32 and 1.02 m RMS) were similar in magnitude to those reported by Baltsavias *et al.* (2001), despite being derived from much larger scale images.

The elevation quality of Midtre Lovénbreen and Austre Brøggerbreen DEMs processed in the previous two chapters were also compared with the results of other studies utilising photogrammetry to derive surface models of Svalbard glaciers (e.g. Etzelmüller *et al.*, 1993; Fox and Nuttall, 1997; Rippin *et al.*, 2003; Kohler *et al.*, 2007). Both Etzelmüller *et al.* (1993) and Fox and Nuttall (1997) used photography from the NPI S90-1 (1990) epoch and a network of field-measured GCPs to construct DEMs of Finsterwalderbreen, southern Spitsbergen. Etzelmüller *et al.* (1993) compared DEM elevations with 22 ground-surveyed check points, measured two days before the aerial photography, and estimated their DEM to be accurate to ±1.2 m RMS on areas of ice with good texture and ±3.0 m RMS on poorer textured terrain. Fox and Nuttall (1997) used 6 field-measured GCPs to control their model, calculated RMS residual coordinate errors of 0.75 m in x and y and 0.42 m in z, and (in the absence of any independent check data) assumed the same errors as Etzelmüller *et al.* (1993). DEMs from the 1990 epoch at ML and AB could be compared those derived for the same year at Finsterwalderbreen given that they had the same image quality and scale. Unfortunately, aerial photos of Finsterwalderbreen were scanned at 25 μm by Etzelmüller *et al.* (1993), whereas ML and AB photos were scanned at 10 μm. This is likely to account for the differences in error between DEMs.

The quality of DEM elevations generated using the methodology outlined in chapter 5 were compared directly with previously published results at the same glaciers using some of the same aerial photographs. Both Rippin *et al.* (2003) and Kohler *et al.* (2007) have previously used photogrammetrically-derived DEMs and contour maps to measure surface elevation and glacier volume changes at Midtre Lovénbreen. Rippin *et al.* (2003) differenced surface elevation data from a contour map (derived from aerial photographs) of the glacier in 1977, from a DEM generated using digital photogrammetry from 1995 aerial photographs. The 1977 contour map was digitised using GIS tools, and errors were estimated as ±5 m in x and y and ±10 m in z from a consideration of errors in the original map and errors inherent to the digitising technique. In comparison, errors calculated in chapter 6 for the ML 1977 DEM using the same set of aerial photographs were ±0.32 m (in z). The 1995 DEM used 7 total-station surveyed GCPs, which for reasons of safety and accessibility were restricted to locations entirely within the glacier forefield (Figure 7.1, A). The model was fixed further up-glacier with tie-points only and large shadow covered regions (the reason this epoch was not selected in this work) were omitted from the DEM.

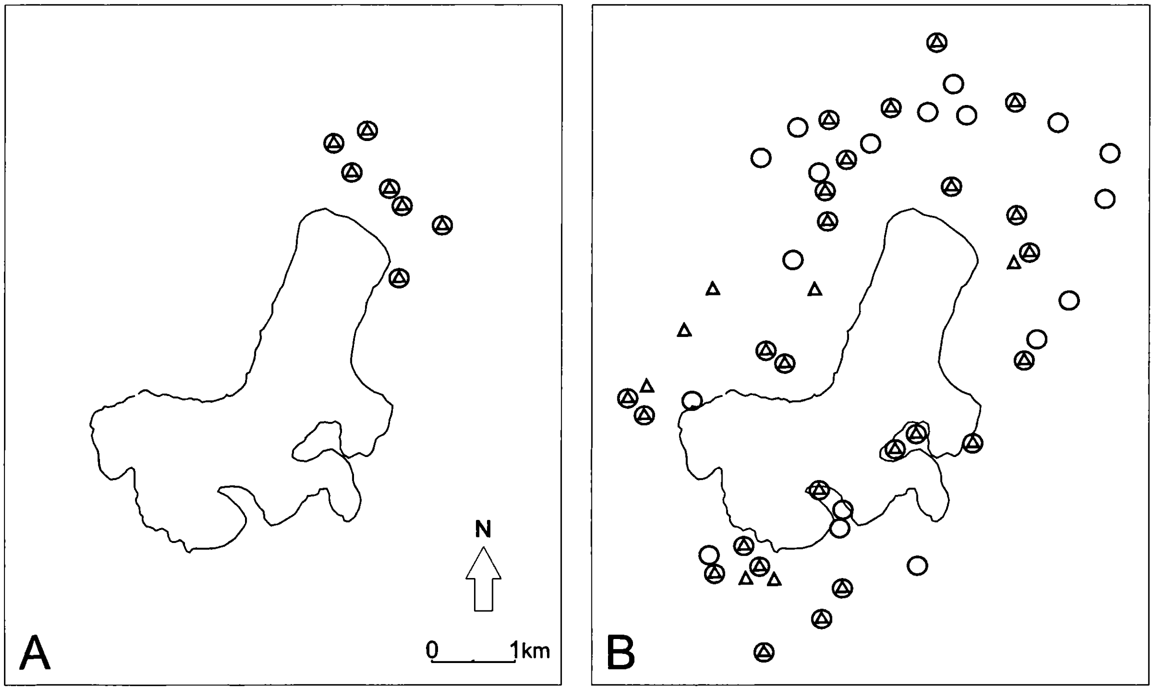

Figure 7.1: Approximate distribution of GCPs for 1995 Midtre Lovénbreen photogrammetry from Rippin *et al.* (2003) (A), and for historical photogrammetric epochs in chapter 6 (B) (see also, Figure 6.1). Triangles = horizontal control, circles = vertical, circles containing triangle = 3D control.

In the absence of time-coincident check-data, Rippin *et al.* (2003) used elevations from a 1998 GPS survey to estimate DEM accuracy. The mean elevation difference was 23.2 m (14.1 m below 250 m a.s.l and 32.1 m above 240 m a.s.l) and after applying a correction based on this systematic error, 9.8 m (2.0 m below 240 m a.s.l. and 17.3 m above 240 m a.s.l). The distribution of errors about this mean was not given. Wolf and Dewitt (2000) recommend an absolute minimum of three vertical and two horizontal control points in each stereo model to orientate a block of stereo images. Although it is difficult to directly compare the elevation accuracy of the DEM of Rippin *et al.* (2003) with any of those processed in this work (due to differences in scanning resolution and image scale), it is clear that the large systematic errors in their work were a result of inadequate GCP distribution. The lidar-as-ground-control methodology permitted the measurement of large numbers of GCPs (e.g. Figure 7.1 B) which helped to accurately control photogrammetric models.

Kohler *et al.* (2007) estimated the volume changes of Midtre Lovénbreen between 1936 and 2005 using geodetic data from a range of sources. Contour maps (derived from photogrammetry) were used to measure ice surface elevations in 1936, 1962, 1969 and 1977. Elevations from 1995 were processed from vertical aerial photographs, and DEMs from 2003 and 2005 were processed from airborne lidar data (see section 4.2). Errors in their epochs were estimated from the standard deviation of elevation differences over low-slope non-ice terrain, compared to the lidar 2005 surface. Errors were larger for the photogrammetric data (1995) than the contemporary lidar data, and progressively older for each of the older contour maps. Errors for the contour map epochs were estimated as around ±17 m, ±6 m, ±7 m and ±5 m for 1936, 1962, 1969 and 1977, respectively. Comparison of the directly comparable 1977 epoch showed that the lidar-derived GCP model had much lower error (0.32 m RMS) than the photogrammetric contour maps. Additionally, unlike those of Kohler *et al.* (2007), errors calculated in this work did not increase for older photo epochs. As the same GCPs and photogrammetric processing steps were used (and the historical images were of the same image scale and scanning resolution), errors were broadly similar between years (Table 7.1).

7.2.1 DEM Quality Summary

Like-for-like comparisons between DEMs generated photogrammetrically in different published studies were difficult due to differences in image scale, scanning resolution and photo and GCP quality. However, it was shown that lidar-controlled photogrammetric models have the capacity to produce DEMs of a similar accuracy to those derived from field-measured control points. Errors in this work were similar in magnitude to those from previous studies using field-measured control, although it is possible that this may be partly a result of higher scanning resolution. Larger errors at the earlier epochs were probably due to greater image scales (1:50 000 for 1966, 1977 and 1990 photos compared to 1:11 000 in 2003) but may also be overestimated as a result of the procedure used to measure error. Changes in forefield terrain (which was differenced between each photo model and a lidar reference surface in 2005) may result in larger error estimates. Elevation errors were shown to be smaller than those associated with contour maps generated from the same photographs, and large numbers of GCPs allowed lidar-controlled models to be accurately adjusted, thus avoiding the systematic errors that are common to poorly controlled glacier photogrammetry. An alternative approach to assessing the quality of DEM surfaces may be to compare information from the photogrammetric parallax-matching coefficient for each of the glacier models (e.g.

Kääb, 2005). Also, systematic errors may be reduced using multi-temporal image tie-points and photogrammetric blocks to co-register models between two or more epochs.

7.3 Glacier Geometry and Volume Change

The changes measured at Midtre Lovénbreen and Austre Brøggerbreen in the previous chapter were compared and contrasted with previously published photogrammetric estimates of geometry and volume change, where available. Trends in frontal retreat and volume loss are discussed with possible glaciological explanations offered for these changes. Following this, section 7.3.3 discusses the use of reference epochs in the derivation of glacier volume changes, in particular how sampling issues related to the choice of reference epoch affect estimates of volume change.

7.3.1 Midtre Lovénbreen

Calculations of glacier frontal change at ML indicated that the snout had retreated at an increasing rate (Table 6.4). Although this trend was not entirely uniform, it was coincident with the trend of increasingly negative glacier mass balance (Figure 6.16). Examination of centre-line elevation profiles of the glacier forefield and terminus from each measurement epoch revealed that the terrain underlying the snout since its position in 1966 had a fairly uniform slope angle (Figure 7.2). This suggested that topography was likely to have been a relatively minor control on changes in the rate of glacier retreat since 1966. The calculated retreat between 1977 and 1990 was 276.34 m, or a rate of 21.26 m yr^{-1}.

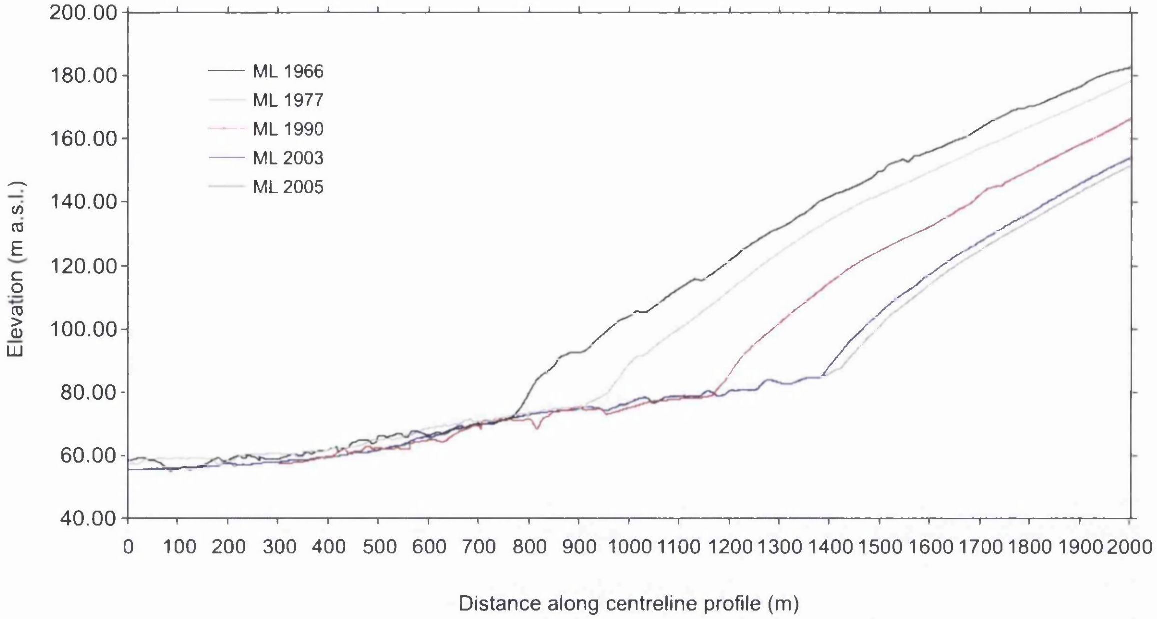

Figure 7.2: Centre-line elevation profiles showing frontal retreat at Midtre Lovénbreen, 1966–2005.

Rippin *et al.* (2003) also calculated glacier volume changes between 1977 and 1995. A poor quality contour map (1977) and an inadequately controlled photogrammetric model (1995, see Figure 7.1) resulted in a volume change estimate with very large error margins; 7.1 × 10^7 (± 1.98 × 10^8) m^3. This corresponded to an annual volume loss of 3.9 × 10^6 (± 1.1 × 10^7) m^3 yr^{-1}. To directly compare volume changes for the same time period using DEMs processed with the lidar-as-ground-control technique, the total volume change between 1977 and 1990 was combined with 5 years of the annual change rate between the 1990 and 2003 epochs. The total glacier volume change derived using this calculation was 2.97 (± 0.65) × 10^7 m^3, corresponding to an average annual volume loss of 1.65 (± 0.36) × 10^6 m^3 yr^{-1}. Both the total volume loss and annual volume change rate are less than half those estimated by Rippin *et al.* (2003). These results suggested that the analysis of Rippin *et al.* (2003) overestimated volume loss at Midtre Lovénbreen between 1977 and 1995 by ~ 2.4 times.

It was also possible to compare annual area-averaged volume changes from consecutive DEM differencing at ML ($\overline{\delta h/\delta t}$), to the results presented by Kohler *et al.* (2007). The earliest period between DEM measurements in these results (1966–1977) was compared to values generated by Kohler *et al.* (2007) from differencing contour maps from 1969 and 1977. Mean $\delta h/\delta t$ between 1966 and 1977 using lidar-controlled DEMs was -0.16 (± 0.19) m yr^{-1} (Table 6.10). For the period 1969 to 1977, Kohler *et al.* (2007) calculated $\overline{\delta h/\delta t}$ as -0.31 m yr^{-1}, approximately twice that calculated by lidar-controlled DEM differencing. The errors associated with contour maps in 1962 and 1977 were large (± 7 m and 5 m, respectively), yet Kohler *et al.* (2007) did not include error bounds on measurements of glacier volume change. The estimate of Kohler *et al.* (2007) was however within the error limits specified by volume change measurements from the lidar-as-ground-control DEM differencing. The period between the next epochs could be compared but was not directly time-coincident, as Kohler *et al.* (2007) calculated $\overline{\delta h/\delta t}$ between 1977–1995 and these results calculated $\overline{\delta h/\delta t}$ between 1977 and 1990. The value of Kohler *et al.* (2007) for this period was -0.33 m yr^{-1}, whilst that from 1977–1990 differencing was -0.31 (± 0.08) m yr^{-1}. There was therefore good agreement between these two results within the specified error limits. A slightly less negative result from lidar-as-ground-control DEM differencing may have been expected given the shorter time period between epochs and the increasingly negative rate of volume change through time (Table 6.10). The next two measurements derived by Kohler *et al.* (2007) were -0.51 m yr^{-1} for the period 1995 to 2003, and -0.69 m yr^{-1} for 2003–2005. Results from the lidar-as-ground-control method gave values of -0.49 (± 0.06) m yr^{-1} for 1990–2003, and -0.52 (± 0.08) m yr^{-1} for 2003 to 2005. Although the time period between DEMs was different, the first comparison showed that the two values were similar within the specified error limits. The calculation of Kohler *et al.* (2007) for the first directly comparable time period between epochs (2003–2005) however, was more negative than that derived in this work.

7.3.2 Austre Brøggerbreen

Rates of frontal retreat at Austre Brøggerbreen were higher than those of Midtre Lovénbreen (Table 6.5) despite the similar geometry of the glacier forefield (Figure 7.3). Like ML, the terrain underlying the glacier snout between its maximum position (in these data) in 1966 and its present position in 2005 was of fairly uniform slope and was therefore unlikely to have been a major control on the rate of glacial retreat. In the case of AB, retreat rates rose continually between the three measurement periods (18.06 m yr^{-1} for 1966–1977, 23.05 m yr^{-1} for 1977–1990, and 26.38 m yr^{-1} for 1990-2005), despite mass change being less negative during the middle measurement period (-0.52 (± 0.18) m yr^{-1} w.e. from 1966–1977, -0.36 (± 0.09) m yr^{-1} w.e. from 1977–1990, and then -0.65 (± 0.05) m yr^{-1} w.e. from 1990–2005).

The only previously published work to compare geodetic products of AB calculated frontal retreat between 1970 and 1990 as ~ 550 m (Pope *et al.*, 2007), corresponding to an annual retreat rate of ~ 27.5 m yr^{-1}. This value was 9.44 m yr^{-1} greater than the 1966–1977 rate, and 4.45 m yr^{-1} greater than the 1977–1990 rate, calculated using orthorectified photos from lidar-controlled photogrammetric models. Pope *et al.* (2007) also estimated volume change geodetically by differencing DEMs of the glacier surface in 1970 and 1990. In order to fill large gaps in the data the entire area of the glacier was divided into 50 m contour bands. The average elevation change from the constituent difference pixels in each band

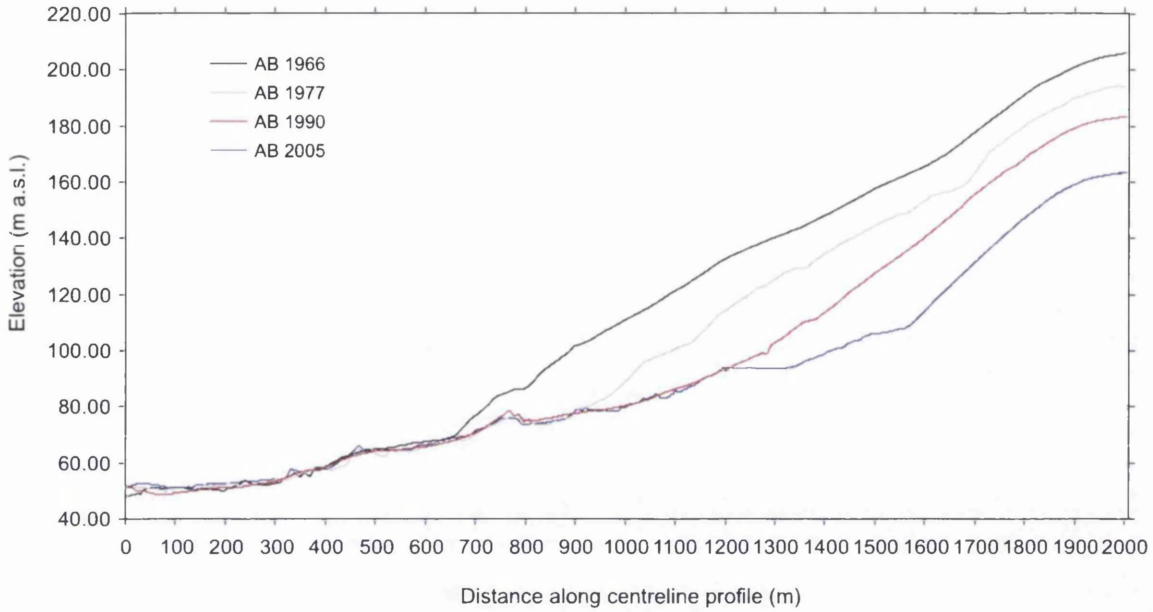

Figure 7.3: Centre-line elevation profiles showing frontal retreat at Austre Brøggerbreen, 1966–2005.

was calculated and each of these values were assigned to all pixels comprising the area of the elevation band. Using this approach Pope *et al.* (2007) calculated volume change over the 20 year period between 1970 and 1990 as -1.18 (± 0.33) m yr^{-1}. In constrast, volume change calculated using the lidar-as-ground-control approach was -0.58 (± 0.20) m yr^{-1} w.e. for 1966–1977 and -0.40 (± 0.10) m yr^{-1} w.e. for 1977–1990. These results suggested that the approach of Pope *et al.* (2007) may have overestimated glacier volume change. Volume change calculated by Pope *et al.* (2007) was more than twice that of the 1966–1977 estimate of this work, and approximately three times the estimate of the 1977–1990 value derived using lidar-controlled DEM differencing. This may have been a result of the averaging procedure employed by Pope *et al.* (2007). Their method assumed that volume changes were uniform within elevation bands and that areas of no data thinned by the average for the entire elevation band. This does not take into account local variations in surface elevation change due to factors including topographic shading, slope and aspect (e.g. Arnold *et al.*, 2006a), and may over-estimate volume change by skewing results toward regions of successful image-matching, that is where surface texture was better (i.e. bare ice).

7.3.3 Sampling Issues

The choice of reference epoch was important when deriving and comparing measurements of glacier elevation and volume change. Calculating change measurements relative to a particular epoch can be useful when comparing more than one glacier from non time-coincident epochs. For example, elevation changes at Midtre Lovénbreen, Slakbreen and along a profile of Wedel Jarls Land (central and southern Spitsbergen, respectively) were compared relative to data collected in 2003 (at ML and SK) and 2002 (at WJ) (Kohler *et al.*, 2007). The reason for calculating elevation differences relative to these epochs was that each record spanned different time periods since 1936. The Wedel Jarls Land record had only 3 measurement epochs whilst ML had 7. This comparison meant that elevation changes were averaged over longer time-periods and could be plotted together for comparison purposes. Elevation changes were calculated in this way using data generated from lidar-controlled photogrammetry at ML and AB (Figure 6.15). This approach allowed direct comparison of elevation changes over the full range of measurement periods. Differencing 1966 elevations from 2005 elevations revealed that ML thinned on average by 13.76 (± 2.00) m (or, 0.35 (± 0.05) m yr^{-1}), whilst at the same time AB thinned by 19.79 (± 1.05) (or, 0.51 (± 0.03) m yr^{-1}). Despite an additional epoch of measurement in 2003 at ML, average elevation changes for the last measurement period at AB (1990–2005) could be compared over the same timescale at ML. These results showed that AB continued to thin at a greater rate (0.72 (± 0.05) m yr^{-1} compared to 0.62 (± 0.07) m yr^{-1} at ML).

The main disadvantage of calculating elevation and volume changes relative to a fixed reference epoch is that any variations in the rate of change between epochs within the overall measurement will be averaged into a single value. For example, it was not possible to measure the volume loss between 1966 and 1977 when using the 1966–2005 comparison. In the case of ML and AB, the average rate of elevation change per pixel derived from differencing consecutive DEMs between 1966 and 1977 was 0.17 (± 0.20) m yr^{-1} and 0.60 (± 0.18) m yr^{-1}, respectively. These values were 0.18 m yr^{-1} less and 0.09 m yr^{-1} more, than the respective long-term (1966–2005) averages at ML and AB. Differencing consecutive models at AB revealed a fall in the rate of average annual elevation change between 1977 and 1990 that was otherwise masked by the rates of change calculated relative to the reference of 2005 (Table 6.7). These differences highlighted the fact that care should be taken to ensure comparison between results from DEM differencing are relative to the appropriate reference epoch.

7.4 Mass Change

This section discusses trends in glacier mass change. Firstly, geodetic mass changes derived using the lidar-as-ground-control methodology (in water equivalent units) are compared to those from previous geodetic studies. Following this, the results of chapter 5 are compared and constrasted to the field-measured record of mass balance, collected by the Norwegian Polar Institute at Midtre Lovénbreen since 1968, and at Austre Brøggerbreen since 1967.

The next section investigates the variability of changes in geodetic mass change distribution at both glaciers, particularly addressing the issue of mass loss by elevation and the representivity of a centre stake-line for small glacier mass balance. After this, the relationship between geodetic mass change and the instrumental temperature and precipitation record is explored. Finally, this section attempts to place mass change results from ML and AB into a local and regional context by comparing with other records from around Svalbard and the wider Arctic.

7.4.1 Geodetic Mass Change

Comparison of previously published estimates of volume change at ML and AB were presented in sections 7.3.1 and 7.3.2. This section now briefly compares published water equivalent mass changes at ML and AB with those calculated in section 6.6.3. The annual mass balance estimate of Rippin *et al.* (2003) between 1977 and 1995 was -0.61 m yr^{-1} w.e. Error bounds were not given with this value but may be assumed to be large given that errors in their volume calculations exceeded the magnitude of any measured changes. Geodetic mass change at ML for the period 1977–1990, measured using differenced lidar-controlled photogrammetric models, was -0.27 (± 0.07) m yr^{-1} w.e., less than half the estimate of Rippin *et al.* (2003).

Water equivalent mass balances were not given by Kohler *et al.* (2007), but may be calculated from mean annual area-averaged volume changes by multiplying by 0.9 (see section 6.6.3). The acceleration in thinning rate reported at ML by Kohler *et al.* (2007) translated to mass changes of -0.14, -0.18, -0.28, -0.30, -0.46 and -0.62 m yr^{-1} w.e. for the periods 1936–1962, 1962–1969, 1969–1977, 1977–1995, 1995–2003 and 2003–2005. Comparison of the results of chapter 6 and those of Kohler *et al.* (2007) revealed broad agreement in the magnitude of changes in geodetic mass change (Figure 7.4). While direct comparisons were difficult to make due to the different time periods between epochs and the lack of error estimates in the the results of Kohler *et al.* (2007), both methods recorded the trend of increasingly negative mass change. In addition, rates of geodetic mass change were the same (within error bounds) between the two methods from the mid 1970s to 1990 and from 1995 to 2003 (Figure 7.4). Interestingly, the rate of geodetic mass change between 2003 and 2005 derived using the same (lidar) data and the same method, were significantly different. The value calculated in this work was -0.47 (± 0.08) m yr^{-1} w.e., while the estimate of Kohler *et al.* (2007) was -0.62 m yr^{-1} w.e. As both the data and methods were the same, the discrepancy between these results must have been caused by differences in the delineation of glacier area. This finding highlights the importance of accurate delineation of glacier boundaries in the geodetic determination of mass balance.

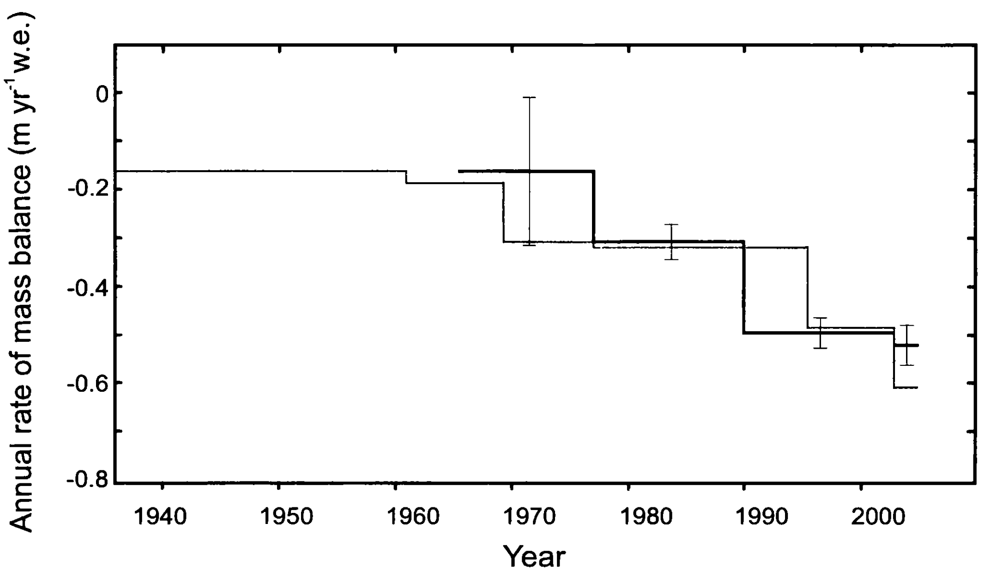

Figure 7.4: Comparison of geodetic mass change at Midtre Lovénbreen from lidar-controlled photogrammetric DEM differencing (black line with error bars) and from differencing geodetic data from a range of sources (Kohler *et al.*, 2007, grey line).

At Austre Brøggerbreen, the only geodetic estimate of mass change was that derived by Pope *et al.* (2007). This value, derived by averaging volume changes over 50 m elevation contour bands (see section 7.3.2), was -1.06 (± 0.30) m yr^{-1} w.e. between 1970 and 1990. In comparison, the estimate derived using the lidar-as-ground-control methodology for the period 1977–1990 was -0.36 (± 0.09) m yr^{-1} w.e. Within error bounds the estimate of Pope *et al.* (2007) was therefore ~ 2–4 times more negative than that derived from lidar-controlled photogrammetric models. Pope *et al.* (2007) used a limited number of field-measured GCPs and a DEM extraction parameter sensitivity analysis to derive photogrammetric elevations. Large areas of the glacier surface rejected by their analysis as unreliable were assigned volume changes using the averaging procedure detailed above. These results indicated that the averaging procedure employed by Pope *et al.* (2007) may significantly overestimate geodetic glacier mass change.

7.4.2 Field Mass Balance

The availability of field-measured mass balance data (section 2.5.1.1) from Midtre Lovénbreen and Austre Brøggerbreen provided a unique opportunity to validate results from lidar-controlled photogrammetric processing of archival imagery. With records of field data beginning in 1968 and 1967 respectively, ML and AB have the longest annual Arctic mass balance records (Dowdeswell *et al.*, 1997). The records are unique in both their length and quality (no yearly data is missing) and coincide almost perfectly with long-term records of change derived from aerial photographs. Importantly, comparison of geodetic with field-measured balance data will allow an assessment of the utility of this technique for historical mass balance reconstruction and, if successful, should allow greater confidence to be placed in geodetic results from data processed with this method at glaciers lacking in historical field measurements.

7.2.4.1. Midtre Lovénbreen

The field-measured record of mass balance at ML runs from 1968 to 2006 (Figure 7.5). With the exception of 1987 and 1991 net mass balance has been negative for every year in the dataset. The data show a large degree of variability with at least 8 individual years throughout the record showing net balances close to zero.

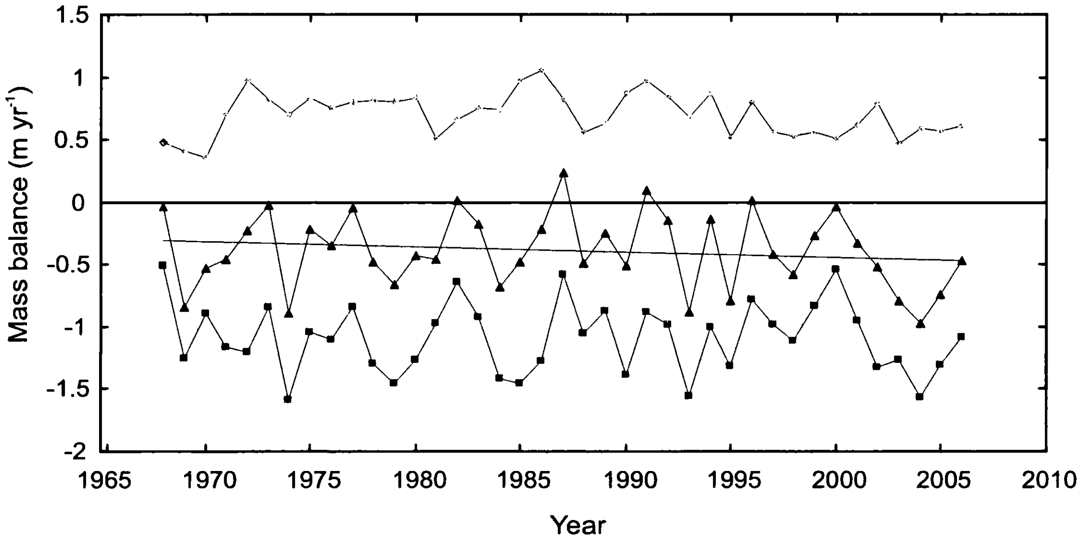

Figure 7.5: Field-measured mass balance at Midtre Lovénbreen, NW Svalbard. Light grey, diamonds (top) represent winter balance, dark grey, squares (bottom) summer balance, and black, triangles (centre) net annual balance (with linear fit trendline). Data from Lefauconnier *et al.* (1999) and J. Kohler (2007, pers. comm.)

A linear trendline fitted to the data suggested increasingly negative net mass balance. However, linear regression of the curve showed that the the trend was not significant at the 95% confidence level (R^2 0.03). In order to compare field-measured data to geodetic mass balance derived from lidar-controlled photogrammetric DEM differencing, mean annual net balances were calculated for the years comprising the period between each historical photography epoch (Table 7.2).

Comparison of field and geodetic measurements revealed that the two techniques showed

Epoch	Average field-measured net balance (m yr^{-1})	Geodetic mass change (m yr^{-1})
1966–1977	-0.36	-0.14 (± 0.16)
1977–1990	-0.33	-0.27 (± 0.07)
1990–2003	-0.38	-0.42 (± 0.06)
2003–2005	-0.83	-0.47 (± 0.08)

Table 7.2: Average field-measured net balance and geodetic mass change derived from differencing lidar-controlled photogrammetric models at Midtre Lovénbreen.

similar results for the middle two periods, yet were significantly different for the first and last periods between photographic epochs. Between 1966 and 1977 the average field net balance was -0.36 m yr^{-1}, while geodetic measurement gave a value of -0.14 (± 0.16) m yr^{-1}. Even within error bounds, the geodetic value was less negative than the field value. For the following two epochs (1977–1990 and 1990–2003), geodetic mass changes were similar to field-measured balances (within specified error bounds). The increasingly negative rate of geodetic mass change between 1977–1990 and 1990–2003 was evident yet less pronounced in the field-measured record (a decrease of 0.05 m yr^{-1}, compared to a decrease of 0.16 m yr^{-1}). The average rate of net mass balance actually reduced (became less negative by 0.03 m yr^{-1}) between 1966–1977 and 1977–1990 when measured by field methods, whereas the rate of geodetic balance was more negative, by 0.14 m yr^{-1}, for the same period. Finally, average field-measured net balance for the final measurement period (2003–2005) was significantly more negative (by -0.36 m yr^{-1}) than geodetic mass change. This may suggest that thinning along sections of the glacier centreline was greater than elsewhere on the ice surface between these two years.

7.2.4.2. Austre Brøggerbreen

The field mass balance record of Austre Brøggerbreen is officially the longest of any Arctic glacier, extending back to 1967 (Lefauconnier and Hagen, 1990; Haeberli, 1998) (Figure 7.6). Perhaps unsurprisingly for the neighbouring glacier, the mass balance record is very similar to that of ML (Figure 7.5). The linear trendline fitted to net balance data again suggested increasingly negative balance through time, but like ML was not statistically significant at the 95% confidence level (R^2 0.06).

Comparison of field-measured balance with geodetic mass changes between each photogrammetric epoch revealed that estimates from both measures were broadly similar (Table 7.3). Between 1966 and 1977 average field-measured net balance was -0.45 m yr^{-1}. Geodetic

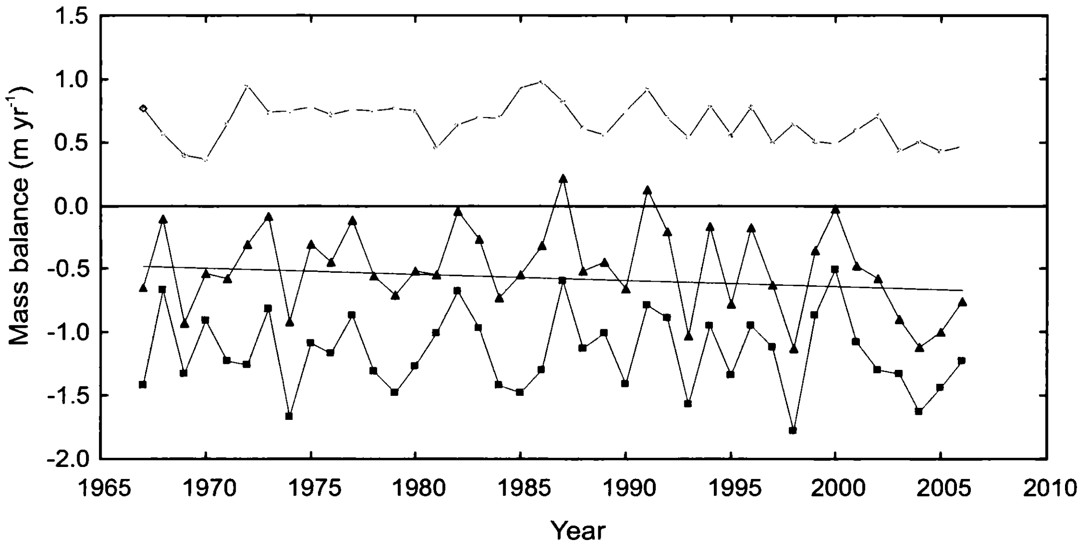

Figure 7.6: Field-measured mass balance at Austre Brøggerbreen, NW Svalbard. Light grey, diamonds (top) represent winter balance, dark grey, squares (bottom) summer balance, and black, triangles (centre) net annual balance (with linear fit trendline). Data from Lefauconnier and Hagen (1990) and J. Kohler (2007, pers. comm.)

Epoch	Average field-measured net balance (m yr^{-1})	Geodetic mass change (m yr^{-1})
1966–1977	-0.45	-0.52 (± 0.18)
1977–1990	-0.41	-0.36 (± 0.09)
1990–2005	-0.57	-0.65 (± 0.05)

Table 7.3: Average field-measured net balance and geodetic change derived from differencing lidar-controlled photogrammetric models at Austre Brøggerbreen.

measurements gave a value of -0.52 (± 0.18) m yr^{-1}, slightly higher but similar within the specified error bounds. Average field balance fell during the following epoch, to -0.41 m yr^{-1}, a trend that was also seen in the geodetic mass change results. Average geodetic mass change fell to -0.36 (± 0.09) m yr^{-1}, a value statistically similar to the field-measured rate, within the limits of stated errors. Both methods recorded an increase in negative mass change for the final epoch, with both values being more negative than at any other period in the record (Table 7.3). The geodetic mass change rate between 1990 and 2005 was -0.65 (± 0.05) m yr^{-1}, slightly more negative than the -0.57 m yr^{-1} calculated by averaging net field mass balance.

A number of studies comparing geodetically-derived mass balance with field-measured balances on Svalbard have suggested that field measurements may underestimate the real mass balance (Hagen *et al.*, 2000; Rippin *et al.*, 2003). At ML this hypothesis was supported by the results of an energy balance model used to reconstruct mass balance between 1980 and 1989 (Fleming *et al.*, 1997). This study calculated a mean annual balance of -0.44 m yr^{-1} w.e. compared with a measured balance over the same period of -0.27 m yr^{-1} w.e. Geodetic mass change results, calculated by differencing lidar-controlled photogrammetric DEMs, did not support this hypothesis. At ML, geodetic mass changes for the first (1966–1977) and last (2003–2005) measurement periods were 0.22 and 0.36 m yr^{-1} less negative than those measured in the field. Geodetic mass changes during the periods 1977–1990 and 1990–2003 were the same as those measured in the field (within error limits, Table 7.2). At AB, geodetic mass changes were very similar to field-measured balances, within specified error limits. Geodetic balance was more negative than field balance for just one period (1990–2005), and by only 0.08 (± 0.05) m yr^{-1}. It is likely that the relatively poor elevation quality and large error estimates of volume changes derived by DEM (Rippin *et al.*, 2003) and contour map (Hagen *et al.*, 2000) differencing led to results that overestimated mass changes. This finding highlights the crucial importance of data quality when using DEMs to measure changes in glacier volume and inferring geodetic mass change.

7.4.3 Geodetic Mass Change Distribution

The quality and coverage of elevation data from each of the historical photographic epochs at ML and AB permitted an examination of changes in the spatial distribution of volume change and geodetic mass change. The aim of this analysis was to examine the extent to which a single volume change measurement (in the case of field-measured mass balance, at select points along the glacier centre-line) was representative of the changes in mass occuring across a particular elevation band. As geodetic mass changes were derived from differencing DEMs covering almost the entire area of the ice surface, this analysis may help to explain some of the discrepancies recorded between geodetic and field balances (e.g. Table 7.2 and 7.3).

Each of the lidar-controlled photogrammetric difference models was delineated into classes based on the elevations of their constituent earliest epoch DEM. For example, pixels in the 1966–1977 ML difference DEM were grouped into elevation bands based on the distribution of elevations of the 1966 surface. Pixels at ML were grouped into 9 classes of 50 m elevation bands from 50–100 m a.s.l to 450–500 m a.s.l. AB, which has ice at higher elevations than ML, had 10 classes from 50–100 m a.s.l to 500–550 m a.s.l. Pixels from each of the difference models were grouped into these elevation bands and the mean area-averaged volume change ($\overline{\delta h/\delta t}$) and water equivalent geodetic mass changes calculated (see section 6.6). These area-averaged geodetic mass changes were then compared to geodetic mass change derived from volume change at a single point at the centre of each elevation band. The point in each band was located by creating a vector along the centreline of the glacier (following the stake line used to measure field mass balance, e.g. Figure 7.2 and 7.3) and extracting a single volume change measurement from the individual pixel where the centre of the elevation band (e.g. at 125 m a.s.l. in the 100–150 band) intersected the centreline vector. Comparisons were then made between area-averaged geodetic mass change for each elevation band (at each glacier, and for each period) and geodetic mass change determined from a single point measurement at the centre of each band.

Area-averaged and centre point geodetic mass changes for each 50 m elevation band between epochs at ML and AB were given in Tables 7.4 and 7.5 respectively. At Midtre Lovénbreen, delineation of geodetic mass change into elevation bands showed that the glacier experienced unprecedented negative mass change between all epochs, and at all elevations. No single elevation band between any epoch experienced a positive average geodetic mass change (Table 7.4). Comparison between measurement epochs revealed that geodetic mass changes were generally more negative at each successive period. An example of this was the 300–350 m a.s.l. elevation band which had area-averaged mass changes of -0.10, -0.27, -0.38 and -0.46 m yr^{-1} w.e. between 1966–77, 1977–90, 1990-03 and 2003–05, respectively. This finding supported the increasingly negative rate of glacier-wide geodetic mass change reported in section 6.6.3 (Table 6.10). Within measurement periods, geodetic mass changes were less negative at higher elevation bands. This finding was expected given the geometry of the glacier and the spatial patterns of elevation change (Figures 6.8–6.11). The largest negative changes tended to occur within the 50–100, 100–150 and 150–200 m a.s.l. bands. With the exception of the 2003–2005 period, geodetic mass change was more negative between 100–150 m a.s.l than between 50–100 m a.s.l. The reason for this was probably that average elevation changes were lower at the snout of the glacier where the tongue thinned and retreated. A similar temperature regime just 50–100 m further up glacier and larger ice volumes available for melting will have resulted in larger elevation changes within these bands.

ML

Period	Elevation band (m a.s.l.)	Area-averaged mass change for band (m yr^{-1} w.e.)	Point mass change (m yr^{-1} w.e.)	Difference (m yr^{-1} w.e.)
1966–77	50–100	-0.85	-1.22	-0.37
	100-150	-0.94	-0.80	+0.14
	150-200	-0.48	-0.48	0.00
	200-250	-0.21	-0.12	-0.09
	250-300	-0.14	-0.25	-0.11
	300-350	-0.10	0.14	+0.24
	350-400	-0.05	-0.05	0.00
	400-450	-0.17	0.49	+0.66
	450-500	-0.07	0.20	+0.27
1977–90	50–100	-1.00	-1.10	-0.10
	100-150	-1.40	-1.50	-0.10
	150-200	-0.84	-0.83	+0.01
	200-250	-0.50	-0.50	0.00
	250-300	-0.34	-0.27	+0.07
	300-350	-0.27	-0.28	-0.01
	350-400	-0.16	-0.11	+0.05
	400-450	-0.22	-0.41	-0.19
	450-500	-0.14	0.10	+0.04
1990–03	50–100	-0.68	-0.67	+0.01
	100-150	-1.36	-1.31	+0.05
	150-200	-0.86	-0.77	+0.09
	200-250	-0.55	-0.52	+0.03
	250-300	-0.44	-0.45	-0.01
	300-350	-0.38	0.29	+0.67
	350-400	-0.35	-0.29	+0.06
	400-450	-0.23	0.31	+0.54
	450-500	-0.32	0.25	+0.57
2003–05	50–100	-1.33	-1.65	-0.32
	100-150	-1.17	-1.03	+0.14
	150-200	-0.76	-0.86	-0.10
	200-250	-0.59	-0.62	-0.03
	250-300	-0.52	-0.45	+0.13
	300-350	-0.46	-0.23	+0.23
	350-400	-0.43	-0.50	-0.07
	400-450	-0.31	-0.29	+0.02
	450-500	-0.30	-0.07	+0.23

Table 7.4: Area-averaged and single-point geodetic mass change for 50 m elevations bands at Midtre Lovénbreen, between 1966 and 2005.

AB

Period	Elevation band (m a.s.l.)	Area-averaged mass change for band (m yr^{-1} w.e.)	Point mass change (m yr^{-1} w.e.)	Difference (m yr^{-1} w.e.)
1966–77	50–100	-0.95	-0.83	+0.12
	100-150	-1.33	-1.45	-0.12
	150-200	-1.05	-0.89	+0.16
	200-250	-0.74	-0.84	-0.10
	250-300	-0.49	-0.62	-0.13
	300-350	-0.32	-0.42	-0.10
	350-400	-0.28	-0.50	-0.22
	400-450	-0.34	-0.84	-0.50
	450-500	-0.05	0.22	+0.27
	500-550	0.03	0.72	+0.75
1977–90	50–100	-0.54	-0.85	-0.31
	100-150	-1.25	-1.48	-0.23
	150-200	-0.80	-0.75	+0.05
	200-250	-0.50	-0.66	-0.16
	250-300	-0.29	-0.16	+0.13
	300-350	-0.08	-0.36	-0.28
	350-400	0.05	0.44	+0.39
	400-450	0.07	0.19	+0.12
	450-500	0.05	0.09	+0.04
	500-550	-0.34	-0.79	-0.44
1990–05	50–100	-0.49	-	-
	100-150	-1.12	-1.23	-0.11
	150-200	-1.21	-1.14	+0.07
	200-250	-0.91	-0.83	+0.08
	250-300	-0.70	-0.75	-0.05
	300-350	-0.48	-0.47	+0.01
	350-400	-0.34	-0.40	-0.06
	400-450	-0.31	-0.32	-0.01
	450-500	-0.40	-0.34	+0.06
	500-550	-0.37	-0.29	+0.08

Table 7.5: Area-averaged and single-point geodetic mass change for 50 m elevations bands at Austre Brøggerbreen, between 1966 and 2005.

Similar trends were also observed at neighbouring Austre Broggerbreen (Table 7.5). Area-averaged mass changes at AB were predominantly negative, but with small positive changes at the highest elevation band between 1966–77 (500–550 m a.s.l., 0.03 m yr^{-1} w.e.), and between 350–500 m a.s.l. between 1977–90 (0.05, 0.07 and 0.05 m yr^{-1} w.e., respectively). The results showing these three elevation bands experiencing positive geodetic mass changes during this period appear to be in agreement with geodetic mass changes of the entire area of AB which showed a slight decrease (less negative) after the first measurement period (Table 6.10). Similar to ML, changes were generally more negative during the latest epoch (in this case, 1990–2005), and tended to be largest at the lower elevation bands (Table 7.5).

Comparison of area-averaged geodetic mass changes with those derived from a single point volume change measurement at the centre of each elevation band revealed a variety of differences. The average (signless) difference in geodetic mass change for all elevation bands at ML during 1966–77 was 0.21 m yr^{-1} w.e. This average comprised several epochs where the point geodetic mass change measurement was the same as the average of the elevation band (i.e. zero difference, at 150–200 and 350–400 m a.s.l.), up to a band with a difference of 0.66 m yr^{-1} w.e. (400-450 m a.s.l.). The same comparison for AB gave an average difference of 0.25 m yr^{-1} w.e. between 1966–77. The average differences for the remaining measurement periods at ML were 0.06, 0.23, and 0.14 m yr^{-1} w.e., for 1977–90, 1990-03 and 2003–05 respectively. At AB, average differences between area-averaged and point geodetic mass changes were 0.22 and 0.05 m yr^{-1} w.e. for the measurement periods 1977–90 and 1990–05. Large differences between individual point and area-averaged geodetic mass changes were particularly evident at higher elevations bands. At ML, examples included the 400–450 band during 1966–77, and the 300–350, 400–450 and 450–500 bands during 1990–03, where geodetic mass change differences were all greater than 0.50 m yr^{-1} w.e. Each of these examples had a positive geodetic mass change for the single point measurement, yet the average for the elevation band was negative. At AB, the largest geodetic mass change differences were 0.50 and 0.75 m yr^{-1} w.e. for the 400–450 and 500–550 m a.s.l. bands between 1966–77, and 0.39 m yr^{-1} w.e. for the 350–400 m a.s.l. band between 1977–90 (Table 7.5).

These measurements highlighted a potential problem of extracting a single point measurement to represent the geodetic mass change of an entire elevation band. Small regions of thinning or thickening may not necessarily be representative of a wider area, and may cause geodetic mass balance to be inaccurately measured. In the case of ML, the two highest elevation bands between 1966–77, the highest band between 1977–90 and the two highest bands between 1990–03 all had positive point mass changes, yet negative change as averaged over the entire elevation band area (Table 7.4). It is likely that drifting snow or local topographic factors such as slope, aspect or shading resulted in positive elevation changes. In these examples, positive elevation changes were measured at single points in the centre of each elevation band, yet the area-averaged mass change for each band was negative. Of the examples above at AB, point geodetic mass change 0.50 m yr^{-1} w.e. less than the area-average was measured at 400–450 m a.s.l. between 1966–77. At 500-550 m a.s.l. for the same period the point measurement was 0.75 m yr^{-1} greater than the the area-average for the band. Between 1977–90 at 350–400 m a.s.l. the point measurement was 0.39 m yr^{-1} greater than the area-average. In these examples measurements were taken from points with geodetic mass changes both lower and higher than the average of the elevation band. Differences of this magnitude mean that point measurements of geodetic mass change may significantly over or underestimate the true geodetic mass balance of the elevation band. Care should therefore be taken when interpreting glacier-wide mass change measurements derived from interpolating centreline balances from single point or profile measurements.

7.4.4 Drivers of Mass Change

In order to understand changes in the geodetic mass change of Midtre Lovénbreen and Austre Brøggerbreen, NW Svalbard, it was necessary to examine the climatological parameters that provide the dominant control on changes in glacier mass. Data collected by the Norwegian Meteorological Institute from the nearest meteorological station in the settlement of Ny Ålesund were available from 1967 to 2005. The available data were in the form of monthly mean temperatures and monthly mean summed precipitation. Data prior to 1973 were to be used with caution as their provenence was unknown, while data from 1974 onwards were collected in the same way from the same site, and are therefore deemed to be more trustworthy (J. Kohler, 2007, pers. comm.). Previously published work has identified a strong statistical relationship (R = 0.90) between both net mass balance and positive summer temperatures and winter precipitations at Austre Brøggerbreen (Lefauconnier and Hagen, 1990), and net mass balance and summer temperatures and winter precipitation (R = 0.83) at Midtre Lovénbreen (Lefauconnier *et al.*, 1999). Changes in geodetic mass balance over the period 1966–2005 at ML and AB were therefore placed in the context of changes in summer temperature and winter precipitation in the Ny Ålesund region for the period of meteorological data availability (1967–2005).

Geodetic mass change measurements at ML and AB coincided with a period of mean summer (June - August) temperature increase and no clear long-term trend in winter (October - May) precipitation in Ny Ålesund (Figure 7.7). Increasingly negative glacier geodetic mass change was consistent with the observed trends in summer temperature and winter precipitation. Mean summer temperatures have risen since around 1980 and are now higher than at any time since records began. This finding suggested that the driver for increased glacier thinning, volume change and increasingly negative mass balance was warmer average summer temperatures causing additional glacier melt. The record of annual winter

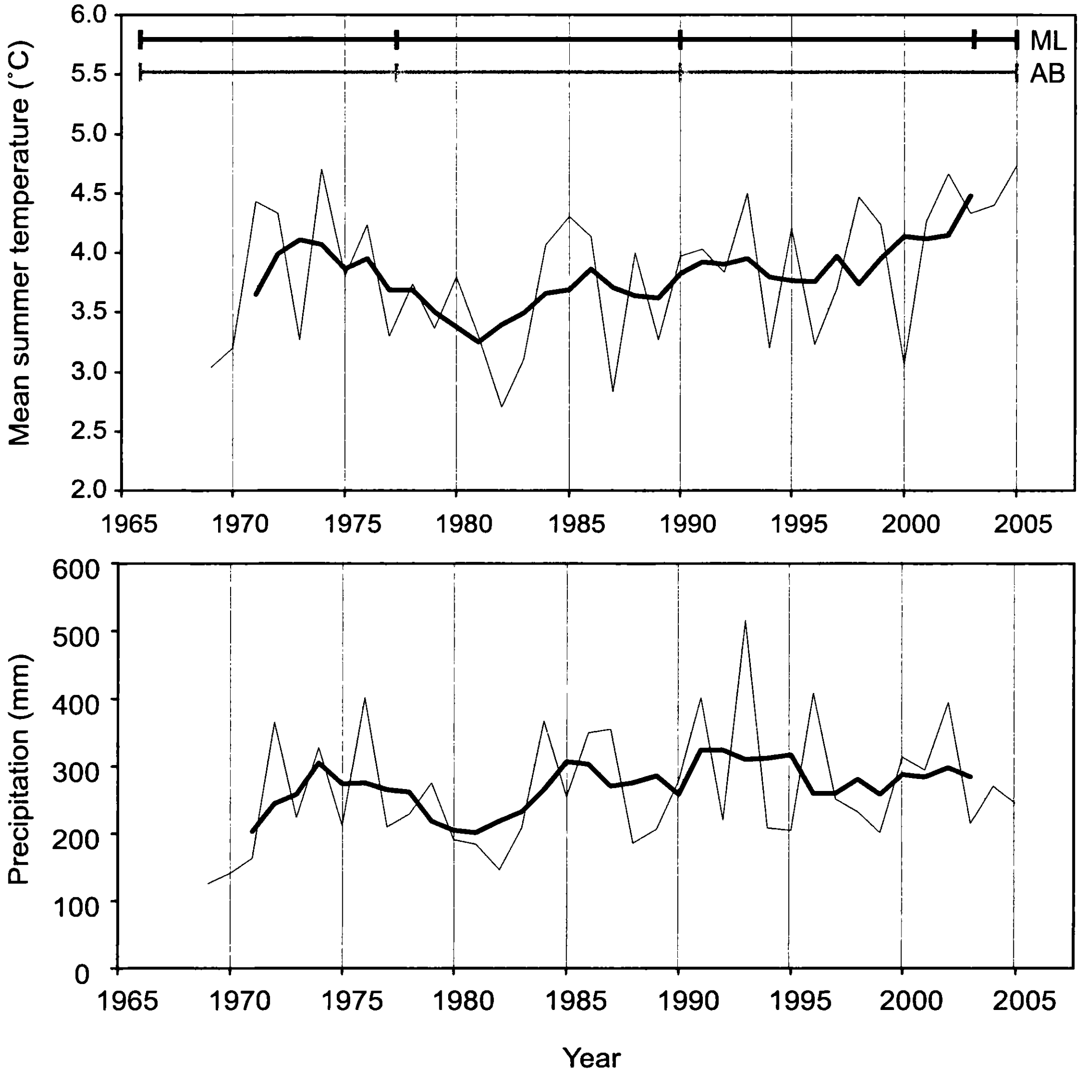

Figure 7.7: Mean summer (June - August) temperature (top) and summed winter (October - May) precipitation (below) with 5-year moving averages, from Ny Ålesund, NW Svalbard. Data from the Norwegian Meteorological Institute. Bars at the top show measurement periods for ML and AB.

precipitation showed no clear trend since records began in 1967. However, decreasing winter balance measurements at both ML and AB since 1990 (Figures 7.5 and 7.6) may suggest a decreasing trend in winter accumulation which may contribute to the increasing rate of mass loss at both glaciers.

The mean summer temperature record from Ny Ålesund may also help to explain the decrease in geodetic mass change (less negative rate) at Austre Brøggerbreen between 1977–1990 (Table 6.10). The reduction in geodetic mass change from -0.52 (± 0.18) m yr^{-1} w.e. (1966–77) to -0.36 (± 0.09) m yr^{-1} w.e. (1977–90) may be explained by a coincident reduction in summer temperatures between 1977 and 1982. Two years of close to zero mass balance in 1977 and 1982, and a year of positive net mass balance in 1987 (Figure 7.6) were likely to have been caused by decreasing summer temperatures between 1977–1982 and record low temperature summers in 1982 and 1987 (Figure 7.7).

7.4.5 Regional and Arctic Mass Balance

Due to a paucity of long-term glacier change measurements on Svalbard there were relatively few studies with which to compare results to. Between 1950 and 1988, Hagen and Liestøl (1990) investigated the long-term field-measured balances of five glaciers (including ML and AB) and estimated their average mass balance rate as -0.53 m yr^{-1} w.e. Dowdeswell *et al.* (1997) estimated the rate to be -0.55 m yr^{-1} w.e., averaged over three glaciers around the archipelago (see section 2.6.3). An analysis of estimated balance / altitude curves for 13 regions throughout Svalbard including a term for mass loss by iceberg calving, estimated the overall total net mass balance as -0.12 (± 0.03) m yr^{-1} w.e. (Hagen *et al.*, 2003). The present day rate of mass balance at ML calculated in chapter 6 (-0.47 (± 0.08) m yr^{-1} w.e.) was similar to the rates calculated by Hagen and Liestøl (1990) and Dowdeswell *et al.* (1997), within specified error bounds, yet larger than the estimate of Hagen *et al.* (2003). The rate at AB (-0.65 (± 0.05) m yr^{-1} w.e.) was more negative than any other previously published estimate. Combining the mass change rates from ML and AB into an average value for the most recent epoch (2003–05), resulted in a value of -0.56 (± 0.07) m yr^{-1} w.e.; slightly larger than those previously reported by Hagen and Liestøl (1990) and Dowdeswell *et al.* (1997), yet similar within the specified error limits.

None of the three previously mentioned long-term studies detected any changes in the rate of mass balance. The results of this work suggested that the rate of geodetic mass change at ML has become increasingly negative since 1966, and the rate at AB increasingly negative since 1990. The only work to previously report this increasing negative mass change was Kohler *et al.* (2007). The results derived using lidar-controlled photogrammetric DEMs were shown to be similar to those derived by Kohler *et al.* (2007) at ML using a range of geodetic data sources (Figure 7.4). Kohler *et al.* (2007) also identified an increasing rate of thinning at a previously measured profile in Wedel Jarls Land, and a similar increase in thinning rate (and hence, mass balance) at Slakbreen, in central Spitsbergen. Comparison of geodetic mass changes derived in this work with those expected of present day ice-melting on Svalbard derived from surface deformation measurements revealed some discrepancy. The average present day (2003–05) geodetic mass change between ML and AB was -0.56 (± 0.07) m yr^{-1} w.e., while Sato *et al.* (2006) suggested that an equivalent balance of at least -0.75 m yr^{-1} w.e. was necessary to explain contemporary uplift rates. It should be noted however, that ML and AB are both small, low elevation glaciers in the same part of NW Svalbard, presumably experiencing the same or very similar climatic conditions (section 7.4.4). Kohler *et al.* (2007) reported greater rates of present-day ice melting at Slakbreen further to the south, and suggested that archipelago-wide mass balance signal may be more negative than that reported at ML.

One of the defining characteristics of Arctic glacier mass balance during recent years has been thinning and negative mass balance of low-lying glaciers and ice-sheets, and some localised thickening of higher elevation glaciers and ice-sheet interiors (e.g. Krabill *et al.*, 2000a; Abdalati *et al.*, 2004; Johannessen *et al.*, 2005; Zwally *et al.*, 2006). Although neither ML and AB exist at particularly high elevations, their high latitude location is thought to be particularly sensitive to changes in climate (ACIA, 2005). The results of this work showed that small regions of positive geodetic mass change occurred at higher elevations of AB, coincident with a particularly cold period in the late 1970s to early 1980s. Since 1990, in response to continued increases in mean summer temperatures, ML and AB thinned at an increasing rate, at all elevations. These results suggest that the rate of negative geodetic glacier mass balance on Svalbard will continue to rise in response to projected increases in average summer temperatures.

7.4.6 Mass Change Summary

Discussion of results derived from differencing lidar-controlled photogrammetric DEMs revealed that this technique provided a valuable method for monitoring changes in glacier volume. Comparison of these results with those from previously published geodetic studies showed that DEM surfaces of variable quality (such as those derived by Rippin *et al.* (2003) and Pope *et al.* (2007)) may have overestimated mass loss by between 2–4 times. Within the range of errors, geodetic mass changes derived in this work compared well to results derived from differencing a range of geodetic sources including contour maps, thus confirming the findings of Kohler *et al.* (2007) that geodetic mass change has become increasingly negative at Midtre Lovénbreen over the past 40 years. Although negative balances at Austre Brøggerbreen have not increased at a uniform rate, the present period had the most negative geodetic mass change of any period at either glacier. Comparison between geodetic and field-measured balances revealed that two of the periods at ML were similar (within errors) and two were significantly different, with the geodetic approach resulting in mass changes less negative than those derived from field-measurements (between 1966–77 and 2003–05). At AB, geodetic and field-measured balances were the same or very similar (within errors) for all three periods. The hypothesis suggested by previous authors that field-measurements may underestimate the true mass balance (Etzelmüller *et al.*, 1993; Hagen *et al.*, 2000; Rippin *et al.*, 2003) was not supported by the results of this work. A comparison of area-averaged geodetic mass changes for individual elevation bands with single point geodetic changes at the centre of each band showed that differences of more than 0.50 m yr^{-1} w.e. were possible. This finding highlighted the importance of glacier-wide averaged measurements of volume change (and hence, mass change) and may explain some of the differences between changes derived from geodetic (area-averaged) and field (collected from a single point) measurements. Examination of metereological data from Ny Ålesund suggested that increasingly negative glacier mass change was associated with increasing mean summer air temperatures, and possibly with reduction in winter precipitation since 1990. The average present-day geodetic mass change of these two glaciers was shown to be similar to values derived for the entire mass balance of Svalbard from selected field mass balance records. However, the increasingly negative rate of mass change identified at these glaciers suggests that NW Svalbard glacier mass balance will continue to become even more negative in response to further Arctic atmospheric warming.

7.5 Chapter Summary

Improving the quality of glacier elevation change measurements derived from photogrammetric processing is essential if these data are to be integrated into studies of regional contributions to sea-level rise. This chapter has discussed the extent to which DEMs collected from photogrammetric models controlled using lidar-derived GCPs were comparable to the elevation quality of other photogrammetric glacier studies. Although like-for-like comparisons were difficult due to different photographic epochs, flying heights and scanning resolutions, lidar-derived GCPs can produce DEMs of similar levels of accuracy to those derived from field-measured control points. The results of this work showed that elevation errors from lidar-controlled photogrammetric models were smaller than those from contour maps and that large numbers of GCPs avoided the systematic errors that are common to poorly-controlled glacier photogrammetry. Examination of geodetic mass changes calculated from differencing these improved DEMs showed that geodetic results were similar to field measurements yet identified an increasingly negative mass change trend, geodetic point changes did not necessarily represent the true change of a particular elevation band, and that the predominant driver of this trend was increases in mean summer air temperatures in the Ny Ålesund region.

Chapter 8

Summary and Conclusions

8.1 Summary

The main aim of this research was to make an assessment of the quality (vertical elevation accuracy) of swath-based airborne lidar data collected over a High Arctic small valley-glacier in order to utilise the point cloud data as ground control for photogrammetric DEMs and to use this technique to measure glacier volume changes and geodetic mass change over the past 40 years. The use of external spatial datasets for deriving photogrammetric GCPs is an existing technique and in some cases is included in the capability of specialised software tools (e.g. PCI Geomatica). However, development and application of new approaches in remote-sensing and particularly continued integration of existing sensor information and data sources are useful in order to maximise the utility of current datasets and to extend measurements of glacier volume change into regions where no historical data exists. If accurate sea-level rise calculations are to be made from the melt contribution of small glaciers and ice-sheets then approaches must be devised and new datasets generated for extending mass change records. Similarly, non-linear dynamic behaviour of glaciers may complicate any climate signal extracted from short-term balance measurements. To avoid this, existing records of change must be improved and extended retrospectively. Metric stereo-photographs held in archive offer a vast resource for potentially measuring accurate and precise changes in glacier mass. The work presented in this thesis offered a technique to exploit this resource using high-quality, high-spatial resolution contemporary airborne lidar data.

The precision and accuracy of airborne lidar data collected over a high Arctic summer ice surface were investigated using relative and absolute measures. A computationally efficient differencing method was used to investigate the distribution and magnitude of errors from repeat lidar measurements of the same terrain (within overlaps), at high spatial resolution

(1 m pixel spacing), directly comparing more than 10 million coincident pixels. Elevation precision was also investigated over different surface types and over different slope angles. Lidar elevation accuracy was assessed by comparing elevations with a large dataset of independent check data over the glacier surface and forefield. These results were used to select the areas providing the highest quality lidar elevation points which were then identified in aerial photographs and extracted as three-dimensional ground control points (GCPs).

Once GCPs had been selected a variety of experiments were undertaken to optimise the control of photogrammetric models using large numbers of lidar-derived GCPs. Photogrammetric models were setup, optimised and DEMs collected from them without the need to measure a single GCP in the field. It should be noted here that it is possible to aerotriangulate contemporary aerial photographs if time-coincident GPS and INS data are available. Previous studies on Svalbard and elsewhere have shown that poor quantity and particularly poor distribution of GCPs were likely to result in inaccurate DEM surfaces. This was especially a problem in glacial and glaciated areas where issues of safe access and logistics meant that large areas around many glaciers were inaccessible by foot. The ability to measure ground control at points surrounding the glacier is essential to producing well-controlled and therefore accurate surface models. Results showed that utilising very large numbers of control points allowed DEMs to be collected with similar or better vertical accuracy than those produced from smaller numbers of better quality GCPs.

This method was applied to two glaciers in NW Svalbard, Midtre Lovénbreen and Austre Brøggerbreen, which are unique among Arctic glaciers for having long and complete annual field-measured mass balance records. These two glaciers therefore offered an excellent opportunity to compare the results of this new approach with known and trusted validation data. DEM quality and glacier elevation changes, volume changes and changes in geodetic mass change were compared to previous studies using photogrammetry in glacial environments, previous estimates of long-term mass balance, field-measured mass balance and previous efforts to derived geodetic mass balance at both glaciers. Results showed that models and measurements generated using this technique compared well to previously published estimates. Long-term mass changes over the last 40 years at these two glaciers were correlated with annual meteorological data and shown to be coincident with increases in summer air temperatures. Providing airborne lidar data are available and the coverage of the data is such that known non-moving terrain can be identified in aerial photographs, these results showed that accurate and precise measurements can be made from historical aerial imagery controlled with raw lidar elevation points.

8.2 Conclusions

The findings of this work may be described in terms of the following key questions:

1. What were the precision and accuracy of lidar elevation data over a High Arctic glacier surface and surrounds, and how did they vary?

- The precision of lidar elevation data was measured by differencing overlapping datapoints in adjacent flightlines, and resulted in a mean difference of 0.02 m (standard deviation 0.71 m) from more than 10 million individual pixel comparisons.
- Precision varied within the lidar swath footprint, with residuals of $\sim \pm 0.10$ m towards the centre of the swath and $\sim \pm 0.40$ m towards swath edges, perpendicular to direction of flight. Residuals were larger over mountainous and steep-sloping terrain (standard deviation of elevation residuals rose consecutively for progressively steeper slope classes), and a small number of large residuals, attributable to crevassing and heavily incised meltwater channels, were present on the glacier surface.
- Accuracy was estimated by comparing lidar elevations with GPS check data points. Comparison of all survey points from all days resulted in a RMS error of ±0.17 m. Plotting residuals by survey day revealed that some of this variability was due to surface melt on the glacier during the course of check data surveying. Residuals collected closest to airborne surveying (2 days either side) had a RMS error of ±0.14 m.
- Plotting GPS elevation residuals within lidar swath boundaries showed that the effects of scan angle geometry on elevation precision were not evident in the elevation accuracy results.

2. How successful were lidar point cloud-derived GCPs for controlling photogrammetric glacier surface models?

- The coverage and spatial resolution of lidar datasets allowed the identification and extraction of large numbers of GCPs. Models at ML and AB were controlled with up to 50 GCPs, well-distributed around the glacier and throughout the stereo overlaps of archive photography. Photogrammetric bundle adjustment parameter results were consistently improved with the addition of GCPs and resultant DEM accuracy improved for models controlled with larger numbers of control points. Although models controlled with 'sub-optimally' chosen GCPs from the edges of lidar data swaths were of poorer elevation accuracy, DEMs collected from models controlled with 35–40

GCPs or more had fewer systematic errors, and with RMS errors between ±0.22–0.32, approached the quality of lidar DEM surfaces.

- An important implication of this improvement in DEM quality was that measurements of glacier volume change over a two year period using models controlled with larger numbers of GCPs were within $\sim 4\%$ of a 'benchmark' measurement of volume change from lidar-to-lidar DEM differencing. Photogrammetric volume change measurements of an equivalent quality to those from lidar differencing were therefore achievable providing GCPs were well-chosen (i.e. within swath centres and well distributed in the photos), and at least 20–25 points could be measured. Poorly chosen or too few GCPs resulted in DEMs with large errors, which then over-estimated glacier volume change by as much as 50%.

3. How did the application of this technique improve photogrammetric glacier surface models derived from archival aerial photography sources?

- In the absence of check data, the elevation accuracy of historical models was estimated by comparing non-glacier, low-slope land differences (the forefield) between each photo model and a DEM derived from the lidar data used to supply GCPs. In all cases, RMS elevation errors were less than ~1 m (ranging from 0.32–1.02 m). Like-for-like comparisons were difficult but lidar-derived GCPs can produce DEMs of a similar accuracy to those processed from standard field-surveyed control points.
- Two previous studies using poorly controlled models with few GCPs were shown to overestimate glacier elevation changes by 2–4 times.
- Models controlled with large numbers of GCPs, especially at the highest elevations, allowed derivation of elevation data for the majority of the glacier surface with no apparent reduction in accuracy at higher ice surface elevations.

4. What were the changes in volume and extent of Midtre Lovénbreen and Austre Brøggerbreen during the last 40 years?

- ML and AB retreated from their ice front positions in 1966 by respectively 524.43 m (or, 13.45 m yr^{-1}) and 926.20 m (or, 23.75 m yr^{-1}), to their current (2005) positions, with rates of retreat between periods coincident with their geodetic mass balance.
- ML lost a total of 7.12 (± 1.00) × 10^7 m^3 of ice between 1966 and 2005, while AB lost 23.56 (± 1.25) × 10^7 m^3 for the same time period.
- Both ML and AB showed increasingly negative rates of mean area-averaged volume change between consecutive epochs. ML thinned at an increasing rate since 1966

with its 2003–2005 rate almost twice that of 1966–77. AB, despite gaining some mass at higher elevations between 1977–1990 (although with an overall negative balance signal), is now losing volume at a rate of -0.72 (± 0.05) m yr^{-1}, a higher rate than at any time in its 39 year record.

5. What geodetic mass change trends were evident for ML and AB and how did they compare to field-measurements and instrumental meteorological parameters?

- The annual rate of geodetic mass change at ML increased (became more negative) for each consecutive epoch. At AB, the rate of geodetic mass change fell slightly between 1977–90, but increased again between 1990–05. At ML, geodetic mass changes at the middle two periods (1977–2003) were the same as field balances, within errors. The first (1966–77) and last (2003–05) periods were less than field-measured balances. Geodetic changes were the same or very similar as field-balances for all years at AB. These results did not support the hypothesis that field measurements may underestimate the true mass balance.
- The drivers for increased glacier thinning and negative geodetic glacier mass change were warmer mean summer air temperatures causing additional glacier melt, possibly combined with a decreasing trend in winter accumulation. The period of less negative balance at AB (1977–90) was explained by a reduction in summer air temperatures during those years including two record cold summers in 1982 and 1987, although the same effect was not seen at ML.

6. How did NW Svalbard geodetic mass changes compare to other work at the same glaciers and to estimates of archipelago-wide balance trends?

- The trend of increasingly negative geodetic mass change at ML confirmed the findings of a previous study that used data from a range of geodetic sources. Increasingly negative mass change at AB since 1990 was identified for the first time.
- An average present day geodetic mass change rate of -0.56 (± 0.07) m yr^{-1} w.e. at ML and AB was slightly larger than 2 previous estimates based on averaged field-balance measurements, and significantly larger than an analysis of estimated balance / altitude curves for all of Svalbard. However, this value was based on a sample of just two glaciers in NW Svalbard and is therefore not representative of an archipelago-wide trend.
- The average rate of present day geodetic mass change was less than the value necessary to explain contemporary crustal uplift rates, suggesting that more negative balances are likely at other glaciers on Svalbard.

8.3 Suggestions for Further Work

A number of further research priorities have been identified and are summarised in this section. This research showed that lidar data can be successfully applied as ground control for historical photogrammetry of glaciers. Two examples in NW Svalbard demonstrated that the technique can provide high-quality historical models, volume change measurements within ~4% of a lidar-lidar comparison, and long-term geodetic mass balance measurements that are similar to field-measured balances within the range of errors. Given the results of this work, greater confidence may be placed in the results of well-controlled photogrammetric geodetic glacier mass balance studies. Given the variation between the results of this work and those of some previously published (photogrammetric) geodetic mass balance studies, it would be useful to work towards a standard approach for the estimation of errors in geodetic mass balances from photogrammetric data. Examination of the literature showed that numbers of GCPs, their spatial distribution, elevation quality and block adjustment parameter results were rarely detailed. In addition, few studies provided comprehensive error assessment statistics. In these circumstances it was difficult to precisely ascertain the quality of DEM surfaces, and from there the accuracy and precision of glacier volume change and geodetic mass balance results. Research activity in this direction will encourage the integration of photogrammetric measurements into global estimates of small glacier and ice-sheet mass balance. This in turn will allow better estimates of the contribution of these ice masses to sea-level rise.

The most logical next step is to use this method to derive geodetic measurements for glaciers elsewhere on Svalbard. Given that just a few glaciers have long-term field-measurements, this technique can be applied to remote glaciers around the archipelago to generate a clearer picture of regional mass balance. This is necessary in order to accurately measure the contribution of Svalbard ice masses to sea-level rise over the past 50 years and to model future contributions in a changing climate. Efforts are underway to apply these techniques to historical photographs of 8 glaciers distributed around the archipelago as part of the NERC-funded SLICES project (Sea-Level from ICE on Svalbard, PI: Murray).

Similarly, opportunities for application of the technique to other regions of the cryosphere hold great potential. Areas such as the margins of the Greenland ice-sheet, the Antarctic Peninsula, and small glaciers and ice-sheets in the Canadian High Arctic have extensive metric aerial photography archives, often stretching as far back as the 1950s. Utilisation of the methods presented in this work with such archived survey and reconnaisance photography offers the potential to reconstruct glacier mass changes for regions with little or no mass balance data, and to extend existing records of mass change beyond the era of satellite altimetry-based measurements. Similar techniques may be used to generate improved area-wide elevation change measurements using data from satellite sensors with along- (e.g.

ASTER) or across- (e.g. SPOT) track stereo capability.

While the methods presented here have been shown to be a powerful tool for exploiting historical image archives, a major limitation of their further use in studies throughout the Earth's glaciated regions is the availability of airborne lidar data. Laser scanning instruments can be prohibitively expensive and the total costs of hardware, scanner implementation, airborne operations and data processing have slowed uptake of the technology. A promising line of research involves the integration of other altimetry data with aerial imagery. A pilot study by Schenk *et al.* (2005) showed that it was possible to adjust a photogrammetric block to control points derived from satellite laser altimetry tracks acquired by the Geosciences Laser Altimeter System (GLAS) aboard NASA's Ice, Cloud and Land Elevation satellite (ICESat). The freely available, global repeat track coverage of these data may permit accurate control solutions without the need for either field-survey or airborne data acquisition. Dependent on the quality and distribution of photographs, the spatial resolution of satellite altimetry data will allow elevation coverage of greater areas, potentially making this technique applicable to larger glaciers and the fast-flowing outlets of large ice-sheets.

References

Abdalati, W. and W. Krabill, 1999a. Application of aircraft laser altimetry to glacier and ice cap mass balance studies, *International Archives of Photogrammetry and Remote Sensing*, **32**(3), 161–166.

Abdalati, W. and W. Krabill, 1999b. Calculation of ice velocities in the Jakobshavns Isbræ area using airborne laser altimetry, *Remote Sensing of Environment*, **67**, 194–204.

Abdalati, W., W. Krabill, E. Frederick, S. Manizade, C. Martin, J. Sonntag, R. Swift, R. Thomas, J. Yungel and R. Koerner, 2004. Elevation changes of ice caps in the Canadian Arctic Archipelago, *Journal of Geophysical Research*, **109**, doi:10.1029/2003JF000045.

ACIA, 2005. Arctic Climate Impact Assessment, Cambridge University Press, New York.

Ackermann, F., 1978. Experimental investigation into the accuracy of contouring from DTM, *Photogrammetric Engineering and Remote Sensing*, **44**(12), 1537–1548.

Ackermann, F., 1999. Airborne laser scanning- present status and future expectations, *ISPRS Journal of Photogrammetry and Remote Sensing*, **54**, 64–67.

Adalgeirsdóttir, G., K.A. Echelmeyer and W.D. Harrison, 1998. Elevation and volume changes on the Harding Icefield, Alaska, *Journal of Glaciology*, **44**(148), 570–582.

Adams, J.C. and J.H. Chandler, 2002. Evaluation of lidar and medium scale photogrammetry for detecting soft-cliff coastal change, *Photogrammetric Record*, **17**(99), 405–418.

Albertz, J. and J. Kreiling, 1975. Photogrammetric Guide, Herbert Vichmann Verlag, Karlsruhe.

Andreassen, L.M., 1999. Comparing traditional mass balance measurements with long-term volume change extracted from topographic maps: A case study of Storbreen glacier in Jotunheimen, Norway, for the period 1940-1977, *Geografiska Annaler*, **81**(A(4)), 467–476.

Arendt, A.A., K.A. Echelmeyer, W.D. Harrison, C.S. Lingle and V.B. Valentine, 2002. Rapid wastage of Alaska glaciers and their contribution to rising sea level, *Science*, **297**, 382–386.

Arnold, N.S., W.G. Rees, B.J. Deveraux and G.S. Amable, 2006a. Evaluating the potential of high-resolution airborne LIDAR data in glaciology, *Interational Journal of Remote Sensing*, **27**(5–6), 1233–1251.

Arnold, N.S., W.G. Rees, A.J. Hodson and J. Kohler, 2006b. Topographic controls on the surface energy balance of a high Arctic valley glacier, *Journal of Geophysical Research*, **111**, F02011, doi:10.1029/2005JF000426.

Arthern, R.J., D.P. Winebrenner and D.G. Vaughan, 2006. Antarctic snow accumulation mapped using polarization of 4.3-cm wavelength microwave emission, *Journal of Geophysical Research*, **111**, D06107, doi:10.1029/2004JD005667.

ASPRS, 2003. Manual of Photogrammetry, 5th Edition, John Wiley and Sons, London.

Atkinson, P.M., 1999. Geographical information science: geostatistics and uncertainty, *Progress in Physical Geography*, **23**(1), 134–142.

Bahr, D.B., M.F. Meier and S.D. Peckham, 1997. The physical basis of glacier volume-area scaling, *Journal of Geophysical Research*, **102**(20), 355–362.

Ballantyne, C.K., 2002. Paraglacial geomorphology, *Quaternary Science Reviews*, **21**, 18–19.

Baltsavias, E.P, 1999a. Airborne laser scanning: basic relations and formulas, *ISPRS Journal of Photogrammetry and Remote Sensing*, **54**, 199–244.

Baltsavias, E.P., 1999b. Airborne laser scanning: existing systems and firms and other resources, *ISPRS Journal of Photogrammetry and Remote Sensing*, **54**, 164–198.

Baltsavias, E.P, 1999c. A comparison between photogrammetry and laser scanning, *ISPRS Journal of Photogrammetry and Remote Sensing*, **54**, 83–94.

Baltsavias, E.P., 1999d. On the performance of photogrammetric scanners, Photogrammetric Week '99', Wichmann Verlag, Heidelberg, 155–173.

Baltsavias, E.P., E. Favey, A. Bauder, H. Bosch and M. Pateraki, 2001. Digital surface modelling by airborne laser scanning and digital photogrammetry for glacier modelling, *Photogrammetric Record*, **17**(98), 243–273.

Bamber, J.L., W.B. Krabill, V. Raper and J. Dowdeswell, 2004. Anomalous recent growth of part of a large Arctic ice cap: Austfonna, Svalbard, *Geophysical Research Letters*, **31**(12), L12402.

Bamber, J.L., W.B. Krabill, V. Raper, J.A. Dowdeswell and J. Oerlemans, 2005. Elevation changes measured on Svalbard glaciers and ice caps from airborne laser data, *Annals of Glaciology*, **42**, 202–208.

Barbarella, M. and C. Gordini, 2006. Kinematic GPS survey as validation of LIDAR strips accuracy, *Annals of Geophysics*, **49**(1), 21–33.

Behan, A., 2000. On the matching accuracy of rasterized scanning laser altimeter data, *International Archives of Photogrammetry and Remote Sensing*, **33**(B2), 75–82.

Bennett, M.R., D. Huddart, M.J. Hambrey and J.F. Ghienne, 1996. Moraine development at the High-Arctic valley glacier Pedersenbreen, Svalbard, *Geografiska Annaler. Series A, Physical Geography*, **78**(4), 209–222.

Berthier, E., Y. Arnaud, D. Baratoux, C. Vincent and F. Rémy, 2004. Recent rapid thinning of the "Mer de Glace" glacier derived from satellite optical images, *Geophysical Research Letters*, **31**, L17401, doi:10.1029/2004GL020706.

Berthier, E., Y. Arnaud, C. Vincent and F. Rémy, 2006. Biases of SRTM in high-mountain areas: Implications for the monitoring of glacier volume changes, *Geophysical Research Letters*, **33**, L08502, doi:10.1029/2006GL025862.

Bevan, S.L., 2006. The spatial distribution of mass balance on Austfonna in Svalbard determined using satellite radar interferometry, (Ph.D. thesis, University of Wales Swansea).

Bevan, S.L., A.J. Luckman, T. Murray, H. Sykes and J. Kohler, 2007. Positive mass balance during the late 20th century on Austfonna, Svalbard, revealed using satellite radar interferometry, *Annals of Glaciology*, **46**, 117–122.

Birdseye, C.H., 1940. Stereoscopic Photogrammetric Mapping, *Annals of the Association of American Geographers*, **1**, 1–24.

Björnsson, H., Y. Gjessing, S-E. Hamran, J.O. Hagen, O. Liestøl, F. Pálsson and B. Erlingsson, 1996. The thermal regime of sub-polar glaciers mapped by multi-frequency radio-echo sounding, *Journal of Glaciology*, **42**(140), 23–32.

Blankenship, D.D., S.D. Kempf, D.L. Morse, M.E. Peters, R.E. Bell and R.B. Arko, 1999. Airborne laser altimetry over the central West Antarctic ice sheet, *International Archives of Photogrammetry and Remote Sensing*, **32**(3), 167.

Blankenship, D.D., D.L. Morse, C.A. Finn, R.E. Bell, M.E. Peters, S.D. Kempf, S.M. Hodge, M. Studinger, J.C. Behrendt and J.M. Brozena, 2001. Geological controls on the initiation of rapid basal motion for West Antarctic ice streams; a geophysical perspective including new airborne radar sounding and laser altimetry results, Alley, R.B. and R.A. Bindschadler, eds., The West Antarctic ice sheet: behaviour and environment, American Geophysical Union, Washington, DC, Antarctic Research Series 77, 105–121.

Box, J.E., D.H. Bromwich, B.A. Veenhuis, L-S. Bai amd J.C. Stroeve, J.C. Rogers, K. Steffen, T. Haran and S-H. Wang, 2006. Greenland ice sheet surface mass balance variability (1988 to 2004) from calibrated polar MM5 output, *Journal of Climate*, **19**(12), 2783–2800.

Braithwaite, R.J., 2002. Glacier mass balance: the first 50 years of international monitoring, *Progress in Physical Geography*, **26**(1), 76–95.

Braithwaite, R.J., Y. Zhang and S.C.B. Raper, 2002. Temperature sensitivity of the mass balance of mountain glaciers and ice caps as a climatological characteristic, *Zeitschrift fur Gletscherkunde und Glazialgeologie*, **38**, 35–61.

Brasington, J., B.T. Rumsby and R.A. McVey, 2000. Monitoring and modelling morphological change in a braided gravel-bed river using high-resolution GPS-based survey, *Earth Surface Processes and Landforms*, **25**, 973–990.

Brecher, H.H., 1986. Surface velocity determination on large polar glaciers by aerial photogrammetry, *Annals of Glaciology*, **8**, 22–26.

Brecher, H.H. and L.G. Thompson, 1993. Measurement of the retreat of Qori Kalis glacier in the tropical Andes of Peru by terrestrial photogrammetry, *Photogrammetric Engineering and Remote-Sensing*, **59**(6), 1017–1022.

Brock, B.W., I.C. Willis and M.J. Sharp, 2000. Measurement and parameterization of albedo variations at Haut Glacier d'Arolla, Switzerland, *Journal of Glaciology*, **46**(155), 675–688.

Brown, D.G. and A.F. Arbogast, 1999. Digital photogrammetric change analysis as applied to active coastal dunes in Michigan, *Photogrammetric Engineering and Remote-Sensing*, **65**(4), 467–474.

Burman, H., 2000. Adjustment of laser scanner data for correction of orientation errors, *International Archives of Photogrammetry and Remote Sensing*, **33**(B3), 125–132.

Burman, H., 2002. Laser strip adjustment for data calibration and verification, *International Archives of Photogrammetry and Remote Sensing*, **34**(A3), 67–72.

Burrough, P.A. and R.A. McDonnell, 2000. Principles of Geographical Information Systems, Oxford University Press, Oxford.

Butler, J.B., S.N. Lane and J.H. Chandler, 1998. Assessment of DEM quality characterising surface roughness using close range digital photogrammetry, *Photogrammetric Record*, **19**(92), 271–291.

Chandler, J.H., 1999. Effective application of automated digital photogrammetry for geomorphological research, *Earth Surface Processes and Landforms*, **24**, 51–63.

Chandler, J.H. and R. Moore, 1989. Analytical photogrammetry: a method for monitoring slope instability, *Quarterly Journal of Engineering Geology*, **22**, 97–110.

Chandler, J.H. and C.J. Padfield, 1989. Automated digital photogrammetry on a shoestring, *Photogrammetric Record*, **12**(71), 637–663.

Chandler, J.H., K. Shiono, P. Rameshwarden and S.N. Lane, 2002. Meauring flume surfaces for hydraulics research using a Kodak DCS460, *Photogrammetric Record*, **17**(9), 39–61.

Charlton, M.E, A.R.G Large and I.C Fuller, 2003. Application of airborne lidar in river environments: the River Coquet, Northumberland, UK, *Earth Surface Processes and Landforms*, **28**, 299–306.

Chasmer, L. and C. Hopkinson, 2001. Using airborne laser altimetry and GIS to assess scale-induced radiation loading errors in a glaciarised basin, *Proc. 58th Eastern Snow Conf.*, 195–205.

Chen, J. L., C.R. Wilson and B.D. Tapley, 2006. Satellite gravity measurements confirm accelerated melting of Greenland ice sheet, *Science*, **313**(5795), 1958–1960.

Christensen, E.L., N. Reeh, R. Forsberg, J.H. Jørgensen, N. Skou and K. Woelders, 2000. A low-cost glacier-mapping system, *Journal of Glaciology*, **46**(154), 531–537.

Church, J.A., J.M. Gregory, P. Huybrechts, M. Kuhn, K. Lambeck, M.T. Nhuan, D. Qin and P.L. Woodworth, 2001. Changes in Sea-Level, Houghton, J.T. and D. Yihui, eds., IPCC Third Scientific Assessment of Climate Change, Cambridge University Press, New York, 640–693.

Clark, M.L., D.B. Clark and D.A. Roberts, 2004. Small-footprint lidar estimation of sub-canopy elevation and tree height in a tropical rainforest landscape, *Remote Sensing of Environment*, **91**(1), 68–89.

Cobby, D.M, 2002. The Use of Airborne Scanning Laser Altimetry for Improved River Flood Protection, (Ph.D. thesis, University of Reading).

Cobby, D.M, D.C Mason and I.J Davenport, 2001. Image processing of airborne scanning laser altimetry data for improved river flood modelling, *ISPRS Journal of Photogrammetry and Remote Sensing*, **56**, 121–138.

Cobby, D.M, D.C Mason, M.S Horritt and P.D Bates, 2003. Two-dimensional hydraulic flood modelling using a finite-element mesh decomposed according to vegetation and topographic features derived from airborne scanning laser altimetry, *Hydrological Processes*, **17**(10), 1979–2000.

Cocard, M., A. Geiger, H-G. Kahle, Y. Peter and P. Milas, 1997. Regional sea surface determination by using airborne laser techniques, Annales Geophysicae, vol. 5(1) of *XXII General Assembly of EGS*, 191.

Cogley, J.G., 1999. Effective sample size for glacier mass balance, *Geografiska Annaler*, **81A**(4), 497–507.

Cogley, J.G., 2005. Mass and energy balances of glaciers and ice sheets, Anderson, M.G., ed., Encyclopedia of Hydrological Sciences, vol. 4, John Wiley, Hoboken, New Jersey, 2555–2573.

Cook, A.J., A.J. Fox, D.G. Vaughan and J. Ferrigno, 2005. Retreating glacier fronts on the Antarctic Peninsula over the past half-century, *Science*, **308**(5721), 541–544.

Cooper, M.A.R., 1998. Datums, coordinates and differences, Lane, S.N., K.S. Richards and J.A. Chandler, eds., Landform Monitoring, Modelling and Analysis, Wiley, Chichester, 21–35.

Cooper, M.A.R. and P.A. Cross, 1988. Statistical concepts and their application in photogrammetry and surveying, *Photogrammetric Record*, **12**(71), 637–663.

Cox, L.H. and R.S. March, 2004. Comparison of geodetic and glaciological mass-balance technique, Gulkana Glacier, Alaska, U.S.A, *Journal of Glaciology*, **50**(170), 363–370.

Crombaghs, M.J.E., R. Brügelmann and E.J. de Min, 2000. On the adjustment of overlapping strips of laser altimeter height data, *International Archives of Photogrammetry and Remote Sensing*, **33**(B3), 230–237.

Csathó, B., T. Schenk, R. Thomas and W. Krabill, 1996. Remote sensing of polar regions using laser altimetry, *International Archives of Photogrammetry and Remote Sensing*, **31**(B1), 42–47.

Cubasch, U., G.A. Meehl, G.J. Boer, R.J. Stouffer, M. Dix, A. Noda, C.A. Senior, S. Raper and K.S. Yap, 2001. Projections of Future Climate Change, Houghton, J.T. and D. Yihui, eds., IPCC Third Scientific Assessment of Climate Change, Cambridge University Press, New York, 525–582.

Daniels, R.C., 2001. Datum conversion issues with spot elevation data, *Photogrametric Engineering and Remote Sensing*, **67**, 735–740.

Davenport, I.J, R.B Bradbury, G.Q.A Anderson, G.R.F Hayman, J.R Krebs, D.C Mason, J.D Wilson and N.J Veck, 2000. Improving bird population models using airborne remote sensing, *International Journal of Remote Sensing*, **21**(13–14), 2705–2717.

Davis, C.H., Y. Li, J.R. McConnell, M.M. Frey and E. Hanna, 2005. Snowfall-driven growth in East Antarctic ice sheet mitigates recent sea-level rise, *Science*, **308**(5730), 1898–1901.

Derose, R.C., B. Gomez, M. Marden and N.A. Trustrum, 1998. Gully erosion in Mangutu Forest, New Zealand, estimated from digital elevation models, *Earth Surface Processes and Landforms*, **23**, 1045–1053.

Desmet, P.J.J., 1997. Effects of interpolation errors on the analysis of DEMs, *Earth Surface Processes and Landforms*, **22**, 563–580.

Dowdeswell, J.A., J.O. Hagen, H. Björnsson, A.F. Glazovsky, W.D. Harrison, P. Holmlund, J. Jania, R.M. Koerner, B. Lefauconnier, C.S.L. Ommanney and R.H. Thomas, 1997. The mass balance of circum-Arctic glaciers and recent climate change, *Quaternary Research*, **48**, 1–14.

Dyugerov, M.B. and M.F. Meier, 2005. Glaciers and the changing Earth system: A 2004 snapshot, Occasional Paper 58, Institute of Arctic and Alpine Research, University of Colorado, Boulder, Colorado, 1–117.

Dyurgerov, M.B. and M.F. Meier, 1997. Year-to-year fluctuations of global mass balance of small glaciers and their contribution to global sea-level change, *Arctic and Alpine Research*, **29**, 392–402.

Echelmeyer, K.A., W.D. Harrison, C.F. Larson, J., J.E. Mitchell, J. DeMallie, B. Rabus, G. Adalgeirsdóttir and L. Sombadier, 1996. Airborne surface profiling of glaciers: a case study in Alaska, *Journal of Glaciology*, **42**(142), 538–547.

Eiken, T., J.O. Hagen and K. Melvold, 1997. Kinematic GPS-survey of geometry changes on Svalbard glaciers, *Annals of Glaciology*, **24**, 157–163.

El-Ashrey, M.R. and H.R. Wanless, 1967. Shoreline features and their changes, *Photogrammetric Engineering*, **33**, 184–189.

Elseberg, D.H., W.D. Harrison, K.A. Echelmeyer and R.M. Krimmel, 2000. Quantifying the effects of climate and surface change on glacier mass balance, *Journal of Glaciology*, **47**(159), 538–547.

ERDAS, 1997. ERDAS Field Guide, *Tech. rep.*, ERDAS Inc., Atlanta, Georgia.

Etzelmüller, B., G. Vatne, R.S. Ødegard and J.L. Sollid, 1993. Mass balance and changes of surface slope, crevasse and flow pattern of Erikbreen, Northern Spitsbergen: an application of a geographical information system (GIS), *Polar Research*, **12**(2), 131–146.

Favey, E., A. Geiger, G.H. Gudmundsson and A. Wehr, 1999. Evaluating the potential of an airborne laser scanning system for measuring volume changes of glaciers, *Geografiska Annaler*, **81A**(4), 555–561.

Favey, E. and A. Schlatter, 1998. Geoidbestimmung am Lac Lêman, *Tech. Rep. 282*, Institut für Geodäsie und Photogrammetrie, ETH, Zürich, Switzerland.

Favey, E., A. Wehr, A. Geiger and H.-G. Kahle, 2002. Some examples of European activities in airborne laser techniques and an application in glaciology, *Journal of Geodynamics*, **34**(3), 347–355.

FEMA, 2000. Map Modernisation Plan, Federal Emergency Management Agency, National Flood Insurance Program, Washington, D.C.

Filin, S. and B. Csathó, 2002. Improvement of elevation accuracy for mass-balance monitoring using in-flight laser calibration, *Annals of Glaciology*, **34**, 330–334.

Finsterwalder, R., 1954. Photogrammetry and glacier research with special reference to glacial retreat in the eastern Alps, *Journal of Glaciology*, **2**, 306–315.

Fleming, K.M., J.A. Dowdeswell and J. Oerlemans, 1997. Modelling the mass balance of northwest Spitsbergen glaciers and responses to climate change, *Annals of Glaciology*, **24**, 203–210.

Florinsky, I.V., 1998. Combined analysis of digital terrain models and remotely-sensed data in landscape investigations, *Progress in Physical Geography*, **22**(1), 33–60.

Førland, E.J. and I. Hansen-Bauer, 2002. Increased precipitation in the Norwegian Arctic: True or false?, *Climatic Change*, **46**, 458–509.

Fountain, A.G. and A. Vecchia, 1999. How many stakes are required to measure the mass balance of a glacier?, *Geografiska Annaler*, **81A**(4), 563–572.

Fowler, R.A., 2000. The low-down on lidar, *Earth Observation Magazine*, **9**(3).

Fox, A.J. and M.J. Gooch, 2001. Automatic DEM generation for Antarctic terrain, *Photogrammetric Record*, **19**(98), 275–290.

Fox, A.J. and A.-M. Nuttall, 1997. Photogrammetry as a research tool for glaciology, *Photogrammetric Record*, **15**(89), 725–737.

Fraser, C., D. Jonas and D. Turton, 1999. Report on 1998 airborne laser scanner trials, *Tech. rep.*, AAM Surveys, Brisbane, Queensland.

French, J.R., 2003. Airborne lidar in support of geomorphological and hydraulic modelling, *Earth Surface Processes and Landforms*, **28**, 321–335.

Fryer, J.G., J.H. Chandler and M.A.R. Cooper, 1994. On the accuracy of heighting from aerial photographs and maps: implications to process modellers, *Earth Surface Processes and Landforms*, **19**, 577–583.

Funk, M., R. Morelli and W. Stahel, 1997. Mass balance of Griesgletscher 1961-1994: different methods of determination, *Zeitschrift für Gletscherkunde und Glazialgeologie*, **33**(1), 41–55.

Garvin, J.B. and R.S. Williams, 1993. Geodetic airborne laser altimetry of Breidamerkurjökull and Skeidarájökull, Iceland and Jakobshavns Isbræ, West Greenland, *Annals of Glaciology*, **17**, 397–385.

Geiger, A., M. Cocard, Y. Peter and H-G. Kahle, 1994. Precise DGPS and self-calibrating laser altimetry for airborne marine geoid determination, Institute of Navigation, Satellite Division, 7th International Technical Meeting, Salt Lake City, Utah, 471–476.

Geist, T., E. Lutz and J. Stötter, 2003. Airborne laser scanning technology and its potential for applications in glaciology, *International Archives of Photogrammetry and Remote Sensing*, **34**(3).

Geist, T., H. Elvehøy, M. Jackson and J. Stötter, 2005. Investigations on intra-annual elevation changes using multi-temporal airborne laser scanning data: case study Engabreen, Norway, *Annals of Glaciology*, **42**, 195–201.

Ghosh, S.K., 1988. Analytical Photogrammetry, Pergamon Press, New York.

Giles, P.T. and S. Franklin, 1996. Comparison of derivative topographic surfaces of a DEM generated from stereoscopic SPOT images with field measurements, *Photogrammetric Engineering and Remote Sensing*, **62**(10), 1165–1171.

Gooch, M.J. and J.H. Chandler, 1999. Accuracy assessment of digital elevation models generated using the ERDAS Imagine Orthomax digital photogrammetric system, *Photogrammetric Record*, **16**(93), 519–531.

Gooch, M.J. and J.H. Chandler, 2001. Failure prediction in automatically generated digital elevation models, *Computers and Geosciences*, **27**, 913–920.

Granshaw, S.I., 1980. Bundle adjustment methods in engineering photogrammetry, *Photogrammetric Record*, **10**, 181–207.

Gregory, J.M. and J. Oerlemans, 1998. Simulated future sea-level rise due to glacier melt based on regionally and seasonally resolved temperature changes, *Nature*, **391**, 474–476.

Greuell, W. and J. Oerlemans, 2004. Narrowband-to-broadband albedo conversion for glacier ice and snow: equations based on modeling and ranges of validity of the equations, *Remote Sensing of Environment*, **89**(1).

Haeberli, W., 1998. Historical evolution and operational aspects of worldwide glacier monitoring, Haeberli, W., M. Hoelzle and S. Suter, eds., Into the Second Century of World Glacier Monitoring- Prospects and Strategies, A contribution to the IHP and GEMS. Prepared by the WGMS, UNESCO Publishing, Paris, 35–51.

Hagen, J.O., B. Etzelmüller and A.M. Nuttall, 2000. Runoff and drainage pattern derived from digital elevation models, Finsterwalderbreen, Svalbard, *Annals of Glaciology*, **31**, 147–152.

Hagen, J.O., O. Liestøl, E. Roland and T. Jørgensen, 1993. Glacier atlas of Svalbard and Jan Mayen, Norsk Polarinstitutt Meddelelser NR.129, Oslo.

Hagen, J.O. and O. Liestøl, 1990. Long-term glacier mass-balance investigations in Svalbard, 1950–1988, *Annals of Glaciology*, **14**, 102–106.

Hagen, J.O., K. Melvold, T. Eiken, E. Isaksson and B. Lefauconnier, 1999. Mass balance methods on Kongsvegen, Svalbard, *Geografiska Annaler*, **81A**(4), 593–601.

Hagen, J.O., K. Melvold, F. Pinglot and J.A. Dowdeswell, 2003. On the net mass balance of the glaciers and ice caps in Svalbard, Norwegian Arctic, *Arctic, Antarctic and Alpine Research*, **35**(2), 264–270.

Hagen, J-.O. and N. Reeh, 2003. *In situ* measurement techniques: land ice, Bamber, J.L. and A.J. Payne, eds., Mass Balance of the Cryosphere, Cambridge University Press, Cambridge, UK, 1–8.

Hall, S.A., I.C. Burke, D.O. Box, M.R. Kaufman and J.M. Stoker, 2005. Estimating stand structure using discrete-return lidar: an example from low-density fire-prone ponderosa pine forests, *Forest Ecology and Management*, **208**(1–3), 189–209.

Hambrey, M.J., M.R. Bennett, J.A. Dowdeswell, N.F. Glasser and D. Huddart, 1999. Debris entrainment and transfer in polythermal valley glaciers, *Journal of Glaciology*, **45**(149), 69–86.

Hansen, J. and D. Jonas, 2000. Airborne laser scanning or aerial photogrammetry for the mine surveyor, AAM Surveys, Brisbane, Queensland.

Hansen-Bauer, I. and E.J. Førland, 1998. Long-term trends in precipitation and temperature in the Norwegian Arctic: Can they be explained by changes in atmospheric circulation patterns?, *Climate Research*, **10**, 143–153.

Harding, D.J., M.A. Lefsky, G.G. Parker and J.B. Blair, 2001. Laser altimeter canopy height profiles- methods and validation for closed-canopy broad-leaved forests, *Remote Sensing of Environment*, **76**(3), 283–297.

Hastenrath, S. and A. Ames, 1995. Recession of Yanamarey glacier in Cordillera-Blanca, Peru, during the 20th century, *Journal of Glaciology*, **34**, L06501, doi:10.1029/2006GL029185.

Hodgson, M.E. and P. Bresnahan, 2004. Accuracy of airborne lidar-derived elevation: Empirical assessment and error budget, *Photogrammetric Engineering and Remote Sensing*, **70**(3), 331–339.

Hofmann-Wellenhof, B., H. Lichtenegger and J. Collins, 2001. GPS Theory and Practice, Springer Wien, New York.

Hofton, M.A, J.B Blair, J.-B Minster, J.R Ridgway, N.P Williams, J.L Bufton and D.L. Rabine, 2000. An airborne laser altimetry survey of Long Valley, California, *International Journal of Remote Sensing*, **21**(12), 2413–2437.

Hopkinson, C. and M.N. Demuth, 2006. Using airborne lidar to assess the influence of glacier downwasting on water resources in the Canadian Rocky Mountains, *Canadian Journal of Remote Sensing*, **32**(2), 212–222.

Howat, I.M., I. Joughin and T. Scambos, 2007. Rapid changes in ice discharge from Greenland outlet glaciers, *Science*, **315**(5818), 1559–1561.

Hubbard, A., I.C. Willis, M.J. Sharp, D.W.F. Mair, P.W. Nienow, B. Hubbard and H. Blatter, 2000. Glacier mass-balance determined by remote sensing and high-resolution modelling, *Journal of Glaciology*, **46**(154), 491–498.

Huising, E.J and L.M Gomes-Pereira, 1998. Errors and accuracy estimates of laser data acquired by various laser scanning systems for topographic applications, *ISPRS Journal of Photogrammetry and Remote Sensing*, **53**, 245–261.

IPCC, 2007. Climate Change 2007: The Physical Science Basis, Summary for Policymakers, *Tech. rep.*, Intergovernmental Panel on Climate Change, Geneva, Switzerland.

Isaksson, E., J. Kohler, V. Pohjola, J. Moore, M. Igarashi, L. Karlöf, T. Martma, H. Meijer, H. Motoyama, R. Vaikmäe and R.S.W. Van de Wal, 2005. Two ice-core δ^{18}O records from Svalbard illustrating climate and sea-ice variability over the last 400 years, *The Holocene*, **15**(4), 501–509.

Jacobsen, F.M. and W. Theakston, 1997. Monitoring glacier changes using a global positioning system in kinematic mode, *Annals of Glaciology*, **24**, 314–319.

James, T.D., 2003. Error Identification and Correction Methods for Automatically Derived Digital Elevation Models, (Ph.D. thesis, University of Leeds).

James, T.D., T. Murray, N.E. Barrand and S.L. Barr, 2006. Extracting photogrammetric ground control from lidar DEMs for change detection, *Photogrammetric Record*, **21**(116), 312–328.

Jiskoot, H., T. Murray and P. Boyle, 2000. Controls on the distribution of surge-type glaciers in Svalbard, *Journal of Glaciology*, **46**(154), 412–422.

Johannessen, O.M., K. Khvorostovsky, M.W. Miles and L.P. Bobylev, 2005. Recent ice-sheet growth in the interior of Greenland, *Science*, **310**(5750), 1013–1016.

Johns, T.C., R.E. Carnell, J.F. Crossley, J.M. Gregory, J.F.B. Mitchell, C.A. Senior, S.F.B. Tett and R.A. Wood, 1997. The second Hadley Centre coupled ocean-atmosphere GCM: Model description, spinup and validation, *Climate Dynamics*, **130**(2), 103–134.

Jonas, D. and P. Byrne, 2003. Airborne laser scanning: beyond its formative years, *Tech. rep.*, AAM Surveys, Brisbane, Queensland.

Joughin, I., 2002. Ice-sheet velocity mapping: a combined interferometric and speckle-tracking approach, *Annals of Glaciology*, **34**, 195–201.

Joughin, I., W. Abdalati and M. Fahnestock, 2004. Large fluctuations in speed on Greenland's Jakobshavn IsbræGlacier, *Nature*, **432**, 608–610.

Kääb, A., 2000. Photogrammetric reconstruction of glacier mass balance using kinematic ice-flow model: a 20 year time-series on Grubengletscher, Swiss Alps, *Annals of Glaciology*, **31**, 45–52.

Kääb, A., 2004. Combination of SRTM3 and repeat ASTER data for deriving alpine glacier flow velocities in the Bhutan Himalaya, *Remote Sensing of Environment*, **94**, 463–474.

Kääb, A., 2005. Remote sensing of mountain glaciers and permafrost creep, Schriftenreihe Physische Geographie, ISBN 3 85543 244 9.

Kääb, A. and M. Funk, 1999. Modelling mass balance using photogrammetric and geophysical data: a pilot study at Griesgletscher, Swiss Alps, *Journal of Glaciology*, **45**(151), 575–583.

Kääb, A. and M. Vollmer, 2000. Surface geometry, thickness changes and flow fields on creeping mountain permafrost: automatic extraction by digital image analysis, *Permafrost and Periglacial Processes*, **11**, 315–326.

Kaser, G., J.G. Cogley, M.B. Dyurgerov, M.F. Meier and A. Ohmura, 2006. Mass balance of glaciers and ice caps: Consensus estimates for 1961–2004, *Geophysical Research Letters*, **33**, L19501, doi:10.1029/2006GL027511.

Kasser, M. and Y. Egels, 2002. Digital Photogrammetry, Taylor and Francis, London.

Kennett, M. and T. Eiken, 1997. Airborne measurement of glacier surface elevation by scanning laser altimeter, *Journal of Glaciology*, **24**, 293–296.

Kilian, J., 1994. Calibration methods for airborne laser systems, *International Archives of Photogrammetry and Remote Sensing*, **30**(1), 42–46.

Kohler, J., T.D. James, T. Murray, C. Nuth, O. Brandt, N.E. Barrand, H.F. Aas and A. Luckman, 2007. Acceleration in thinning rate on western Svalbard glaciers, *Geophysical Research Letters*, **34**, L18502, doi:10.1029/2007GL030681.

Konecny, G., 2003. Geoinformation: Remote Sensing, Photogrammetry and Geographic Information Systems, Taylor and Francis, London.

Krabill, W., W. Abdalati, E.B. Frederick, S.S Manizade, C.F. Martin, J. Sonntag, R. Swift, R. Thomas, C. Wright and J. Yungel, 2000a. Greenland ice sheet: High-elevation balance and peripheral thinning, *Science*, **289**, 428–430.

Krabill, W., W. Abdalati, E.B. Frederick, S. Manizade, C.F. Martin, J. Sontag, R.N. Swift, R.H. Thomas, W. Wright and J. Yungel, 2002. Aircraft laser altimetry measurement of elevation changes of the Greenland ice sheet: technique and accuracy assessment, *Journal of Geodynamics*, **34**, 357–376.

Krabill, W., E.B. Frederick, S. Manizade, C.F. Martin, J. Sontag, R.N. Swift, R.H. Thomas, W. Wright and J. Yungel, 1999. Rapid thinning of parts of the southern Greenland ice sheet, *Science*, **283**, 1522–1524.

Krabill, W., E. Hanna, P. Huybrechts, W. Abdalati, J. Cappelen, B. Csatho, E.B. Frederick, S. Manizade, C.F. Martin, J. Sonntag, R.N. Swift, R.H. Thomas and J. Yungel, 2004. Greenland Ice-Sheet: Increased coastal thinning, *Geophysical Research Letters*, **31**, L24402, doi:10.1029/2004GL021533.

Krabill, W., R.H. Thomas, K. Jezek and S. Manizade, 1995a. Greenland ice sheet thickness changes measured by laser altimetry, *Geophysical Research Letters*, **22**(17), 3241–2344.

Krabill, W., R.H. Thomas, C.F. Martin, R.N. Swift and E.B. Frederick, 1995b. Accuracy of airborne laser altimetry over the Greenland ice sheet, *International Journal of Remote Sensing*, **16**, 1211–1222.

Krabill, W., C.W. Wright, R.N. Swift, E.B. Frederick, S.S Manizade, J. Yungel, C.F. Martin, J. Sonntag, M. Duffy, W. Huisander and J.C. Brock, 2000b. Airborne laser mapping of Assateague National Seashore Beach, *Photogrammetic Engineering and Remote Sensing*, **16**(1), 65–71.

Kraus, K. and N. Pfeifer, 1998. Determination of terrain models in wooded areas with with airborne laser scanner data, *ASPRS Journal of Photogrammetry and Remote Sensing*, **53**, 193–203.

Krimmel, R.M., 1987. Mass balance and volume of South Cascade Glacier, Washington, 1958–1985, Glacier Fluctuations and Climatic Change, Kluwer, Amsterdam, 193–207.

Krimmel, R.M., 1999. Analysis of difference between direct and geodetic mass balance measurements at South Cascade Glacier, Washington, *Geografiska Annaler*, **81A**(4), 635–658.

Kubik, K. and A.G. Botman, 1976. Interpolation accuracy for topographic and geological surfaces, *ITC Journal*, **2**, 236–274.

Lane, S.N., 2001. The measurement of river channel morphology, Gravel Bed Rivers V, New Zealand Hydrological Society, Wellington, New Zealand, 100–110.

Lane, S.N., T.D. James and M. Crowell, 2000. Application of digital photogrammetry to complex topography for geomorphological research, *Photogrammetric Record*, **16**(95), 793–821.

Lane, S.N., T.D. James, H.D. Pritchard and M. Saunders, 2003. Photogrammetric and laser altimetric reconstruction of water levels for extreme flood event analysis, *Photogrammetric Engineering and Remote Sensing*, **18**(104), 293–307.

Lane, S.N., K.S. Richards and J.H. Chandler, 1993. Developments in photogrammetry; the geomorphological potential, *Progress in Physical Geography*, **17**(3), 306–328.

Lane, S.N., K.S. Richards and J.H. Chandler, 1994. Developments in monitoring and terrain modelling of small-scale riverbed topography, *Earth Surface Processes and Landforms*, **19**, 349–368.

Latypov, D., 2002. Estimating relative lidar accuracy information from overlapping flight lines, *ISPRS Journal of Photogrammetry and Remote Sensing*, **56**, 236–245.

Latypov, D., 2005. Effects of laser beam alignment tolerance on lidar accuracy, *ISPRS Journal of Photogrammetry and Remote Sensing*, **59**(6), 361–368.

Lefauconnier, B. and J.O. Hagen, 1990. Glaciers and climate in Svalbard: Statistical analysis and reconstruction of the Brøggerbreen mass balance for the last 77 years, *Annals of Glaciology*, **14**, 148–152.

Lefauconnier, B., J.O. Hagen, Jon Børre Ørbæk, K. Melvold and E. Isaksson, 1999. Glacier balance trends in the Kongsfjorden area, western Spitsbergen, in relation to the climate, *Polar Research*, **18**(2), 307–313.

Lewin, J. and M.M.M. Manton, 1975. Welsh floodplain studies: the nature of floodplain geometry, *Journal of Hydrology*, **25**, 37–50.

Lewin, J. and M.J.C. Weir, 1977. Morphology and recent history of the Lower Spey, *Scottish Geographical Journal*, **93**, 45–51.

Li, Z., 1988. On the measure of digital terrain model accuracy, *Photogrammetric Record*, **12**(72), 873–877.

Li, Z., 1992. Variation of the accuracy of digital terrain models with sampling interval, *Photogrammetric Record*, **14**(79), 113–128.

Li, Z., 1993a. Mathematical models of the accuracy of digital terrain model surfaces linearly constructed from square gridded data, *Photogrammetric Record*, **14**(82), 661–674.

Li, Z., 1993b. Theoretical models of the accuracy of digital terrain models: an evaluation and some observations, *Photogrammetric Record*, **14**(82), 651–660.

van Lipzig, N.P.M., E. van Meijgaard and J. Oerlemans, 2002. The spatial and temporal variability of the surface mass balance in Antarctica: results from a regional climate model, *International Journal of Climatology*, **22**, 1197–1217.

Liu, H.X., Z.Y. Zhao and K.C. Jezek, 2007. Synergistic fusion of interferometric and speckle-tracking methods for deriving surface velocity from interferometric SAR data, *IEEE Geoscience and Remote Sensing Letters*, **4**(1), 102–106.

Luckman, A.J., T. Murray, R. de Lange and E. Hanna, 2006. Rapid and synchronous ice-dynamic changes in East Greenland, *Geophysical Research Letters*, **33**, L03503, doi:10.1029/2005GL025428.

Luthcke, S.B., H.J. Zwally, W. Abdalati, D.D. Rowlands, R.D. Ray, R.S. Nerem, F.G. Lemoine, J.J. McCarthy and D.S. Chinn, 2006. Recent Greenland ice mass loss by drainage system from satellite gravity observations, *Science*, **314**(5803), 1286–1289.

Lutz, E., T. Geist and J. Stötter, 2003. Investigations of airborne laser scanning signal intensity on glacial surfaces- utilising comprehensive laser geometry modeling and orthophoto modeling (a case study: Svartisheibreen, Norway), *International Archives of Photogrammetry and Remote Sensing*, **34**(3).

Maas, H.-G., 2000. Least-squares matching with airborne laserscanning data in a TIN structure, *International Archives of Photogrammetry and Remote Sensing*, **33**(3A), 548–555.

Maas, H.-G., 2001. On the use of pulse reflectance data for laserscanner strip adjustment, *International Archives of Photogrammetry and Remote Sensing*, **34**(3), 53–56.

Maas, H.-G., 2002. Methods for measuring height and planimetry discrepancies in airborne laserscanner data, *Photogrammetric Engineering and Remote Sensing*, **68**(9), 933–940.

Magnussen, S. and P. Boudewyn, 1998. Derivation of stand heights from airborne laser scanner data with canopy-based quantile estimators, *Canadian Journal for Research*, **28**, 1016–1031.

Makarovic, B., 1972. Information transfer in construction of data from sampled data, *Photogrammetria*, **28**(4), 111–130.

Mason, D.C, D.M Cobby, M.S Horritt and P.D Bates, 2003. Floodplain friction parameterisation in two-dimensional river flood models using vegetation heights derived from airborne scanning laser altimetry, *Hydrological Processes*, **17**(9), 1711–1732.

McIntosh, K., A. Krupnik and T. Schenk, 2000. Improvement of automatic DSM generation over urban areas using airborne laser scanner data, International Archives of Photogrammetry and Remote Sensing, vol. 33, 563–570.

Meier, M.F., 1984. Contribution of small glaciers to global sea level, *Science*, **226**, 1418–1421.

Meier, M.F., D.B. Bahr, M.B. Dyurgerov and W.T. Pfeffer, 2005. Comment on "The potential for sea-level rise: New estimates from glacier and ice cap area and volume distributions" by S.C.B Raper and R.J. Braithwaite, *Geophysical Research Letters*, **32**, L17501, doi:10.1029/2005GL023319.

Mills, J.P., D. Schneider, D.M. Barber and P.G. Bryan, 2003. Geometric assessment of the Kodak DCS Pro Back, *Photogrammetric Record*, **18**(103), 193–208.

Mitchell, J.F.B., T.C. Johns, J.M. Gregory and S.F.B. Tett, 1995. Climate response to increasing levels of greenhouse gases and sulphate aerosols, *Nature*, **376**, 501–504.

Monaghan, A.J., D.H. Bromwich, R.L. Fogt, S.H. Wang, P.A. Mayewski, D.A. Dixon, A. Ekaykin, M. Frezzotti, I. Goodwin, E. Isaksson, S.D. Kaspari, V.I. Morgan, H. Oerter, T.D. Van Ommen, C.J. Van der Veen and J.H. Wen, 2006a. Insignificant change in Antarctic snowfall since the International Geophysical Year, *Science*, **313**(5788), 827–831.

Monaghan, A.J., D.H. Bromwich and S.H. Wang, 2006b. Recent trends in Antarctic snow accumulation from Polar MM5 simulations, *Philosophical Transactions of the Royal Society A- Mathematical, Physical and Engineering Sciences*, **364**(1844), 1683–1708.

Monckton, C.G., 1996. An investigation into the spatial structure of error in digital elevation data, Innovations in GIS 1, Taylor and Francis, London, 201–211.

Montane, J.M. and R. Torres, 2006. Accuracy assessment of lidar saltmarsh topographic data using RTK GPS, *Photogrammetric Engineering and Remote Sensing*, **1**(9), 961–967.

Morgan, V.I., I.D. Goodwin, D.M. Etheridge and C.W. Wookey, 1991. Evidence from Antarctic ice cores for recent increases in snow accumulation, *Nature*, **354**(6348), 58–60.

Nuth, C., J. Kohler, H.F. Aas, O. Brandt and J.O. Hagen, 2007. Glacier geometry and elevation changes on Svalbard: a baseline dataset, *Annals of Glaciology*, **46**, 106–116.

Ohmura, A., 2004. Cryosphere during the 20th century, Sparks, R.S.J. and C.J. Hawksworth, eds., The State of the Planet; Frontiers and Challenges in Geophysics, Geophysical Monograph Series 150, AGU, Washington, D.C., 239–257.

Optech, 2005. ALTM System Specifications, Optech.

Østrem, G. and M. Brugman, 1991. Glacier and Mass Balance Measurements - A Manual for Field and Office Work, Canadian Inland Water Branch, reprint series No. 66.

Østrem, G. and N. Haakensen, 1999. Map comparison or traditional mass balance measurements: which methods is better?, *Geografiska Annaler*, **81A**(4), 703–711.

Paterson, W.S.B, 2001. The Physics of Glaciers, 3rd edition, Butterworth-Heinemann, Oxford.

Petzold, B., P. Reiss and W. Stossel, 1999. Laser scanning-surveying and mapping agencies are using a using a new technique for the derivation of digital terrain models, *ISPRS Journal of Photogrammetry and Remote Sensing*, **54**, 95–104.

Pohjola, V.A., T. Martma, H.A.J. Meijer, J.C. Moore, E. Isaksson, R. Vaikmäe and R.S.W. Van de Wal, 2002. Reconstruction of three centuries of annual accumulation rates based on the record of stable isotopes of water from Lomonosovfonna, Svalbard, *Annals of Glaciology*, **35**, 57–62.

Pope, A., A.J. Luckman and T. Murray, 2007. DEM quality assessment for quantification of glacier surface change, *Annals of Glaciology*, **46**, 189–194.

Rabus, B., M. Eineder, A. Roth and R. Bamler, 2003. The shuttle radar topography mission- A new class of digital elevation models acquired by spaceborne radar, *ISPRS Journal of Photogrammetry and Remote Sensing*, **57**, 242–262.

Raper, S.C.B. and R.J. Braithwaite, 2005. The potential for sea-level rise: New estimates from glacier and ice cap area and volume distributions, *Geophysical Research Letters*, **32**, L05502, doi:10.1029/2004GL021981.

Raper, S.C.B. and R.J. Braithwaite, 2006. Low sea-level rise projections from mountain glaciers and icecaps under global warming, *Nature*, **439**(19), 311–313.

Raper, S.C.B., O. Brown and R.J. Braithwaite, 2000. A geometric glacier model for sea level change calculations, *Journal of Glaciology*, **46**, 357–368.

Raper, V., J.L. Bamber and W.B. Krabill, 2005. Interpretation of the anomalous growth of Austfonna, Svalbard, a large Arctic ice cap, *Annals of Glaciology*, **42**, 373–379.

Reeh, N., 1999. Mass balance of the Greenland ice sheet: can modern observation methods reduce the uncertainty, *Geografiska Annaler*, **81A**(4), 753–742.

Reeh, N. and N. Gunderstrup, 1985. Mass balance of the Greenland ice-sheet at Dye 3, *Journal of Glaciology*, **31**(108), 198–200.

Reinhardt, W. and H. Rentsch, 1986. Determination of changes in volume and elevation of glaciers using digital elevation models from the Veragtferner, Ötzal Alps, Austria, *Annals of Glaciology*, **8**, 151–155.

Remondi, B.W., 1985. Performing centimeter level surveys in seconds with GPS carrier phase: initial results, *Navigation*, **32**(4), 368–400.

Rignot, E. and P. Kanagaratnam, 2006. Changes in the Velocity Structure of the Greenland Ice Sheet, *Science*, **311**(5763), 986–990.

Rignot, E., A. Rivera and G. Casassa, 2003. Contribution of the Patagonian icefields of South America to sea level rise, *Science*, **302**, 434–437.

Rignot, E. and R.H. Thomas, 2002. Mass Balance of Polar Ice Sheets, *Science*, **297**(5586), 1502–1506.

Rignot, E., R.H. Thomas, P. Kanagaratnam, G. Casassa, E. Frederick, S. Gogineni, W. Krabill, A. Rivera, R. Russell, J. Sonntag, R. Swift and J. Yungel, 2004. Improved estimation of the mass balance of glaciers draining into the Amundsen Sea sector of West Antarctica from the CECS/NASA 2002 campaign, *Annals of Glaciology*, **39**, 231–237.

Rignot, E., D.G. Vaughan, M. Schmeltz, T. Dupont and D. MacAyeal, 2002. Acceleration of Pine Island and Thwaites Glaciers, West Antarctica, *Annals of Glaciology*, **34**, 189–194.

Rippin, D.M., I.C Willis, N.S. Arnold, A.J. Hodson, J. Moore, J. Kohler and H. Björnsson, 2003. Changes in geometry and subglacial drainage of Midre Lovénbreen, Svalbard, determined from digital elevation models, *Earth Surface Processes and Landforms*, **28**, 273–298.

Sallenger, A.H., W. Krabill, R.N. Swift, J. Brock, J. List, M. Hansen, R.A. Holman, S. Manizade, J. Sontag, A. Meredith, K. Morgan, J.K. Yunkel, E.B. Frederick and H. Stockdon, 2003. Evaluation of airborne topographic lidar for quantifying beach changes, *Journal of Coastal Research*, **19**(1), 125–133.

San, B.T. and M.L. Suzen, 2005. Digital elevation model (DEM) generation and accuracy assessment from ASTER stereo data, *International Journal of Remote Sensing*, **26**(22), 5013–5027.

Sapiano, J., W.D. Harrison and K.A. Echelmeyer, 1998. Elevation, volume and terminus changes of nine glaciers in North America, *Journal of Glaciology*, **44**(146), 119–135.

Sato, T., J. Okuno, J. Hinderer, D.S. Macmillan, H.P. Plag, O. Francis, R. Falk and Y. Fukuda, 2006. A geophysical interpretation of the secular displacement and gravity rates observed at Ny Ålesund, Svalbard in the Arctic- effects of post-glacial rebound and present-day ice melting, *Geophysical Journal International*, **165**, 739–743.

Schenk, T., B. Csathó, C.J. van der Veen, H. Brecher, Y. Ahn and T. Yoon, 2005. Registering imagery to ICESat data for measuing elevation changes on Byrd Glacier, Antarctica, *Geophysical Research Letters*, **32**, L23S05, doi: 10.1029/2005GL024328.

Schenk, T., S. Seo and B. Csathó, 2001. Accuracy study of airborne laser scanning data with photogrammetry, *International Archives of Photogrammetry and Remote Sensing*, **34**(3), 113–118.

Shepherd, A. and D.J. Wingham, 2007. Recent sea-level contribution of the Antarctic and Greenland ice sheets, *Science*, **315**, 1529–1532.

Shepherd, A., D.J. Wingham, J.A.D. Mansley and H.F.J. Corr, 2001. Inland thinning of Pine Island Glacier, West Antarctica, *Science*, **291**(5505), 862–864.

Shi, J. and M. Cannon, 1995. Critical error effects and analysis in airborne DGPS positioning over large areas, *Manuscripta Geodaetica*, **69**, 261–273.

Skaloud, J., M. Kramer and K.P. Schwartz, 1996. Exterior orientation by direct measurement of camera position and attitude, *International Archives of Photogrammetry and Remote Sensing*, **31**(B3), 125–129.

Small, R.J., I.R. Beecroft and D.M. Stirling, 1984. Rates of deposition on lateral moraine embankments, Glacier de Tsidjoure, Valais, Switzerland, *Journal of Glaciology*, **30**, 275–281.

Smith, M.J., D.G. Smith, D.G. Tragheim and M. Holt, 1997. DEMs and ortho-images from aerial photographs, *Photogrammetric Record*, **15**(90), 945–950.

Smith, W.H.F. and P. Wessel, 1990. Gridding with continuous curvature splines in tension, *Geophysics*, **55**(3), 293–305.

Spikes, V.B., B.M. Csathó, G.S. Hamilton and I.M. Whillans, 2003a. Thickness changes on Whillans ice stream and ice stream C, West Antarctica, derived from laser altimeter measurements, *Journal of Glaciology*, **49**(165), 223–230.

Spikes, V.B., B. Csathó and I.M. Whillans, 1999. Airborne laser profiling of Antarctica ice streams for change detection, *International Archives of Photogrammetry and Remote Sensing*, **32**(3), 169–175.

Spikes, V.B., B.M. Csathó and I.M. Whillans, 2003b. Laser profiling over Antarctic ice streams: methods and accuracy, *Journal of Glaciology*, **49**(165), 315–321.

Thomas, R., W. Krabill, E. Frederick and K. Jezek, 1995. Thickening of Jakobshavns Isbræ, West Greenland, measured by airborne laser altimetry, *Annals of Glaciology*, **21**, 259–262.

Torlegard, K., A. Ostman and R. Lindgren, 1986. A comparative test of photogrammetrically sampled digital elevation models, *Photogrammetria*, **41**, 1–16.

Van de Wal, R.S.W. and M. Wild, 2001. Modelling the response of glaciers to climate change by applying volume-area scaling in combination with a high resolution GCM, *Climate Dynamics*, **18**, 359–366.

VanLooy, J., R. Forster and A. Ford, 2006. Accelerating thinning of Kenai Peninsula glaciers, Alaska, *Geophysical Research Letters*, **33**, L21307, doi:10.1029/2006GL028060.

Vaughn, C.R., J.L. Bufton, W.B. Krabill and D. Rabine, 1996. Georeferencing of airborne laser altimeter measurements, *International Journal of Remote Sensing*, **17**, 2185–2200.

Velicogna, I. and J. Wahr, 2005. Greenland mass balance from GRACE, *Geophysical Research Letters*, **32**, L18505, doi:10.1029/2005GL023955.

Velicogna, I. and J. Wahr, 2006a. Acceleration of Greenland ice mass loss in spring 2004, *Nature*, **443**, 329–331.

Velicogna, I. and J. Wahr, 2006b. Measurements of Time Variable Gravity Show Mass Loss in Antarctica, *Science*, **311**, 1754–1756.

Vosselman, G., 2002. On the estimation of planimetric offsets in laser altimetry data, *International Archives of Photogrammetry and Remote Sensing*, **34**(A3), 375–380.

Vosselman, G. and H.-G. Maas, 2001. Adjustment and filtering of raw laser altimetry data, Workshop on Airborne Laserscanning and Interferometric SAR for Detailed Digital Elevation Models, vol. 1, 40.

Wehr, A. and U. Lohr, 1999. Airborne laser scanning: an introduction and overview, *ISPRS Journal of Photogrammetry and Remote Sensing*, **54**, 68–82.

Welch, R., T. Jordan, H. Lang and H. Murakami, 1998. ASTER as a source for topographic data in the late 1990s, *IEEE Transactions on Geoscience and Remote Sensing*, **36**(4), 1282–1289.

Wessel, P. and W.H.F. Smith, 1998. New, improved version of generic mapping tool released, *EOS. Trans. AGU*, **79**(47), 579.

Westaway, R.M., 2001. Development of remote sensing methods for measurement of large gravel-bed braided rivers, (Ph.D. thesis, University of Cambridge.

Willis, I.C., N.S. Arnold, M.J. Sharp, J.-M. Bonvin and B. Hubbard, 1998. Mass balance and flow variations of Haut Glacier d'Arolla, Switzerland using digital terrain modelling techniques, Landform monitoring, modelling and analysis, Wiley, Chichester, 343–361.

Wingham, D.J., A.J. Ridout, R. Scharoo, R.J. Arthern and C.K. Shum, 1998. Antarctic elevation change from 1992 to 1996, *Science*, **282**(5388), 456–458.

Wingham, D.J., A. Shepherd, A. Muir and G.J. Marshall, 2006. Mass balance of the Antarctic ice sheet, *Philosophical Transactions of the Royal Society A- Mathematical, Physical and Engineering Sciences*, **364**(1844), 1627–1635.

Wise, S., 1998. The effect of GIS interpolation errors on the use of DEMs in geomorphology, Landform monitoring, modelling and analysis, Wiley, Chichester, 139–164.

Wolf, P.R., 1983. Elements of Photogrammetry, McGraw-Hill, New York.

Wolf, P.R. and B.A. Dewitt, 2000. Elements of Photogrammetry with Applications in GIS, McGraw-Hill, New York.

Wright, J.W. and P.A. Dahl, 1995. A cheap, quick and safe way of surveying glaciers, *Photogrammetric Record*, **15**(85), 43–50.

Zuo, Z. and J. Oerlemans, 1996. Modelling albedo and specific balance of the Greenland ice sheet: Calculations for the Sondre Stromfjord transect, *Journal of Glaciology*, **42**(141).

Zuo, Z. and J. Oerlemans, 1997. Contribution of glacier melt to sea-level rise since AD 1865; a regionally differentiated calculation, *Climate Dynamics*, **13**, 835–845.

Zwally, H.J., M.B. Giovinetto, J. Li, H.G. Cornejo, M.A. Beckley, A.C. Brenner, J.L. Saba and D. Yi, 2006. Mass changes of the Greenland and Antarctic ice sheets and shelves and contributions to sea-level rise: 1992-2002, *Journal of Glaciology*, **51**(175), 509–527.

Appendix

This appendix contains the C-shell script used to process full area DEMs from lidar flightlines in Generic Mapping Tools (GMT), using a tensioned spline interpolator (Appendix A1). The script was adapted to process DEMs for individual flightlines which were then differenced using GMT tools on the command line. Written by A.J. Luckman and N.E. Barrand and adapted by N.E. Barrand. Also included are scripts remblun.gawk (Appendix A2) and cloudthresh.gawk (Appendix A3) used to remove lidar elevation points above 800 m a.s.l., and remove points with intensity returns of zero, respectively. Written by S.L. Barr and N.E. Barrand.

Appendix A1

```
#! /bin/csh

# Output_coordinates:
# Corner1(E,N): 433431,8756892
# Corner2(E,N): 436431,8754992
# Corner3(E,N): 440131,8760292
# Corner4(E,N): 437231,8762292

# remember to test diff between 1st and last return (probably zero looking at the files)

set tl_northing = 8762292
set tl_easting  = 433431
set br_northing = 8754992
set br_easting  = 440131

#set R_aoi = -R433431/440131/8754992/8762292
set R_aoi = -R$tl_easting/$br_easting/$br_northing/$tl_northing
set utm_zone = 33
set epost = 1
set npost = $epost

if(0) then
  foreach z_col (3 4)
foreach tile (4328756 4348754 4348756 4348758 4348760 4368754 4368756 4368758 4368760
4368762 4388756 4388758 4388760 4408760)
```

```
if(1) dos2unix data/03221_Midreloven/$tile.asc

if(1) then # get just x,y,z from file
gawk -v z_col=$z_col ’{printf("%s\t%s\t%s\n", $1, $2, $z_col)}’ \
< data/03221_Midreloven/$tile.asc \
> xyz/$tile.$z_col.txt
endif

if(1) then
rm -f xyz/all.$z_col.txt
if(1) then # add tiles together
cat xyz/$tile.$z_col.txt >> xyz/all.$z_col.txt
endif
endif

end

if(1) then # convert from ascii to grd file
surface \
xyz/all.$z_col.txt \
$R_aoi \
-I$epost \
-Ggrd/all.$z_col.grd \
-V \
-C1 -N250 -T0.65 # recommended for topography
endif

if(1) then # make simple binary
grd2xyz grd/all.$z_col.grd $R_aoi -Zf > dem/all.$z_col.dem
endif

end
 endif

set pixels = ‘grdinfo grd/all.3.grd | gawk ’{if($10 == "nx:") printf("%d\n", $11)}’‘
set lines  = ‘grdinfo grd/all.3.grd | gawk ’{if($10 == "ny:") printf("%d\n", $11)}’‘
echo pixels = $pixels : lines = $lines
set dem_par = dem/all.3.dem_par
set dem = dem/all.3.dem

if(0) then # make dem_par file
rm -f $dem_par
echo "UTM" > temp
echo "other" >> temp
echo "21" >> temp
repeat 5 echo "" >> temp
```

```
echo $utm_zone >> temp
echo "0 500000" >> temp
echo "out" >> temp
repeat 3 echo "" >> temp
echo $pixels >> temp
echo $lines >> temp
echo $npost $epost >> temp
echo $tl_northing $tl_easting >> temp
create_dem_par $dem_par < temp
rm -f temp
endif

if(0) then #Make some pictures : NB height exaggerated x10
rashgt_shd $dem $dem $pixels $epost $npost 1 0 1 1 45.0 135.0 -1 500 1
rasshd $dem $pixels $epost $npost 1 0 1 1 45 135 1
endif

if(1) then
ras_linear dem/all.4.dem $pixels 1 0 1 1 0 100 1
endif
```

Appendix A2

```
# remblun.gawk#

# Removes x y z lidar pnts where z is equal to 0.
# Writes the remaining points out in x y z col format.

# Input: ascii column in X Y Z format (space/tab deliminated).
# Usage gawk -f remblun.gawk

< input > output{if( $3 > 0.0 ) print $1, $2, $3}
```

Appendix A3

```
# cloudthresh.gawk
# Removes x y z lidar pnts where z is greater than a command line set threshold.
# Writes the remaining points out in x y z col format.

# Input: ascii column in X Y Z format (space/tab deliminated).
# Usage: gawk -f cloudthresh.gawk

-v z=zthresh(int) < input > outputBEGIN{z_thresh = z;}{ if( $3 < z_thresh )
print $1, $2, $3}
```